A STUDY OF NUTATION DAMPERS WITH APPLICATION TO WIND INDUCED OSCILLATIONS

by

FRANÇOIS WELT

B.Sc., Ecole Polytechnique de Montréal, 1979
M.A.Sc., The University of British Columbia, 1983

A THESIS IN PARTIAL FULFILMENT OF

THE REQUIREMENTS FOR THE DEGREE OF

DOCTOR OF PHILOSOPHY

in

THE FACULTY OF GRADUATE STUDY

Department of Mechanical Engineering

We accept this thesis as conforming

to the required standard

THE UNIVERSITY OF BRITISH COLUMBIA

January 1988

3 9

Department of MECHANICAL ENGINEERING

The University of British Columbia
1956 Main Mall
Vancouver, Canada
V6T 1Y3

Date JAN 28, 1988

ABSTRACT

Energy dissipation due to sloshing liquid in torus shaped nutation dampers is studied using the potential flow model with nonlinear free surface conditions in conjunction with the boundary layer correction. Special consideration is given to the case of resonant interactions which were found to yield interesting damping characteristics. An extensive test program with the dampers undergoing steady-state oscillatory translation is then undertaken to establish the optimal damper parameters. Low liquid heights and large diameter ratios with the system operating at the liquid sloshing resonance are shown to result in increased damping, while low Reynolds numbers and presence of baffles tend to reduce the peak efficiency by restricting the action of the free surface. Tests with two-dimensional as well as three-dimensional models in laminar flow and boundary layer wind tunnels suggest that the dampers can successfully control both the vortex resonance and galloping types of instabilities. Applicability of the concept to vertically oscillating structures such as transmission lines is also demonstrated with dampers undergoing a rotational motion about their horizontal axis.

TABLE OF CONTENTS

LIST OF TABLES

LIST OF FIGURES

Figure Page

LIST OF SYMBOLS

a	damper inner to outer radius ratio, R_i/R_0
a_h	free parameter of the Hartlen-Currie lift oscillator model
a_1	Bessel function relation defined in Appendix III, p. 170
a_1^*	dimensionless expression for a_1 defined in Appendix III, p. 170
$\overline{a_1}$	amplitude coefficient of the correction velocity $\vec{u}_2$ defined in Appendix IV, p. 180
A	damper wall area
A_n	higher order terms of the added mass ratio M_a/M_l, $n = 1, ..., 4$; also used as coefficients of the polynomial fit for $\eta_{r,l}$ versus ϵ_0/d in Chapter 3, and C_{fy} versus α in Chapter 4
A_t	wind-tunnel test section area
A_0	aerodynamic model frontal area
AA_n	higher order terms of the reduced damping ratio $\eta_{r,l}$, $n = 1, 2, 3$
AAA_n	higher order terms of the energy ratio $E_{r,l}$, $n = 1, 2, 3$
AK_n	damper geometry dependent coefficients defined in Appendix III, pp. 168-169
b	nutation damper baffle width
b_h	free parameter of the Hartlen-Currie lift oscillator model
b_1	Bessel function relation defined in Appendix III, p. 171
b_1^*	dimensionless expression for b_1 defined in Appendix III, p. 171
$\overline{b_{1,2}}$	Bessel function relations defined in Appendix III, pp. 180-181
B	stability coefficient of the nonplanar solution, eq. III.4, p. 168
B_n	higher order terms of the added mass ratio M_a/M_l, $n = 1, ..., 4$
BB_3	higher order term of the reduced damping ratio $\eta_{r,l}$

BBB_3 higher order term of the energy ratio $E_{r,l}$

C stability coefficient for the nonplanar solution, eq. III.4, p. 168

C_d, C_{d1}, C_{d2} absolute damping coefficient of the one-degree-of-freedom, primary and auxiliary system, respectively

C_e equivalent absolute damping coefficient

C_{fy} aeorodynamic static side force coefficient, $F_y/[\rho_a d_m^2 L_m (V \cos\alpha)^2/2]$

C_{lr} aerodynamic lift coefficient normalized as $C_{lr} = C_l(U/U_r)^2$, where C_l is equivalent to C_{fy} for the moving circular cylinder

C_{l0} aerodynamic static lift coefficient

C_m aerodynamic moment coefficient for 3-D square prisms

CK_n damper geometry dependent variables defined in Appendix III, pp. 172-173

C_4 higher order term of the added mass ratio M_a/M_l defined in Appendix IV, p. 179

$C_n(\lambda_{ni}\hat{r})$ combined 1st and 2nd kind of Bessel function, $J_n(\lambda_{ni}\hat{r}) - \dfrac{J_n'(\lambda_{ni})}{Y_n'(\lambda_{ni})} Y_n(\lambda_{ni}\hat{r})$

d damper cross-section width or diameter

d_i damper inner tube outer diameter

d_m structure or aerodynamic model cross-section width or diameter

d_{mn} 2nd order mode shape coefficients for the potential function $\hat{\Phi}$ defined in Appendix III, pp. 169-170

$d_{1,\ldots,3}$ characteristic dimensions of a damper's sloping cross-section as defined in Fig. 33

D damper outer diameter

D_r aerodynamic drag force

$D_{1,\ldots,10}$ 2nd order amplitude coefficients for $\eta_{r,l}$ defined in Appendix V, p. 195; also used as 3rd order coefficients for $\hat{\Phi}$ in Appendix II ($n = 1,2$), pp. 165-166

DD_1	3rd order coefficient for $\hat{\Phi}$ defined in Appendix II, p. 165
DK_n	damper geometry dependent variables defined in Appendix III, pp. 172, 174
e_{mn}	2nd order mode shape coefficients for the potential function $\hat{\Phi}$ defined in Appendix III, p. 169-170
$\overline{e_1}, \overline{e_2}, \overline{e_{11}}, \overline{e_{22}}$	amplitude coefficients of the 2nd order component of $\vec{u}_2$ as defined in Appendix IV, pp. 181-182
E_d	total dissipated energy by the moving fluid per cycle
$E_{r,l}$	dissipated to total energy ratio, E_d/E_t
$E^*_{r,l}$	energy ratio accounting for Reynolds number, $E_{r,l}\sqrt{Re}$
E_t	total energy of the fluid moving with respect to the damper, eq. 37, p. 37
E_1, E_2	nonlinear coefficients of the 3rd order equation for f_{11}, ς_{21} defined in Appendix III, p. 174
f	exciting frequency
f_n	fundamental natural frequency of the system
f_{n1}, f_{n2}	1st and 2nd natural frequency of system in translation, respectively
f_{mn}	1st or 2nd order planar mode shape coefficients for the potential function $\hat{\Phi}$
f_{rot}	1st rolling natural frequency of the system
f_v	vortex shedding exciting frequency
F	sloshing force acting on the damper wall due to pressure
F^*	damper geometry dependent function defined in Appendix IV, p. 190
F_s	sloshing force transmitted from the fluid to the damper walls
F_y	aerodynamic static side force with respect to the model, $S_p \cos\alpha - D_r \sin\alpha$

$F_{ijkl,ijp}$ 2nd order amplitude coefficients for $\eta_{r,l}$ defined in Appendix V, p. 196

F_0 inertia force generated by the system without damping liquid; also used as the aerodynamic force acting on the system in Appendix VI

F_1 linear coefficient of the 3rd order nonlinear equation for f_{11}, eq. III.2, p. 167

g acceleration due to gravity

g_{nm} hyperbolic function relation defined in Appendix V, p. 196

G_i^{nm} hyperbolic function cross-product integrals defined in Appendix V, p. 196

$G1,..,5$ damper geometry dependent variables defined in Appendix III, pp. 167, 175

GG_i^{nm} hyperbolic function cross-product integrals defined in Appendix V, p. 196

h damper liquid height

$\hat{h}$ dimensionless damper liquid height, h/R_0

h' nutation damper baffle mid-height position

H full-scale structure height

$H3,4$ damper geometry dependent variables defined in Appendix III, p. 175

I total inertia for the rotating system

I_l liquid inertia for system in rotation

$I_{1,\ldots,9}$ Bessel function cross-product integrals defined in Appendix V, p. 193

IA Bessel function cross-product integrals defined in Appendix V, p. 195

ID_i^{nm}, IDD_i^{nm} Bessel function cross-product integrals defined in Appendix V, pp. 193-195

$I2$ combination of hyperbolic and Bessel function cross-products defined in Appendix V, p. 197

JA	Bessel function cross-product integrals defined in Appendix V, p. 195
JJ_{nmp}	Bessel function cross-product integrals defined in Appendix V, p. 194
$J2$	combinations of hyperbolic and Bessel function cross-products defined in Appendix V, p. 197
k	one-degree-of-freedom system stiffness
k_1	spring stiffness of the main system
k_2	spring torsional stiffness of the secondary system
k_{nm}, kk_{nm}	combinations of hyperbolic and Bessel function cross-products defined in Appendix V, p. 197
K_1, K_2, KK_1	nonlinear coefficients of the 3rd order equation for f_{11} defined in Appendix III, p. 167
KK_{nmp}	Bessel cross-product integrals defined in Appendix V, p. 194
l	square root of Reynolds number, i.e., $\sqrt{Re}$
l_p	length of the supporting damper platform, Fig. VI-5
l_{nm}, ll_{nm}	combinations of hyperbolic and Bessel function cross-products defined in Appendix V, p. 197
L	distance of damper center of gravity to pivoting point for the secondary system, Fig. VI-5
L_a	arm length of the pivoting system, Fig. 63
L_m	aerodynamic model length
LL_{nmp}	Bessel function cross-product integrals defined in Appendix V, p. 194
L^2_{nm}, $L_{nm}L_{pq}$, $L_{11}E_3$, $LL_{22}E_3$	2nd order components for $\eta_{r,l}$ defined in Appendix IV, pp. 184-185
m	mass per unit lenght of the full-scale structure
m_l	damping liquid mass of a single, full-scale damper unit
m_p	mass of the damper supporting platform

m_1	mass of the primary system in translation
m_2	equivalent mass of the secondary system
M	total mass of the oscillating system
M_a	added mass due to sloshing liquid
M_i	restoring moment of the torsional spring
M_e	1st modal mass of the structure, eq. VII.6, p. 202
M_l	total mass of the sloshing liquid
M_{nm}^2, $M_{nm}M_{pq}$, $M_{nm}N_{pq}$, $M_{nm}E_p$	2nd order components for $\eta_{r,l}$ defined in Appendix IV, pp. 185-188
$\vec{n}$	vector normal to the free surface
N_{nm}^2, $N_{nm}N_{pq}$, $N_{nm}E_p$	2nd order components for $\eta_{r,l}$ defined in Appendix IV, pp. 188-189
p	pressure exerted by the sloshing liquid
p_{nm}	3rd order coefficients of the potential function $\hat{\Phi}$, eq. II.4, p. 166
P_{11}^i	coefficients of the 3rd order equation for $\hat{\Phi}$ defined in Appendix III ($i = 1, 2$), pp. 171-172
q_i	damper inner tube hole size diameter
Q_{22}	coefficients of the 3rd order equation for $\hat{\Phi}$ defined in Appendix III, p.173
r	damper based moving coordinate in the radial direction
$\hat{r}$	dimensionless moving coordinate, r/R_0
r_{in}	2nd order coefficient for $\hat{\Phi}$ as defined in Appendix IV, p. 192
R	air stream Reynolds number, Vd/ν_a; also used as inner or outer radius in Appendix IV
Re	sloshing liquid Reynolds number, $\omega_e R_0^2/\nu_f$
R_i	damper inner radius

R_0	damper outer radius
s	secondary to primary mass ratio, m_2/m_1
s_0	$\omega_0^2 - \overline{\omega_n}^2(1+s)$
s_1, s_2	$f_{11}^2 - \varsigma_{11}^2$ and $f_{11}^2 + \varsigma_{21}^2$, respectively
S	area of the sloshing liquid's outer boundary
S_p	aerodynamic side force with respect to the flow direction
S_t	Strouhal number
$SUM1, ..., 5$	damper geometry dependent variables defined in Appendix III, pp. 167, 174
t	time
t_{nm}, tt_{nm}	Bessel function cross-products defined in Appendix V, p. 196
T_0	measure of the phase angle ψ_0 as defined in Fig. 19
u'	air stream turbulent intensity
$\vec{u}$	sloshing liquid velocity vector
u_f	free stream velocity for the turbulent boundary layer profile
u_{nm}	Bessel function cross-products defined in Appendix V, p. 196
$\vec{u}_2$	correction velocity due to liquid viscosity
U	air stream dimensionless velocity, $V/\omega_n d_m$; also used as the average potential energy of the sloshing liquid flow in eq. 37, p. 37
U_r	vortex resonance dimensionless velocity, $1/(2\pi S_t)$
U_0	dimensionless galloping onset velocity, $\eta_{r,a}/(\pi A_1)$
$\vec{U}_2$	magnitude of $\vec{u}_2$
v	volume of the damping liquid
v_{nm}, vv_{nm}	Bessel function cross-products integrals defined in Appendix V, p. 196

V	air stream velocity
$\vec{V}$	velocity of the damper walls in translation
V_n	component of $\vec{V}$ in the n direction
VS	damper geometry dependent variables defined in Appendix IV, p. 192
w_{nm}	Bessel function cross-products defined in Appendix V, p. 196
WS	damper geometry dependent variables defined in Appendix IV, p. 192
x	position of the damper in the direction of the excitation
X	output voltage variation in x direction
y	output voltage due to the system response
y_n	output voltage at the nth harmonic of y; also used to describe response of the two-degree of freedom system in Appendix VI (n=1,2), Fig. VI-4
Y	aerodynamic model tip displacement, normalized by d_m
Y_p	dimensionless deflection of the full-scale structure along its height
Y_1, Y_2	amplitude response of the primary and secondary system, respectively
z	position of the liquid along the vertical axis; also used as the vertical axis for the full-scale structure of Appendix VII
$\hat{z}$	dimensionless coordinate, z/R_0
α	air stream angle of attack
α_{mn}	hyperbolic function of the damper liquid height, $\tanh \lambda_{nm} \hat{h}$
β	excitation and damper geometry dependent variable defined in Appendix III, p. 171
β_1	1st order detuning parameter for $\frac{\hat{\omega}_{21}}{\hat{\omega}}$
β_2	2nd order detuning parameter for $\frac{\hat{\omega}_{21}}{\hat{\omega}}$

β_{nm}, β^*_{nm}	hyperbolic functions defined in Appendix V, p. 197
γ_{nm}	2nd order mode shape coefficient of potential function $\hat{\Phi}$ defined in Appendix III, pp. 169-170
Δ_{nm}	2nd order component of the potential function $\hat{\Phi}$
∇	gradient operator
∇_{nm}	2nd order component of the potential function $\hat{\Phi}$
ϵ	amplitude of the excitation velocity, $\epsilon_0\omega$
$\hat{\epsilon}$	dimensionless amplitude of the excitation velocity, ϵ/R_0
ϵ_0	amplitude of the displacement excitation
$\hat{\epsilon}_0$	dimensionless amplitude of the displacement, ϵ_0/R_0
ς_{nm}	1st or 2nd order mode shape coefficients of the potential function $\hat{\Phi}$
η	damping ratio of the oscillatory system, C_e/C_c, where C_c is the system critical damping coefficient
η_2	damping ratio of the secondary system
η_f	free surface elevation of the sloshing liquid
$\hat{\eta}_f$	dimensionless free surface elevation, η_f/R_0
$\eta_{r,a}$	aerodynamic reduced damping ratio, $4\pi\eta\dfrac{M}{\rho_a d_m^2 L_m}$
$\eta_{r,l}$	reduced damping ratio for the nutation damper, $\dfrac{C_e}{2\omega_e M_l}$
$\eta^*_{r,l}$	maximum value of $\eta_{r,l}$ over a range of frequency for a given amplitude of excitation
η_s, η_{s2}	primary and secondary system inherent damping ratio, respectively
θ	angular moving coordinate for the nutation damper
Θ	rotation of the secondary damping device

λ	power coefficient of the exponentially decaying velocity profile for $\vec{U}_2$ as defined in Appendix IV; also used as the exponent for the stability analysis in Appendices II and III
λ_{nm}	nutation damper eigenvalues, solution of $C'_n(\lambda_{nm}a) = 0$
Λ_{nm}	Bessel function relations defined in Appendix V, p. 193
μ	sloshing liquid absolute viscosity coefficient
ν_a	air stream kinematic viscosity coefficient
ν_f	sloshing liquid kinematic viscosity coefficient
ν_1	1st order detuning parameter for $\hat{\omega}$
ν, ν_2	2nd order detuning parameter for $\hat{\omega}$
ξ_{nm}	phase angle between excitation and potential function sinusoidal component of $\hat{\Phi}$
ρ	volumetric mass of the sloshing liquid
ρ_a	volumetric mass of the air stream
τ	dimensionless time, $\omega_{11}t$
τ_0, τ_1, τ_2	various time scales of the expansion defined in eq. 9, p. 18
Φ	potential function for the sloshing liquid flow field
$\Phi^{(n)}$	nth order in the series solution of $\Phi = \sum_n \epsilon^{nq}\Phi^n$, $q = 1/3, 1$
$\tilde{\Phi}$	potential function relative to the moving coordinates r, θ, z
$\hat{\Phi}$	dimensionless potential function, $\frac{\tilde{\Phi}}{R_0^2\omega_{11}}$
Φ_f	potential function for the damper solid body motion
φ_{nm}	phase angle between the excitation and the cosinusoidal component of the potential function $\hat{\Phi}$
ψ	phase angle between excitation and sloshing response
ψ_{nm}	2nd order component of the potential flow solution $\hat{\Phi}$

ψ_0 inherent phase angle between excitation and sloshing response

$\hat{\omega}$ dimensionless exciting frequency, ω_e/ω_{11}

ω_e excitation angular frequency, $2\pi f$

ω_n natural frequency of the one-degree-of-freedom system

$\overline{\omega_n}$ ω_n/ω_2

ω_{n1}, ω_{n2} 1st and 2nd natural angular frequency of the two-degree-of-freedom system, $2\pi f_{n1}$ and $2\pi f_{n2}$, respectively

ω_0 ratio of ω_1/ω_2

ω_1, ω_2 fundamental angular frequency of the primary and secondary system, respectively

ω_{nm} sloshing liquid natural frequencies, $\sqrt{\frac{\lambda_{11} g}{R_0} \tanh \lambda_{11} \hat{h}}$

Ω power coefficient of the exponentially decaying boundary layer correction velocity $\vec{u}_2$

Ω_{nm} 2nd order coefficient for the potential function $\hat{\Phi}$ defined in Appendices II, p. 164, and III, pp. 167, 169-170

ACKOWLEDGEMENT

The author wishes to thank Dr. V.J. Modi for his assistance as well as for providing much of the inspiration during the course of this thesis. The models used during the experiments were constructed in the machine shop and special thanks are due to the technicians for their high quality work and cooperation. Some of Dr. Gartshore's wind tunnel equipment was borrowed. His generosity in permitting its use is greatly appreciated. The fellow graduate students of the Department were very helpful in the realization of this project through the discussion and sharing of technical information. The author wants to express his appreciation for the research assistantship awarded from the Natural Sciences and Engineering Research Council of Canada's grant to Dr. Modi. The author is also very grateful to Louise for her moral support.

1. INTRODUCTION

1.1 Preliminary Considerations

A number of large structures such as smokestacks, tall buildings, bridges and other bluff bodies are known to oscillate under the action of the natural wind. Although there are many possible mechanisms for such behavior, it is the relatively low frequency cross-flow response generated by vortex resonance or galloping that has been often identified as the cause for structural damage. Vortex resonance takes place when the frequency of the alternate vortices in the wake of a structure, being governed by the Strouhal number, coincides with one of the natural frequencies of the structure itself (Fig. 1a). Large amplitudes can generally be reached under conditions of low inherent damping and favorable wind velocities. More recent occurrences involving tall smokestacks have been reported by Hirsch and Ruscheweyh[1], and Chaulia[2]. Conditions creating the presence of an asymmetry in the wake of a bluff body with the wind having a certain angle of attack may cause galloping. It is a type of self-induced oscillation which takes place when the body is aerodynamically unstable while the excitation is generated by the motion itself, as illustrated in Fig. 1(b). A classical example is the galloping of sleeted transmission lines under severe icing conditions.

Due to their widespread occurrences and the extent of damage, prediction and suppression of wind-induced oscillations have been the object of many studies. A

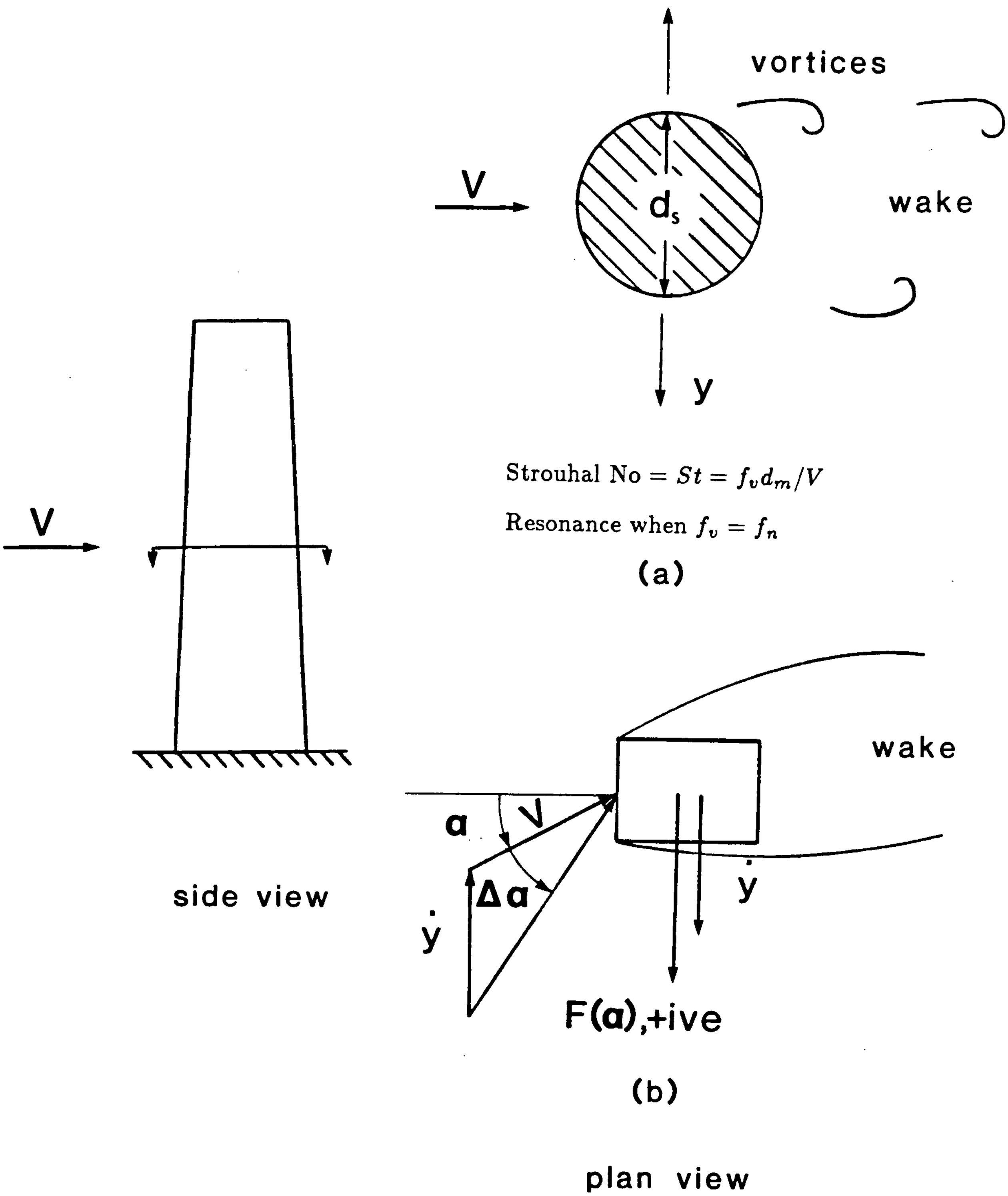

Fig. 1 Wind induced instabilities of bluff bodies undergoing: (a) vortex resonance; (b) galloping

common approach to reduce vortex resonance has dealt with the modification of the fluid mechanics responsible for the time dependent excitation and has led to the design of helical strakes, perforated shrouds, slats and other such devices (Fig. 2a). This is also referred to as an addition of external or aerodynamic damping. The concept of strakes has often been used around steel smokestacks and in ocean engineering applications, although the resulting increase in aero or hydrodynamic drag associated with most of these devices is a serious limitation.

As the response to wind excitations was also found to be quite sensitive to internal damping, another approach has been the installation of various types of passive devices such as tuned mass or impact dampers, hydraulic dashpots, etc. (Fig. 2b). A tuned mass damper essentially consists of an auxiliary mass attached to the main structure by a simple configuration which provides stiffness and damping. It is optimized to acheive minimum response of the primary system to a known excitation. The Stockbridge damper used on transmission lines is another example of such arrangements, where two heavy weights linked by a cable provide counteracting motion while energy is dissipated within the cable strands. Tower or bridge trusses can similarly be equipped with secondary masses supported by a rubber stem[3]. More sophisticated arrangements of counteracting masses have resulted in the development of active systems. The choice of material, size, and performance independent of the wind direction are of course important considerations in their designs.

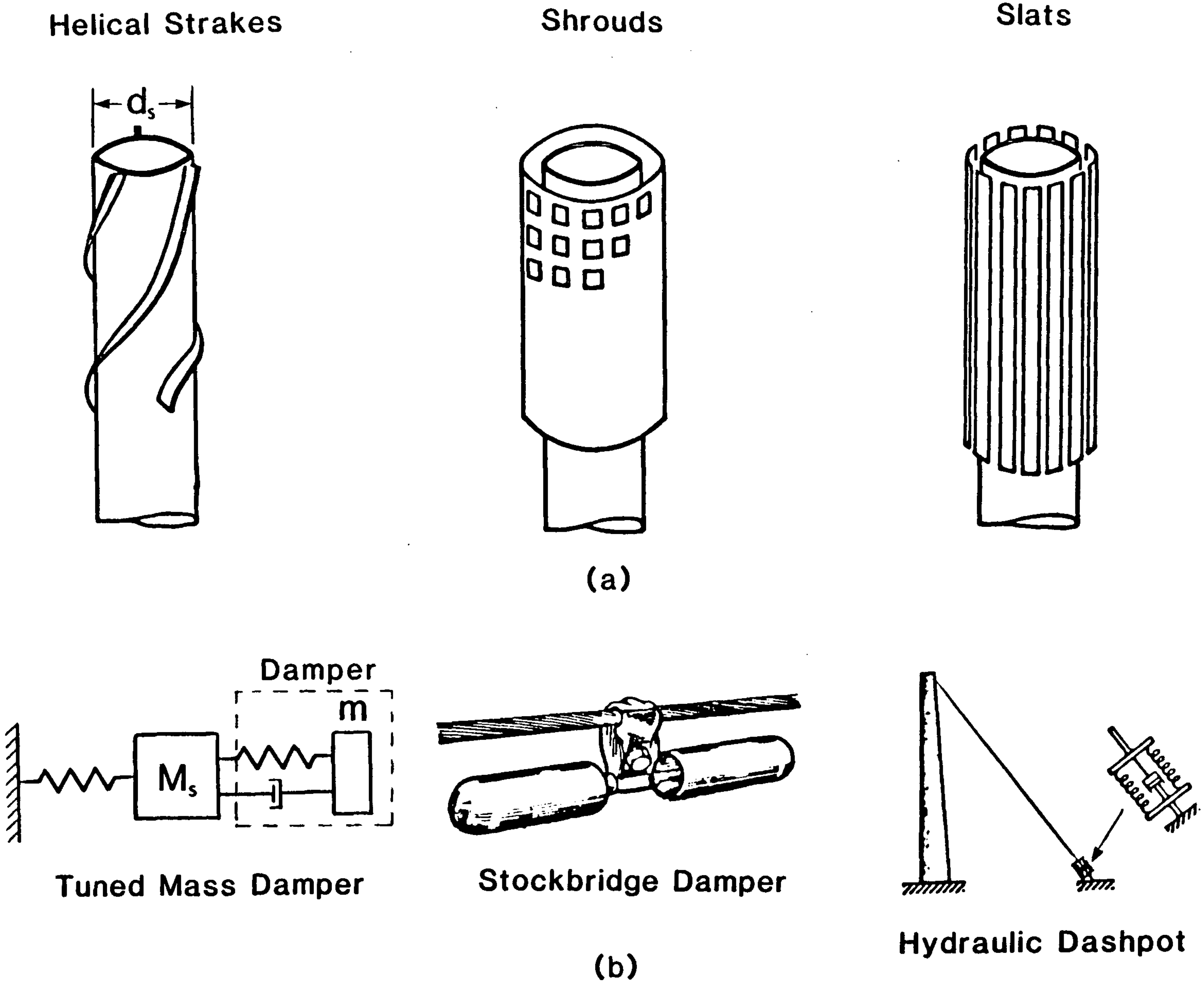

Fig. 2 Several typical devices providing: (a) external damping; (b) internal damping

In the same category of devices belongs a relatively simple concept involving the motion of a liquid within a closed container with dissipation of energy through the action of viscous and turbulent stresses. The presence of a free surface permits significant displacement of the sloshing fluid. This thesis proposes axisymmetric torus shaped containers, also called nutation dampers, as a means to suppress wind-induced oscillations. Motivation for the present investigation came from spacecraft technology where partially filled containers are frequently used to control very long period (90 minutes to around 24 hours) librational motion. As the frequency encountered in wind-induced instabilities of large structures is relatively low, typically less than 1 Hz, it seemed appropriate to explore applicability of nutation dampers to this class of problems.

1.2 Literature Survey

Scruton and Walshe[4] made a significant contribution to the suppression of the vortex resonance type of wind-induced oscillations with the concept of helical strakes for structures of circular cross-sections in the 1950's, while Price[5] introduced the perforated shrouds. A number of other aerodynamic devices, such as the slat configuration[6], were subsequently proposed. A comprehensive classification of the devices and comparative assessments were later undertaken by Zdravkovich[7], as well as Every, King and Weaver[8] who discussed the instabilities of immersed marine cables. Wong and Cox[9] drew a less extensive comparison scheme based on systematic wind tunnel tests. However, only a few studies such as the exploratory work by Naudascher et al.[10] have attacked the problem of galloping instabilities using this approach.

Meanwhile, ways of increasing energy dissipation within structures have received an equal amount of attention. In the 1960's, Reed[11] investigated the applicability of impact dampers to lightmasts and antennas. The installation of hydraulic dashpots on guyed structures was well illustrated by Den Hartog[12], and more recently the addition of viscoelastic material into the walls was modelled analytically by Gasparini et al.[13], with Ogendo et al.[14] presenting results on a full-scale steel smokestack foundation.

However, it is the tuned mass damper, also called dynamic vibration absorber, that has been most popular with a wide range of practical applications to bridges and towers, as indicated by Wardlaw and Cooper[15] as well as Hunt[16]. Performance of the device on steel smokestacks was evaluated and compared against that of helical strakes during wind tunnel tests in smooth flow by Ruscheweyh[17], and results in turbulent flow were given by Tanaka and Mah[18]. Stockbridge dampers, bearing the name of the inventor[19], are used extensively for controlling transmission line oscillations. Their application to this class of problems is still under investigation[20–21]. Several analytical schemes have also been developed by Schäfer and others[22–24] to predict the damped response of conductors. An extension of the concept of tuned mass dampers has been the introduction of active or semi-active systems including a feedback mechanism to control inertia forces[25]. They also have been considered for earthquake applications as indicated by Chowdhury et al.[26] and Yang[27]. Hirsch et al.[28–30] have reviewed this literature at some length.

Another interesting development has been to exploit the liquid motion within a closed container to design suitable dampers. Brunner[31] studied a full-scale tank containing viscous oil flowing through stacks of perforated plates on a smokestack, and Berlamont[32] considered the water tank of a tower fitted with baffles. However, it is Modi et al.[33] who first carried out wind tunnel tests to validate the idea. Very recently, Bauer[34] proposed utilizing the sloshing motion of two immiscible liquids within a rectangular container, while Kwek[35] used a tank of water to provide the auxiliary mass with energy dissipation taking place in the shock absorbers supporting the system.

Liquid sloshing has had limited success with ship stability[16], however, it has been used extensively to control nutation motion of satellites. Although many studies have dealt with its effect on satellite dynamics[36–41], relatively little is known about the damper behavior. A few experimental investigations have been reported by several authors[42–43]. Alfriend[44] tried to theoretically analyse the flow as a rigid slug moving inside the ring and Tossman[45] predicted damping characteristics for a tube fitted with a solid rolling ball. However, one has to turn to the early research efforts at agencies such as NASA or ABMA (which were concerned with fuel-rocket interactions), to find important information about liquid sloshing theory. These contributions are reviewed by Cooper[46] and Abramson[47]. Interests of civil engineers such as Jacobsen[48] and Housner[49–50], to predict water tank response under earthquake excitation, have also contributed to the field.

Earlier studies were aimed at analytical solutions of a potential function for linearized free surface conditions, with typical work by Graham and Rodriguez[51], and Chu[52] for rectangular and elliptical containers under harmonic excitation, respectively. Bauer[53] derived a theory for the straight wall torus. More complicated problems started to be examined, such as the compartimented cylindrical tank[54] or the flexible wall interaction based on a variational approach[55], sometimes requiring numerical procedures[56–58]. Equivalent mechanical models also emerged to simplify analysis[59–60] and reached a high degree of sophistication with models by Bauer[61] and the pendulum analogy by Sayar[62]. Meanwhile, nonlinear free surface conditions were included with Hutton's theory[63] for circular cylinders in particular, to be followed by Woodward and Bauer's approach[64] for the torus case. These formulations were then applied by Abramson[65] and Chen[66] to derive sloshing generated pressure forces on container walls, and were substantiated by experiments. Recently, Miles[67] derived a fairly general theory based on the variational principle proposed by Whitham[68] and others[69–70], and verified Hutton's results for circular cylinders[71]. He also included a solution procedure for the case of resonant interactions encountered in liquid sloshing[72]. This typically nonlinear behavior has been found in many ocean wave problems[77–78], as summarized by Philips[76], as well as in other areas of research[77–78].

Consideration for the damping terms came from Ocean Engineering in the 1950's, with Hunt[79] and Ursell[80] linearizing the momentum equations accounting for viscosity. Case and Parkinson[81] applied the theory to cylindrical containers undergoing small oscillations, while Miles[82] modified it to include surface tension effects. The method is frequently used nowadays[83–84], with additional consideration often given to nonlinear terms[85–86]. Experimental results were obtained by Silviera et al.[87] and Stephens et al.[88] for circular tanks with and without baffles, respectively, while Summer and Stophan[89] found damping characteristics for a spherical container based on a dimensional analysis. More recently, torus shaped nutation dampers were investigated during free vibration tests in a preliminary study[90] at the University of British Columbia.

1.3 Scope of the Investigation

Optimal efficiency of nutation dampers is first sought through a combination of theoretical and experimental procedures aimed at providing a better understanding of the energy dissipation mechanisms during liquid sloshing. Relatively low viscosity fluids are investigated using a nonlinear potential flow model in conjunction with the thin boundary layer correction. The associated theory derived by earlier investigators[53,63,64] for straight wall containers is extended to include a solution for the resonance of the higher order terms found to be present for a certain class of dampers. The method thus predicts the pressure and boundary layer damping forces and provides important information about the controlling parameters, resonant conditions, kinetic energy, etc.

This is followed by an extensive test program to assess validity of the theory as well as to supply more accurate data needed for practical applications. Emphasis is placed on the conditions for maximum damping by generally operating at the natural frequency of the first antisymmetric sloshing mode during free and forced oscillation tests, as suggested by previous investigations[90]. Performance of dampers fitted with additional devices such as baffles is reassessed in this process. The main objective is to arrive at an optimum combination of system parameters such as damper geometry (D, d, h), liquid properties (ρ, ν_f), and external variables of excitation amplitude (ϵ_0) and frequency (ω_e) leading to maximum dissipation of energy through liquid sloshing. Some of the variables are indicated in the sketch below.

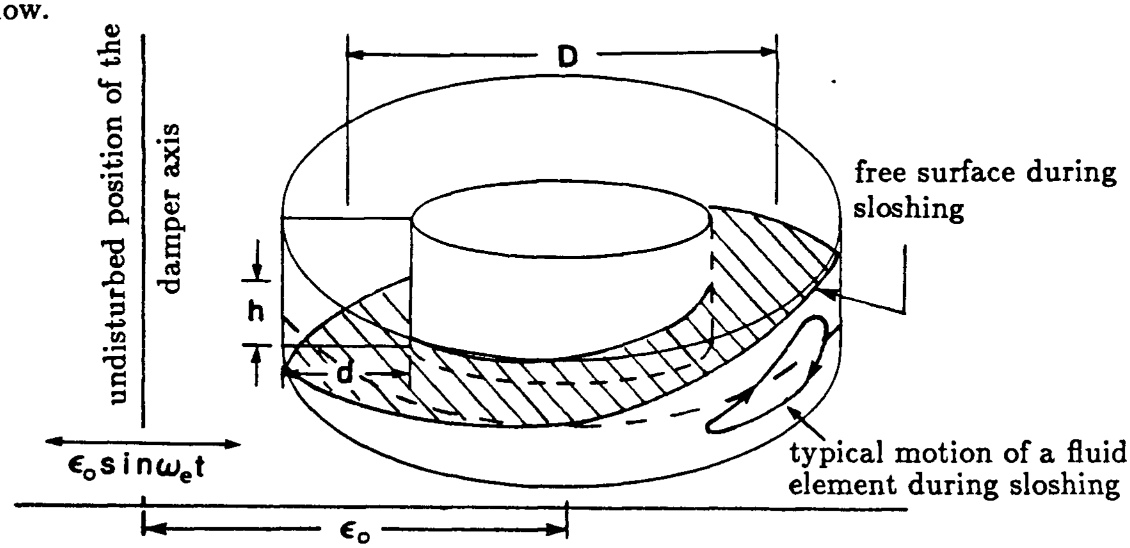

Application of the concept to control vortex resonance and galloping types of wind-induced oscillations is subsequently investigated during wind tunnel tests. Although a successful model to approximate response of circular cross-section geometries is not yet available, considerable experimental data have led to well established empirical procedures[91–92]. Furthermore, the galloping theory has shown to accurately predict oscillations of a square prism with viscous damping[93–94]. Experiments were therefore designed to permit analysis of the response based on this information. Elastically mounted circular and square cylinders fitted with various types of nutation dampers were tested in simulated conditions of smooth and turbulent winds using the closed circuit laminar flow and the boundary layer wind tunnels of the Department. The models underwent either two-dimensional plunging or three-dimensional rotational motion. Quantitative assessment of the damper performance under these highly nonlinear excitation conditions was carried out, and effect of the controlling parameters such as damper geometry, liquid height, internal configuration, etc., compared with the results obtained during the liquid sloshing study to arrive at final recommendations.

2. AN APPROXIMATE ANALYTICAL APPROACH TO PREDICT ENERGY DISSIPATION

2.1 Preliminary Remarks

The velocity field within a simple rigid torus damper oscillating harmonically in translation can be approximated by a potential flow solution with the assumptions that viscous effects are restricted to a small boundary layer region and the flow is laminar. An additional term accounting for the velocity profile at the walls is introduced to assess energy dissipation through the action of the viscous forces. The procedure is similar to the one adopted by Case and Parkinson[81]. Although the variational formulation has lately been quite popular to solve for the potential function, a conventional Eulerian approach is used here to exploit some of the results found by previous investigators. It should be noted that the study is restricted to straight wall dampers to facilitate understanding of the problem, and the pressure forces are calculated applying Bernouilli's equation at the boundaries.

2.2 Potential Flow Solution

2.2.1 Basic Equations

The potential function $\Phi(r, \theta, z, t)$ represents a solution of the differential equation,

$$\nabla^2 \Phi = 0, \tag{1}$$

with the boundary conditions:

$$\frac{\partial \Phi}{\partial n} = V_n \quad \text{at the wall;} \tag{2a}$$

$$\frac{\partial^2 \tilde{\Phi}}{\partial t^2} + g\frac{\partial \tilde{\Phi}}{\partial z} + 2\frac{\partial \tilde{\Phi}}{\partial r}\frac{\partial^2 \tilde{\Phi}}{\partial r \partial t} + \frac{2}{r^2}\frac{\partial \tilde{\Phi}}{\partial \theta}\frac{\partial^2 \tilde{\Phi}}{\partial \theta \partial t} + \ldots = 0; \tag{2b}$$

representing combined kinetic and kinematic conditions at the free surface. Here:

$\Phi = \tilde{\Phi} + \Phi_f$;

$\tilde{\Phi}$ = potential function relative to moving coordinates r, θ, z;

Φ_f = potential function for the damper solid body motion.

Other geometric variables are illustrated in Fig. 3.

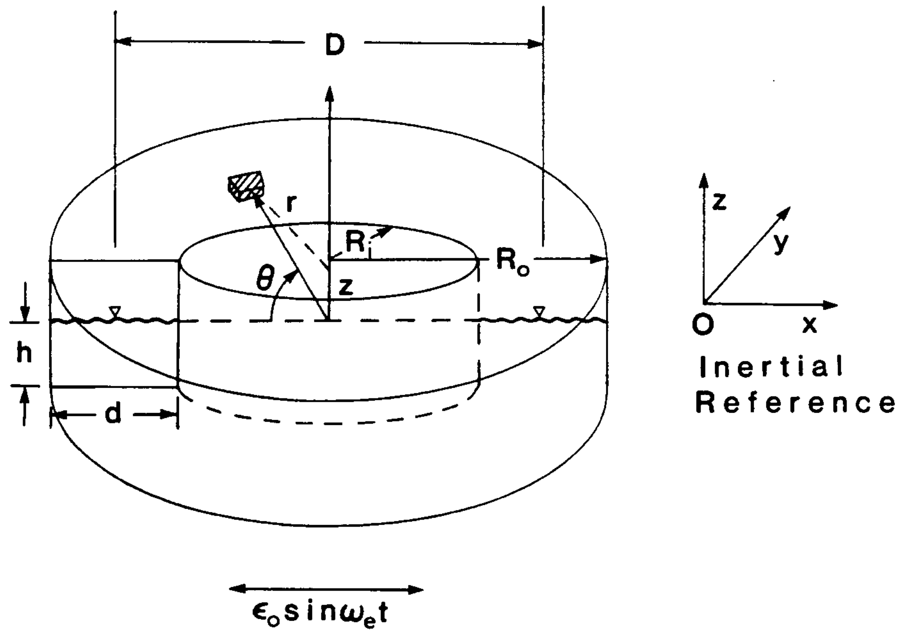

Fig. 3 Geometry of the square section damper selected for analytical study

At this stage, it is convenient to define the dimensionless parameters:

- potential function : $\hat{\Phi} = \dfrac{\tilde{\Phi}}{R_0^2 \omega_{11}}$;
- moving coordinates : $\hat{r} = \dfrac{r}{R_0}$, $\hat{z} = \dfrac{z}{R_0}$;
- excitation amplitude and frequency : $\hat{\epsilon}_0 = \dfrac{\epsilon_0}{R_0}$, $\hat{\omega} = \dfrac{\omega_e}{\omega_{11}}$;
- time : $\tau = \omega_{11} t$.

2.2.2 Linear Solution

As the free surface occupies different orientations during the damper motion, a standard Taylor series expansion of equation (2b) around $z = 0$ is used and a linear solution obtained by neglecting second and higher order terms (Appendix I). Applying the procedure of separation of variables, the linearized system yields a solution in terms of the Fourier-Bessel expansion, as found by Bauer[53], and is presented here in a dimensionless form:

$$\hat{\Phi} = \hat{\epsilon} \sum_i f_{1i} C_1(\lambda_{1i} \hat{r}) \frac{\cosh \lambda_{1i}(\hat{z} + \hat{h})}{\cosh \lambda_{1i} \hat{h}} \cos\theta \cos\hat{\omega}\tau; \tag{3a}$$

where:

$\hat{\epsilon}$ = dimensionless amplitude of the disturbance, $\hat{\epsilon}_0 \hat{\omega}$;

f_{1i} = amplitude coefficient of mode (1,i), i.e. 1st circumferential,

ith transverse mode, $\dfrac{[C_1(\lambda_{1i}) - aC_1(\lambda_{1i} a)]}{[(\hat{\omega}_{1i}/\hat{\omega})^2 - 1]\Lambda_{1i}}$; (3b)

with:

$$a = \frac{R_i}{R_0}, \quad \text{and} \quad \Lambda_{1i} = \frac{1}{2}[C_1^2(\lambda_{1i})(\lambda_{1i}^2 - 1) - C_1^2(\lambda_{1i} a)(\lambda_{1i}^2 a^2 - 1)];$$

ω_{1i} = liquid natural angular frequency in mode (1,i), i.e., $\dfrac{\lambda_{1i} g}{R_0} \alpha_{1i}$;

λ_{1i} = eigenvalue for mode (1,i), representing solution of:

$$C_1'(\lambda_{1i}) = 0, \quad \text{with} \quad C_1(\lambda_{1i}\hat{r}) = J_1(\lambda_{1i}\hat{r}) - \frac{J_1'(\lambda_{1i})}{Y_1'(\lambda_{1i})} Y_1(\lambda_{1i}\hat{r});$$

$$\text{and} \quad \alpha_{1i} = \tanh(\lambda_{1i}\hat{h}), \quad \hat{h} = \frac{h}{R_0}.$$

Note J_1 and Y_1 are Bessel functions of the first and second kind, order one, respectively, and prime denotes differentiation with respect to $\hat{r}$. Of course, the linear solution cannot be expected to be accurate for higher disturbing amplitudes $\hat{\epsilon}$, and is not valid near resonance as the expression for $\hat{\Phi}$ becomes very large and goes to infinity for $\omega_e = \omega_{1i}$. Two cases are therefore considered to extend the analysis to the nonlinear range.

2.2.3 Nonlinear, Nonresonant Solution ($\omega_e \not\approx \omega_{1i}$)

A perturbation method is applied using the process of iteration valid for small parameters $\hat{\epsilon}$ where a third order expansion is assumed, i.e.,

$$\hat{\Phi} = \hat{\epsilon}\hat{\Phi}^{(1)} + \hat{\epsilon}^2\hat{\Phi}^{(2)} + \hat{\epsilon}^3\hat{\Phi}^{(3)} + \dots \quad . \tag{4}$$

Here $\hat{\epsilon}\hat{\Phi}^{(1)}$ is the linear term of section 2.2.2, and $\hat{\Phi}^{(2)}$ can be derived by substituting for $\hat{\epsilon}\hat{\Phi}^{(1)}$ in the second order free surface condition (Appendix I.2). It is found (Appendix II.1) that,

$$\hat{\Phi}^{(2)} = \sum_n \Big[f_{0n} C_0(\lambda_{0n}\hat{r}) \frac{\cosh\lambda_{0n}(\hat{z}+\hat{h})}{\cosh\lambda_{0n}\hat{h}} + f_{2n} C_2(\lambda_{2n}\hat{r}) \frac{\cosh\lambda_{2n}(\hat{z}+\hat{h})}{\cosh\lambda_{2n}\hat{h}} \cos 2\theta \Big] \sin 2\hat{\omega}\tau,$$

where:

f_{0n}, f_{2n} = amplitude coefficients of (0,n), (2,n) mode, respectively;

$\lambda_{0n}, \lambda_{2n}$ = eigenvalues of (0,n), (2,n) mode, respectively, i.e.,

$$\text{solution of}: \quad C_0'(\lambda_{0n}a) = 0 \quad \text{and} \quad C_2'(\lambda_{2n}a) = 0.$$

$\hat{\Phi}^{(3)}$ can similarly be obtained although it was not considered here. The stability condition is presented in Appendix II.2. The solution is not always valid due to the resonance of the nonlinear higher modes at certain values of $\hat{\omega}$, as discussed in section 2.2.5 later. The occurrence of such singularities is, however, localized to a small range of excitation frequencies and is generally not dealt with in this study. One case of interest involves the first transverse, second circumferential mode responsible for the resonant interactions around $\hat{\omega} = 1$, and is treated in the next section.

2.2.4 Nonlinear, Resonant Solution ($\omega_e \approx \omega_{1i}$)

A different expansion is required for the solution around the first axisymmetric circumferential mode ($\hat{\omega} \approx 1$) by taking the excitation to be of the order of the nonlinear terms in equation (2b), i.e.,

$$\hat{\Phi} = \hat{\epsilon}^q \hat{\Phi}^{(1)} + \hat{\epsilon}^{2q} \hat{\Phi}^{(2)} + \hat{\epsilon}^{3q} \hat{\Phi}^{(3)} + ..., \tag{5}$$

where $q \leq 1$, determined through the iterative process. A detuning equality required to eliminate secular terms is defined as

$$(\frac{1}{\hat{\omega}})^2 = 1 - \nu_1 \hat{\epsilon}^q - \nu_2 \hat{\epsilon}^{2q} - ... \quad . \tag{6}$$

The first order equation reduces to the free vibration linear case, i.e.,

$$\frac{\partial^2 \hat{\Phi}^{(1)}}{\partial \tau^2} + \frac{1}{\alpha_{11}\lambda_{11}} \frac{\partial \hat{\Phi}^{(1)}}{\partial z} = 0, \tag{7}$$

for the first transverse mode shapes oscillating at the natural frequencies ω_{1i}, and by neglecting the higher modes leads to the solution of the form

$$\hat{\Phi}^{(1)} = C_1(\lambda_{11}\hat{r}) \frac{\cosh \lambda_{11}(\hat{z} + \hat{h})}{\cosh \lambda_{11}\hat{h}} \Big[f_{11} \cos(\theta + \varphi_{11}) \cos \hat{\omega}\tau + \varsigma_{11} \sin(\theta + \xi_{11}) \sin \hat{\omega}\tau \Big], \tag{8}$$

where f_{11}, ς_{11} are the amplitude coefficients for the solution, and φ_{11}, ξ_{11} are the phase angles in θ. However, for the case where higher circumferential natural frequencies are multiple of the first mode ($\omega_{n1} \approx n\omega_{11}$), additional significant terms appear in equation (8). This is the condition for resonant interactions treated separately in the subsequent analysis.

2.2.4.1 No Interactions ($\omega_{n1} \not\approx n\omega_{n1}$)

The analysis is similar to Hutton's theory for circular cylinders[63] with a major difference in the type of Bessel functions describing the transverse modes. Only a short outline of the procedure and results, useful to introduce the next case, is therefore pesented. Second and third order expressions are found in terms of $\hat{\Phi}^{(1)}$ by substituting relation (8) into (2b). The exponent of the perturbation parameter is required to be $q = 1/3$, and the detuning parameters ν_1 and ν_2 of (6) as well as the coefficients f_{11}, ς_{11} and phase angles φ_{11}, ξ_{11} of (8) are found by setting the secular terms containing $\cos(\theta + \varphi_{11}) \cos \hat{\omega}\tau$ or $\sin(\theta + \xi_{11}) \sin \hat{\omega}\tau$ to zero in the

2nd and 3rd order free surface conditions while using a multiple time-scale analysis. The expansion

$$\tau = \tau_0 + \tau_1 + \tau_2 + ..., \tag{9}$$

where $\tau_0 = \tau$, $\tau_1 = \hat{\epsilon}^{1/3}\tau$, and $\tau_2 = \hat{\epsilon}^{2/3}\tau$, yields two limit cycles:

planar solution: $\varsigma_{11} = \varphi_{11} = \xi_{11} = 0$; and f_{11} satisfying

$$f_{11}(K_1 f_{11}^2 + \nu_2) + F_1 = 0; \tag{10a}$$

$$\text{stable for}: -\frac{F_1}{f_{11}}(\frac{F_1}{f_{11}} - 2K_1 f_{11}^2) < 0, \tag{10b}$$

$$\text{and} - \frac{F_1}{f_{11}}(\frac{F_1}{f_{11}} + KK_1 f_{11}^2) < 0; \tag{10c}$$

nonplanar solution: $\varphi_{11} = \xi_{11} = 0$; with f_{11} satisfying

$$f_{11}[-(KK_1 - 2K_1)f_{11}^2 + \nu_2] + \frac{K_1}{KK_1}F_1 = 0, \tag{11a}$$

$$\text{and} \quad \varsigma_{11}^2 = f_{11}^2 + \frac{F_1}{KK_1}\frac{1}{f_{11}}; \tag{11b}$$

$$\text{stable for}: \frac{-B \pm \sqrt{B^2 - 4C}}{2} < 0, \text{real}. \tag{11c}$$

Here ν_2 is a function of the excitation. F_1, K_1 and KK_1 are damper geometry dependent parameters while B and C vary with f_{11}, K_1, KK_1 (Appendix III.1).

The second order terms are

$$\hat{\Phi}^{(2)} = \nabla_{2n} \sin 2\theta \cos 2\hat{\omega}\tau + (\psi_{0n} + \psi_{2n} \cos 2\theta) \sin 2\hat{\omega}\tau, \tag{12a}$$

where:

$$\psi_{0n} = \Omega_{0n}(f_{11}^2 - \varsigma_{11}^2)C_0(\lambda_{0n}\hat{r})\frac{\cosh \lambda_{0n}(\hat{z} + \hat{h})}{\cosh \lambda_{0n}\hat{h}}; \tag{12b}$$

$$\psi_{2n} = \Omega_{2n}(f_{11}^2 + \varsigma_{11}^2)C_2(\lambda_{2n}\hat{r})\frac{\cosh \lambda_{2n}(\hat{z} + \hat{h})}{\cosh \lambda_{2n}\hat{h}}. \tag{12c}$$

2.2.4.2 Resonant Interactions ($\omega_{n1} \approx n\omega_{11}$)

It is found that, for dampers with a going to 1 and relatively small $\hat{h}$, higher natural frequencies of the first transverse mode tend to be near multiples of ω_{11}. For instance, $\omega_{21} = 1.99\omega_{11}$, $\omega_{31} = 2.96\omega_{11}$, etc., for $a = 0.9$ and $\hat{h} = 0.10$. This particular situation leads to relatively large terms in the nonlinear solution described in the previous section which would make the expansion invalid. The following development recognizes that the superharmonic modes multiple of ω_{11} are now solution of the 1st order free surface condition. The generating solution is then

$$\begin{aligned}
\hat{\Phi}^{(1)} =& C_1(\lambda_{11}\hat{r})\frac{\cosh\lambda_{11}(\hat{z}+\hat{h})}{\cosh\lambda_{11}\hat{h}}\Big[f_{11}\cos(\theta+\varphi_{11})\cos\hat{\omega}\tau \\
&\qquad + \varsigma_{11}\sin(\theta+\xi_{11})\sin\hat{\omega}\tau\Big] \\
&+ C_2(\lambda_{21}\hat{r})\frac{\cosh\lambda_{21}(\hat{z}+\hat{h})}{\cosh\lambda_{21}\hat{h}}\Big[f_{21}\cos(2\theta+\varphi_{21})\cos 2\hat{\omega}\tau \\
&\qquad + \varsigma_{21}\sin(2\theta+\xi_{21})\sin 2\hat{\omega}\tau\Big] \\
&+ C_3(\lambda_{31}\hat{r})\frac{\cosh\lambda_{31}(\hat{z}+\hat{h})}{\cosh\lambda_{31}\hat{h}}\Big[f_{31}\cos(3\theta+\varphi_{31})\cos 3\hat{\omega}\tau \\
&\qquad + \varsigma_{31}\sin(3\theta+\xi_{31})\sin 3\hat{\omega}\tau\Big] \\
&+ etc.,
\end{aligned} \tag{13}$$

where the number of interactions strictly depend on the damper geometry parameters a and $\hat{h}$. The problem, however, becomes quite complex with additional terms in $\hat{\Phi}^{(1)}$, and it is assumed that f_{31}, ς_{31}, f_{41}, etc., are small compared to the coefficients of the first two modes and can be neglected. This was found to be always true for a particular class of dampers (typically $0.5 \leq a \leq 0.6$) where only two interactions occurred. This study is also restricted to the planar mode, and contributions from nonplanar ς_{11} and f_{21} coefficients to stability requirements are ignored. $\hat{\Phi}^{(1)}$ thus reduces to

$$\hat{\Phi}^{(1)} = f_{11}\cos(\theta+\varphi_{11})C_1(\lambda_{11}\hat{r})\frac{\cosh\lambda_{11}(\hat{z}+\hat{h})}{\cosh\lambda_{11}\hat{h}}\cos\hat{\omega}\tau + \varsigma_{21}C_2(\lambda_{21}\hat{r})\sin(2\theta+\xi_{21})\frac{\cosh\lambda_{21}(\hat{z}+\hat{h})}{\cosh\lambda_{21}\hat{h}}\sin 2\hat{\omega}\tau. \quad (14)$$

A second detuning equality as in (6) is now introduced,

$$\frac{\hat{\omega}_{21}^2}{\hat{\omega}^2} = 4 - \beta_1\hat{\epsilon}^q - \beta_2\hat{\epsilon}^{2q} - ..., \quad (15)$$

and a procedure similar to that of the previous case is used to solve for ν_1, ν_2, β_1, β_2, f_{11}, ς_{21}, φ_{11} and ξ_{11}, with secular terms in $\cos(\theta+\varphi_{11})\cos\hat{\omega}\tau$ as well as $\sin(2\theta+\xi_{21})\sin 2\hat{\omega}\tau$ set to zero in both 2nd and 3rd order free surface conditions. This approach is similar to the one employed by Bajkowski et al.[95]. The coefficients f_{11}, ς_{21}, and phase angles φ_{11} and ξ_{11} are now function of the slow time scales τ_1 and τ_2 as defined in (9). Details of the analysis are given in Appendix III.2. The exponent of the perturbation is taken to be $q = 1/3$ as it is desirable to obtain a limiting solution that tends towards the previous case when the interactions become small. The results are as follows:

$$\varphi_{11} = 0, \quad \xi_{21} = -\frac{\pi}{2};$$

with f_{11} and ς_{21} solution of the 3rd order nonlinear system of equations:

$$\begin{aligned} f_{11}(K_1 f_{11}^2 + E_1\varsigma_{21}^2 + \nu_2) + F_1 &= 0; \\ \varsigma_{21}(K_2\varsigma_{21}^2 + E_2 f_{11}^2 + \beta_2) &= 0. \end{aligned} \quad (16)$$

Here $\nu_2 = \nu - a_1^* \varsigma_{21}$, and $\beta_2 = \beta - b_1^* \frac{f_{11}^2}{\varsigma_{21}}$, with ν and β functions of the excitation and damper geometry. The stability condition is represented by

$$(\frac{f_{11}}{\varsigma_{21}})^2 > \frac{-8a_1b_1}{b_1^2}, \tag{17}$$

as shown in Appendix III.2.3. The second order terms are of the form (Appendix III.2.1)

$$\begin{aligned}\hat{\Phi}^{(2)} =& (\psi_{1n}\cos\theta + \Delta_{1n}\cos 3\theta)\cos\hat{\omega}\tau + (\psi_{2n}\cos 2\theta + \Delta_{2n})\sin 2\hat{\omega}\tau \\ &+ (\psi_{3n}\cos 3\theta + \Delta_{3n}\cos\theta)\cos 3\hat{\omega}\tau + (\psi_{4n}\cos 4\theta + \Delta_{4n})\sin 4\hat{\omega}\tau, \quad (18a)\end{aligned}$$

where:

$$\psi_{mn} = \sum_n d_{mn} C_m(\lambda_{mn}\hat{r}) \frac{\cosh\lambda_{mn}(\hat{z}+\hat{h})}{\cosh\lambda_{mn}\hat{h}}; \tag{18b}$$

$$\Delta_{mn} = \sum_n e_{mn} C_p(\lambda_{pn}\hat{r}) \frac{\cosh\lambda_{pn}(\hat{z}+\hat{h})}{\cosh\lambda_{pn}\hat{h}}; \tag{18c}$$

with $p = 4 - m$, for $m = 1, 3, 4$; and $p = 0$, for $m = 2$.

2.2.5 Properties of the Potential Function

2.2.5.1 Variation with Damper Geometry

The amplitude coefficients f_{mn} and ς_{mn} of the various modes depend on the excitation and the damper flow boundary characterized by the variables a and $\hat{h}$. The effect of geometry on the first mode is contained in the terms F_1, K_1, KK_1, etc., as given by relations 3(b), 10(a) or 16. F_1 is the coefficient of the linear solution. It is not a function of $\hat{h}$, and its variation with a is not pronounced, ranging from

1.44 at $a = 0$ (limiting case of the circular cylinder) to 1.17 at $a = 0.5$, as shown in Fig. 4. All dampers should therefore exhibit similar properties in the linear range, i.e., away from resonance. The nonlinear terms are included in K_1 for the planar mode, or a combination of K_1, K_2, E_1, and E_2 for the case of resonant interactions, with KK_1 contributing to the stability of the motion (relation 10c). Unlike F_1, these terms are strongly dependent on a and $\hat{h}$. This is mainly due to the resonance of the nonlinear modes in the proximity of $\hat{\omega} = 1$. In general, K_1 increases as it approaches the natural frequency of one of the higher order terms. For the particular case of interactions with mode (2,1) dealt with in this study, the analysis yields a fairly low value for K_1, with large E_1, E_2 and K_2. Contribution of the latter parameters to the overall nonlinear behavior may however be modest as the amplitude of the interacting mode ς_{21} proved to be usually much smaller than f_{11}.

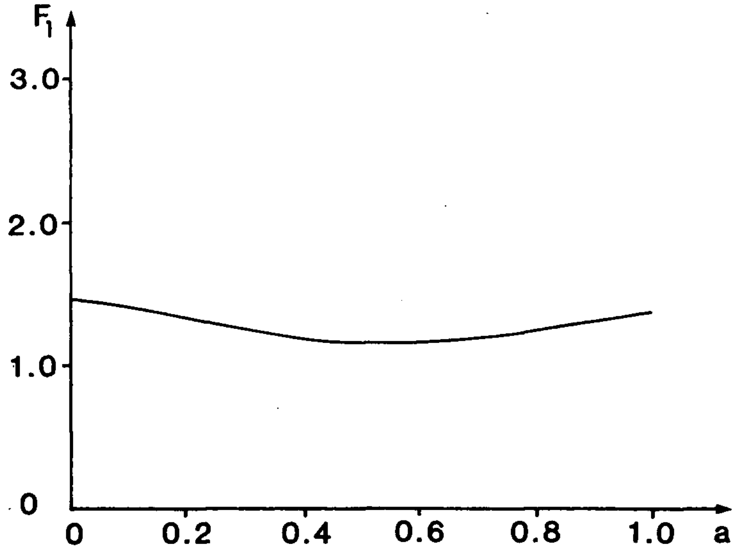

Fig. 4 Variation of the linear coefficient F_1 with a

Plots of the various coefficients versus a show these large fluctuations quite clearly, as illustrated by Fig. 5(a) and (b), for $\hat{h} = 0.1$ and 1.0, respectively. At low $\hat{h}$, resonance of the mode (2,1) is alrealdy felt at $a = 0.4$, with very large, negative K_1 beyond this point (Fig. 5a). The interactions, however, keep K_1 to the order of 0.5 or less, while E_1, E_2 and K_2 start to grow with increasing a. At high $\hat{h}$, resonance of both modes (2,2) and (0,2) result in very large, positive K_1 near $a = 0.20$ and 0.37, respectively (Fig. 5b). The latter becomes quite small beyond resonance, thus suggesting that the response in the first planar mode is very close to that given by the linear solution for $a \geq 0.6$. The motion is, however, quite unstable as KK_1 decreases as well. It should be noted that the potential flow solution was not derived for these resonant modes as they are confined to a narrow range, e.g., from $a = 0.35$ to 0.45 for $\hat{h} = 1.0$ with mode (0,2).

For a damper with a given a, the nonlinear terms can be quite dependent on the liquid height, as shown in Fig. 5(d). No interactions are present throughout the range of $\hat{h}$ considered, but K_1 varies significantly from negative to positive values crossing the x-axis at several points. Negative K_1 implies "hardening" characteristics, i.e., the resonant frequency increases with the amplitude of the excitation, whereas "softening" results from a positive value, and of course the solution is linear for $K_1 = 0$. This general behavior was noticed during earlier work on nonlinear sloshing[66] and can have interesting implications for maximizing energy dissipation, as the absence of nonlinearities theoretically yields infinite response amplitudes and damping at $\hat{\omega} = 1.0$. This condition is met here for $\hat{h} = 0.32$, 0.62 and 0.79, although the motion is unstable for the last two points due to small KK_1. At higher a, resonant interactions with the mode (2,1) are present at low $\hat{h}$ and the trends are similar to those mentioned earlier, i.e., small K_1 and growing E_1, E_2, and K_2 in the interacting region in contrast to a decreasing K_1 away from resonance (Fig. 5c for $a = 0.608$). However, fluctuations across the range of $\hat{h}$ are smaller here, and this damper is expected to be less sensitive to liquid height.

A brief examination of the terms controlling the nonplanar coefficient ς_{11}, i.e. K_1/KK_1 and $(KK_1 - 2K_1)$, suggests that this mode is equally sensitive to liquid height at $a = 0.308$ (Fig. 6a), and to the resonance of the higher modes as shown in Fig. 6(b) for $a = 0.608$.

2.2.5.2 <u>Variation with the Excitation</u>

The nonresonant solution is a function of the frequency $\hat{\omega}$ while the displacement velocity of the damper walls $\hat{\epsilon}$ affects the resonant response in two ways. Firstly, it generates higher nonlinear terms as it grows larger, usually resulting in lower amplitude coefficients f_{11} or ς_{11} as well as important shifts in the resonant frequency (softening or hardening characteristics), as governed by relations (10a), (11a) or (16). Secondly, the resonant region expands as it is required that

$$|\hat{\omega} - 1| < \frac{\nu_1}{2}\hat{\epsilon}^{1/3} + \text{higher order}, \tag{19}$$

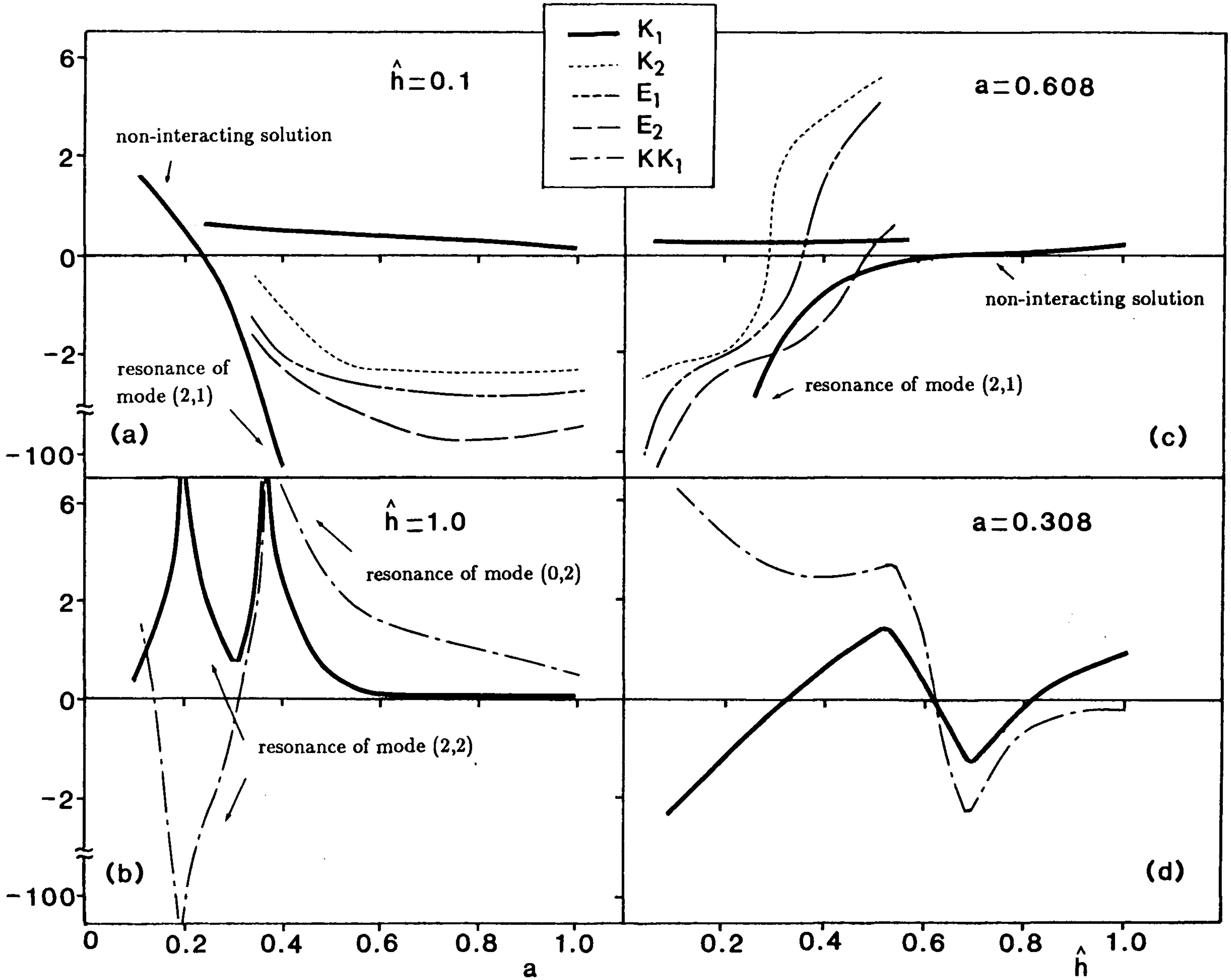

Fig. 5 Planar mode coefficients K_1, KK_1, E_1, E_2 and K_2 as affected by the damper geometry

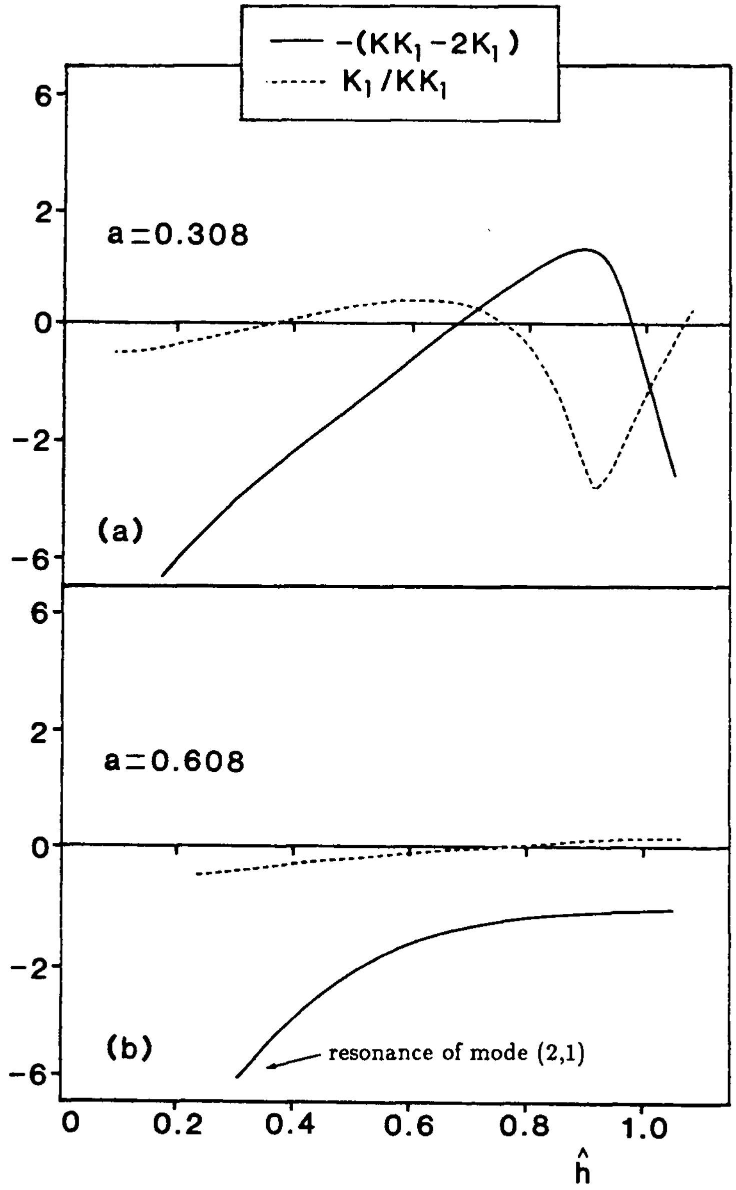

Fig. 6 Nonplanar coefficients $-(KK_1 - 2K_1)$ and K_1/KK_1 as functions of $\hat{h}$ for: (a) a=0.308; (b) a=0.608

from the detuning equality (6). This physically makes sense as a liquid originally sloshing in the nonresonant region under a small excitation may literally resonate at higher amplitudes, with the occurrence of the nonplanar motion. It is interesting to note that the same principle holds for the higher nonlinear modes. For instance, the 2nd order terms of the nonresonant solution should resonate when

$$|\frac{\hat{\omega}_{ln}}{\hat{\omega}} - 2| < \frac{\nu_0 \hat{\epsilon}}{4}, \tag{20}$$

where: $l = 0, 2$; $n = 1, 2, ...$; and ν_0 is of order 1 (Appendix II.1); a condition generally easier to meet with larger $\hat{\epsilon}$. Experiments, however, suggest that ν_0 does not need to be as high as 1, as discussed in Chapter 3. Thus more resonant interactions are expected at higher excitations.

To illustrate how the various regions overlap, Fig. 7(a) and (b) show f_{11}, normalized by $\hat{\epsilon}^{2/3}$ for the resonant solution to account for different expansions, versus $\hat{\omega}$. Two amplitudes $\hat{\epsilon}_0$ and damper geometries are considered. The coefficient f_{01} (now normalized by $\hat{\epsilon}^{4/3}$ at resonance) for the first configuration is presented in Fig. 7(c). Noteworthy are the hardening characteristics with increasing $\hat{\epsilon}_0$ displayed in Fig. 7(a), and the corresponding reduction in f_{11}, as opposed to more linear behavior of the damper with resonant interactions (Fig. 7b). A region with two equilibrium positions is usually present with f_{11} exhibiting the jump phenomenon as one branch ceases to exist or becomes unstable. In the case of $a = 0.608$, and $\hat{h} = 0.196$, both branches collapse near resonance ($\hat{\omega} = 0.98$) while another loop develops at a higher frequency. The interacting coefficient ς_{21} is shown as a fraction of f_{11} in Fig. 7(d) and stays small due to the stability requirements ($|\varsigma_{21}/f_{11}| \leq 0.32$ here, from relation 17).

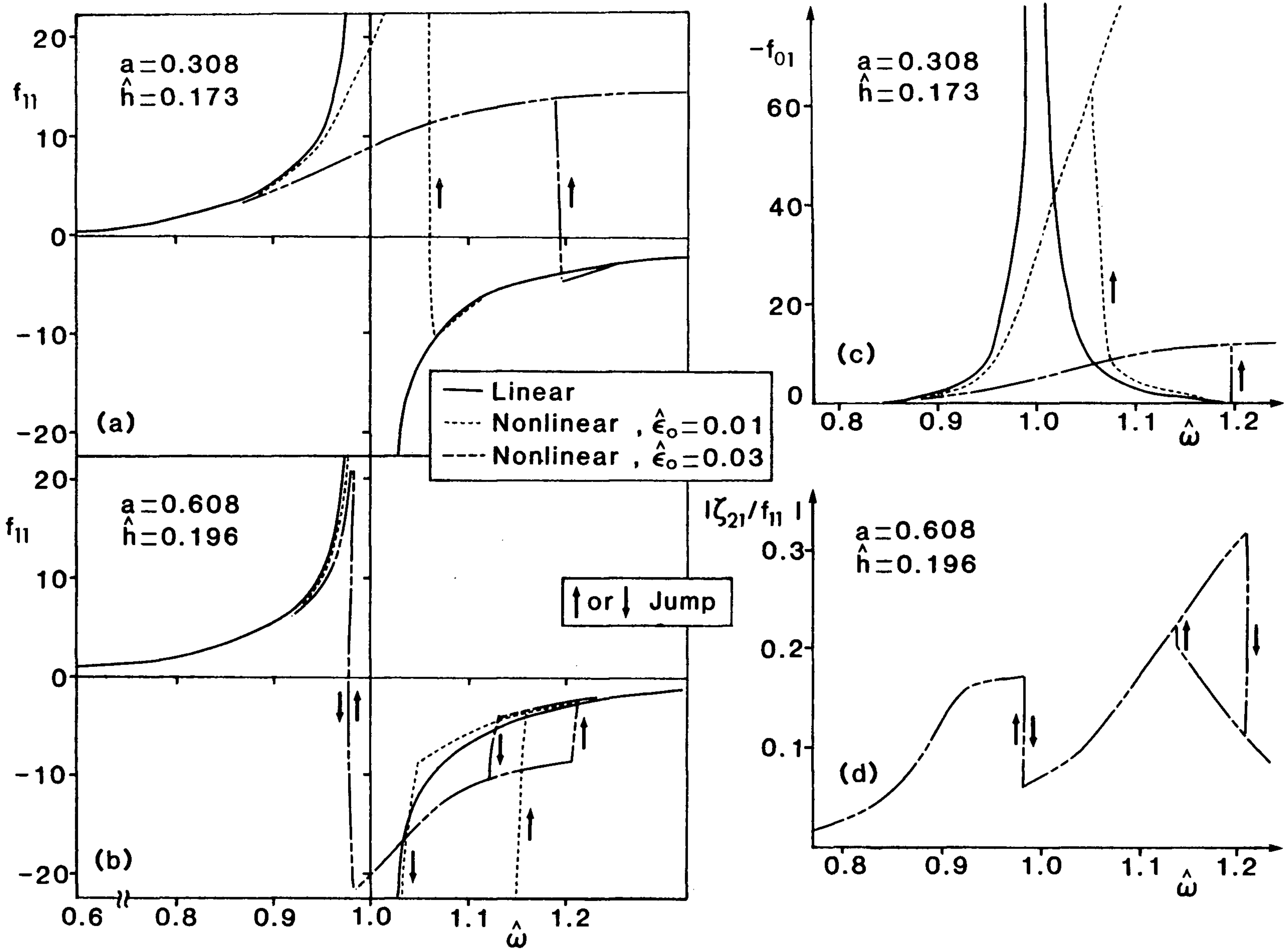

Fig. 7 Variation of f_{11}, f_{01} and ς_{21} versus $\hat{\omega}$ for different damper geometries and amplitudes

2.3 Pressure Forces

The liquid sloshing motion generates a nonuniform pressure on the container wall. The resulting force is

$$F = \int\int_A p\cos\theta dA, \tag{21}$$

where:

$A =$ vertical wall area in contact with the fluid;

$p =$ pressure exerted by the fluid.

p can be found using Bernouilli's equation for unsteady flow,

$$\frac{p}{\rho} + \frac{1}{2}(\nabla\tilde{\Phi})^2 + gz + \frac{\partial\Phi}{\partial t} = 0. \tag{22}$$

F can be nondimensionalized and expressed in terms of an added mass ratio as

$$\frac{M_a}{M_l} = -\frac{F}{M_l\omega_e^2\epsilon_0} - 1, \tag{23}$$

thus indicating the departure of the liquid from the behavior of a corresponding solid mass M_l. Results for the nonlinear potential flow solution, expanded to the 2nd order, are listed below with details of the derivations given in Appendix IV.1.1:

$$\text{(i)}\quad \frac{M_a}{M_l} = \frac{1}{\hat{h}(1-a^2)}\Big\{\sum_i f_{1i}\frac{\alpha_{1i}}{\lambda_{1i}}[C_1(\lambda_{1i}) - aC_1(\lambda_{1i}a)] - \hat{\epsilon}_0^2\hat{\omega}(A_1 - B_1)\Big\}\sin\hat{\omega}\tau - \frac{1}{\hat{h}(1-a^2)}\hat{\epsilon}_0^2\hat{\omega}(A_1 + B_1)\sin\hat{\omega}\tau; \tag{24a}$$

$$\text{(ii)}\quad \frac{M_a}{M_l} = \frac{1}{\hat{h}(1-a^2)}\Big\{\frac{1}{(\hat{\epsilon}_0\hat{\omega})^{2/3}}f_{11}\frac{\alpha_{11}}{\lambda_{11}}[C_1(\lambda_{11}) - aC_1(\lambda_{11}a)] - \frac{A_2}{\hat{\omega}}\Big\}\sin\hat{\omega}\tau - \frac{1}{\hat{h}(1-a^2)}\frac{B_2}{\hat{\omega}}\sin 3\hat{\omega}\tau; \tag{24b}$$

$$\text{(iii)}\quad \frac{M_a}{M_l} = \frac{1}{\hat{h}(1-a^2)}\Big\{\frac{1}{(\hat{\epsilon}_0\hat{\omega})^{2/3}}f_{11}\frac{\alpha_{11}}{\lambda_{11}}[C_1(\lambda_{11}) - aC_1(\lambda_{11}a)]$$

$$+ \frac{1}{(\hat{\epsilon}_0\hat{\omega})^{1/3}} A_3 - \frac{A_4}{\hat{\omega}} \Big\} \sin \hat{\omega}\tau + \frac{1}{\hat{h}(1-a^2)} \Big\{ \Big[\frac{1}{(\hat{\epsilon}_0\hat{\omega})^{1/3}} B_3 - \frac{B_4}{\hat{\omega}} \Big] \sin 3\hat{\omega}\tau - \frac{C_4}{\hat{\omega}} \sin \hat{\omega}\tau \Big\}. \tag{24c}$$

Here cases (i), (ii) and (iii) represent solutions for the nonresonant, resonant without and with interactions, respectively, and the A's and B's as well as C_4 terms contain the second order cross-products given in Appendix IV.1.2.

These expressions were evaluated and used for comparison against experiments. Most of the results are therefore presented in the next chapter, however, a typical curve useful to discuss the solution characteristics and showing the magnitude of the response at $\hat{\omega}$ is presented in Fig. 8. As the flow is dominated by the mode shape of the first order term for low amplitudes, $|\frac{M_a}{M_l}|$ essentially follows the variations set by f_{11} in the planar motion, with a maximum for the lower branch accompanied by a sudden reversal of signs at a resonant point different from $\hat{\omega} = 1.0$ due to nonlinear effects. Calculations show that the nonlinear contribution, in expression (24b) for this particular case, is less than 10%, although it may be larger according to the damper geometry, and was substantial for higher $\hat{\epsilon}$. The ratio of 3rd over 1st harmonic was also found to be of the order of 10%. Meanwhile, the nonplanar response shows a positive added mass beyond resonance that continues to grow until the motion no longer exists. The nonlinear component of $|\frac{M_a}{M_l}|$ and the 3rd harmonic are also larger and amount to 20% of the first order term. The picture is, of course, quite different at higher amplitudes, as the contribution of the higher modes is of the same order as that of the first. Now f_{11} is greatly affected by the nonlinearities and no longer displays a well defined resonant region for $\hat{\epsilon}_0$ as low as 0.3 and $\hat{\omega}$ as high as 2.0 in the case considered here.

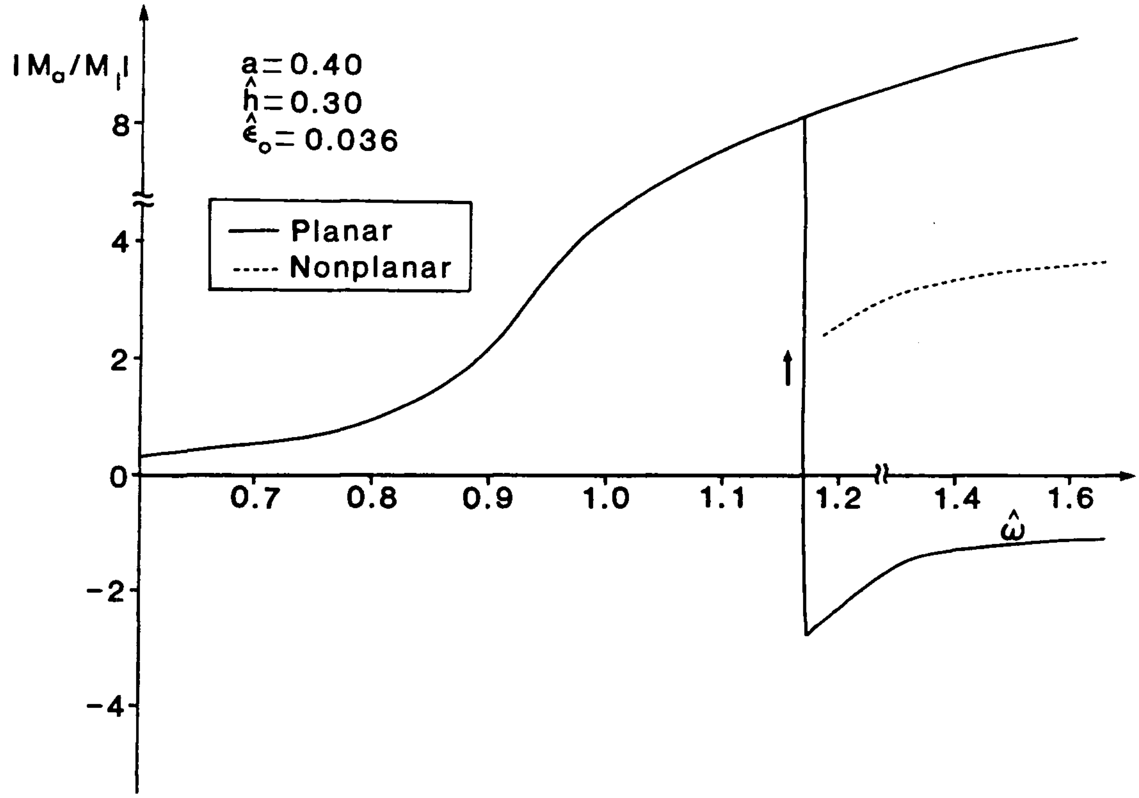

Fig. 8 Typical added mass characteristics at low amplitude

2.4 Damping Forces

2.4.1 Effect of Viscosity

For incompressible flow, the Navier-Stokes equation reduces to[81]

$$(\vec{u}.\nabla)\vec{u} + \frac{\partial \vec{u}}{\partial t} = -\nabla(gz + \frac{p}{\rho}) + \frac{\partial \vec{V}}{\partial t} + \nu_f \nabla^2 \vec{u}, \tag{25}$$

where $\vec{u}$ is the fluid velocity vector in the moving frame of reference and $\dfrac{\partial \vec{V}}{\partial t}$ is the acceleration of the same frame. Substituting $\vec{u} = \nabla\tilde{\Phi} + \vec{u}_2$, where $\vec{u}_2$ is a correction velocity due to viscosity, and recognizing that $\vec{V} = \nabla\Phi_f$,

$$[(\nabla\tilde{\Phi} + \vec{u}_2) \cdot \nabla](\nabla\tilde{\Phi} + \vec{u}_2) + \frac{\partial}{\partial t}(\nabla\tilde{\Phi} + \vec{u}_2)$$
$$= -\nabla(gz + \frac{p}{\rho} + \frac{\partial \Phi_f}{\partial t}) + \nu_f \nabla^2(\nabla\tilde{\Phi} + \vec{u}_2),$$

i.e.,

$$(\nabla\tilde{\Phi} \cdot \nabla)\nabla\tilde{\Phi} + (\vec{u}_2 \cdot \nabla)\nabla\tilde{\Phi} + (\nabla\tilde{\Phi} \cdot \nabla)\vec{u}_2 + (\vec{u}_2 \cdot \nabla)\vec{u}_2 + \frac{\partial \vec{u}_2}{\partial t}$$
$$= -\nabla(gz + \frac{p}{\rho} + \frac{\partial \Phi}{\partial t}) + \nu_f \nabla(\nabla^2\tilde{\Phi}) + \nu_f \nabla^2 \vec{u}_2. \quad (26)$$

Using Bernouilli's equation, i.e., $\frac{1}{2}(\nabla\tilde{\Phi})^2 + gz + \frac{p}{\rho} + \frac{\partial \Phi}{\partial t} = 0$, as well as $\nabla^2\tilde{\Phi} = 0$, reduce the above equation to

$$(\vec{u}_2 \cdot \nabla)\nabla\tilde{\Phi} + (\nabla\tilde{\Phi} \cdot \nabla)\vec{u}_2 + (\vec{u}_2 \cdot \nabla)\vec{u}_2 + \frac{\partial \vec{u}_2}{\partial t} = \nu_f \nabla^2 \vec{u}_2. \quad (27)$$

The corresponding continuity equation is

$$\nabla \cdot (\nabla\tilde{\Phi} + \vec{u}_2) = 0,$$
$$\text{i.e.,} \quad \nabla \cdot \vec{u}_2 = 0. \quad (28)$$

As $\vec{u}_2 = -\nabla\tilde{\Phi}$ at the wall, the correction is of the order of the potential flow solution, and an expansion of the following form is assumed

$$\vec{u}_2 = \epsilon^q \vec{u}_2^{(1)} + \epsilon^{2q} \vec{u}_2^{(2)} + \epsilon^{3q} \vec{u}_2^{(3)} + ..., \quad (29)$$

where $q = 1/3$ and 1, at and away from resonance, respectively. Substituting into (27) yields, up to the 2nd order:

$$\frac{\partial \vec{u}_2^{(1)}}{\partial t} - \nu_f \nabla^2 \vec{u}_2^{(1)} = 0; \quad (30a)$$

$$\frac{\partial \vec{u}_2^{(2)}}{\partial t} - \nu_f \nabla^2 \vec{u}_2^{(2)} + (\vec{u}_2^{(1)} \cdot \nabla)\vec{u}_2^{(1)} + (\nabla\tilde{\Phi}^{(1)} \cdot \nabla)\vec{u}_2^{(1)} + (\vec{u}_2^{(1)} \cdot \nabla)\nabla\tilde{\Phi}^{(1)} = 0. \quad (30b)$$

The linear differential equation (30a) leads to a relatively simple solution for $\vec{u}_2^{(1)}$ under simplifying assumptions[80]. $\vec{u}_2^{(2)}$ is then derived by substituting for $\vec{u}_2^{(1)}$ in (30b). Details of the analysis and expressions for the correction velocities are presented in Appendix IV.2.1.

2.4.2 Energy Dissipation and Reduced Damping Ratio

On integration of the work done by the viscous stresses, the expression for energy dissipation rate in a viscous liquid can be shown to be[96],

$$\frac{dE_d}{dt} = \mu \int_v |\nabla \times \vec{u}|^2 dv + \int_S (\vec{n} \cdot \nabla)|\vec{u}|^2 dS - 2\int_S \vec{n} \cdot \vec{u} \times (\nabla \times \vec{u}) dS. \quad (31)$$

Setting $\vec{u} = \nabla\tilde{\Phi} + \vec{u}_2$, considering $\nabla \times \nabla\tilde{\Phi} = 0$ (irrotational flow), and $\vec{u} = 0$ at the boundaries gives

$$\frac{dE_d}{dt} = \mu\Big[\int_v (\nabla \times \vec{u}_2)^2 dv + \int_{z=\eta_f} (\vec{n} \cdot \nabla)|\nabla\tilde{\Phi}|^2 dS\Big]. \quad (32)$$

Here η_f represents the instantaneous free surface elevation, i.e., deviation from the undisturbed horizontal height. It must be noted that the first term expresses the contribution from the shear forces at the damper walls, and the second term is the effect of the free surface, often neglected in this type of analysis. The integral over a cycle permits calculation of an equivalent reduced damping ratio defined as,

$$\eta_{r,l} = \frac{C_e}{2\omega_e M_l}, \quad (33)$$

where : C_e = equivalent absolute damping coefficient, $\dfrac{E_d}{\pi\omega_e\epsilon_0^2}$;

E_d = total energy dissipated per cycle.

$\eta_{r,l}$ is therefore the damping ratio η of a single degree of freedom system of rigid mass M, damping coefficient C_e, and natural frequency ω_e, divided by the mass ratio $\dfrac{M_l}{M}$. Recognizing that the total energy of a solid mass M oscillating harmonically with a displacement $x = \epsilon_0 \sin\omega_e t$ is $\dfrac{1}{2}M\epsilon_0^2\omega_e^2$, it is also the ratio of dissipated to total energy of a corresponding rigid mass M_l during a cycle, divided by 4π. An expression more representative of the dissipation as a fraction of the actual energy in the flow is defined in the next section. Contribution from the boundary layer at the damper walls, complete to the second order without including the effect of the streaming layer (Appendix IV.2.1.2), is given below. Here relations (i),(ii) and (iii) correspond to the cases of nonresonant and resonant cases, as explained before:

$$\text{(i)}\quad \eta_{r,l} = \frac{1}{\hat{h}(1-a^2)}\frac{1}{\sqrt{Re}}\frac{1}{4\sqrt{2}}\Big\{\sum_m\sum_n f_{1m}f_{1n}[kk_{11}(m,n) + ll_{11}(m,n) + I2_{11}(m,n) + J2_{11}(m,n)] + \hat{\epsilon}_0^2\hat{\omega}^2 AA_1\Big\}; \qquad (34a)$$

$$\text{(ii)}\quad \eta_{r,l} = \frac{1}{\hat{h}(1-a^2)}\frac{1}{\sqrt{Re}}\frac{1}{4\sqrt{2}}\Big\{\frac{1}{(\hat{\epsilon}_0\hat{\omega})^{4/3}}(f_{11}^2 + \varsigma_{11}^2)[kk_{11}(1,1) + ll_{11}(1,1) + I2_{11}(1,1) + J2_{11}(1,1)] + \frac{AA_2}{(\hat{\epsilon}_0^{8/3}\hat{\omega}^{2/3})}\Big\}; \qquad (34b)$$

$$\text{(iii)}\quad \eta_{r,l} = \frac{1}{\hat{h}(1-a^2)}\frac{1}{\sqrt{Re}}\frac{1}{4\sqrt{2}}\Big\{\frac{f_{11}^2}{(\hat{\epsilon}_0\hat{\omega})^{4/3}}[kk_{11}(1,1) + ll_{11}(1,1) + I2_{11}(1,1) + J2_{11}(1,1)] + \sqrt{2}\varsigma_{21}^2[kk_{22}(1,1) + 4ll_{22}(1,1) + I2_{21}(1,1) + 4J2_{21}(1,1)] + \frac{BB_3}{(\hat{\epsilon}_0\hat{\omega}^2)} + \frac{AA_3}{(\hat{\epsilon}_0^{2/3}\hat{\omega}^{8/3})}\Big\}; \qquad (34c)$$

kk's ,ll's, $I2$'s and $J2$'s are combinations of Bessel and hyperbolic function cross-products (Appendix V.2.3), while AA's and BB_3 contain the higher order solutions as shown in Appendix IV.2.2.1.

The smaller contribution from the boundary layer at the free surface is obtained to the 1st order only with the following results for the 3 cases:

$$\text{(i)}\quad \eta_{r,l} = \frac{1}{\hat{h}(1-a^2)}\frac{1}{Re}\Big\{\sum_m\sum_n f_{1m}f_{1n}\lambda_{1n}\alpha_{1n}[IA_{11}(m,n) + JA_{11}(m,n) + \Lambda_{1n}]\Big\}; \tag{35a}$$

$$\text{(ii)}\quad \eta_{r,l} = \frac{1}{\hat{h}(1-a^2)}\frac{1}{Re}\frac{1}{(\hat{\epsilon}_0\hat{\omega})^{4/3}}(f_{11}^2 + \varsigma_{11}^2)\lambda_{11}\alpha_{11}[IA_{11}(1,1) + JA_{11}(1,1) + \Lambda_{11}]; \tag{35b}$$

$$\text{(iii)}\quad \eta_{r,l} = \frac{1}{\hat{h}(1-a^2)}\frac{1}{Re}\frac{1}{(\hat{\epsilon}_0\hat{\omega})^{4/3}}\Big\{f_{11}^2\lambda_{11}\alpha_{11}[IA_{11}(1,1) + JA_{11}(1,1) + \Lambda_{11}] + \varsigma_{21}^2\lambda_{21}\alpha_{21}[IA_{22}(1,1) + 4JA_{22}(1,1) + \Lambda_{22}]\Big\}. \tag{35c}$$

It should be noted that the corresponding damping force has to be 90° out of phase with the excitation in order to dissipate energy. Fig. 9 shows the reduced damping ratio versus $\hat{\omega}$ for the same damper and excitation used during the added mass discussion (Fig. 8). $\eta_{r,l}$ clearly reaches a maximum at resonance, with magnitude one or two orders higher than that at $\hat{\omega} < 0.9$, or > 1.2 for the lower branch of the planar motion, as it is a function of the square of the amplitude coefficient f_{11}. As expected, the free surface boundary layer contribution is small and is of the order of 1% throughout the range of $\hat{\omega}$ considered. Although the wetted area along the walls is the same as that of the damper bottom in this case (the ratio of the two areas is $\frac{2\hat{h}}{(1-a)}$ for a torus), the analysis suggests that there is more dissipation at the walls, by a factor of $1.2 - 1.5$ for the planar, and around a factor of 2.0 for the

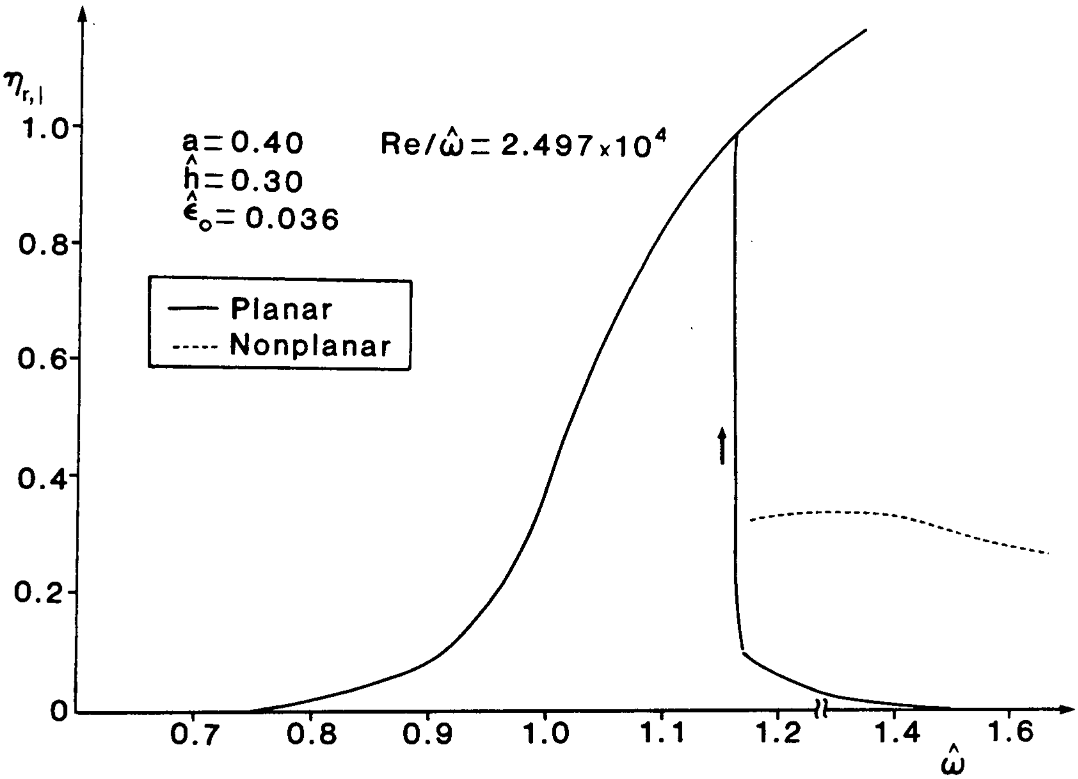

Fig. 9 Typical variation of theoretical $\eta_{r,l}$ versus $\hat{\omega}$

nonplanar mode. The higher velocities near the free surface are in fact responsible for such behavior. Very low contribution from bottom surface is usually found at larger $\hat{h}$ as the velocity gradients become weak near $\hat{z} = -\hat{h}$, suggesting that high liquid heights be avoided for optimizing energy dissipation. Nonlinear terms are small for the planar motion at low amplitudes, but are significant in the nonplanar mode (of the order of 20%). Their magnitude is comparable to that of the first order term at higher $\hat{\epsilon}_0$ (≥ 0.30) as was the case for the added mass. Of interest is the fairly constant value of $\eta_{r,l}$ with $\hat{\omega}$ beyond resonance for the nonplanar motion.

2.4.3 Energy Ratio $E_{r,l}$

A quantity reflecting energy dissipation efficiency is defined here as

$$E_{r,l} = \frac{E_d}{E_t}, \tag{36}$$

where E_d refers to the dissipated energy of relation (31), and E_t is the average total energy stored in the liquid relative motion during a cycle,

$$E_t = T + U, \tag{37}$$

$$\begin{aligned} \text{where :} \quad T &= \text{average kinetic energy,} \quad \frac{\omega_e}{2\pi}\int_0^{2\pi/\omega_e}\left[\frac{1}{2}\rho\int_v (\nabla\tilde{\Phi})^2 dv\right]dt; \\ U &= \text{average potential energy,} \quad \frac{\omega_e}{2\pi}\int_0^{2\pi/\omega_e}\left[\rho\int_v gz dv\right]dt. \end{aligned}$$

Using the expression of η_f as a function of $\tilde{\Phi}$ (Appendix I.3), substituting for $\tilde{\Phi}$, and integrating using a procedure similar to the one applied to the calculation of the added mass (Appendix IV.1.1) yields

$$E_{r,l} = 4\hat{h}(1 - a^2)\frac{\eta_{r,l}}{\hat{E}_t}, \tag{38}$$

where $\hat{E}_t$ is as follows for the various cases of nonresonant, resonant without and with interactions corresponding to (i), (ii) and (iii):

$$\begin{aligned} \text{(i)} \quad \hat{E}_t = \sum_i \Big\{ &\alpha_{11}\lambda_{11}\hat{\omega}^2 f_{1i}^2 \frac{\Lambda_{1i}}{\lambda_{1i}^2} + f_{1i}\sum_j f_{1j}\beta_{11}(i,j)[IA_{11}(i,j) \\ &+ JA_{11}(i,j) + \alpha_{1i}^2\Lambda_{1i}]\Big\} + (\hat{\epsilon}_0\hat{\omega})^2 AAA_1; \end{aligned} \tag{39a}$$

$$\begin{aligned} \text{(ii)} \quad \hat{E}_t = \frac{1}{(\hat{\epsilon}_0\hat{\omega})^{4/3}}(f_{11}^2 + \varsigma_{11}^2)\Big\{ &\frac{\alpha_{11}}{\lambda_{11}}\hat{\omega}^2\Lambda_{11} + \beta_{11}[IA_{11}(1,1) \\ &+ JA_{11}(1,1) + \alpha_{11}^2\Lambda_{11}]\Big\} + \frac{1}{(\hat{\epsilon}_0\hat{\omega})^{2/3}} AAA_2; \end{aligned} \tag{39b}$$

$$(iii)\quad \hat{E}_t = \frac{1}{(\hat{\epsilon}_0\hat{\omega})^{4/3}}\Big\{(\hat{\omega}^2\alpha_{11}\lambda_{11})[f_{11}^2\frac{\Lambda_{11}}{\lambda_{11}^2} + 4\varsigma_{21}^2\frac{\Lambda_{21}}{\lambda_{21}^2}] + f_{11}^2\beta_{11}(1,1)[IA_{11}(1,1)$$
$$+ JA_{11}(1,1) + \alpha_{11}^2\Lambda_{11}] + \varsigma_{21}^2\beta_{22}(1,1)[IA_{22}(1,1) + 4JA_{22}(1,1)$$
$$+ \alpha_{21}^2\Lambda_{21}]\Big\} + \frac{1}{(\hat{\epsilon}_0\hat{\omega})}BBB_3 + \frac{1}{(\hat{\epsilon}_0\hat{\omega})^{2/3}}AAA_3; \qquad (39c)$$

where the BBB's coefficients represent the effect of 1st and 2nd order term cross products, and the AAA's coefficients include nonlinear terms only (see Appendix IV.2.3).

It can be shown that the first order term in the expression for $E_{r,l}$ is independent of the amplitude of excitation for a given $\eta_{r,l}$. However, it is a function of frequency as the potential energy contains acceleration terms. For a given damper liquid and geometry, the Reynolds number increases with $\hat{\omega}$, which further contributes to the general downward trend shown in Fig. 10. The higher orders seem to present similar energy dissipation efficiencies as no significant changes in the curves occur at larger $\hat{\epsilon}_0$.

To assess the effect of the geometry only, a parameter accounting for the variation of the Reynolds number is defined as

$$E_{r,l}^* = E_{r,l}\sqrt{Re}, \qquad (40)$$

since the reduced damping ratio was shown to be essentially proportional to $1/\sqrt{Re}$. It is plotted versus $\hat{h}$ and a in Fig. 11(a) and (b), respectively. Results indicate that low liquid heights and larger a's are most effective at dissipating energy. How-

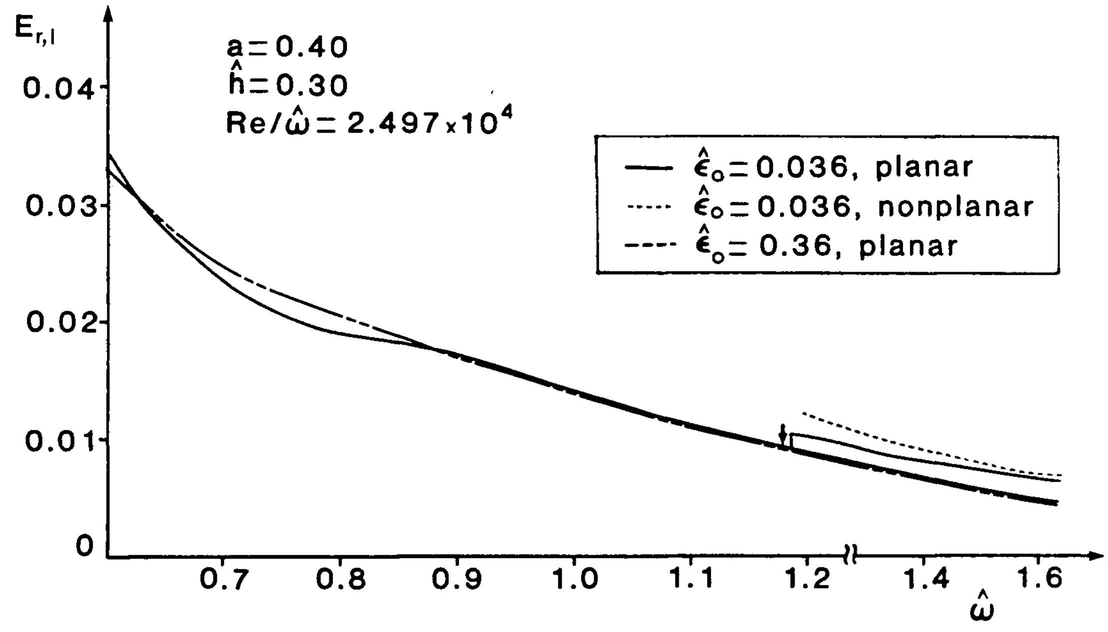

Fig. 10 Typical curves showing variation of $E_{r,l}$ with frequency and amplitude

ever, the potential flow approach is less reliable at smaller $\hat{h}$ as the boundary layer occupies a more significant part of the liquid volume. The rapid growth of $E^*_{r,l}$ for $\hat{h} \leq 0.26$ in Fig. 11(a) may therefore not occur in practice. It may also be noted (Fig. 11b) that the downward trend with decreasing a is somewhat stalled below 0.40. The velocity gradients, however, become unrealistically large near the damper inner wall as a tends to 0 since the curvature effects were neglected in the analysis. The results obtained for small values of this parameter cannot therefore be fully trusted. Overall, the curves present useful trends with relatively short, slender dampers (small $\hat{h}$, and a closer to 1) particularly effective in optimizing energy dissipation. Finally, the nonplanar motion consistently exhibited higher $E_{r,l}$ compared to the planar mode, as illustrated in Fig. 10.

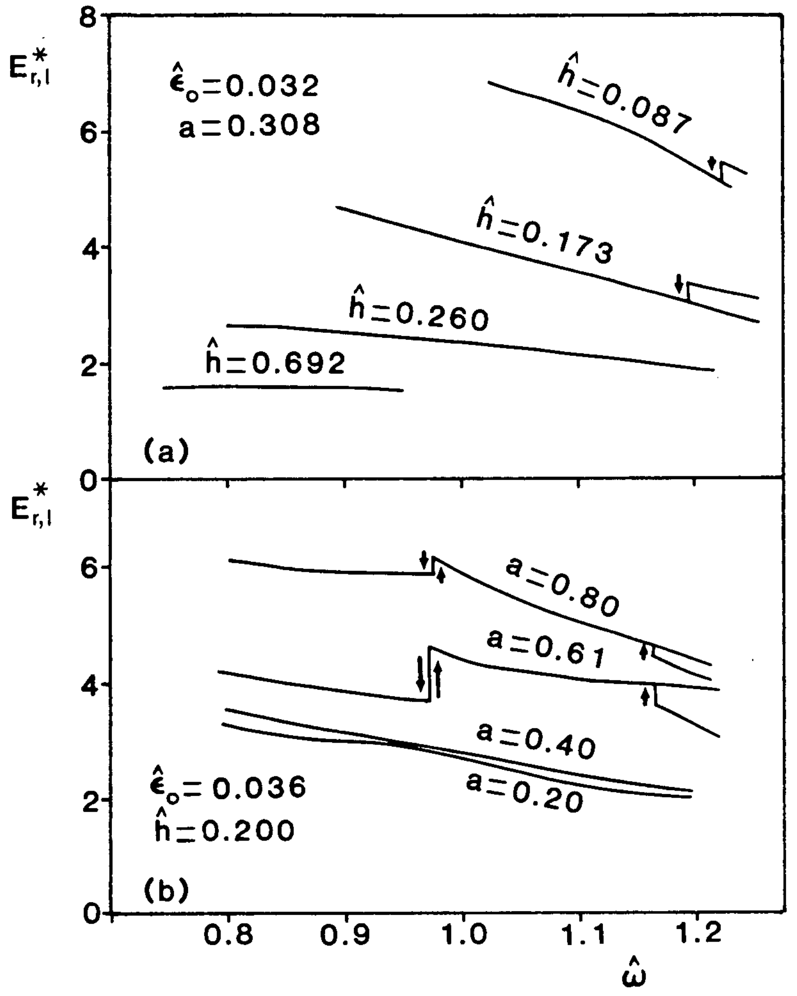

Fig. 11 $E^*_{r,l}$ versus $\hat{\omega}$ as affected by: (a) $\hat{h}$; (b) a

All the calculations for the theoretical solution were carried out on the main frame computer (Michigan Terminal System) using a Fortran program.

3. EXPERIMENTAL DETERMINATION OF DAMPER CHARACTERISTICS

3.1 Preliminary Remarks

Experiments in steady-state forced excitation with the damper undergoing a translational motion were designed to assess the theoretical predictions and further evaluate performance. The controlling dimensionless variables discussed in the previous chapter were varied and the effect of internal devices such as baffles investigated. Initially, a flow visualization study was undertaken to confirm the qualitative nature of the mode shapes. This was followed by an extensive set of measurements of the sloshing horizontal force transmitted from the fluid to the damper walls.

3.2 Test Arrangement and Models

A Scotch-Yoke mechanism connected to a horizontal frame free to slide over supporting bearings, available in the Department, was upgraded to provide a smooth sinusoidal excitation (Fig. 12). A high inertia fly wheel driven by a D.C. motor generates a steady harmonic motion at frequencies as low as 0.7 Hz and damper amplitudes as high as 4 cm. The system can be operated safely up to 5 Hz for average amplitudes of oscillation, or higher for very short strokes (< 1 cm). A VARIAC rheostat along with adjustable eccentricity of the Scotch-Yoke provided the means to vary the frequency and amplitude of excitation.

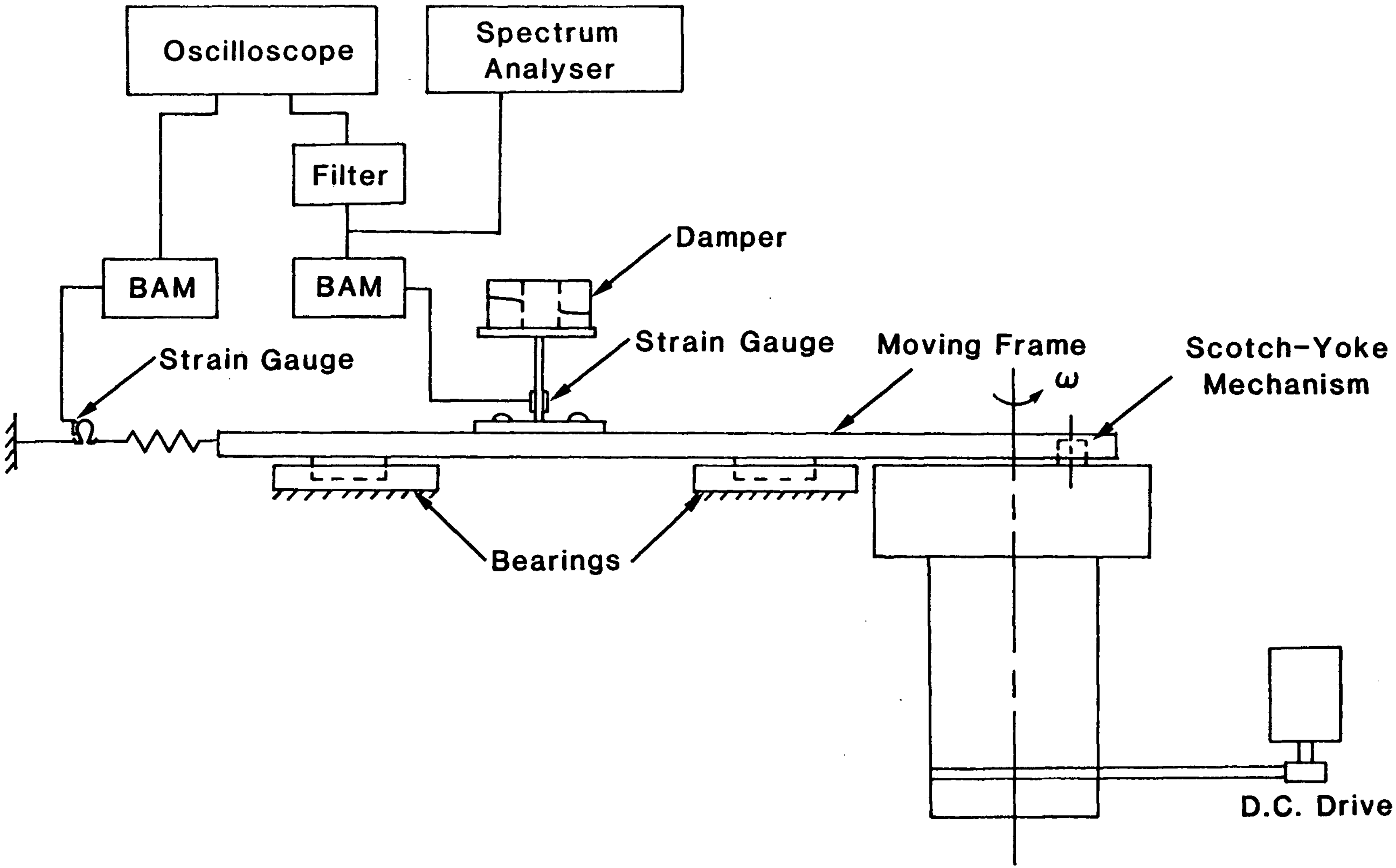

Fig. 12 Test Arrangement

Two strain gauge arrangements were mounted on the apparatus: the first one was installed at the base of the damper supporting beam to measure the response of the sloshing liquid, while the second arrangement, a part of the ring shaped bracket, was attached to the main frame by a short spring to record the displacement.

Careful design of the damper support was necessary to obtain proper sensitivity for minimal beam deflection, required to be small here compared to the main frame amplitude of excitation. An aluminum plate, (0.318 cm thick, 20.3 cm long and 3.81 cm wide), clamped to the moving base and fitted with a horizontal platform to hold the container, was used to provide a linear range of strain versus horizontal sloshing forces with minimal impact due to pitching moments. The natural frequency was much greater than that of the excitation, from approximately 40 Hz without damper to 12 Hz under larger loads. The output signal was amplified through a Bridge Amplifier Meter (BAM, Ellis Associates) before being directed to a Spectrum Analyser (Model SD335, Spectral Dynamics Corporation). A filter (Model 335, Krohn-Hite) and a dual channel storage oscilloscope (Tektronics 564, Vertical Amplifier Type 3A3, Time Base 2B67) were connected in parallel to record the excitation from the other source simultaneously. The analysis in the frequency domain showed the magnitude of the response at different harmonics while the time domain measurements yielded the phase angle between the response and the excitation needed to calculate pressure and damping forces.

Small scale transparent plexiglas torus shaped dampers with square or rectangular cross-section, such as shown in Fig. 13(a), were constructed in the Department's machine shop. Various sizes were required to investigate important dimensionless parameters, and two models were fitted with baffles and inner tube (Fig. 13b,c) found to be effective under certain conditions of excitation[90] (Table I). Limited experiments were also carried out with circular cross-section dampers.

Table I Details of the damper models used in the test program

Damper #	d (cm)	D (cm)	Capacity (ml)	Internal Configuration	Cross-Section
1	2.86	5.40	140	plain	square
2	2.86	5.40	140	baffles	square
3	2.86	5.40	126	inner tube	square
4	3.50	7.31	147	plain	square
5	3.79	6.99	315	plain	square
6	3.15	7.55	235	plain	square
7	2.84	11.7	297	plain	square
8	1.42	3.93	39	plain	square
9	4.70	4.70	326	plain	square
10	2.20	2.20	38	plain	square
11	3.50	15.9	640	plain	square
12	2.98	8.08	177	plain	circular
13	1.55	23.6	140	plain	circular

3.3 Flow Visualization

An inspection of the various mode shapes was first conducted with the dampers

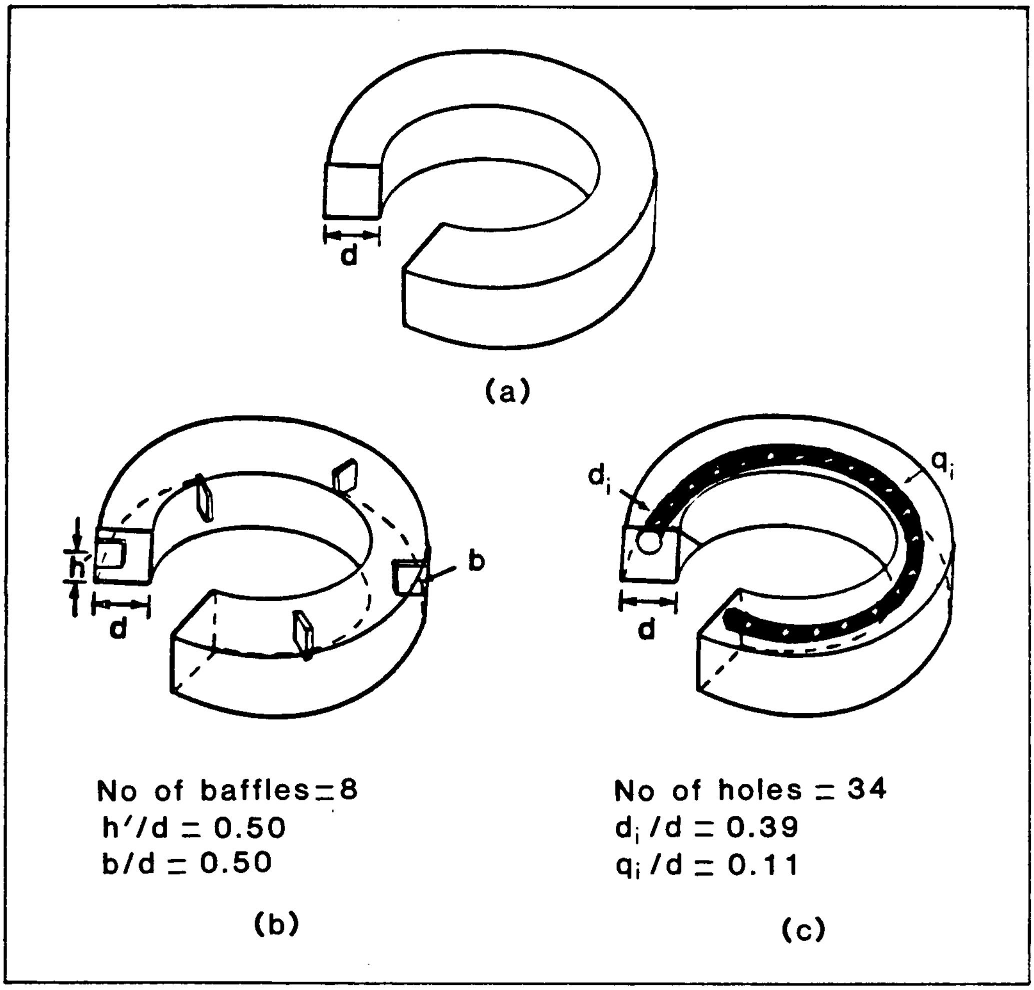

Fig. 13 Sketch showing several damper model internal configurations: (a) plain; (b) baffles; (c) inner tube

oscillating near their natural sloshing frequencies. The conventional dye injection procedure and photographic equipment were used to visualize the free surface elevation and its qualitative agreement with the theoretical predictions as given by relation (I.10).

A large amplitude antisymmetrical motion with a stationary node at 90° to the direction of the excitation, and zero node across the radius, characterized the first mode shape studied using dampers 5 and 11, as predicted from the harmonic

($\cos\theta$) and Bessel function $C_1(\lambda_{11}\hat{r})$ dependence of the 1st order potential flow solution (relation 8) along θ and r coordinates, respectively (Fig. 14a). The small variation of the surface elevation in the radial direction at a given angle θ (Fig. 14b), and the general pattern along the outer wall (Fig. 14c) suggests reasonable qualitative agreement. At times, a discontinuous wave front, however, appeared to be present. The nonplanar mode was observed at slightly higher amplitudes or frequencies, with a large swirling action about the damper circumference, seemingly 90° out of phase in time and angular position with the excitation. The similarity between the free surface shape in the radial direction for this mode and that of the planar motion, for a given θ (Fig. 15), is again consistent with relation (8). It should be noted that the occurrence of the nonplanar response more readily took place for higher liquid heights in the torus.

Although less useful for the purpose of this study, higher transverse modes were excited at their corresponding natural frequencies. They all exhibited a single circumferencial node at $\theta = 90°$, with minimum and maximum free surface elevation at 0° and 180° angles, and a number of transverse nodes at times more difficult to identify (1 for the 2nd mode, 2 for the 3rd, etc.). They are in agreement with the Bessel function $C_1(\lambda_{1n}\hat{r})$ dependence of relation (3a), and are shown in Fig. 16, 17, and 18. Of course, such modes distort the free surface plane considerably, with nonlinear effects becoming more pronounced at higher frequencies. Furthermore, theoretical calculations show that the spacing between two eigenvalues becomes

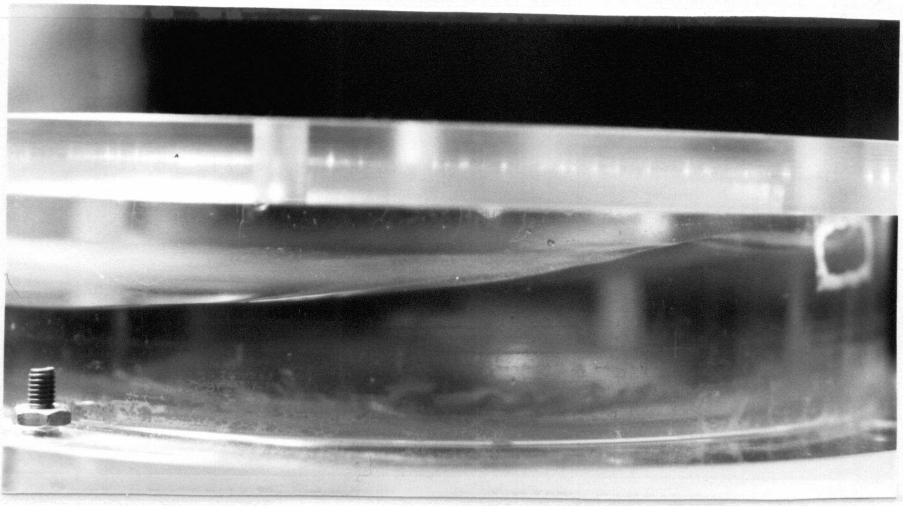

(a)

(b)

Theoretical Modes

$C_1(\lambda_{11}\hat{r})$

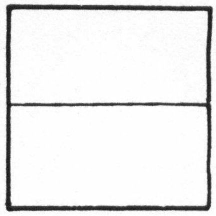

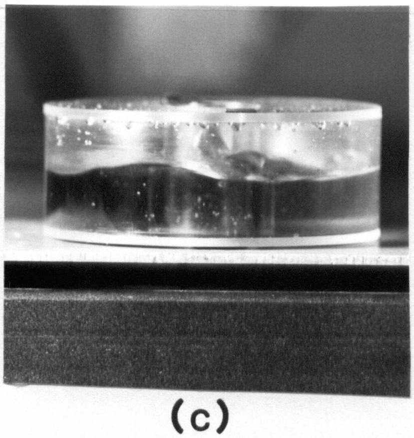

(c)

$\cos\theta$

Fig. 14 1st planar mode exhibiting: (a) antisymmetric motion about circumference; (b) variation across $\hat{r}$; (c) variation along θ

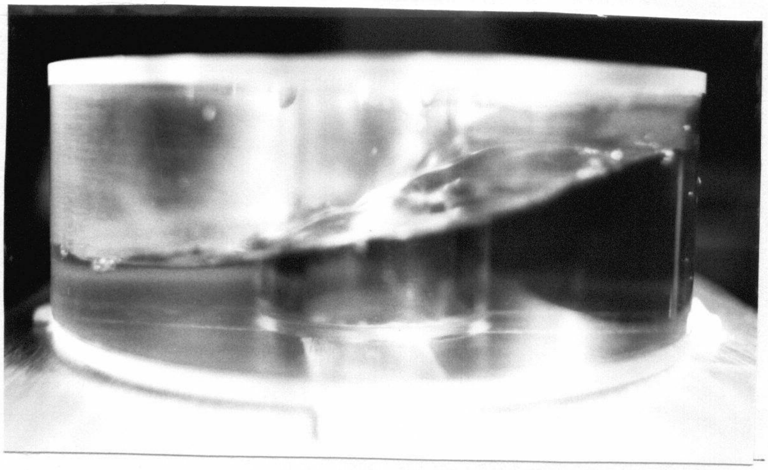

Theoretical
Modes

$C_1(\lambda_{11}\hat{r})$

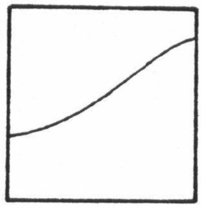

Fig. 15 1st nonplanar mode shape

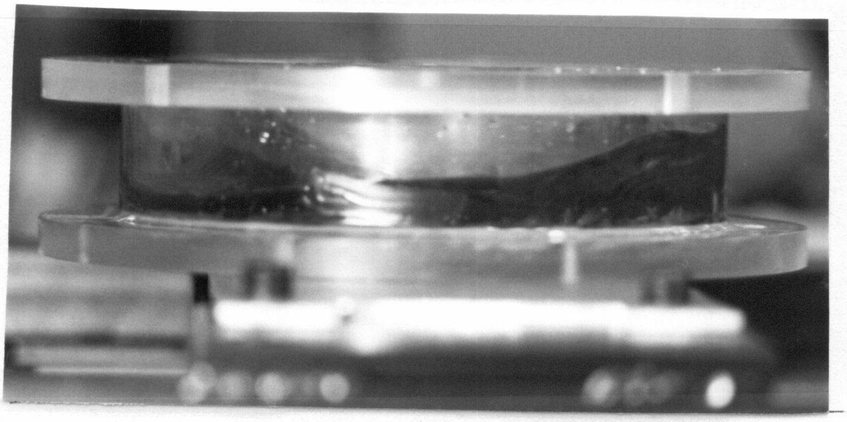

$C_1(\lambda_{21}\hat{r})$

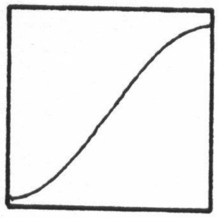

(a)

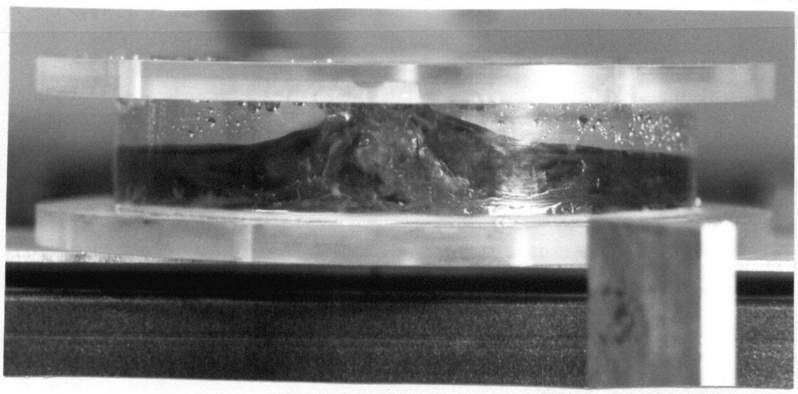

(b)

Fig. 16 Mode (1,2) shown as: (a) in the plane of the excitation; (b) perpendicular to the same plane

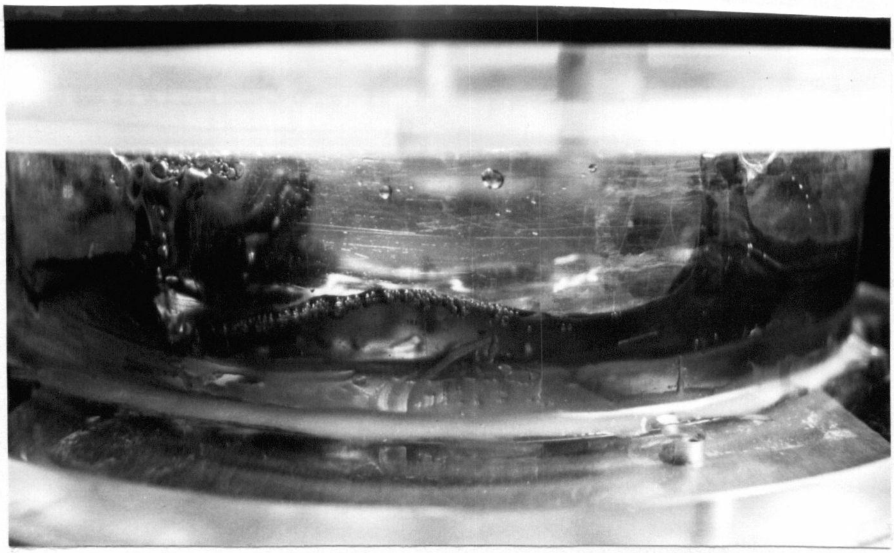

Theoretical Modes

$C_1(\lambda_{31}\hat{r})$

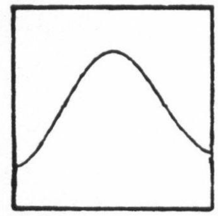

(a)

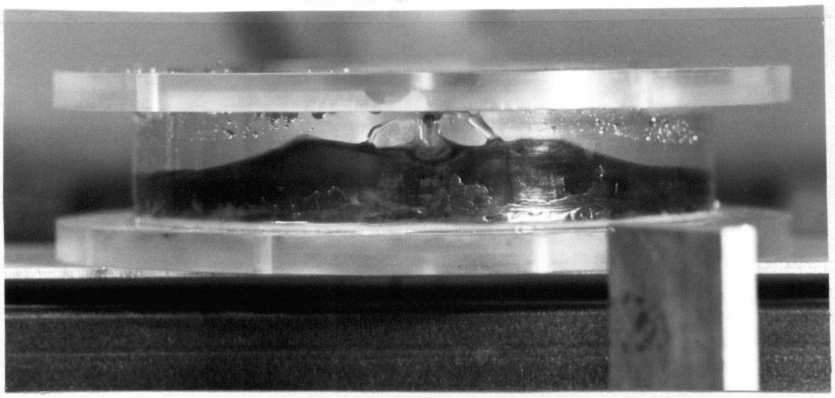

(b)

Fig. 17 Mode (1,3) shown as: (a) in the plane of the excitation; (b) perpendicular to the same plane

$C_1(\lambda_{41}\hat{r})$

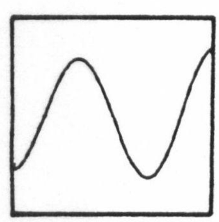

Fig. 18 Close-up view of mode (1,4)

increasingly narrower, thus making the identification of the modes less obvious. Noteworthy is the apparent absence of turbulence throughout most of the flow field for at least the first two resonant states, a condition that was assumed for the theoretical development. No attempt was made to visualize the modes corresponding to 2nd and higher order nonlinear terms.

3.4 Added Mass and Reduced Damping Ratio

3.4.1 General Procedure

A force F_s transmitted from the sloshing fluid to the rigid damper walls in the direction of excitation causes the supporting beam to deflect proportionally to its magnitude provided the system is elastic and operates far away from its resonant state. An additional force F_0 generated by the system's own inertia is proportional to the amplitude and frequency square of the excitation,

$$F_0 = M_0 \omega_e^2 \epsilon_0 \cos \omega t, \tag{41}$$

where M_0 is the equivalent mass of the support (general "moving base" problem in vibrations). It contributes to the overall strain recorded by the sensor. A dynamic calibration procedure, consisting of measuring the output voltage after loading the support with dead weights under various conditions of amplitudes and frequencies, was therefore adopted to estimate M_0 as well as the slope of the response curve (Fig. 19a). An initial static calibration, with the system at rest undergoing bending under a known stress, was used to verify the results. This is shown in Fig. 19(b), where the y-axis represents the response as recorded by the spectrum analyser at the exciting frequency ω_e, for the case of dynamic testing, while the oscilloscope provided the results for the static procedure. The other channel recorded the displacement of the moving frame and a simple calibration curve was produced by direct measurements of the stroke versus output voltage (Fig. 19c). Furthermore, phase angles between the excitation and response of the beam at the driving frequency were derived from real time measurements on the dual channel oscilloscope. As the system damping is due to the aerodynamic drag along the damper support as well as the hysteresis damping within the beam, and is very low compared with the effect of liquid sloshing, the frequency dependent phase shift ψ_0 introduced by the instrumentation (mainly the filter) was found by simply running the experiment without the damping fluid (Fig. 19d).

The experimental determination of the four variables: sloshing force F_s, amplitude ϵ_0 and frequency ω_e of the excitation, and the corresponding phase angle ψ, supplied the necessary information for calculation of the added mass and damping ratios

$$|\frac{M_a}{M_l}| = (\frac{|(F_s)|}{M_l \epsilon_0 \omega_e^2} - 1)\cos\psi; \text{ and } \quad \eta_{r,l} = \frac{|F_s|}{2M_l \epsilon_0 \omega_e^2}\sin\psi; \tag{42}$$

where $|\frac{M_a}{M_l}|$ and $|F_s|$ refer to the magnitude of the component oscillating at the exciting frequency. The higher harmonics of the added mass can similarly be found as

$$|\frac{M_a}{M_l}|_n = \frac{|F_s|_n}{M_l \epsilon_0 \omega_e^2}, \tag{43}$$

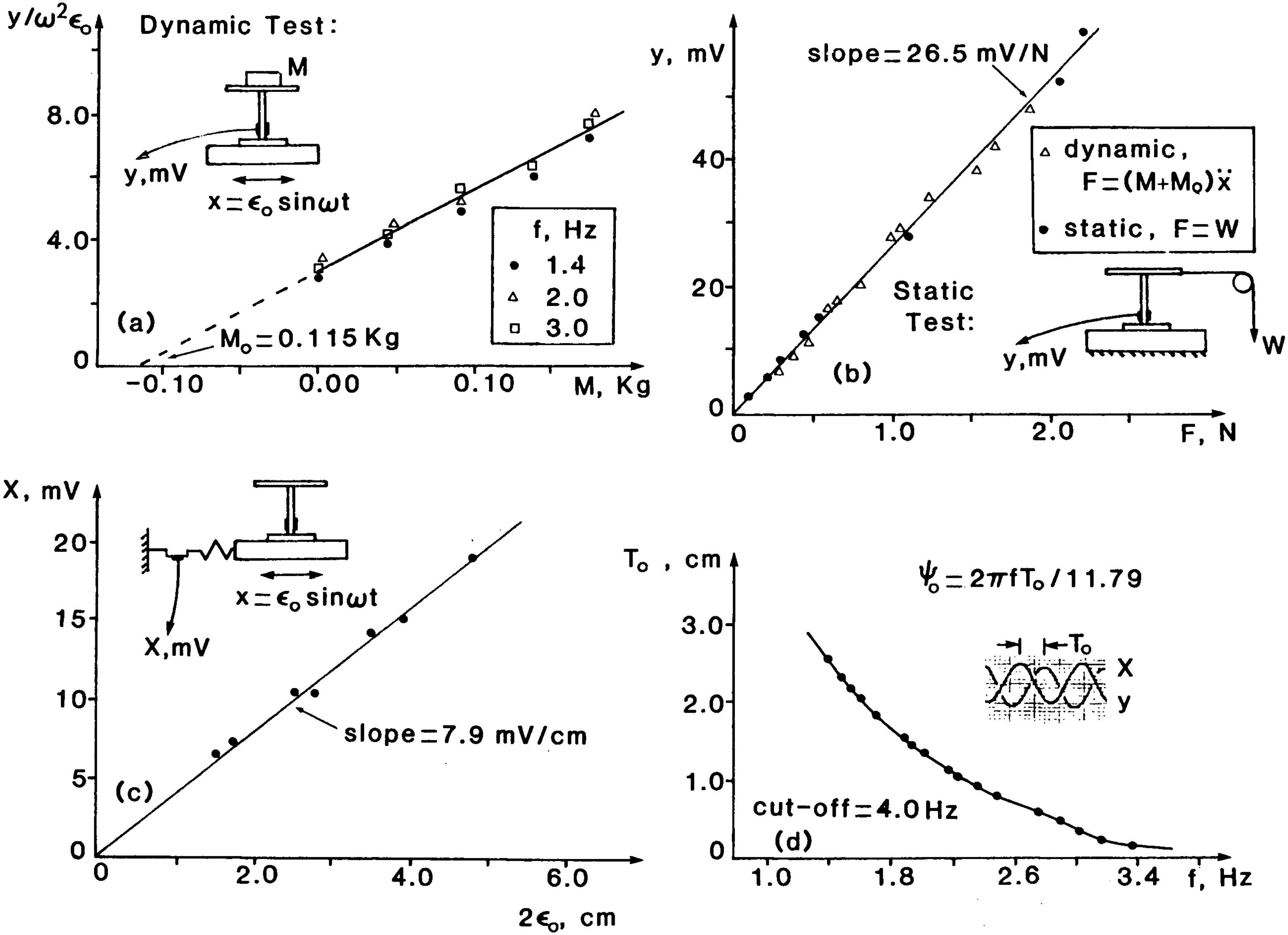

Fig. 19 Calibration curves to determine: (a) M_0; (b) slope for the response using both static and dynamic procedures; (c) slope for the excitation; (d) phase angle between response and excitation

where n denotes the rank of the harmonic considered. No provision was made for the estimation of the total energy contained in the liquid motion.

3.4.2 Results and Discussion

From the theoretical development, the added mass and reduced damping ratios are expected to be a function of the set of dimensionless parameters $(\hat{\omega}, \hat{\epsilon}_0, a, \hat{h}, Re)$, representative of the excitation and damper characteristics. For convenience, the equivalent variables ϵ_0/d, D/d and h/d defined as:

$$\frac{\epsilon_0}{d} = \frac{\hat{\epsilon}_0}{1-a}; \quad \frac{D}{d} = \frac{1+a}{1-a}; \quad \text{and} \quad \frac{h}{d} = \frac{\hat{h}}{1-a}; \tag{44}$$

were adopted, and tests conducted through their systematic variation. Additional information concerning the effect of internal configuration and corresponding parameters was also included in the study. Results mainly describe the damper behavior under excitations near the first sloshing frequency ω_{11}, as it is the condition of maximum damping, with the accuracy of the phase angle measurements diminishing away from resonance. Tests in free vibrations using an apparatus similar to that of reference 90 were carried out to extend the data in the low damping region. The significant findings of the test program are summarized in the following subsections.

(i) General Shape of the Output Signals

The excitation was first established to be purely sinusoidal (Fig. 20a), and the response was, in general, dominated by the driving frequency (Fig. 20b). A number of superharmonics, odd multiples of the fundamental frequency (i.e., $3\omega_e t$, $5\omega_e t$, etc.), were also present as indicated by the spectrum analyser record (Fig. 20c). This is in good agreement with the assumed expansion for the potential function and the form of the derived added mass, as nonlinear even harmonics were found to be symmetrical in θ and therefore cancel out when integrated over the damper wall. The higher resonant frequency of the damper support was often visible (at around 12 Hz here), but its effect on the first harmonics of the sloshing response was assumed to be negligible.

(ii) Effect of Frequency

As predicted by the theoretical model, the response is very sensitive to the frequency $\hat{\omega}$. At relatively low amplitudes of excitation, a dramatic rise in the reduced damping ratio accompanied by a reversal in sign for the added mass characterizing resonance was generally observed. The maximum $\eta_{r,l}$ usually coincided with $|\frac{M_a}{M_l}| = 0$ at a frequency slightly different from 1, as shown in Fig. 21 for a half-full damper with $D/d = 4.1$. The nonplanar mode generally took place for dampers with higher h/d or lower D/d ratios, extending the high damping region until the motion ceased to exist. For the case of $h/d = 0.5$, $D/d = 1.89$, this corresponded to $\hat{\omega} \approx 1.15$ (Fig. 22). The theory generally anticipated these trends, although the damping curves are often too narrow with peaks higher than those measured (Fig. 21). In other cases, no solution near resonance can be found, thus preventing the occurrence of a large peak in $\eta_{r,l}$ (Fig. 22). The stability boundaries for the

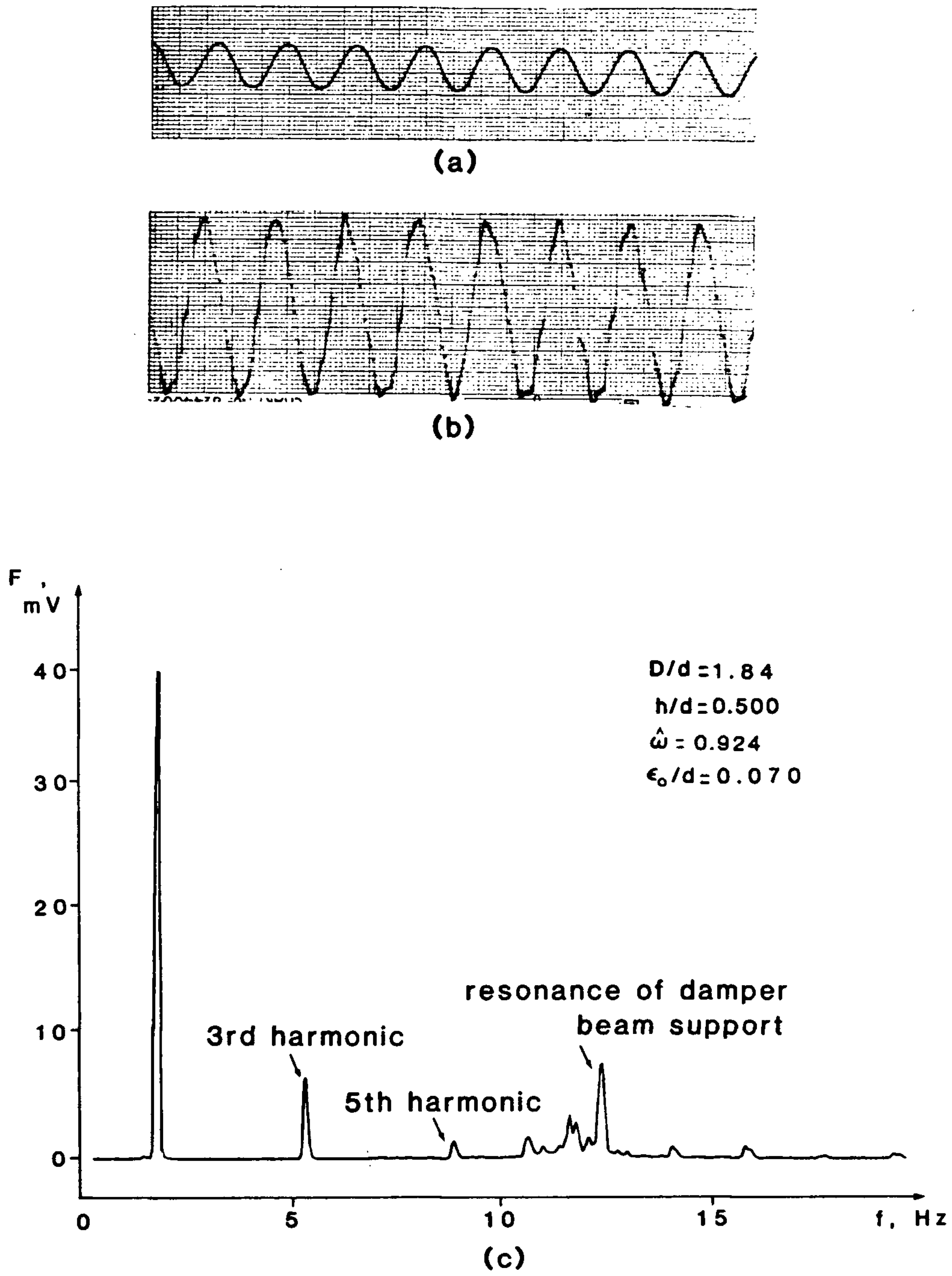

Fig. 20 Output signals showing: (a) moving frame displacement; (b) damper support beam deflection; (c) frequency spectrum of the response

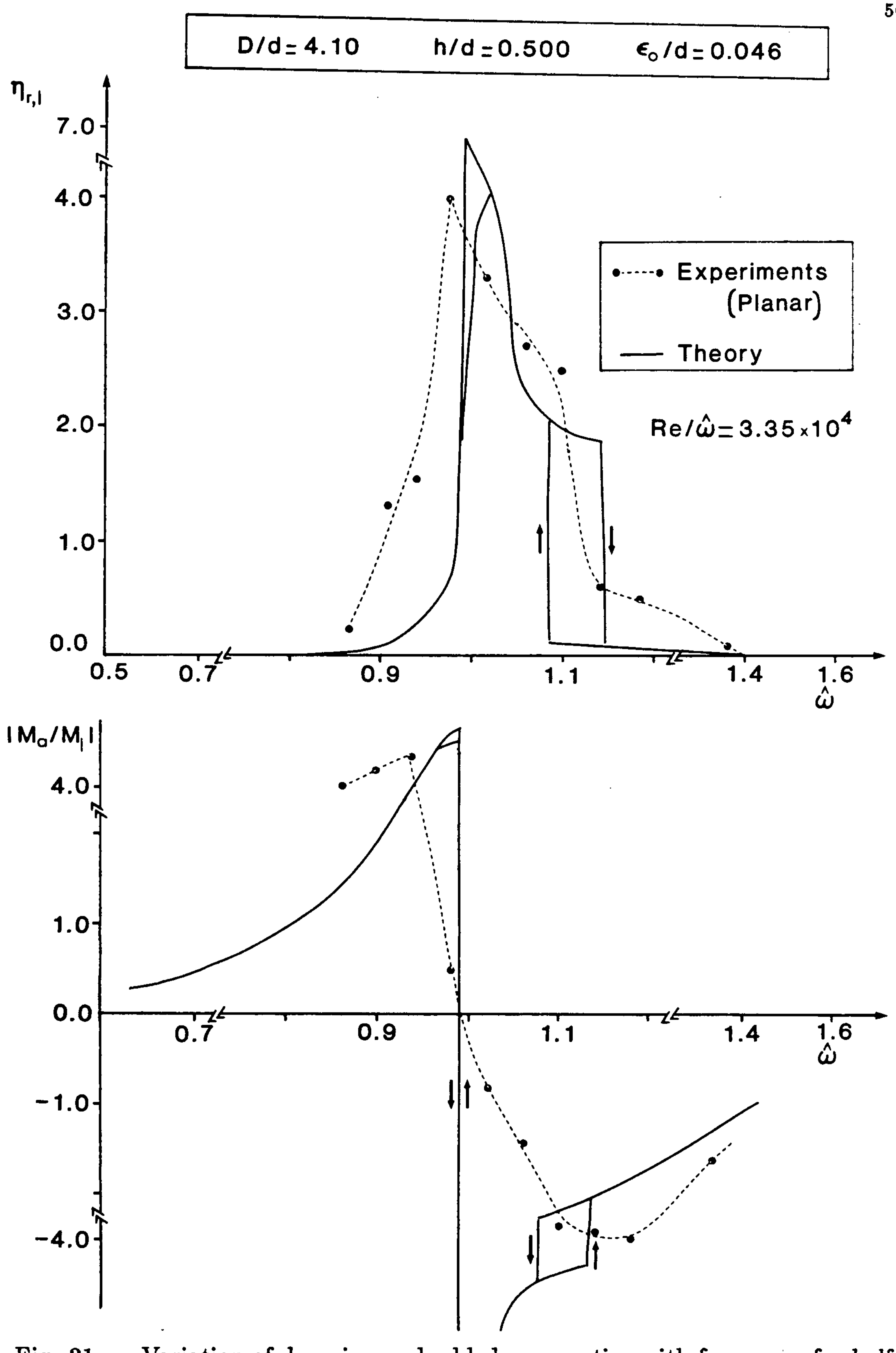

Fig. 21 Variation of damping and added mass ratios with frequency for half-full damper#7

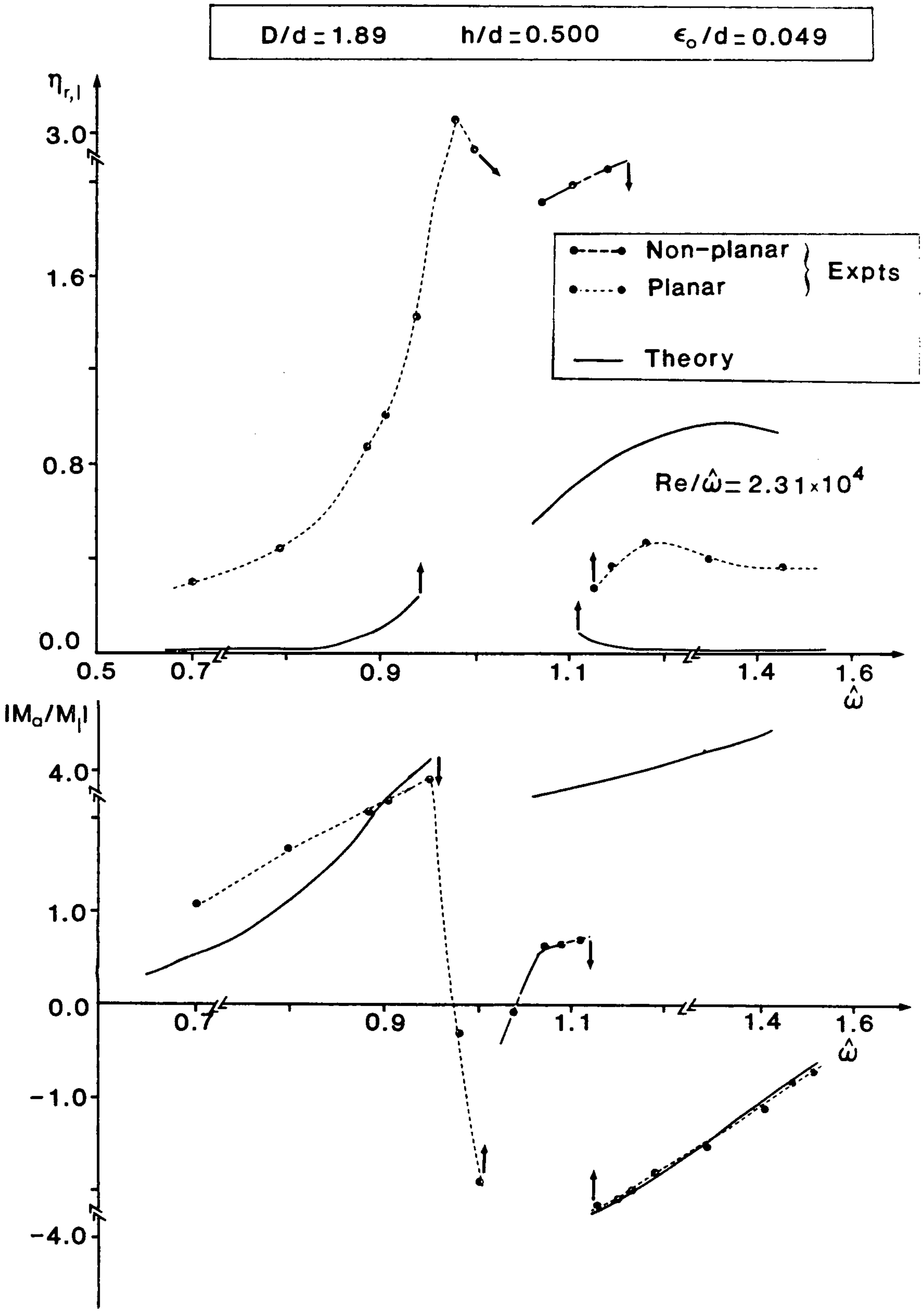

Fig. 22 Variation of damping and added mass ratios with frequency for half-full damper#1

planar mode are realistic, but the nonplanar region extends beyond what is experimentally observed with underestimated $\eta_{r,l}$. Predictions for the added mass are, in general, quite reasonable with, at times, very good agreement in the linear range (e.g., $1.1 \geq \hat{\omega} \geq 1.4$ in Fig. 22). However, experimental values for the nonplanar motion were usually much smaller than expected.

The potential flow solution for the case of resonant interactions was used for the damper of Fig. 21 resulting in two stable positions beyond resonance. The upper branch yields a damping ratio that remains high past $\hat{\omega} = 1$ and seems to follow the experimental damping curve until $\eta_{r,l}$ suddenly drops at $\hat{\omega} = 1.14$. The accurate prediction of the resonant point quite close to $\hat{\omega} = 1.0$, indicative of weak nonlinearities, is also very encouraging. At higher amplitudes, the effect of frequency was less pronounced with usually smaller peaks recorded. This is not surprising as nonlinear terms are now expected to be quite large.

(iii) Effect of Amplitude

In the nonlinear range, ϵ_0/d has similar effects on the damper behavior as $\hat{\omega}$: the occurrence of a resonant peak often followed by a nonplanar motion for certain conditions of excitation and geometries. When $\hat{\omega} > 1.0$, the liquid motion is originally planar and small at low amplitude (linear range). However, it becomes unstable with a large jump in both $\eta_{r,l}$ and $|\frac{M_a}{M_l}|$ as the nonplanar mode takes over (Fig. 23). A gradual reduction in damping then accompanies a further increase in

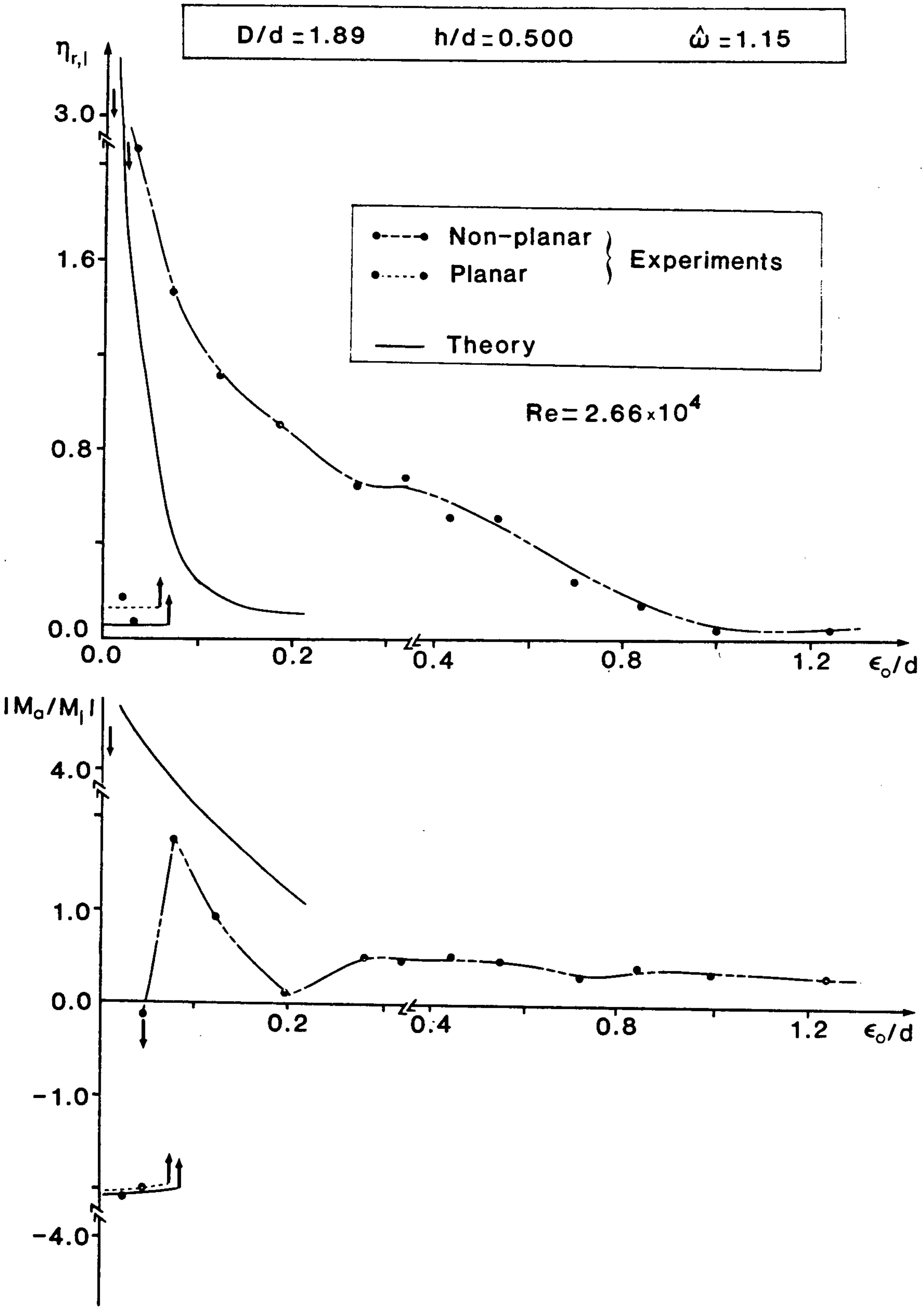

Fig. 23 Effect of amplitude on $|\frac{M_a}{M_l}|$ and $\eta_{r,l}$ for half-full damper#1

ϵ_0/d whereas very large $\eta_{r,l}$ can be obtained with decreasing amplitudes.

For $\hat{\omega} < 1.0$, an optimal damping is reached as the liquid goes through resonance with $|\frac{M_a}{M_l}| = 0$ (Fig. 24a), followed by a rather unsettled motion which fails to attain the fully nonplanar mode. However, such trends for $\hat{\omega} > 1.0$ or $\hat{\omega} < 1.0$ can be reversed through the damper geometry and liquid height, as shown in Fig. 24(b). This particular behavior is related to the "softening" or "hardening" characteristics of the damper (i.e., reduction or increase in the resonant frequency with amplitude) as discussed in Chapter 2, and is generally predicted by the potential flow model. Here again, the calculations for the nonplanar mode yield a lower damping and higher added mass than those of the experiments (Fig. 23), thus suggesting significant dissipative mechanisms in the main flow field. The theory properly indicates a large region of unstable flow for the case of Fig. 24(a), but fails to find a solution at resonance, a situation already encountered while studying the variation with $\hat{\omega}$. The results for the unstable nonplanar mode are indicated in this case for comparison against experiments, and show reasonable trends for the added mass and damping ratios. Finally, the hardening characteristics of the low liquid height damper of Fig. 24(b) yield a predicted resonant point at $\epsilon_0/d \approx 0.06$, as opposed to a measured value higher than 0.14, that was never reached as the planar mode then became unstable. A possible cause for such dicrepancies may rest with the relative size of the boundary layer thickness, not accounted for in this analysis, that changes the effective h/d, or makes the potential flow approach questionable when

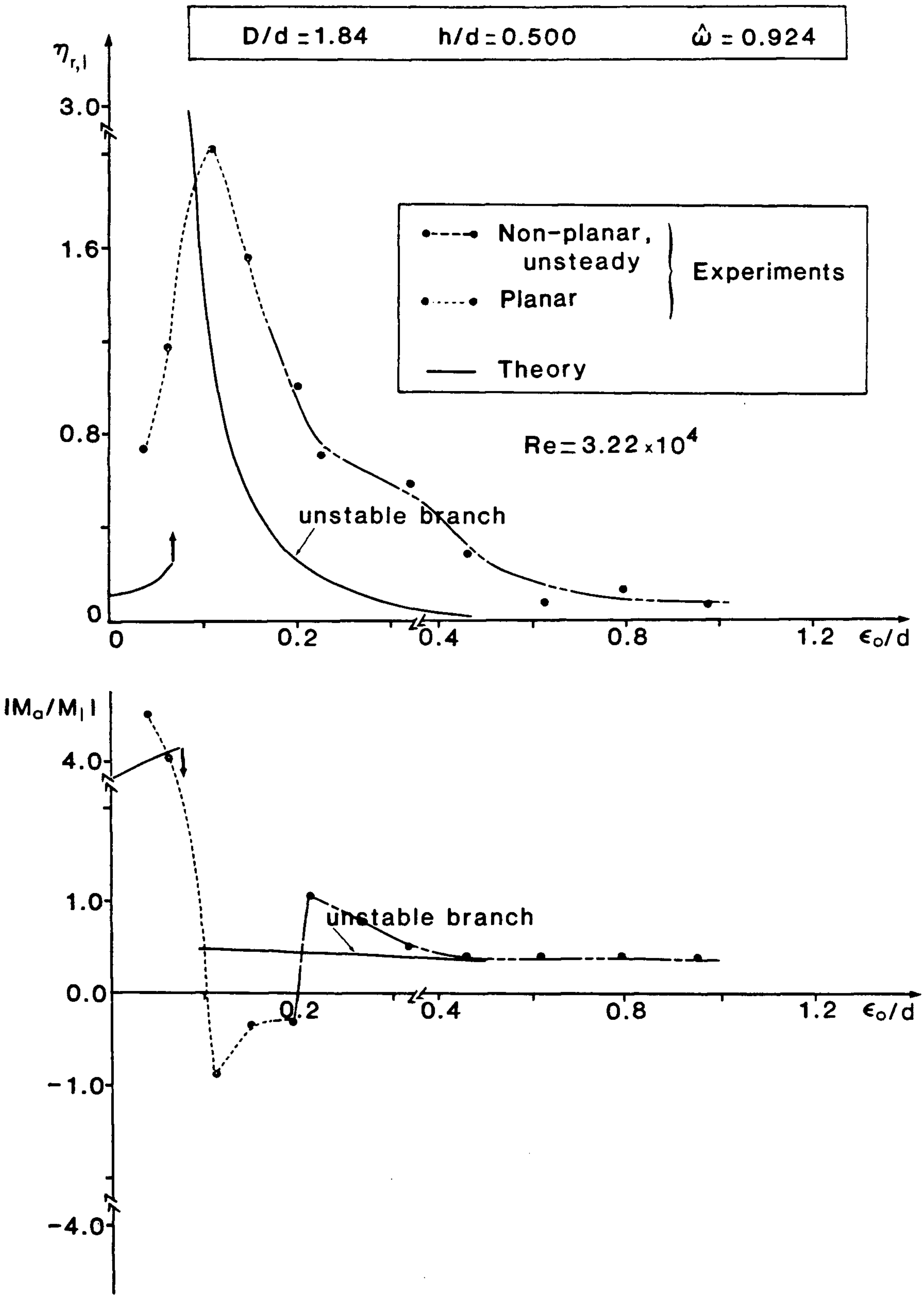

Fig. 24 Resonant behavior of damper#5 with: (a) $h/d = 0.5$ and $\hat{\omega} < 1$

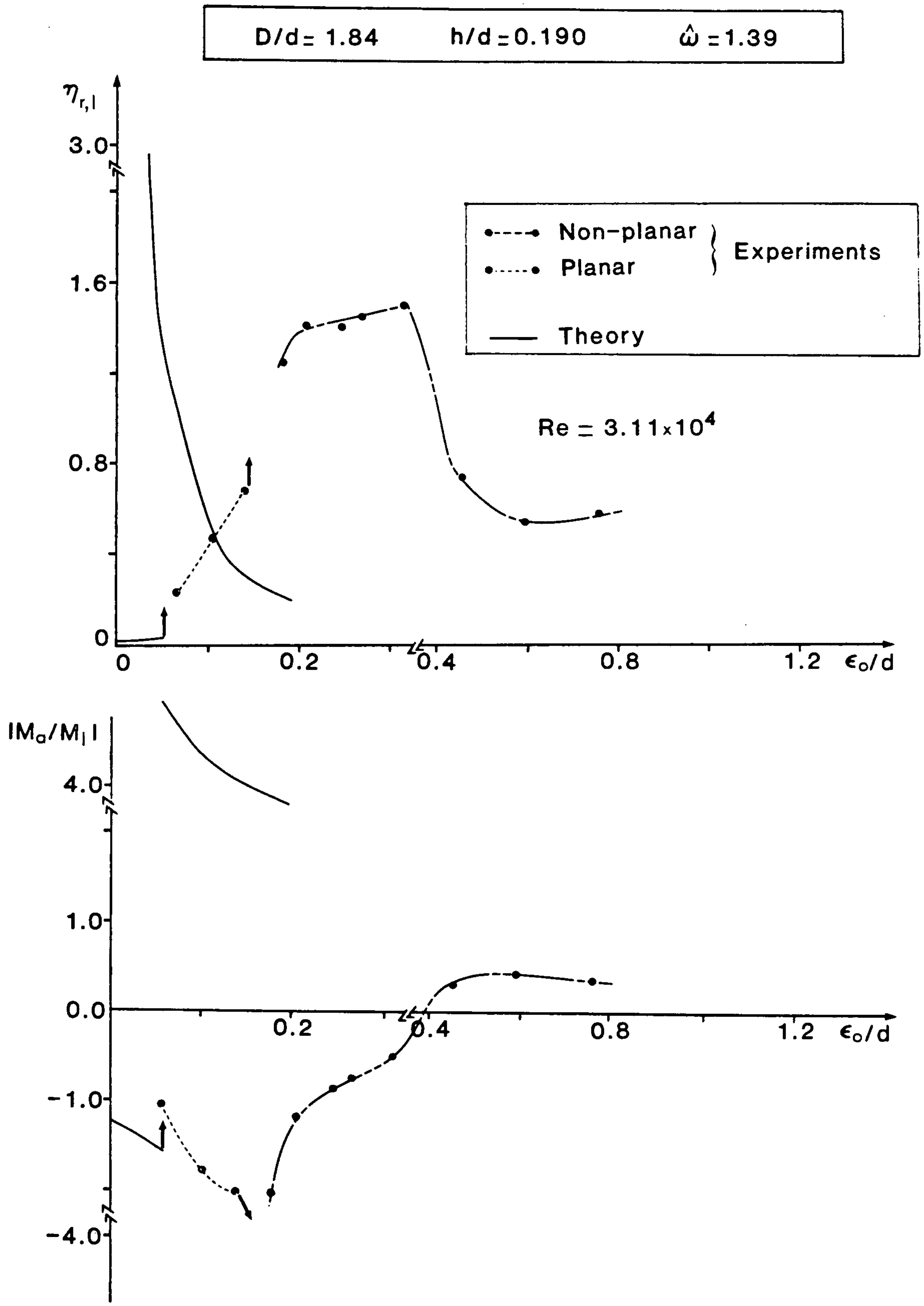

Fig. 24 Resonant behavior of damper#5 with: (b) $h/d = 0.19$ and $\hat{\omega} > 1$

h/d is small. This is further discussed in the following paragraph. In all the cases, the predicted resonant peaks are narrower than those measured (Fig. 25). The right trends are however discernable at lower ϵ_0/d. Of course, the theory cannot be expected to be realistic for higher amplitudes as the assumed expansion for the perturbation method becomes invalid and turbulence dominates the flow.

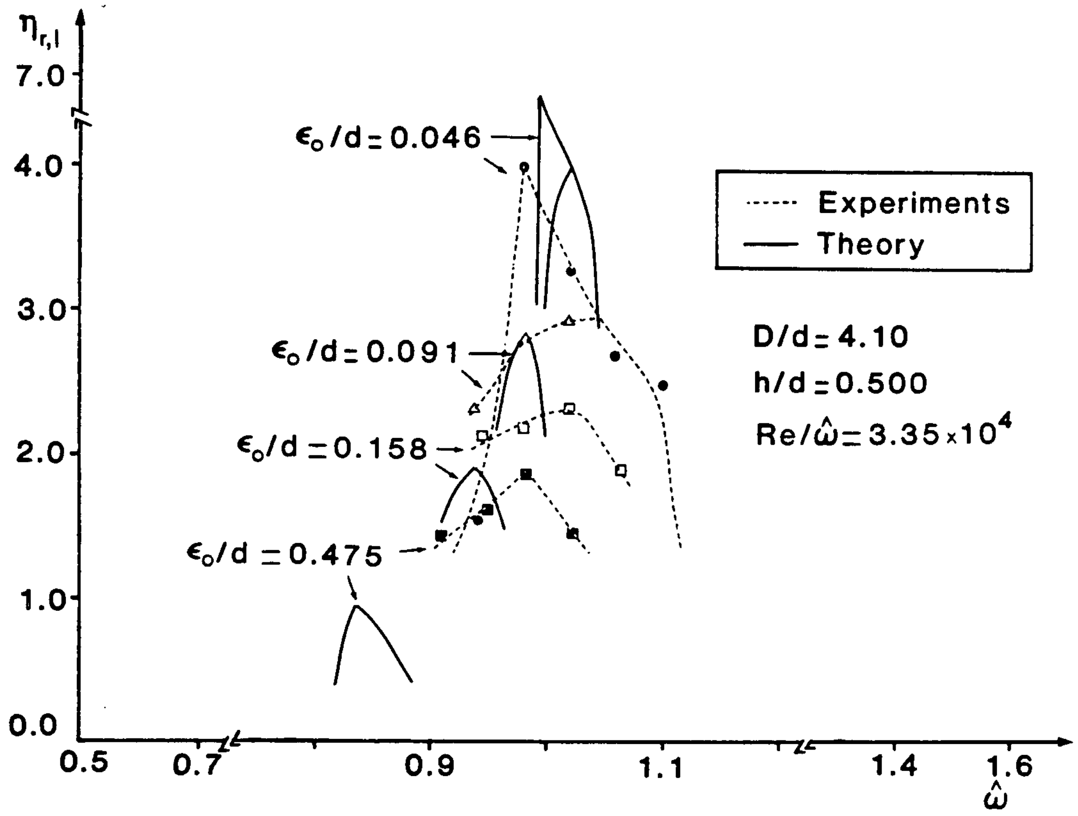

Fig. 25 Peak damping ratios as affected by amplitude

(iv) Effect of Liquid Height

This geometric parameter significantly affects the position of the resonant region, as discussed during the theoretical development. For the damper of Fig. 26, a value of $h/d = 0.48$ is expected to result in a purely linear response (i.e., $K_1 = 0$

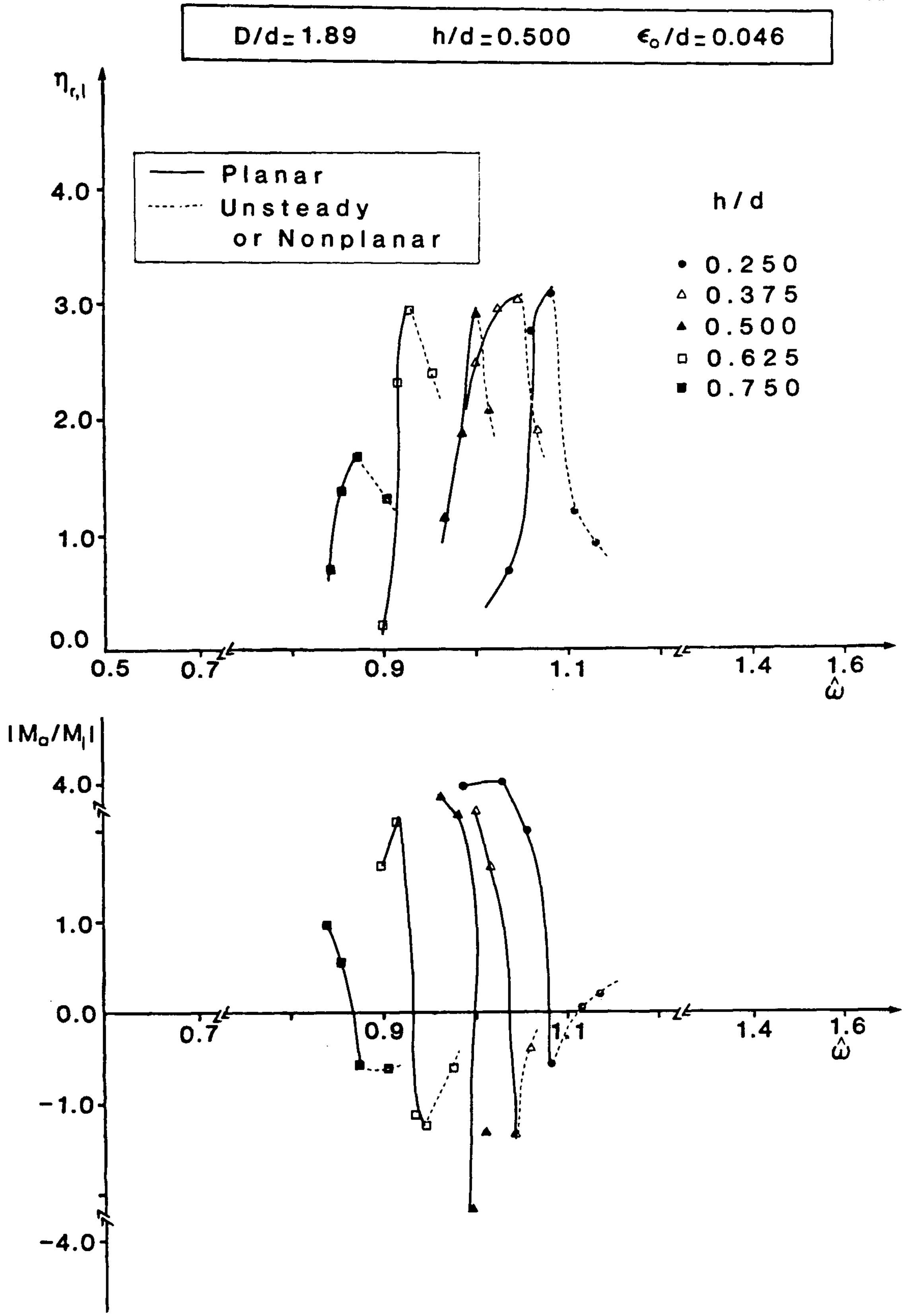

Fig. 26 Maximum damping and added mass ratios for various liquid heights at $\epsilon_0/d = 0.046$

in relation 10a of Chapter 2) with resonance at $\hat{\omega} = 1.0$, and infinite damping and added mass ratios. This is supported by the experiments, as $h/d = 0.5$ generates a pronounced peak near $\hat{\omega} = 1.0$. However, the peak value of $\eta_{r,l}$ is around 3.0 and is essentially somewhat insensitive to liquid height in the range $h/d \leq 0.625$. In general, a shift in the resonant frequency with liquid height was not as severe as that predicted by the theory. The potential flow solution still continues to provide the right softening or hardening trends for the damper with various h/d as illustrated in Fig. 27 (higher amplitudes). Resonance for $h/d \geq 0.75$ is no longer possible as the planar mode becomes unstable thus suggesting, once more, that high liquid heights be avoided in designing a damper. At higher D/d ratios, both theory and experiments indicate a more linear behavior as it is the case of resonant interactions discussed earlier, with smaller shifts in the resonant frequency and well defined peak responses (Fig. 28).

The experimental results proved to be quite useful in assessing the theoretical model. For instance, the energy dissipation in the potential flow regime is obviously not negligible as the sloshing action is well contained at resonance in spite of the relatively small nonlinear effects at certain liquid heights, as discussed earlier. This may be responsible for the weaker than predicted nonlinear effects at other h/d. Moreover, the theory is again shown to be less reliable at low liquid heights, possibly due to a relatively large boundary layer thickness.

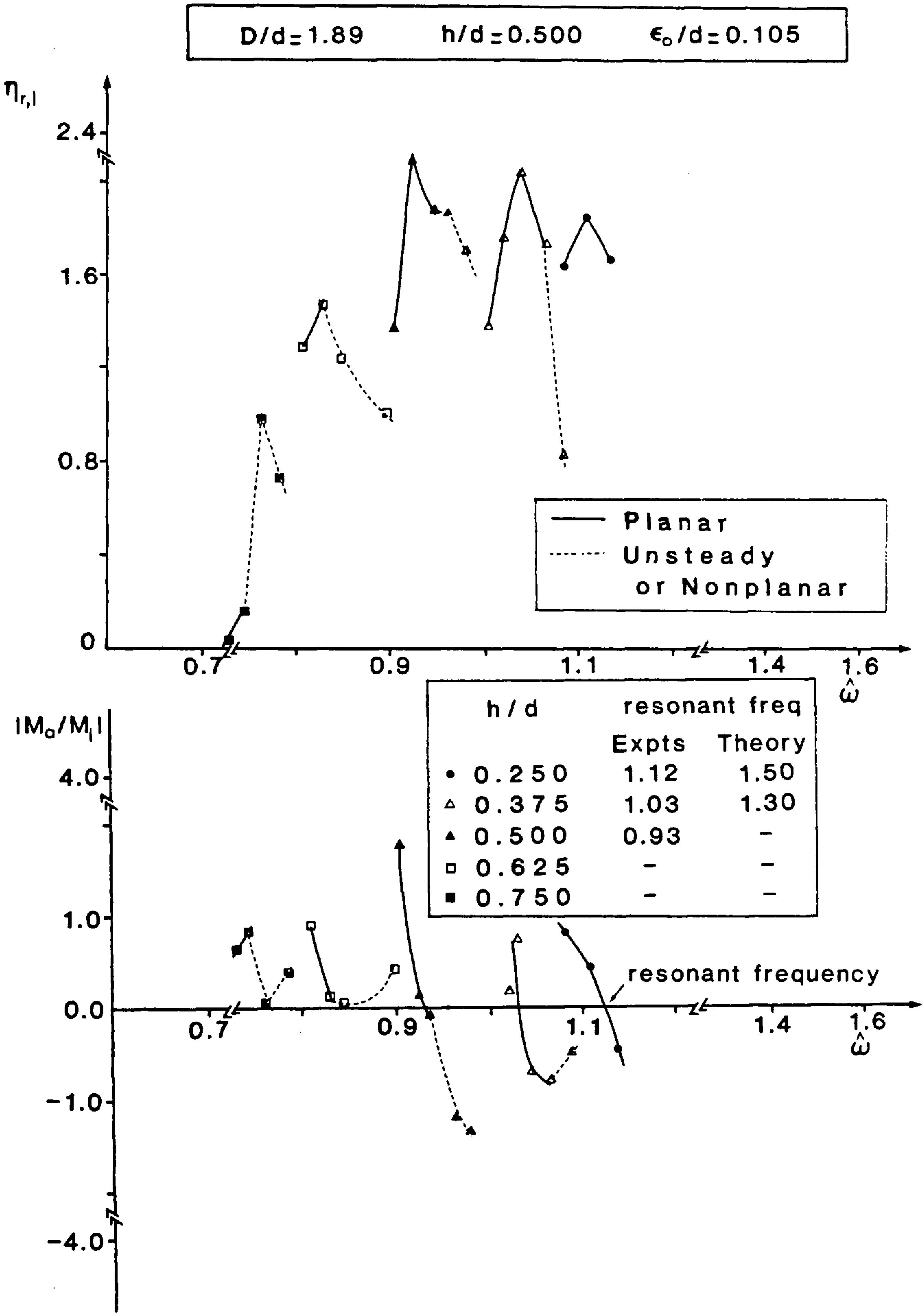

Fig. 27 Variation of the peak response with liquid height for damper#1 at $\epsilon_0/d = 0.105$

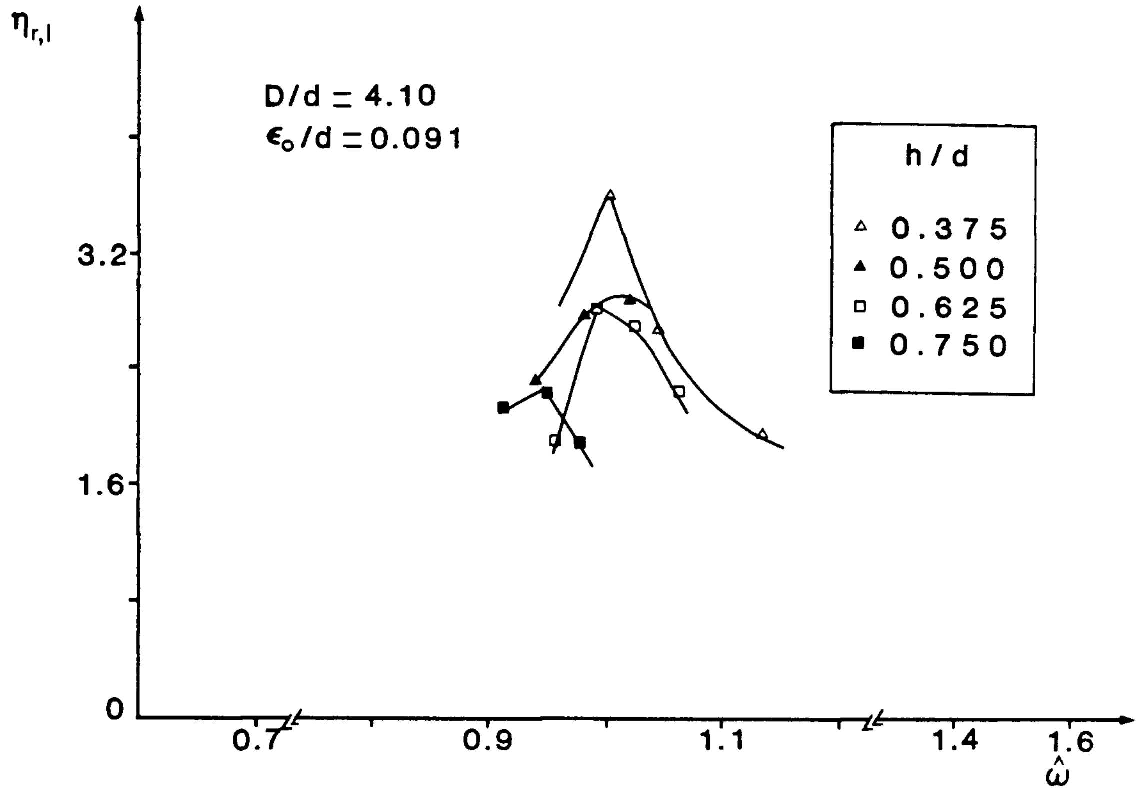

Fig. 28 Variation of the peak damping ratio with liquid height for damper#7 at $\epsilon_0/d = 0.091$

(v) Effect of Diameter Ratio

Maximum damping ratios have been shown to be higher for $D/d = 4.10$ due to the smaller nonlinear effects (Fig. 21), a result supported by the theoretical development of the resonant interactions. In fact, experiments indicate a continuous improvement in the performance with increasing diameter ratio. The frequency spectrum curves of Fig. 29 exhibit smaller superharmonic response as D/d is changed from 1.84 to 2.40 (ratio of 3rd/1st harmonic from 0.57 to 0.37 despite a slightly higher ϵ_0/d), while the maximum $\eta_{r,l}$ in the frequency domain remains

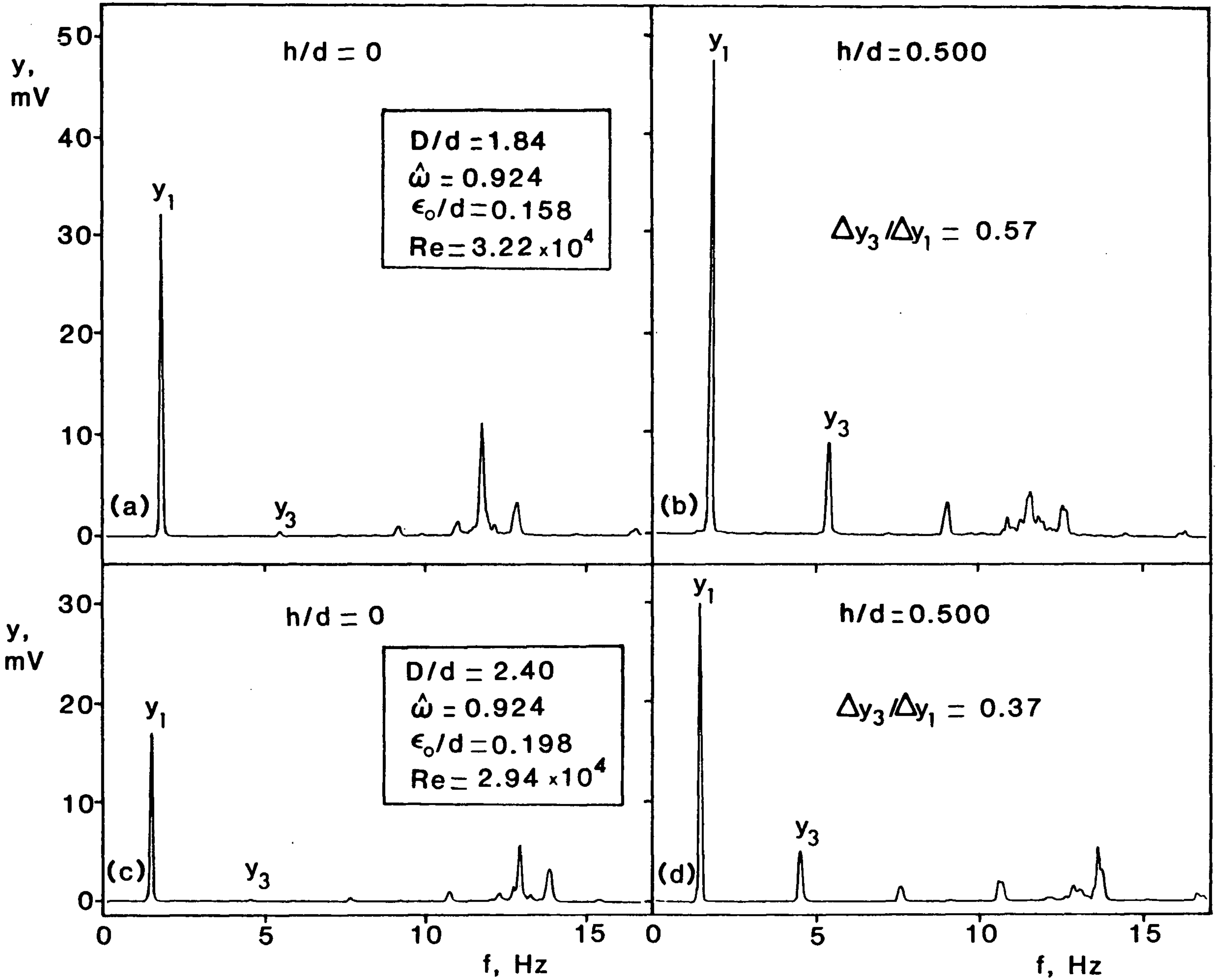

Fig. 29 Frequency spectrum of the response for damper#5 and #6 showing the effect of D/d

higher with amplitude as the diameter ratio varies from 1.0 to 4.1 (Fig. 30). It should be mentioned that the curves for the response without damping liquids are also presented in Fig. 29 as their peak amplitudes have to be substracted from the total response to obtain the net sloshing force. Results for very slender dampers ($D/d \geq 10.0$) suggest that the trends persist[90], promising a very efficient design. Theoretical predictions are not always straightforward as the transition point from the no interaction to interacting solution has to be arbitrarily chosen. Both formulations should converge, however, the latter becomes unstable as the interactions weaken (increasing ς_{21} coefficient) while the other is not yet representative of the situation. Unaccounted viscous effects may again be responsible for generating the experimentally observed stable transition range. Furthermore, the estimated boundary given by relation (20), where $\hat{\epsilon}$ is substituted by $\hat{\epsilon}^{1/3}$ at resonance, also suggests that ν_0 should be smaller than 1.0 for better agreement with experiments.

(vi) Reynolds Number Effect

The equations of Chapter 2 along with previous investigations dealing with the sloshing motion linear range[87-90] established the reduced damping to be proportional to $Re^{-1/2}$. The present tests however indicate this may not be the case near resonance, as shown for two different geometries in Fig. 31. Several liquids such as water, alcohol, kerosene, and oil of different viscosities, as well as two damper sizes with otherwise identical geometric parameters h/d and D/d, were used to vary the

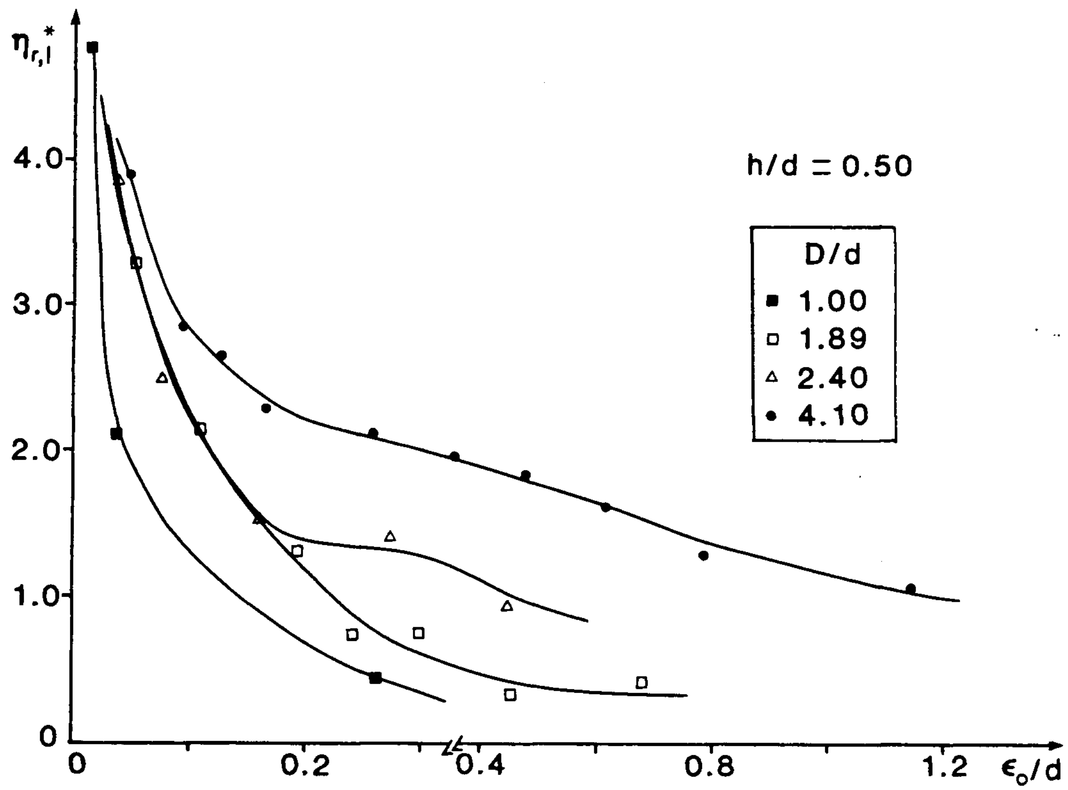

Fig. 30 Maximum damping ratios versus amplitude for various D/d

Reynolds number. Results show that $\eta_{r,l}$ and $|\frac{M_a}{M_l}|$ remain generally unaffected by a change in Re in the nonplanar mode (for Re as low as 1.73×10^4 in Fig. 31a), with a slight downward trend in the planar mode (Fig. 31b). At very low Reynolds number (580 or 700 in Fig. 31), the curves drop significantly with the planar motion becoming stable over the entire range of excitation amplitude. Hence, it can be speculated that the higher dissipative effects at lower Re are offset by a reduction in the sloshing motion through the combined action of dissipation in the main flow field and the larger boundary layer thickness. Although dominant, the nonlinearities alone are not the only mechanisms restricting the response at resonance. The importance of small damping terms at $\hat{\omega} = 1$ can be well illustrated by the analogy

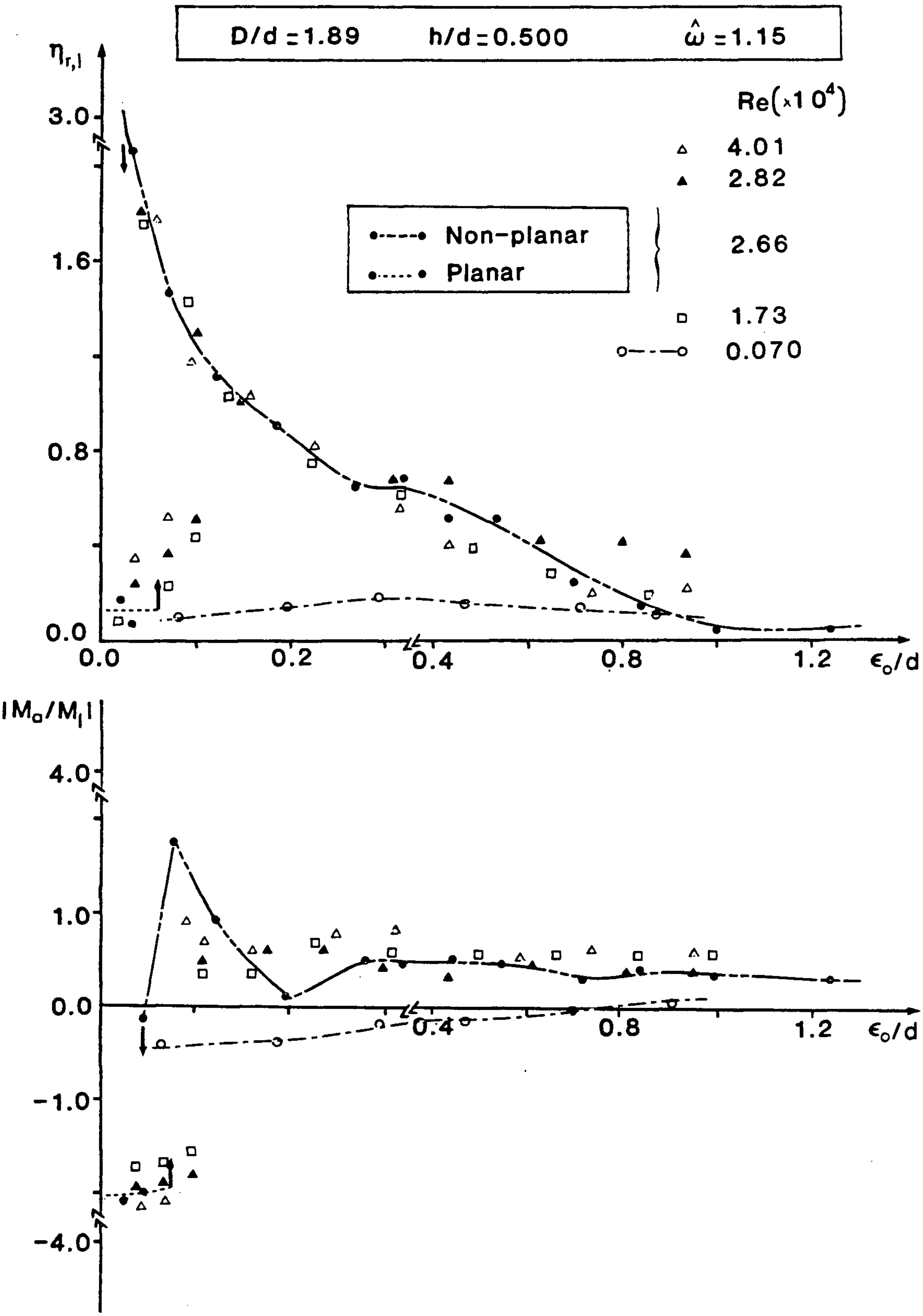

Fig. 31 Damping and added mass ratios as affected by *Re* for dampers with: (a) $D/d = 1.89$

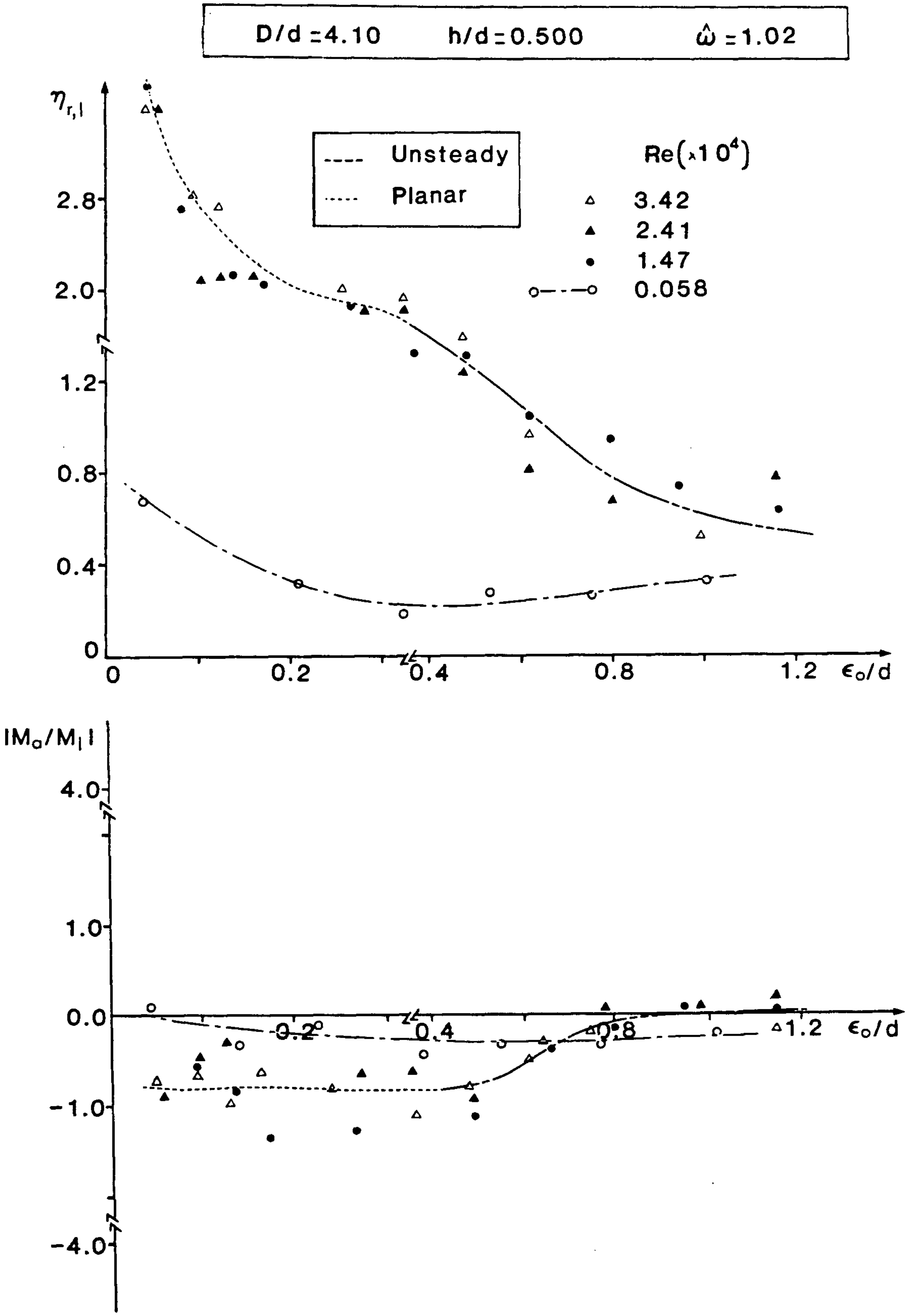

Fig. 31 Damping and added mass ratios as affected by *Re* for dampers with: (b) $D/d = 4.10$

of a simple mass-spring-dashpot linear system (Appendix VI), for which inertia and stiffness are otherwise the controlling parameters in the nonresonant region. The liquid sloshing response also exibits a gradual sign reversal in the added mass near resonance, as pointed out earlier. This is in contrast to a sudden jump characteristic of an undamped model. As the energy dissipation is quite motion-dependent here, the addition of even small viscous effects in the flow might be sufficient to improve the present formulation. A further point of interest is the absence of variation in the resonant frequency with changing Reynolds number, for all the dampers considered in this study. The smaller free stream (potential region) at lower Re due to an increased boundary layer thickness is also accompanied by a larger D/d ratio, eventually resulting in a cancellation effect and the observed trend.

(vii) Effect of Configuration

Baffles or inner tube positioned inside the damper have shown some success at promoting energy dissipation for a certain range of frequencies, as reported by previous investigations[90]. The study is extended here into the optimal region of resonance by using 3 dampers with $D/d = 1.89$. Typical results are presented in Fig. 32 which suggests that the baffle configuration generally suppresses the nonplanar mode (Fig. 32a, $\hat{\epsilon}_0 \geq 0.03$). Furthermore, the added mass was found to be lower than that for the plain damper, thus indicating a reduction in the amount of sloshing motion. The effects are somewhat different with the inner tube where the interference with the free surface now generates a negative added mass at low amplitude. Although more dissipative mechanisms are present, such as the formation of a wake behind the baffles, or increased friction against the tube, the additional restrictions imposed on the flow result in a net loss in $\eta_{r,l}$. A similar picture is obtained by varying the frequency (Fig. 32b), with lower maximums for the added mass and damping ratios. The peak response for $\eta_{r,l}$ appears to be wider prior to resonance, as expected for such systems, however, the absence of nonplanar motion for the baffle arrangement and the interference with the inner tube yield an overall lower efficiency for $\hat{\omega} > 1.0$. As in the case for low Reynolds number flows, any configuration preventing the large motion of the free surface appear to affect the damper performance. Note the change in the resonant frequency with the introduction of the baffles ($|\frac{M_a}{M_l}| = 0$ at $\hat{\omega} = 0.92$). The inner tube-liquid contact was also found to make the planar mode more stable well into the region where the rotating motion would have otherwise started with a plain configuration.

(viii) Note on Damper Cross- Section

The cross-sectional shape allowing for larger sloshing motion is likely to maximize the damper efficiency. Straight wall containers (i.e., square or rectangular cross-section) were studied here as they are easier to construct and simpler to analyse theoretically. Some tests on circular cross-section models were also conducted with the performance comparable or lower than that of an otherwise similar straight wall damper. For instance, a geometry with $D/d = 3.00$ and $h/d = 0.5$ yielded a peak $\eta_{r,l} = 2.2$ at resonance, for an amplitude $\epsilon_0/d = 0.06$. The same trends were

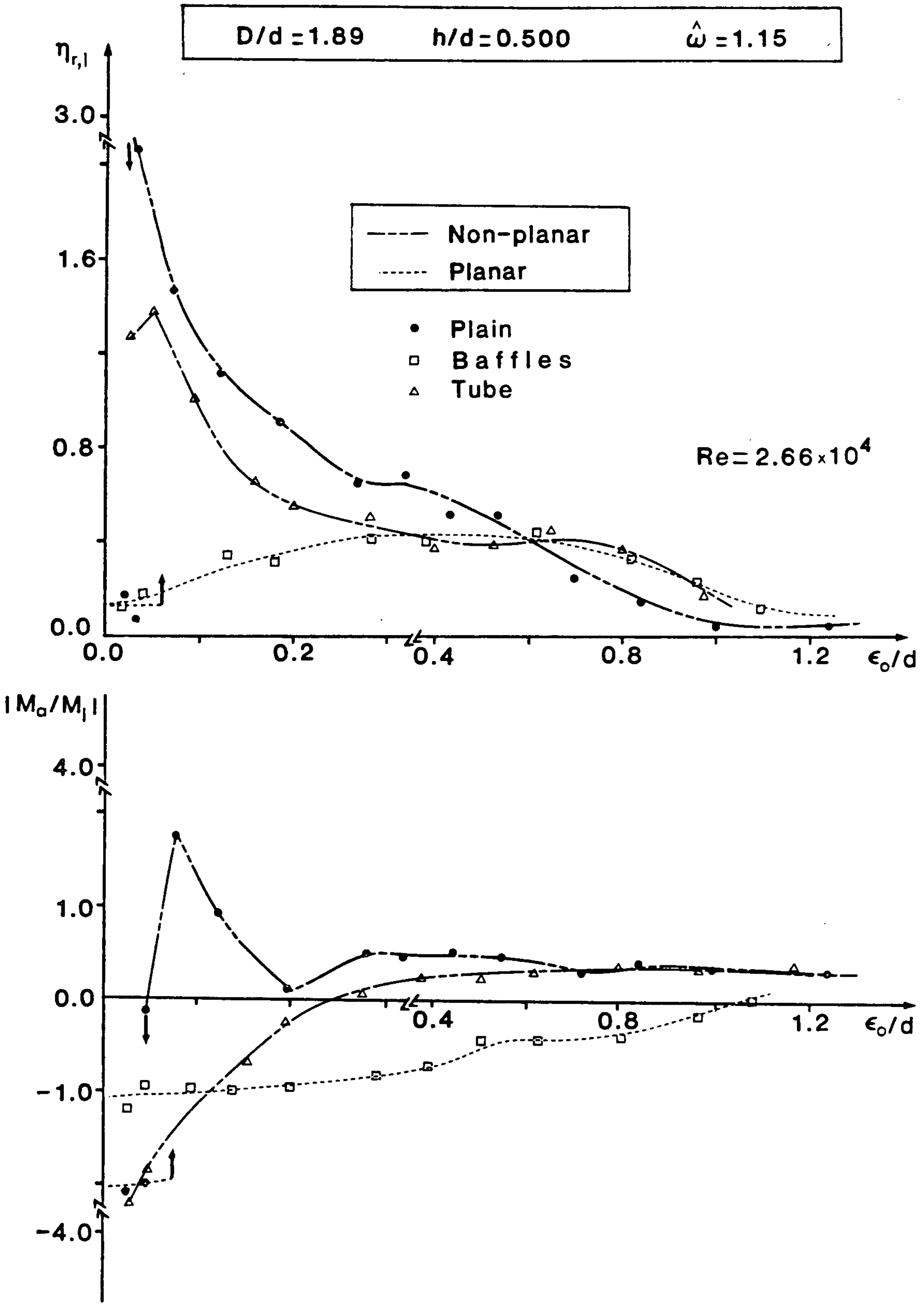

Fig. 32 Effect of internal configuration on $\eta_{r,l}$ and $|\frac{M_a}{M_l}|$ versus: (a) ϵ_0/d

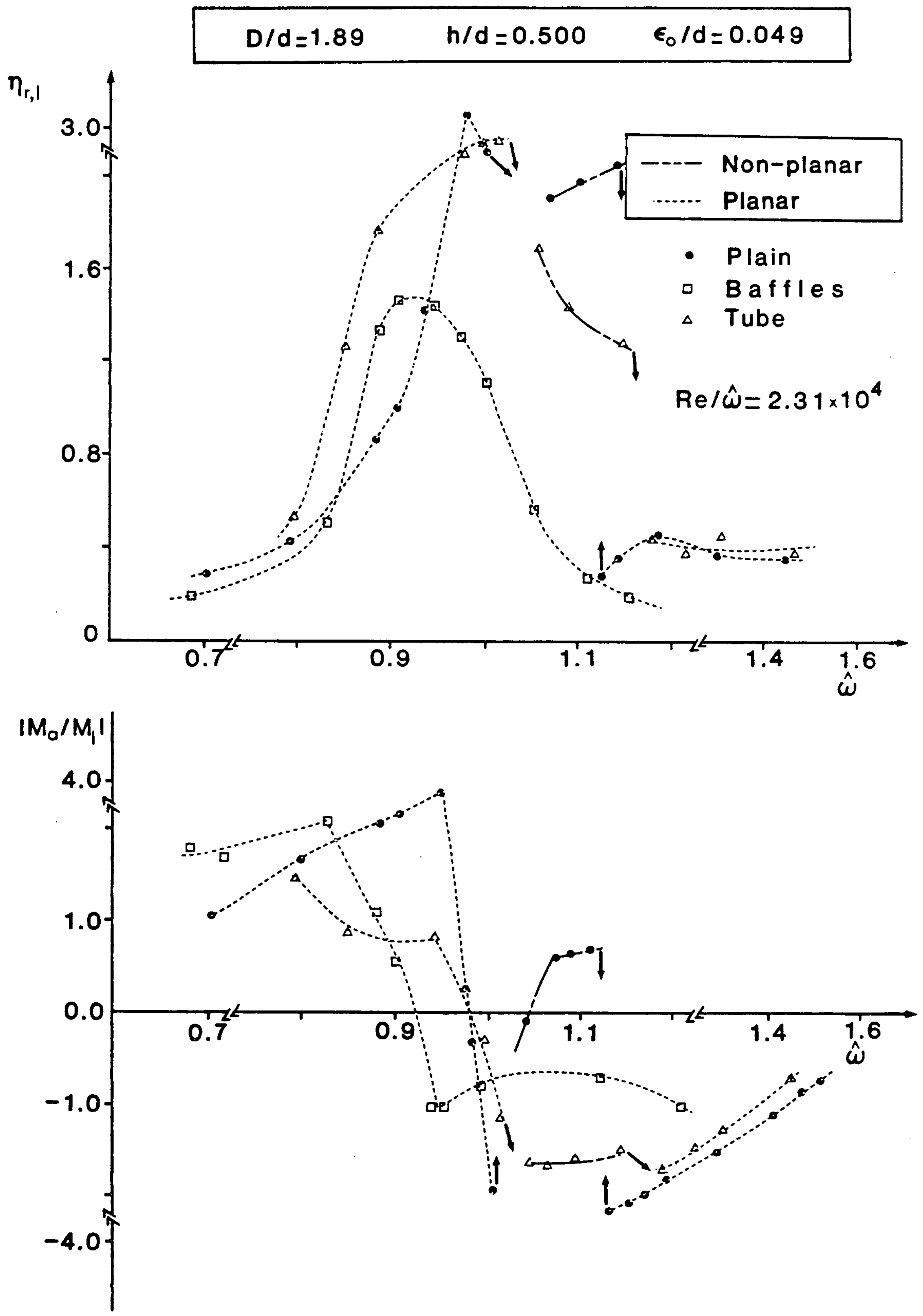

Fig. 32 Effect of internal configuration on $\eta_{r,l}$ and $|\frac{M_a}{M_l}|$ versus: (b) $\hat{\omega}$

observed during free oscillation experiments, although here resonance was more difficult to establish and no quantitative results could be obtained in this region. An interesting concept consisting of a sloping cross-section (Fig. 33), allowing for the breaking of the liquid sloshing waves, was similarly tried. The logarithmic decrement method showed some improvements are possible for particular geometric ratios of d_1/d, d_2/d and d_3/d over the square geometry. More systematic tests in forced oscillations would have to be conducted to validate the idea. The introduction of flexible walls is another area to be examined.

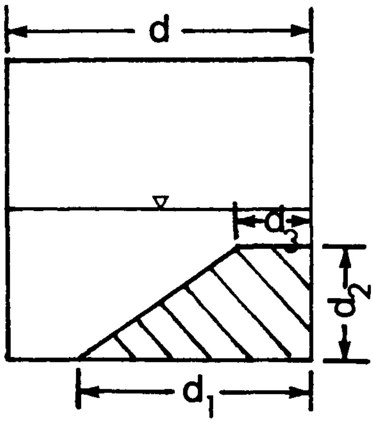

Fig. 33 Proposed sloping cross-section

3.4.3 Comparison with Free Oscillation Tests

The distinct character of the free oscillation tests and associated apparatus[90] (Fig. 34) provided a means to verify the steady-state excitation results. The additional parameters representing the amplitude decay $d\epsilon_0/dt$, the small rotational motion induced by the pivoting arm, and the variation in the natural frequency due to fluid-structure interactions, are variables likely to influence the response. Fig. 35

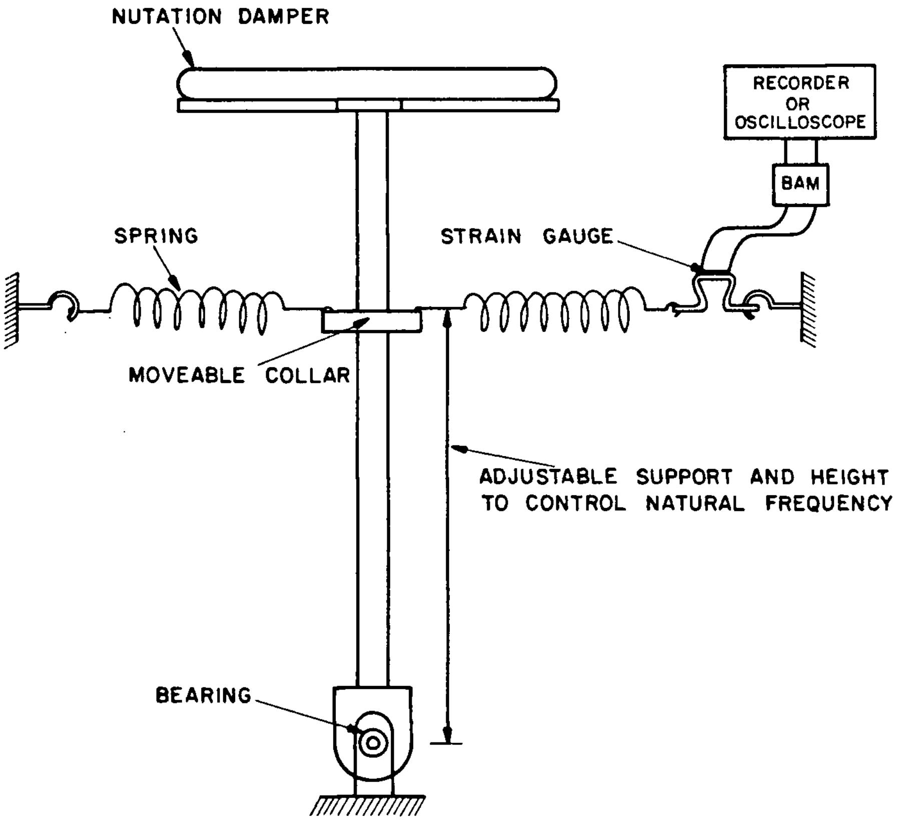

Fig. 34 Apparatus used for free oscillation tests

compares some results as given by the two methods. The amplitude decay approach clearly tends to smooth the curves due to the transient effects (Fig. 35a). In most cases, $\eta_{r,l}$ is lower than its corresponding value for the forced vibration tests (Fig. 35b). This is not surprising as the flow is likely to need some time to respond to the increase in $\eta_{r,l}$ with dimishing amplitude. Furthermore, the boundary for the transition from planar to nonplanar motion is delayed. The trends are, however, the same and the shift in magnitude could be attributed to the system rotation, as discussed in the next chapter. It should be pointed out that $d\epsilon_0/dt$ was minimized by using a large dead weight (i.e., small fluid to total mass ratio). The reduced damping ratio was taken as

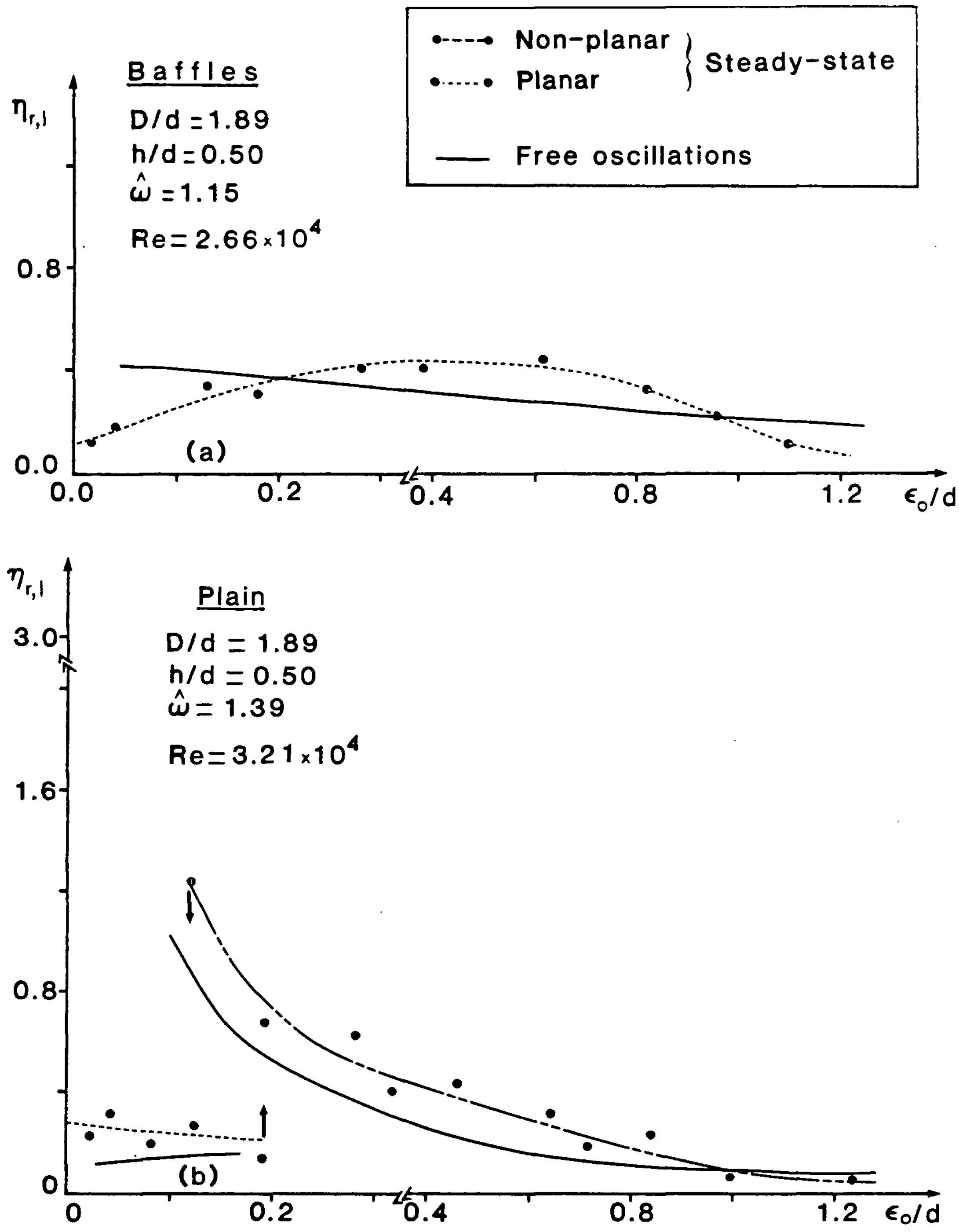

Fig. 35 Damping characteristics versus ϵ_0/d as obtained by steady-state and free oscillation experiments for: (a) damper with baffles; (b) plain damper

$$\eta_{r,l} = \frac{\ln x_1/x_m}{2\pi m}\frac{I_l}{I} \tag{45}$$

according to the logarithmic decrement method normalized for the relative inertia of the fluid. Here:

x_m = system amplitude for the mth cycle;

$\frac{I_l}{I}$ = fluid to total inertia ratio for the pivoting system (equivalent to M_l/M for translation).

The relation is valid for discrete values of amplitude corresponding to m=1, 2, etc., and can be made continuous by taking the limit as m tends to 0, i.e.,

$$\eta_{r,l}(x) = \lim_{m \to 0} \frac{\ln x_1/x_m}{2\pi m}\frac{I_l}{I}, \tag{46}$$

$$\text{or} \quad \eta_{r,l}(x) = -\frac{1}{2\pi}\frac{dx/dm}{x}\frac{I_l}{I}, \tag{47}$$

where x is the amplitude function,

$$x(m) = x_m. \tag{48}$$

A polynomial fit for the envelope of amplitude decay was then applied to facilitate the analysis,

$$x(m) = A_0 + A_1 m + A_2 m^2 + ..., \tag{49}$$

as shown in Fig. 36, which yields

$$\eta_{r,l}(x) = -\frac{1}{2\pi}\left[\frac{A_1 + 2mA_2 + ... + pm^{(p-1)}A_p}{A_0 + A_1 m + ... + A_p m^p}\right]\frac{I_l}{I}. \tag{50}$$

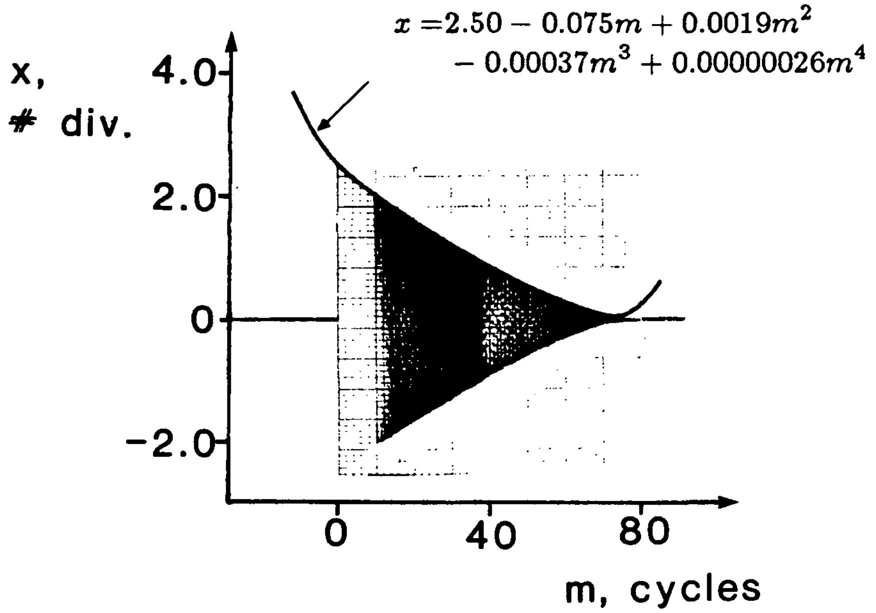

Fig. 36 Amplitude decay for the half-full damper#1 oscillating at $\hat{\omega} = 0.924$ with an initial displacement of $\epsilon_0/d = 1.28$ (chart recorder Type TR322, Gulton Industries)

3.5 Concluding Comments

This experimental program combined with the theoretical development have resulted in an in-depth understanding of the nutation damper behavior. The major findings are summarized below:

- The damping characteristics are entirely governed by the liquid motion. The condition of resonance with the damper operating at its first sloshing natural frequency results in a substantial gain in $\eta_{r,l}$. Any configuration restricting the action of the free surface, such as baffle arrangements, inner tubes, or even high viscosity fluids, further contributes to a drop in efficiency.

- Nonlinearities play a major role at resonance. They should be minimized as they generally limit the liquid motion, reflected by a reduction in damping and added mass ratios. They are also responsible for the softening or hardening characteristics governing the response versus the amplitude of excitation. The appearance of the nonplanar mode has often beneficial effects as it extends the high efficiency region beyond resonance.

- Whenever possible, long and slender dampers with relatively low liquid heights (high D/d and $h/d \leq 0.5$) should be used as they exhibit weaker nonlinear effects. When resonance can only be met at smaller diameter ratios, particular h/d can also be found to provide similar characteristics.

- The theory serves as a useful tool in understanding the damper behavior. The resonant frequency at low amplitudes, as well as the hardening or softening trends, are often properly predicted. The peak response and the nonlinear effects are, however, too pronounced and suggest that significant dissipation takes place in the main flow field. The analysis is quite demanding, in terms of time and efforts, since many cases of resonant interactions need to be considered, at times leading to unstable solutions. However, the procedure provides considerable insight into the effect of the various controlling parameters.

- Damping forces outside the boundary layer are likely to restrict the motion of the main stream at resonance (lower peaks for $\eta_{r,l}$ and $|\frac{M_a}{M_l}|$) while promoting dissipation elsewhere (wider region). A numerical approach for solving the full Navier-Stokes equation would therefore be more accurate. However, the three dimensionality of the flow and its time dependence, combined with the highly nonlinear free surface boundary condition, would make this process fairly costly. Furthermore, the presence of such phenomena as discontinuous, turbulent wave fronts mentioned in section 3.3 would still be unaccounted for. Improvements to the potential flow solution could also be implemented to correct for the boundary layer thickness. The variational method, allowing for the introduction of an empirical dissipative term in the equation of the main flow field[67] is another possible avenue of research.

- Finally, turbulence was never found to be beneficial as $\eta_{r,l}$ did not change its trends at higher amplitudes or frequencies of excitation (with the transition from laminar to turbulent flow).

4. WIND INDUCED INSTABILITY STUDY

4.1 General Description

Effectiveness of the dampers in controlling vortex resonance and galloping instabilities was assessed in both laminar ($u'/V < 0.1\%$) and turbulent flows for two and three-dimensional bluff bodies undergoing translation and rotation, respectively. The closed circuit laminar flow wind tunnel with a test section of $0.69 \times 0.91 \times 2.44$ m, and the large boundary layer tunnel (24.4 m long, with an initial cross-section of 1.58×2.44 m) fitted with 20.74 m of roughness board upstream of the model to produce desired boundary layer thickness and turbulence intensity, were used to simulate the external environment. Dampers were mounted on a variety of aerodynamic models with square or circular cross-sections. The two-dimensional arrangement, useful for predicting the response of tall structures such as smokestacks, buildings, etc., spanned the height of the laminar flow wind tunnel, while a horizontal set-up simulated a transmission line configuration. The rotational motion was studied with three-dimensional models of finite aspect ratio.

4.2 Two-Dimensional Tests in Laminar Flow

4.2.1 Preliminary Remarks

Although the natural wind is essentially turbulent, the vortex resonance and galloping response of two-dimensional, square and circular cylinders in laminar flow has been well documented. Consistent empirical results[91] combined with the development of a successful galloping theory[93] permit an approximation of the cross-flow oscillations, provided the aerodynamic reduced damping $\eta_{r,a}$, also called mass-damping[6] or stability parameter[8], is known. These tests are therefore well suited for the evaluation of the nutation damper characteristics under conditions of nonlinear, wind-induced forcing excitations. As the amplitude growth of the model response is usually assumed to be slow until a limit cycle is reached, due to relatively high $\eta_{r,a}$ in wind engineering problems, the steady-state results of Chapter 3 should apply.

4.2.2 Test Arrangement and Model Description

A rigid frame located outside the wind tunnel and supporting four air bearings, in turn carrying a sliding shaft at top and bottom on which aerodynamic models were mounted in a vertical position, was used to conduct the two-dimensional tests (Fig. 37). Four springs provided the structural stiffness and an inductance coil type displacement transducer recorded the amplitude response. This already available set-up, specifically designed for the study of aeroelastic problems, was also equipped with eddy current magnetic dampers. More information on the test facility is given in reference 97. Relatively large (10.2 cm $\approx$ 4") yet light models were constructed in the Department's machine shop to produce the desired instability region, with $\eta_{r,a}$ as low as 2.0 to 3.0 to allow for some flexibilty in the choice of nutation damper size. A smaller 5.1 cm (2") square cross-section cylinder was also used to evaluate the performance for a different value of aerodynamic reduced damping ratio. 0.64

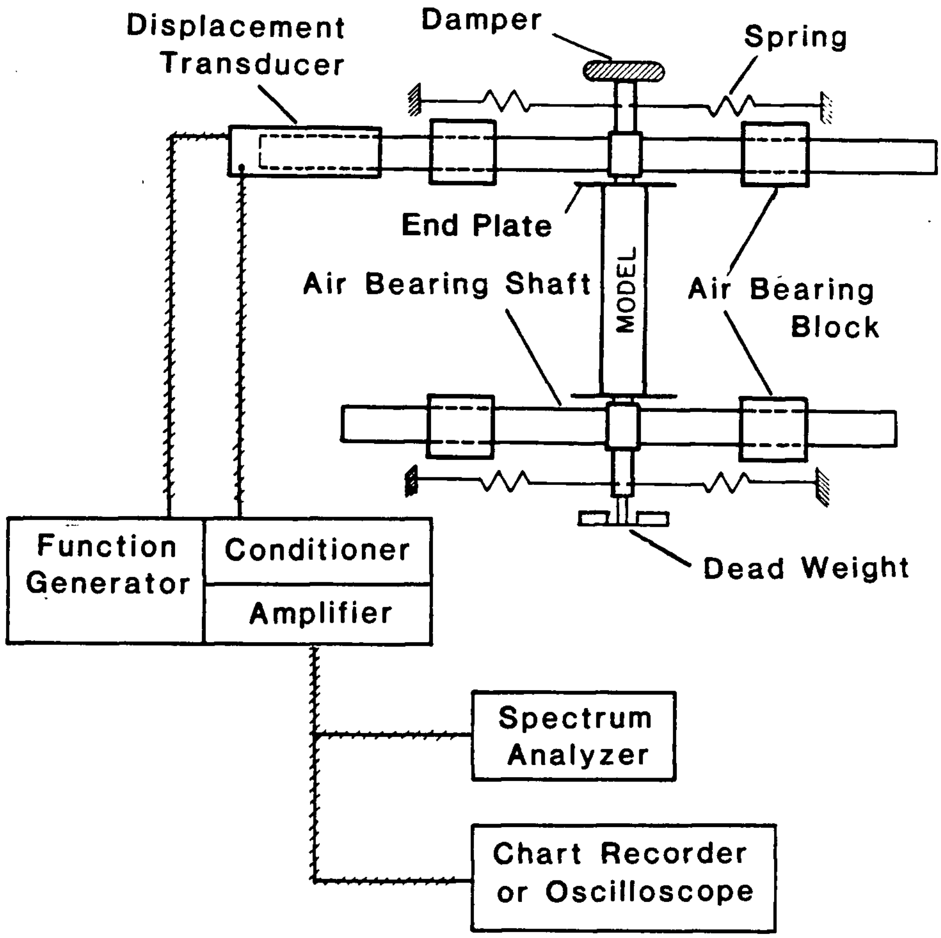

Fig. 37 Wind tunnel set-up for two-dimensional tests

cm (0.25") thick balsa wood provided reasonable bending and torsional stiffness while two thin aluminum plates bonded to the balsa wood defined sharp edges of the square configuration. The 10.2 cm diameter circular cylinder was made of 0.64 cm thick PVC pipe section. The models were provided with medium size end plates, following a careful design procedure, as explained in section 4.2.4. The details are given in Table II. Although the model weight ranged from 349 to 786 g, the moving shafts, clamping mechanisms, and damper supports contributed more to the inertia of the oscillating system (1094g ±37 g, according to springs used). It could also be changed with the addition of metallic plates inside the model, or dead weight outside the tunnel for finer adjustments.

Table II Physical description of the two-dimensional aerodynamic models

MODEL#	1	2	3
CROSS-SECTION	102 mm	51 mm	102 mm
LENGTH (mm)	673	673	673
MATERIAL	BALSA & ALUMINUM	BALSA & ALUMINUM	PCV
MASS (g)	786	349	745
END PLATES	204 mm, 305 mm	102 mm, 251 mm	204 mm, 305 mm

Static force measurements on the square cross-section models were carried out with the six-component pyramidal strain gauge balance (Aerolab). Drag D_r and forces perpendicular to the flow S_p were recorded over a range of angle of attack α giving the side force,

$$F_y = S_p \cos\alpha - D_r \sin\alpha, \tag{51}$$

useful in prediction of the galloping response.

4.2.3 Calibration Procedure

The displacement transducer was connected to a chart recorder and a spectrum analyser (same instruments as in Chapter 3). A static calibration procedure with the chart recorder responding to a given displacement of the model resulted in the curve of Fig. 38(a). The peak amplitude y of a purely sinusoidal signal such as that obtained during the vortex resonance or galloping excitation was measured by the spectrum analyser, and in turn calibrated against the recorder. It gave a constant value of 31.78 mV/cm (Fig 38b).

4.2.4 Model Characteristics

Although large end plates, or the more recent double plate configuration[97], are desirable to reproduce conditions of two-dimensionality[98], the drag and weight penalties can weaken the excitation and response during the dynamic tests. This was assessed during a preliminary determination of the static side force coefficient on the 5.1 cm square cross-section (Fig. 39a). Results clearly indicate a relatively lower initial slope of C_{fy} versus α, for both the no end plate and the large end plate configurations, known to delay the galloping instability. Less pronounced trends were observed for the 10.2 cm size square model (Fig. 39b). Medium size end plates, sufficient to minimize the effect of suction caused by slots in the tunnel walls were therefore adopted. Of course, the slots were necessary to permit vibrational motion of the system. More results dealing with this particular aspect are discussed in the next section. The position of the plates also played a significant role in earlier

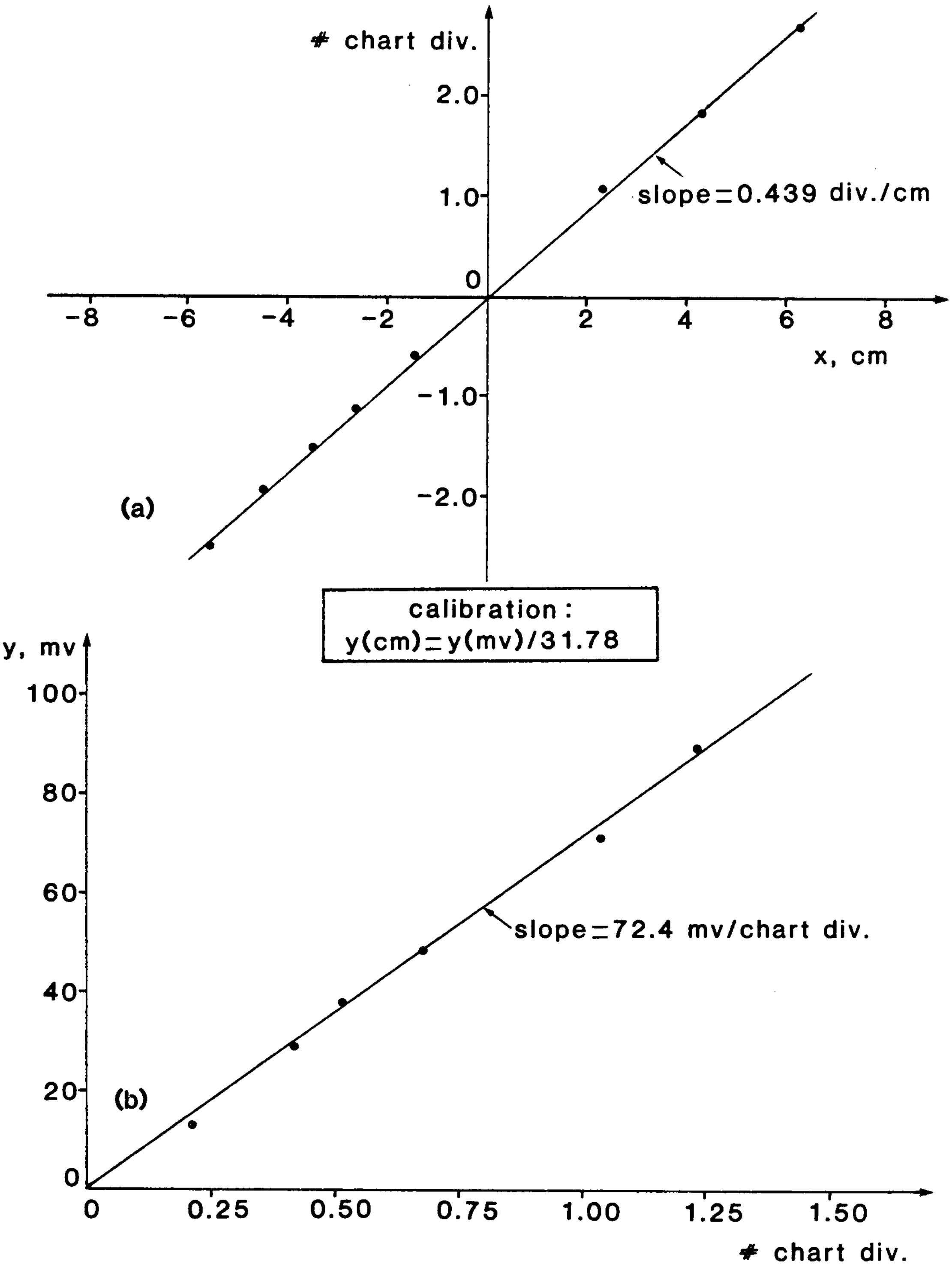

Fig. 38 Calibration constants used during the tests for: (a) chart recorder; (b) spectrum analyser

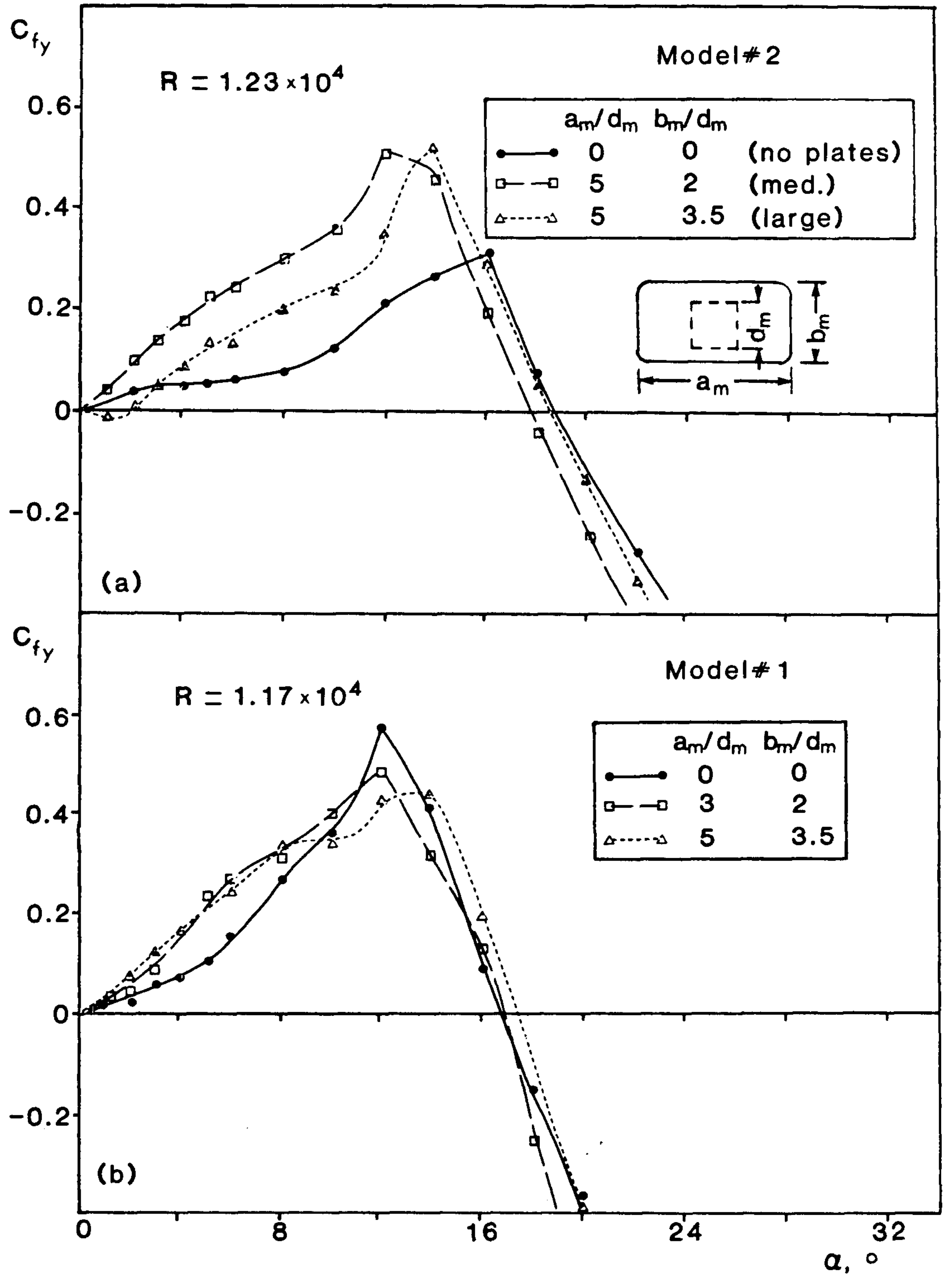

Fig. 39 Effect of end plate dimension on C_{fy} for: (a) model#2; (b) model#1

tests on an aluminum, 7.6 cm (3 in) diameter circular cylinder. Presence of a 1.27 cm plate-wall gap resulted in a vortex resonance response much lower than expected. A smaller gap of 0.63 cm, necessary to install the models, was used in all subsequent experiments.

The high blockage ratio (11%) of the 10.2 cm section model (model #3) was responsible for larger peak displacements, compared to the standard vortex resonance response for a circular cylinder[91], as shown in Fig. 40. With a shift in dimensionless amplitude Y but otherwise similar shape, this curve can be used as the reference for the nutation damper performance. The response at different levels of $\eta_{r,a}$ was obtained by activating the electromagnetic dampers at different voltage settings. As expected, the damping ratios were found to be essentially constant with amplitude, over the range considered (Fig. 41). The logarithmic decrement method in conjunction with the amplitude decay polynomial fit approximation, used in the analysis of data, was described earlier towards the end of Chapter 3. The inherent system damping η_s (i.e., no damper, 0 mA) was also found to be constant at low Y but quickly increased beyond a certain threshold. This is in agreement with earlier studies using such test facilities[99], and is beleived to be caused by the higher bending stresses at larger amplitudes. The deformation during the initial displacement may however be different from that applied by the distributed loading of the air flow pressure field and such a rise in η_s may not occur during the dynamic tests. The galloping response can be predicted by the quasi-steady theory

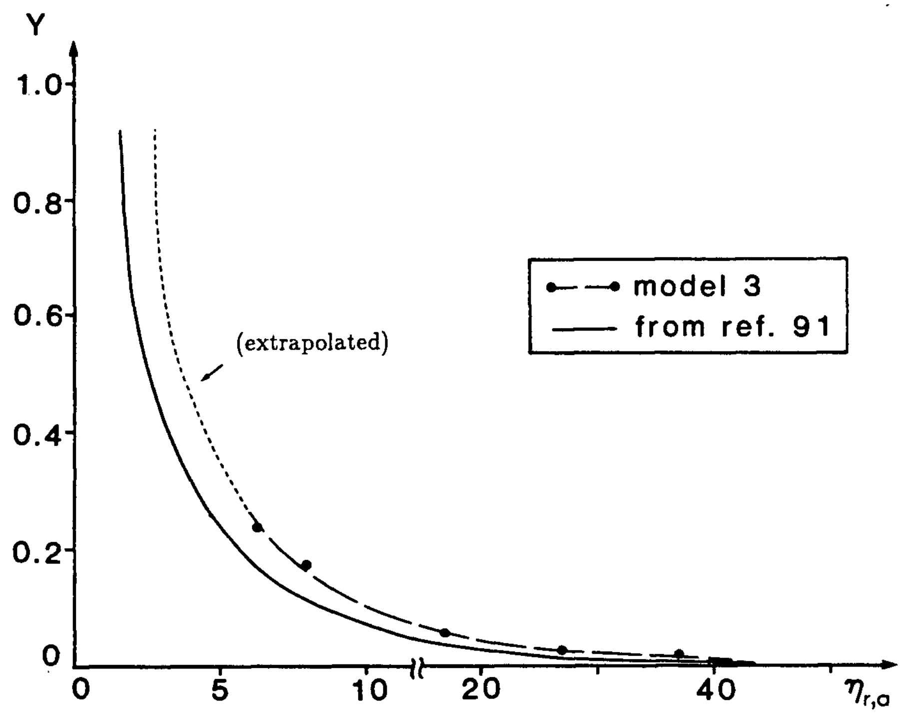

Fig. 40 Maximum displacements of model#3 undergoing vortex resonance

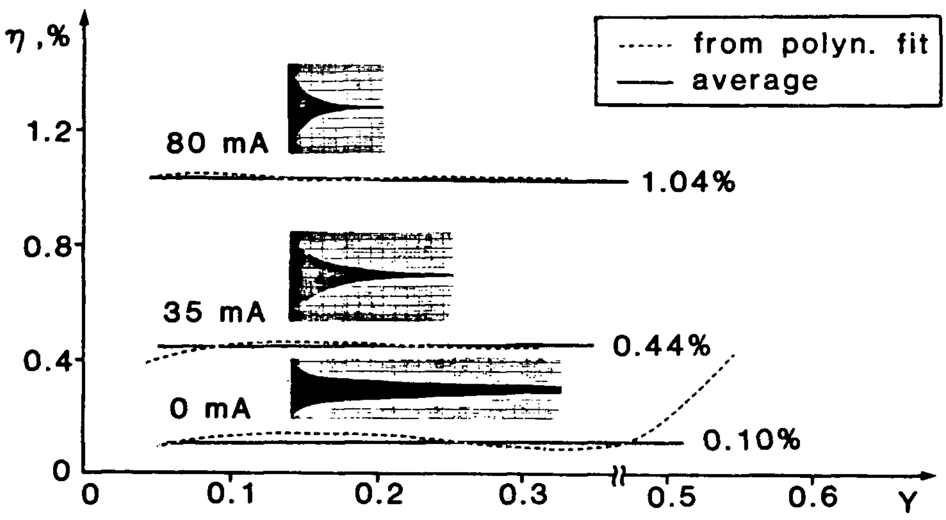

Fig. 41 System damping for different electromagnetic damper settings

using the measured side force coefficients of model#1 and 2 shown in Fig. 42. The results for model#2 (5.1 cm side) compared quite well with those by Brooks[100]. The higher blockage ratio in Fig. 42(b) causes the C_{fy} values to be larger at small angles of attack. The $dC_{fy}/d\alpha$ slopes at $\alpha = 0°$ are approximately 2.6 and 4.6 for the two models, respectively. The galloping response prediction, obtained using a 13th order polynomial approximation for C_{fy}, agreed with the experimental results for the electromagnetic damper set at higher $\eta_{r,a}$ (i.e., galloping onset velocity U_0 far from vortex resonance U_r), as illustrated in Fig. 43(a) and (b). For a lower value of the aerodynamic damping, both vortex resonance and galloping regions overlap, and the response is rather insensitive to $\eta_{r,a}$ until the latter is large enough for a distinct peak near U_r (Fig. 43c). The data were taken for a model natural frequency of 2.00 Hz, and agree with the low turbulence data of reference 97. The validity of the curve at several other frequencies was also established by changing the stiffness of the test arrangement, as shown in Fig. 44.

A well defined response to the vortex shedding excitation was often visible on the frequency spectrum outside resonance, particularly for the 10.2 cm models (Fig. 45a). With the record of the correponding wind velocity, a Strouhal number of 0.196 was found for the circular cross-section (Fig. 45b), whereas the square configuration yielded $St = 0.127$ and 0.139, for the 5.1 and 10.2 cm side, respectively (Fig. 45c). The accuracy of the data was lower for the smaller model due to the reduced aerodynamic forces.

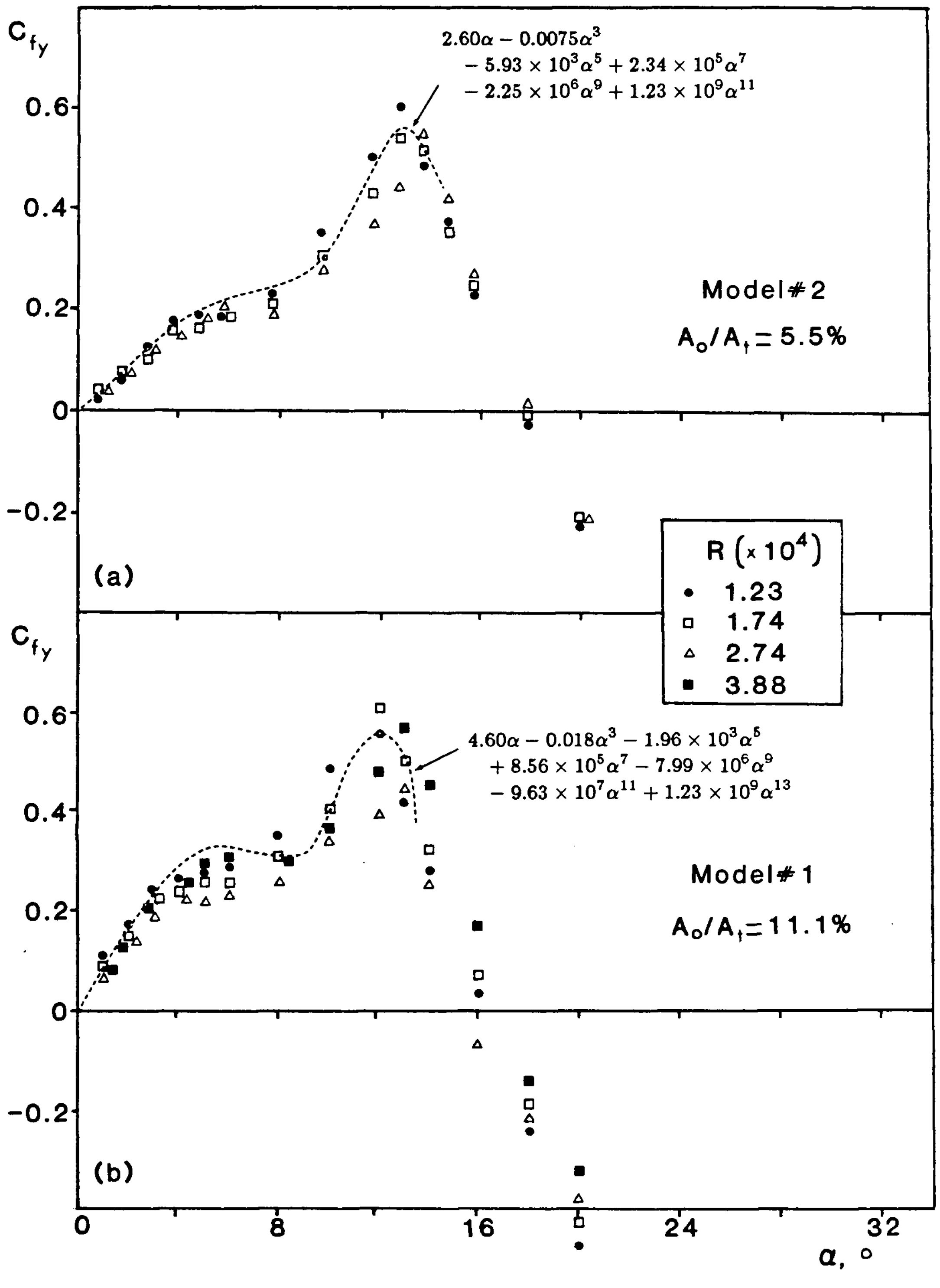

Fig. 42 C_{fy} versus α for: (a) model#2; (b) model#1

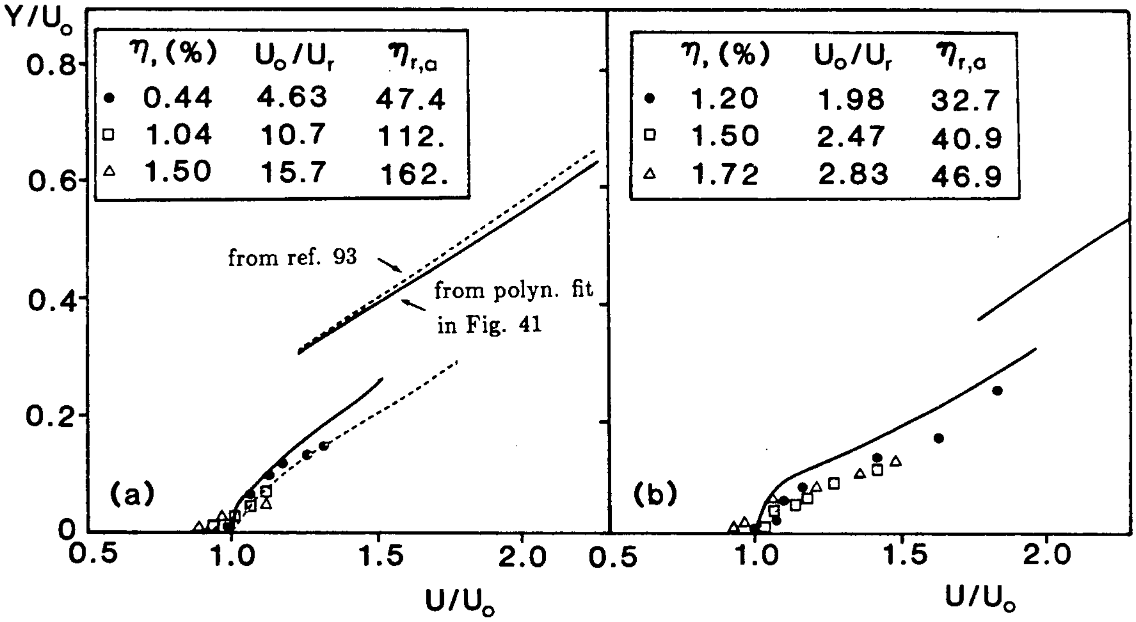

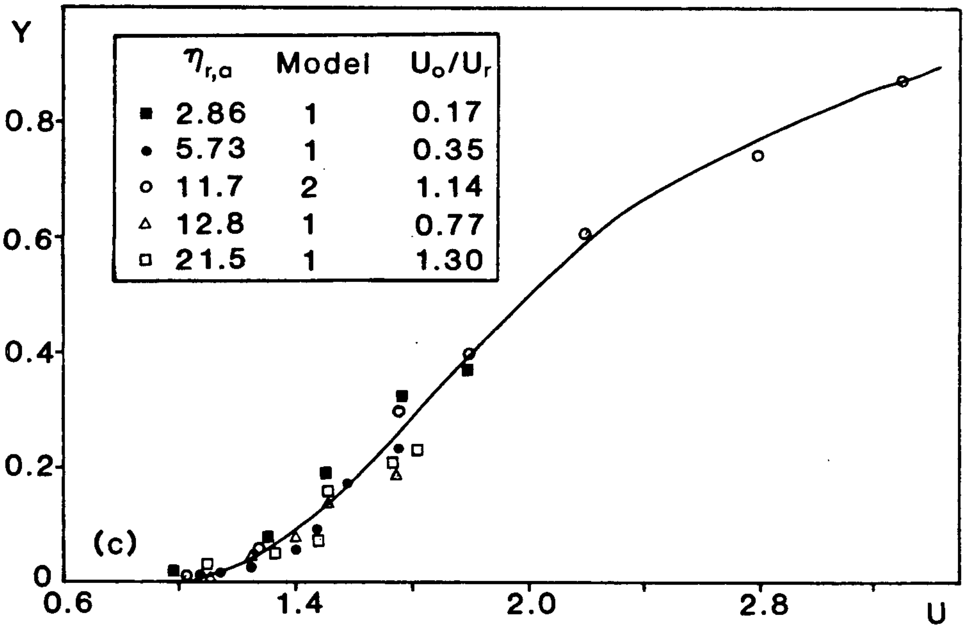

Fig. 43 Galloping response for: (a) model#2 with high damping; (b) model#1 with high damping; (c) low damping

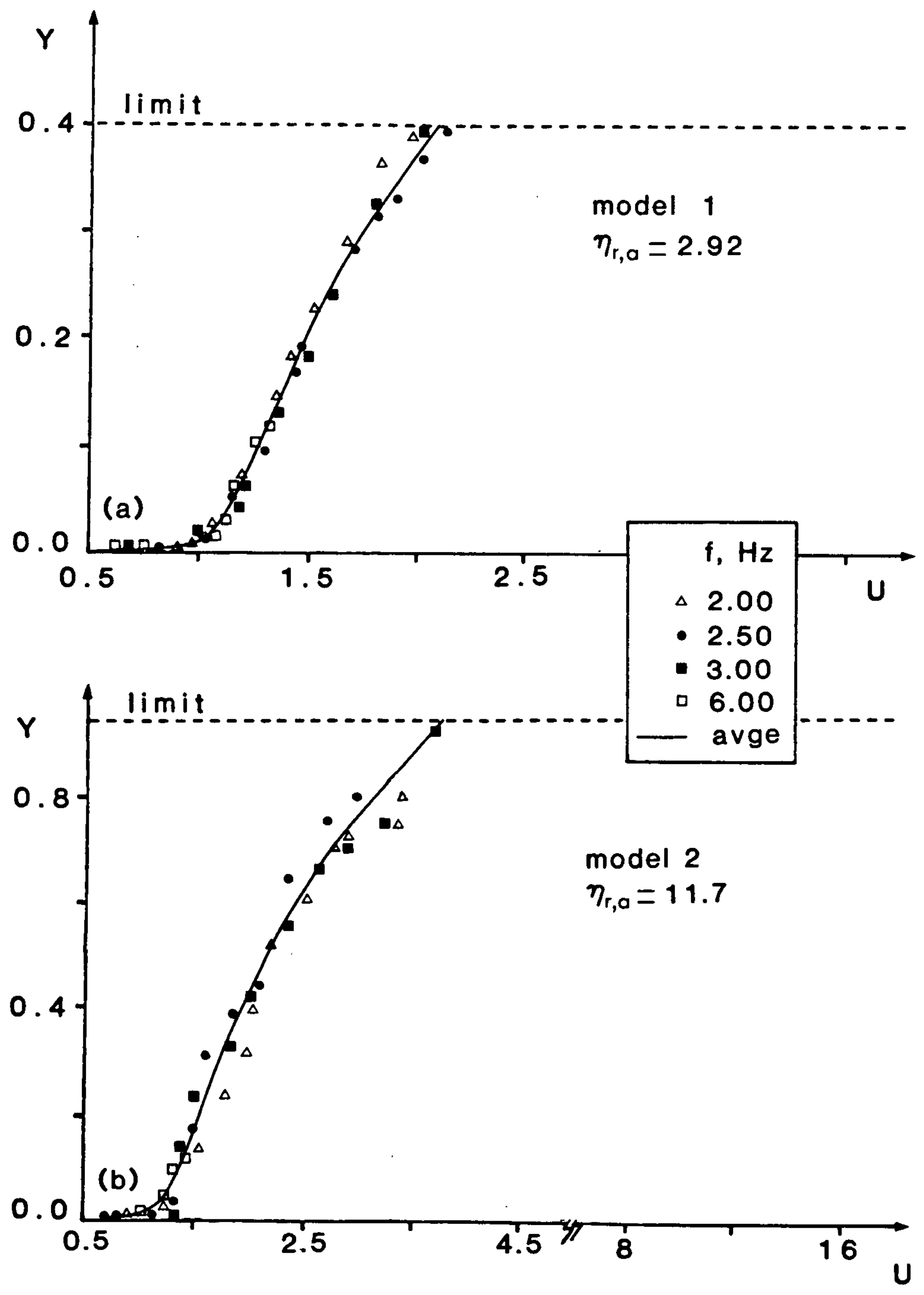

Fig. 44 Response of a two-dimensional square cylinder without damper for: (a) model#1; (b) model#2

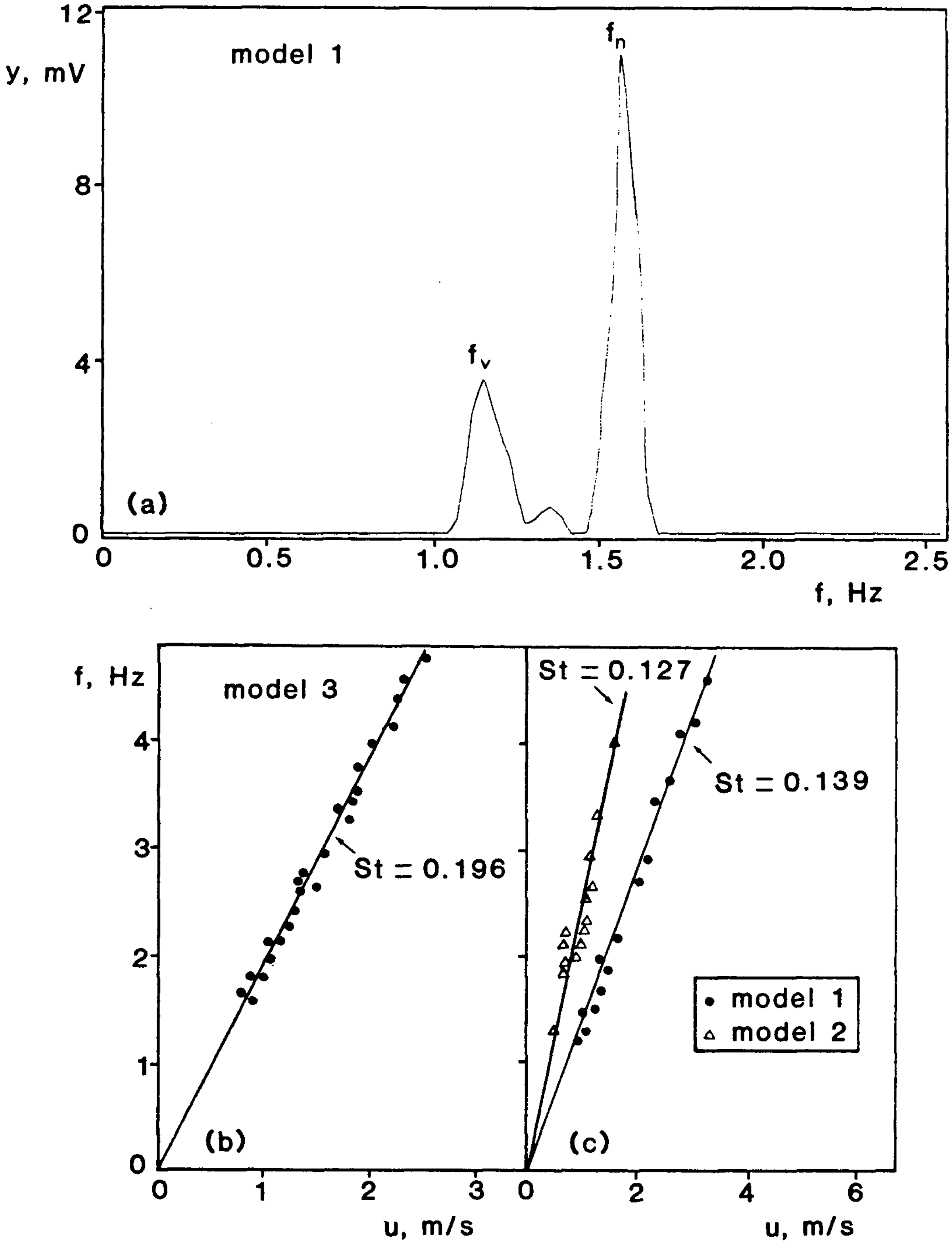

Fig. 45 Vortex shedding excitation on two-dimensional models showing: (a) frequency spectrum of the response; (b) Strouhal number for the circular cylinder; (c) Strouhal number for square cross-sections

4.2.5 Results and Discussion

4.2.5.1 Vortex Resonance Response of a Circular Cylinder

The tests were conducted at a frequency of 2.50 Hz with the response of the model without dampers exceeding the physical limits imposed by the slot size in the wind tunnel walls allowing for the motion. The addition of damper#1 with various liquid heights resulted in a significant reduction in amplitude even for $h/d = 0.125$, as shown in Fig. 46(a). The oscillations were almost completely eliminated at $h/d \geq 0.5$ with the damper operating near its first natural sloshing frequency, established to generate high damping ratios at low amplitude with the occurrence of the nonplanar mode. Quantitative information can be obtained by recognizing that the aerodynamic reduced ratio $\eta_{r,a}$ is related to $\eta_{r,l}$ (liquid reduced damping ratio) through

$$\eta_{r,l} = (\frac{1}{4\pi}\eta_{r,a}\frac{1}{M/\rho_a L_m d_m^2} - \eta_s)\frac{1}{M_l/M}, \tag{52}$$

where L_m and d_m are the model length and diameter, respectively; ρ_a is the air density; M is the total system mass; and η_s is the inherent damping determined to be 0.105% for small oscillations during the experiments. Using the model characteristic curve of Fig. 40, the peak amplitudes $Y = 0.094$, 0.05, and near 0, associated with $h/d = 1/8$, 1/4 and 1/2, correspond to $\eta_{r,a} \approx 12.5$, 20.0, and ≥ 40.0, respectively. This in turn requires $\eta_{r,l}$ to be of the order of 0.36, 0.31 and ≥ 0.35, respectively. This is indeed the case with $h/d = 1/2$ as observed in Chapter 3 (p. 59) where $\eta_{r,l}$ was found to be greater than 2.0 in the nonplanar mode at low excitation amplitude. Similarly, the half-full baffle and tube configurations suppressed the oscillations (Fig. 46b), while for the more slender damper#13 operating far from its resonant frequency a large response persisted (Fig. 46c).

Although no data for damper#1 with $h/d = 1/8$ and $1/4$ were obtained for these conditions during the steady-state experiments, a record of the amplitude decay was taken prior to switching on the wind to assess the damping (Fig. 47). Despite $\hat{\omega}$ being much smaller than 1.0, the nonlinear effects at higher amplitudes produce a resonant peak at $\epsilon_0/d = 0.25$ and 0.45, for $h/d = 1/4$ and $1/8$, respectively, due to the hardening characteristics at low liquid height. Larger values of $\eta_{r,l} = 0.50$ and 0.59 are also obtained for the two h/d ratios at an amplitude of $\epsilon_0/d = 0.18$ (i.e., $Y = 0.05$) and 0.334 ($Y = 0.094$), respectively, as compared to $\eta_{r,l} \approx 0.31$ and 0.36 estimated from the response during the wind tunnel tests. Possible innaccuracies may enter due to the fairly flat slope of Fig. 40 in the range considered here, with small errors in Y leading to a large variation in $\eta_{r,a}$. Furthermore, it was shown that the logarithmic decrement method does not follow the fluctuations in damping with ϵ_0/d precisely (section 3.4.3), therefore $\eta_{r,l}$ is likely to be lower prior to attaining the resonant peak . The order of magnitude and the relative amount of damping for the two liquid heights are, however, quite comparable in both cases.

Several approaches are available to verify the value of $\eta_{r,l}$. One way would be to use available data on the excitation due to vortex shedding. A fairly compre-

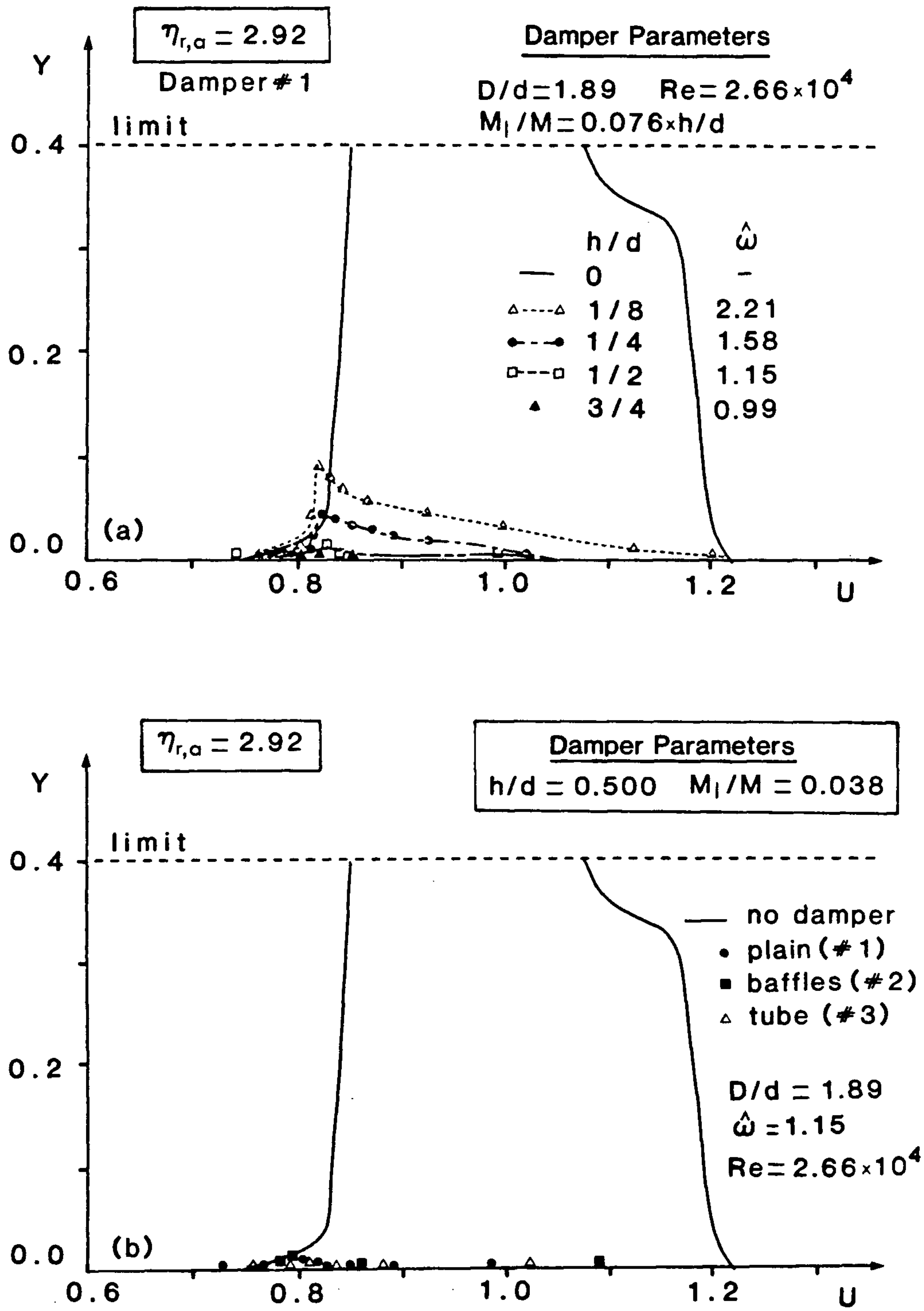

Fig. 46 Vortex resonance response on model#3 showing: (a) effect of liquid height and $\hat{\omega}$; (b) effect of internal configuration

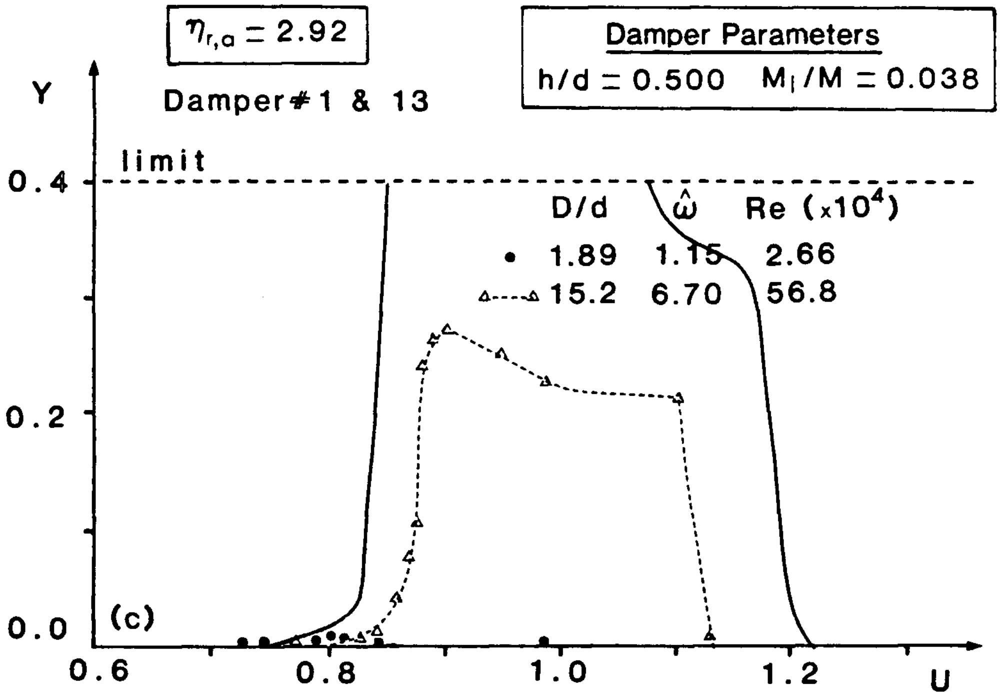

Fig. 46 Vortex resonance response on model#3 showing: (c) effect of diameter ratio and $\hat{\omega}$

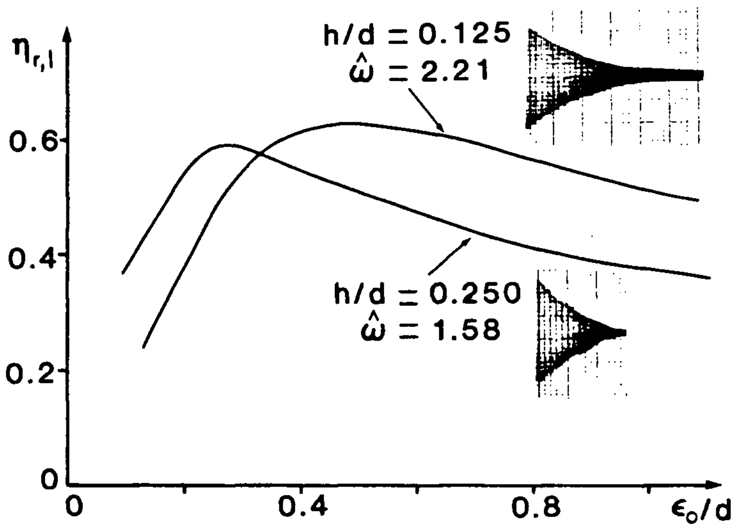

Fig. 47 Variation of $\eta_{r,l}$ with amplitude during free oscillations for damper#1 with $h/d = 1/8$ and $1/4$

hensive study by Diana and Falco[101] permits the prediction of the response over a wider range of U. With the knowledge of the work done on the model by the wind, at various amplitudes and frequencies , an iterative procedure based on the input to dissipated energy balance results in the comparison of Fig. 48. Noticeable discrepancies are apparent although the general trends are well reproduced. An alternate approach is the partly successful Hartlen-Currie oscillator model[102] requiring the empirical determination of the variables a_h and b_h, using the lightly damped response here (Figs. 49a, b), and applying it to the model fitted with nutation dampers (Figs. 49c, d). The static lift coefficient C_{l0} when taken to be the same as that determined by Feng[103] underestimated the response for $h/d = 1/8$ and $1/4$ (with no solution generated beyond the resonant peak), as shown in Fig. 49(c). The input damping ratios were based on $\eta_{r,l} = 0.36$ and 0.31 for $h/d = 1/8$ and $1/4$, respectively, as found earlier from Fig. 40. Furthermore, the half-full damper corresponding to $\eta_{r,l} \geq 0.35$ was found to suppress the oscillations (not shown). A higher C_{l0} of 0.5 to account for the larger blockage ratio was then considered and peak amplitudes closer to the experimental results obtained (Fig. 49d). A minimum $\eta_{r,l}$ of 0.62 was then needed for $h/d = 1/2$ to bring Y down to near 0. Overall, the method further verifies the level of the input damping ratios, as the predicted left-hand side of the response curve matches the data.

In general, vortex resonance can be controlled using nutation dampers with a mass less than 1% of the total weight of the system (model#1 with $h/d = 1/8$). Even

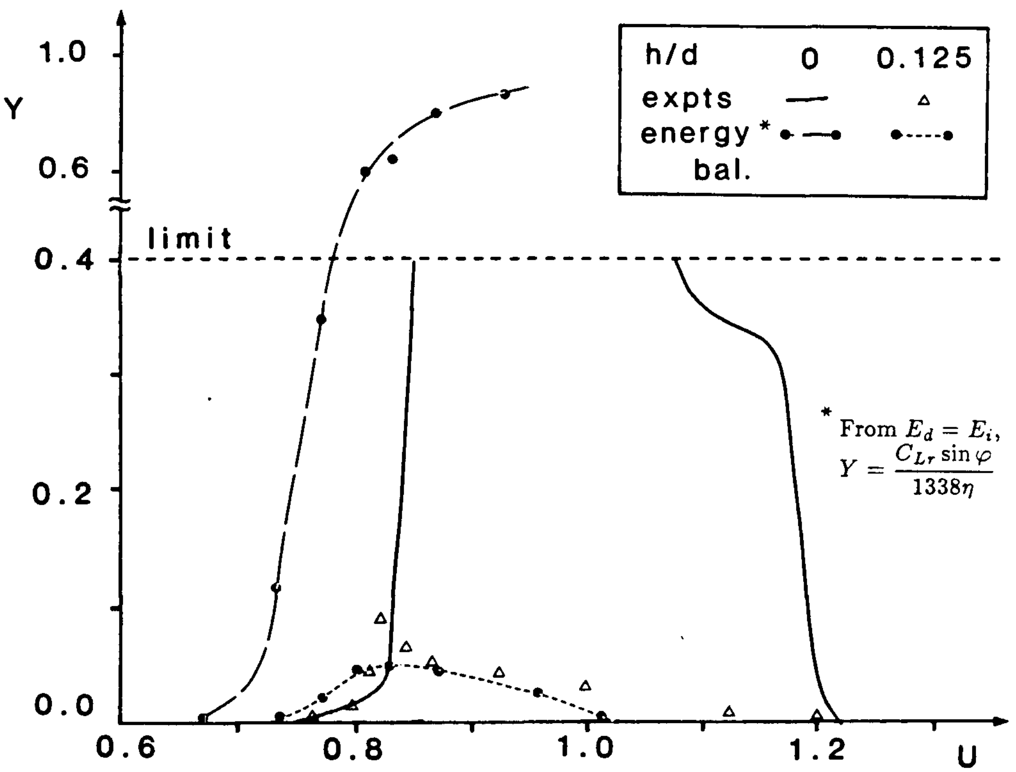

Fig. 48 Comparison between experiments and predictions based on the energy balance method

smaller sizes with $\hat{\omega}$ closer to 1 are expected to perform equally well. The higher blockage ratio of the 10.2 cm diameter model, responsible for a larger excitation than that in free air, makes this estimate conservative.

4.2.5.2 Vortex Resonance and Galloping Response of a Square Cylinder

The dampers were first mounted under the more unstable conditions of model#1 with a low initial aerodynamic damping ratio of 2.92. Qualitatively, they perform according to the characteristics determined in Chapter 3, with the frequency parameter $\hat{\omega}$ closer to 1.0 more successful at delaying the onset of galloping and virtually suppressing the vortex resonance peak (Fig. 50a). The tube and baffle configura-

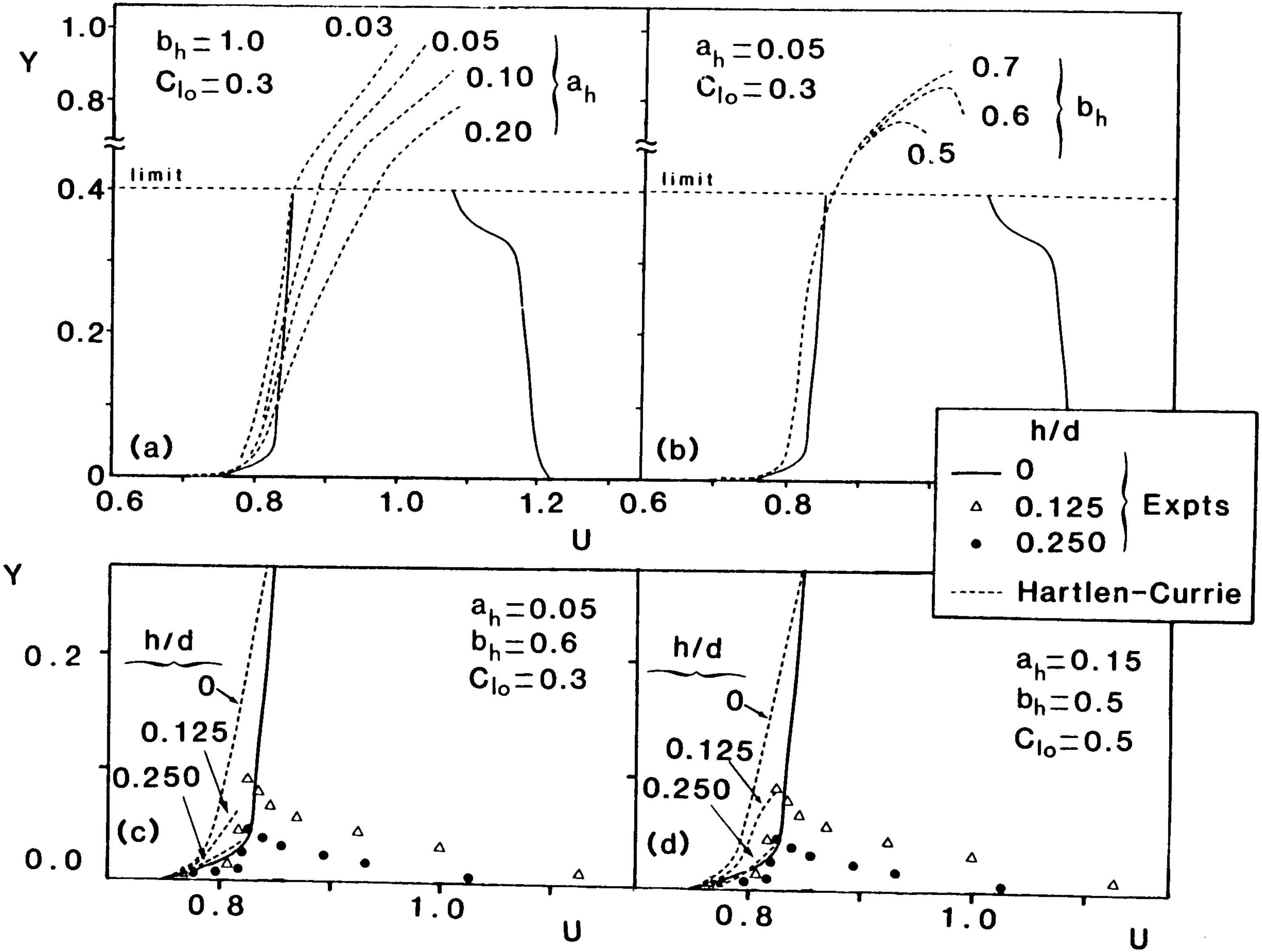

Fig. 49 Predictions of the Hartlen-Currie model showing: (a) determination of a_h with empty damper; (b) determination of b_h; (c) response with partially-filled damper and $C_{l0} = 0.3$; (d) response with $C_{l0} = 0.5$

tions were found to be relatively less efficient with the galloping onset velocity U_0 of 3.9 and 2.65, respectively, as compared to 4.0 for the plain damper (Fig. 50b). Of course, the problem is made more complicated by the highly amplitude dependent damping ratio. For instance, it has been established that $\eta_{r,l}$ exhibits a jump at $\hat{\omega} = 1.15$ and 1.39, with low amplitude excitation, followed by a rapid decrease in efficiency with ϵ_0 (section 3.4.2). This does not appear to prevent the build-up of oscillations under vortex resonance, however, Y subsequently stays close to zero until U_0 is reached. On the other hand, a gradual increase in response began around $U_0 = 2.0$ for $\hat{\omega} = 0.92$, with $\eta_{r,l}$ reaching a maximum at higher amplitude (Chapter 3, p. 61) and hence further delaying the onset of instability (Fig. 50a).

Experiments with the smaller model#2 continue to show $\hat{\omega}$ to be the governing parameter. The half-full damper essentially suppressed the galloping instability over the entire range of U, while $h/d = 7/8$ allowed for a high response at $U \approx 14$ in spite of the larger mass (Fig. 51a). It may be pointed out that the wind speed was limited to $U < 18$ to prevent possible damage to the model and the loss of air bearing low friction characteristics under a large static load. Oscillations quickly appear for $h/d = 1/8$ with an initial low damping ratio but the hardening characteristics, leading to sloshing resonance at higher amplitudes, resulted in the stalling of the response until the excitation becomes strong enough at $U \approx 4.8$. Meanwhile, the damper with $D/d = 15.2$ ($\hat{\omega}$ much larger than 1.0) is quite uneffective with Y still following the low damping, combined vortex resonance-galloping curve (Fig.

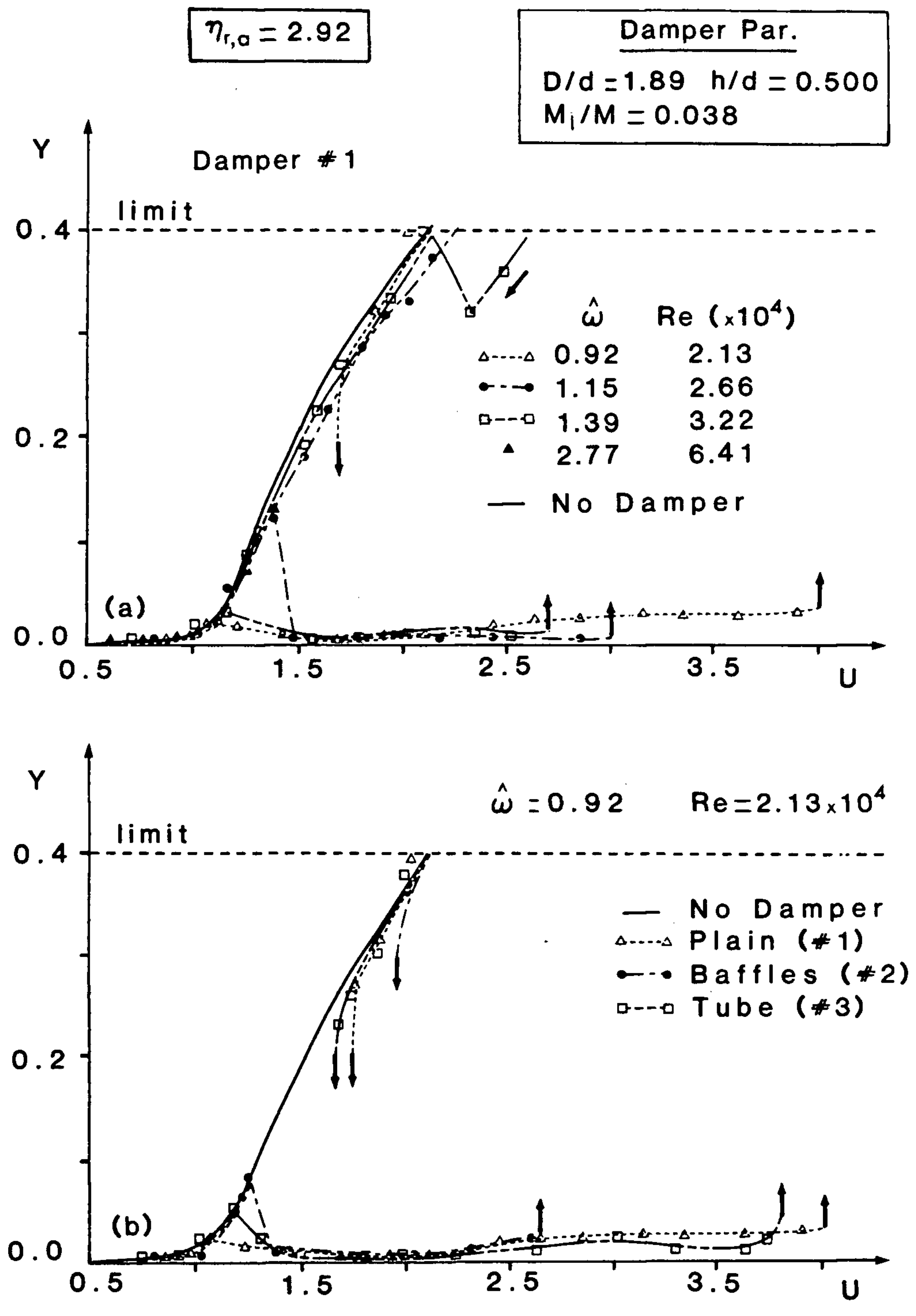

Fig. 50 Galloping response of model#1 showing: (a) effect of frequency; (b) effect of internal configuration

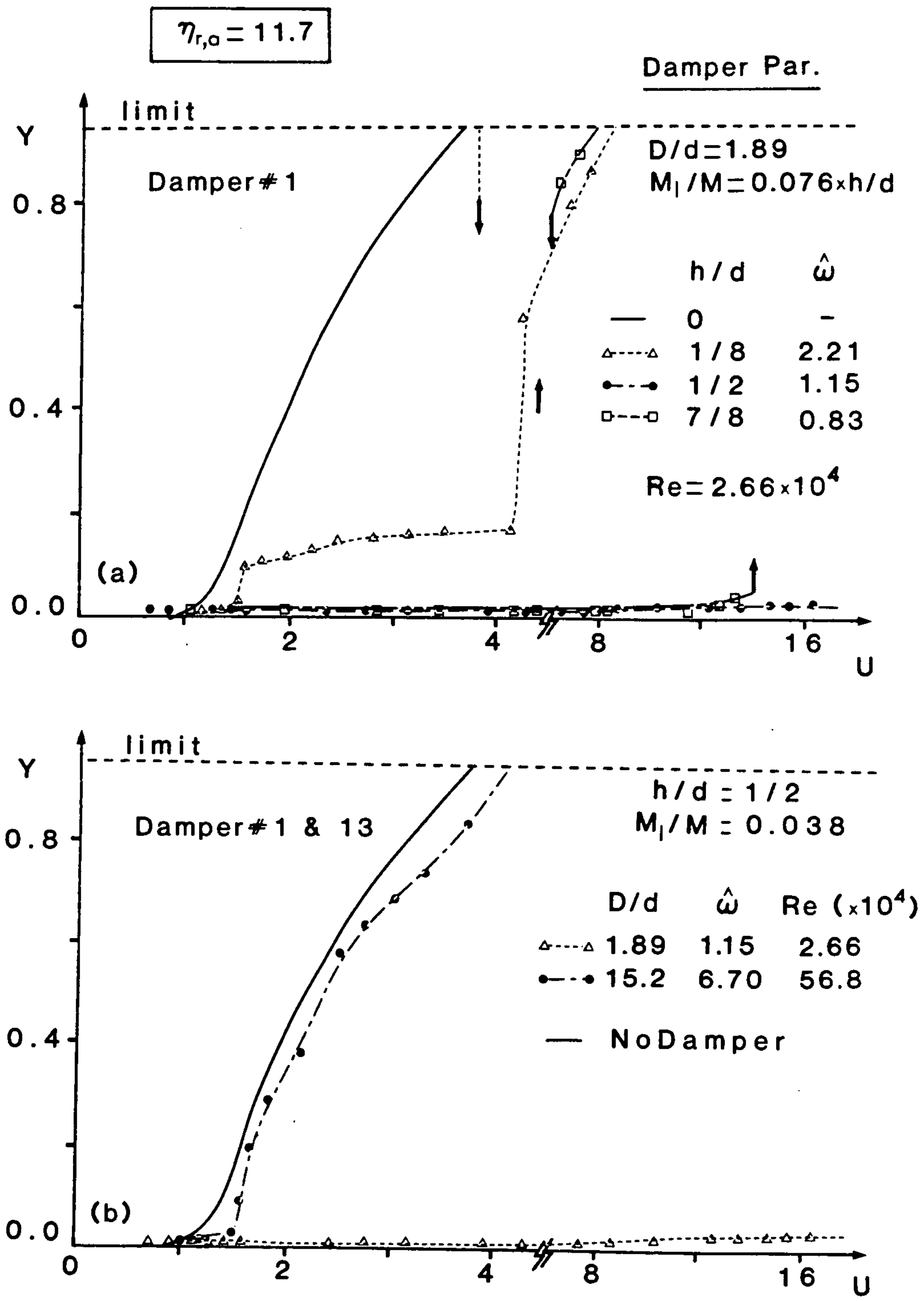

Fig. 51 Galloping response of model#2 showing: (a) effect of liquid height and $\hat{\omega}$; (b) effect of diameter ratio and $\hat{\omega}$

51b). This corresponds to $\eta_{r,a} \leq 21.5$, according to Fig. 43(c) showing the data for the electromagnetic damper tests, a condition certainly met here.

The nutation damper performance can be further assessed using the galloping theory. The latter proved to be reasonably accurate at predicting the system response with viscous damping (section 4.2.4). In principle, it should be applicable to any energy dissipation function through the definition of an equivalent viscous damping ratio, provided the time derivatives are small, and the vortex resonance velocity U_r is much lower than ${U_0}^{99}$ (galloping onset velocity). With the knowledge of $\eta_{r,l}$ versus Y and the necessary modification to the stability analysis (Appendix VII.1), an attempt was made to compute the response of the half-full damper#1 mounted on the 10.2 cm square-section model. Analytical results are compared with the experimental data in Fig. 52(a). The theory predicts that the onset of galloping should be considerably delayed as $\eta_{r,l}$ is high at low amplitudes. Moreover, there exists an upper stable branch, fairly constant with increasing wind speed, due to the diminishing damping ratio with Y. However, experiments conducted at several values of $\hat{\omega}$ showed that the system starts to gallop before U_0 is reached, without stabilizing at the higher limit cycle. This behavior suggests that the transient effects are important. The energy dissipation is of course generated by the liquid motion, and some lapse of time for the system initially at rest is likely to be needed before the damping level reaches the steady-state conditions of Chapter 3. Meanwhile, the structure may gain momentum with $\eta_{r,l}$ further dropping at higher amplitude, thus leading to an even larger response.

Results for the 5.1 cm diameter model show better agreement with the theory (Fig. 52b). The half-full damper successfully postponed galloping to $U \geq 18$, although no upper branch for Y in the range 0.2 to 0.5 was found. Oscillations beyond the physical limits of the test facility ($Y \geq 1.2$) could however be excited by imparting a large disturbance at $U \approx 0.9$. The configuration with $h/d = 1/4$ essentially followed the lower branch of the predicted response. The general trend for $h/d = 1/8$ is also fairly representative of the experimental data with a shift along the x-axis characteristic of an overestimated damper efficiency at low amplitude. This is probably due to inaccurracies in the input damping coefficient based on the free vibration tests of Fig. 47. From the part of the curve where Y slowly increases from 0.1 to 0.15 with U changing from 1.5 to 4.3, it can be inferred that $\eta_{r,l}$ varies from a very low value (≤ 0.1 at $Y = 0.1$) to about 0.21 at $\epsilon_0/d = 0.26$ ($Y = 0.15$) before the system starts to gallop. This is compatible with the upward trend for $\eta_{r,l}$ until $\epsilon_0/d = 0.5$ (Fig. 47) combined with its value of 0.36 for $\epsilon_0/d = 0.35$ estimated in section 4.2.5.1.

Evaluation of the performance during vortex resonance is more difficult as there is no well established universal response curve characterizing the effect of the system parameters. A comparison between Fig. 50(a) and the data obtained with the electromagnetic dampers (Fig. 43) however shows the half-full configuration oscillating

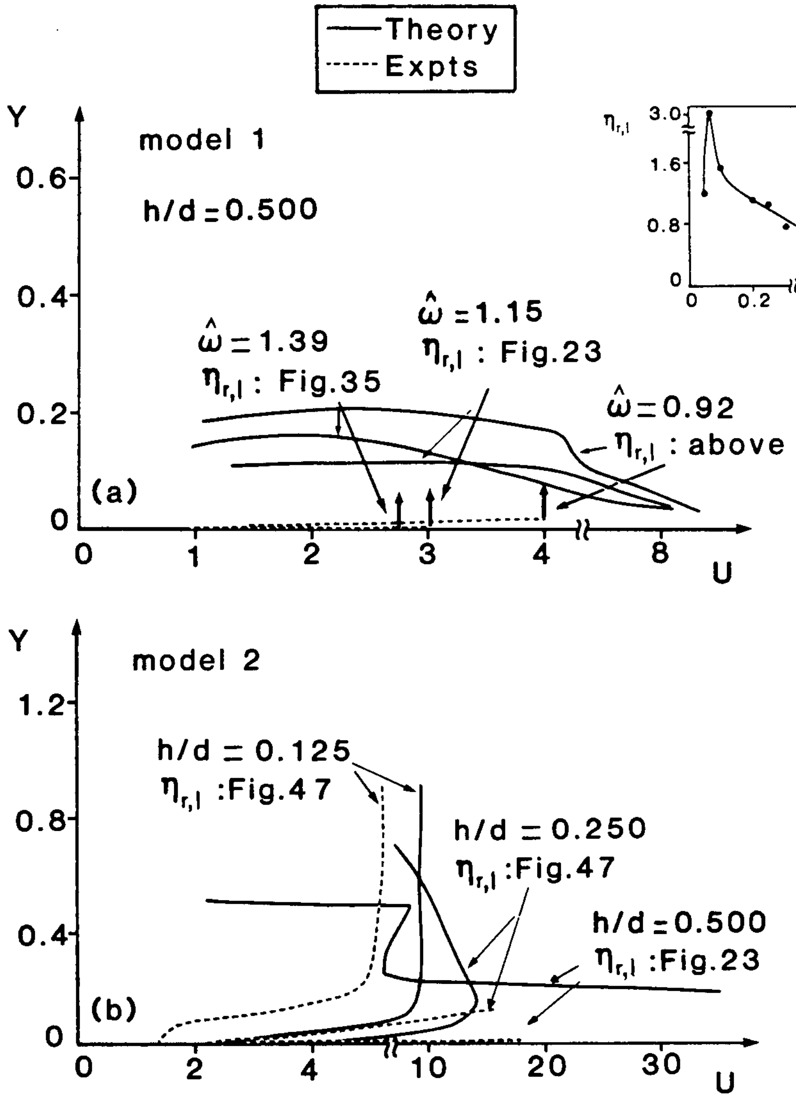

Fig. 52 Predicted galloping response of square prisms fitted with nutation dampers for: (a) model#1; (b) model#2

at $\hat{\omega} = 1.15$ should contribute to an overall η >1.70% at $Y = 0.13$, since a maximum response of 0.16 was recorded at $U = 1.58$ on model#1 with the eddy current damping. Similar conclusions can be drawn at frequencies of $\hat{\omega} = 0.92$ and 1.39. The upper return loop also indicates that η is less than 1% at higher amplitudes. This generally agrees with the results of Chapter 3, although the response for $\hat{\omega} = 1.15$ and 1.39 should have stabilized at a lower Y where $\eta_{r,l}$ is much larger. This again suggests that the acceleration of the structure, initially at rest, is an important factor because of the time needed for the damper to grow to its full potential at low ϵ_0/d. The predictions of the Hartlen-Currie lift oscillator model, originally based on the empirical parameters of reference 104 (i.e., $a_h = 0.13$, $b_h = 2.50$), but subsequently modified to fit the data for the electromagnetic damper tests, are shown in Fig. 53. Assuming they give some indication about the system parameters, the damping ratio for $\hat{\omega} = 1.15$ and 1.39 is of the order of 1.85% (i.e., $\eta_{r,l} = 0.46$), and 6.94% ($\eta_{r,l} = 1.8$) for $\hat{\omega} = 0.92$, which are close to the values of the steady-state experiments, for the maximum amplitudes obtained here. Thus at a lower frequency, the structure appears to capitalize on the initial high damper efficiency.

A comment concerning the aerodynamic model design would be appropriate. Without end plates, damper#1 with $h/d = 1/2$ and $\hat{\omega} = 0.92$ successfully delays galloping (Fig. 54a), while allowing for large vibrations starting at $U = 4.0$ in the presence of end plates (10.2 cm square cylinder). It should be mentioned that the response was identical for both cases in absence of nutation dampers. The effect of model size is illustrated in Fig. 54(b) with damper#1 now postponing the onset of instability beyond $U = 16$ on the 5.1 cm square section.

4.2.6 Concluding Comments

A comparison between the two-dimensional wind-induced oscillation tests and the steady-state forced excitation experiments of Chapter 3, along with the free

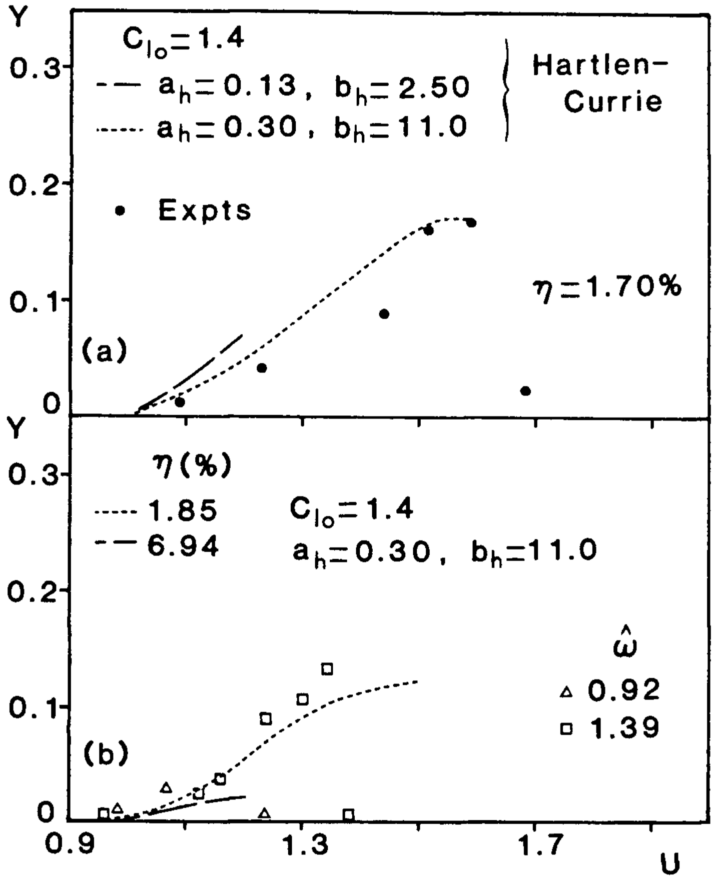

Fig. 53 Hartlen-Currie model predictions for model#1 with: (a) electromagnetic damping; (b) nutation damping

vibrations data using the wind tunnel set-up, has led to the important conclusions summarized as follows:

- The optimal damper parameters obtained through the steady-state analysis help minimize the response during wind-induced oscillations. For instance, liquid sloshing resonance with $\hat{\omega}$ close to 1 resulted in maximum efficiency, while baffle and inner tube arrangements were less effective at reducing vortex resonance and galloping instabilities. Low liquid heights with $\hat{\omega} > 1$ are better suited for restricting the response at high amplitudes, due to their hardening

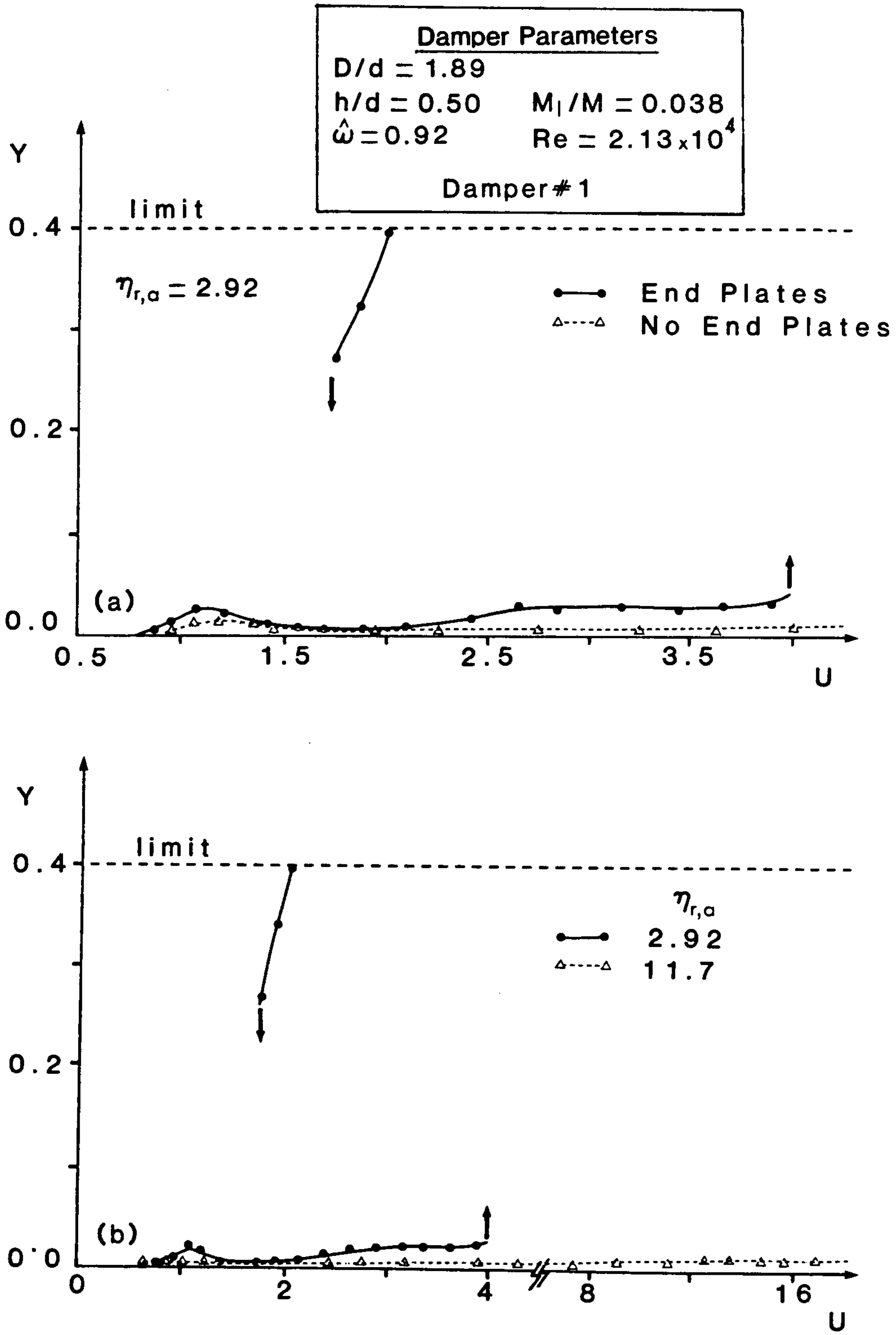

Fig. 54 Response of a square prism with nutation damper as affected by: (a) end plates; (b) model size

characteristics, whereas the opposite is true for larger h/d ratios.

- The semi-empirical galloping theory proved to be useful in studying the energy dissipation characteristics. The Hartlen-Currie model of vortex resonance is promising as it helped establish a good correlation between the left hand side of the response curve and the damping ratios af Chapter 3, for both circular and square cylinders.

- Time dependent parameters involving the acceleration of the model appear to affect the damper performance. Transient effects during liquid sloshing are then significant and a steady-state approximation is no longer sufficient to predict performance on the larger square cross-section. For the weaker excitation of the 5.1 cm square cylinder or the circular model, better agreement with the results of Chapter 3 was observed. In general, dampers whose $\eta_{r,l}$ versus amplitude curves do not drop too quickly are preferred to avoid premature onset of instability.

- Only a small amount of liquid is needed to control the vibrations. The vortex resonance of circular cylinders is limited to $Y \leq 0.1$ with a liquid to total mass ratio less than 1% (damper#1, $h/d = 1/8$). The same arrangement also postponed the onset of galloping by a factor of 4 for the 5.1 cm square model ($U_0 = 4.8$). In the presence of larger excitation of the 10.2 cm square cylinder, a mass ratio of about 4% proved to be more effective ($U_0 = 4.0$ for model#1 at $h/d = 1/2$, $\hat{\omega} = 0.92$). It can be reduced significantly at lower frequencies where resonant sloshing conditions can be met with larger, more efficient D/d ratios.

4.3 Three-Dimensional Tests

4.3.1 Preliminary Remarks

The effectiveness of nutation dampers was next assessed for finite aspect ratio models free to oscillate about a fixed axis. Both the wind-structure interactions as well as the liquid sloshing motion are now more difficult to analyse than those of the two-dimensional case. The experiments conducted in the boundary layer wind tunnel provided valuable information about the energy dissipation under this type of dynamic excitation. A series of tests in both laminar and turbulent flows was conducted to permit a comparison between the different wind environments.

4.3.2 Test Arrangement and Model Description

A 67.6 cm long aluminum rod fastened to a freely rotating shaft, supported by two air bearings, held the aerodynamic model at the upper end and the damper at the bottom (Fig. 55). The arrangement, originally designed by Sullivan[94], was modified to position the damper outside the wind tunnel thus avoiding interference with the flow, as explained in the next section. Furthermore, the original, longitudinally pressure compensated air bearings were found to permit significant oscillations in the in-flow direction at higher wind speeds. Therefore, the arrange-

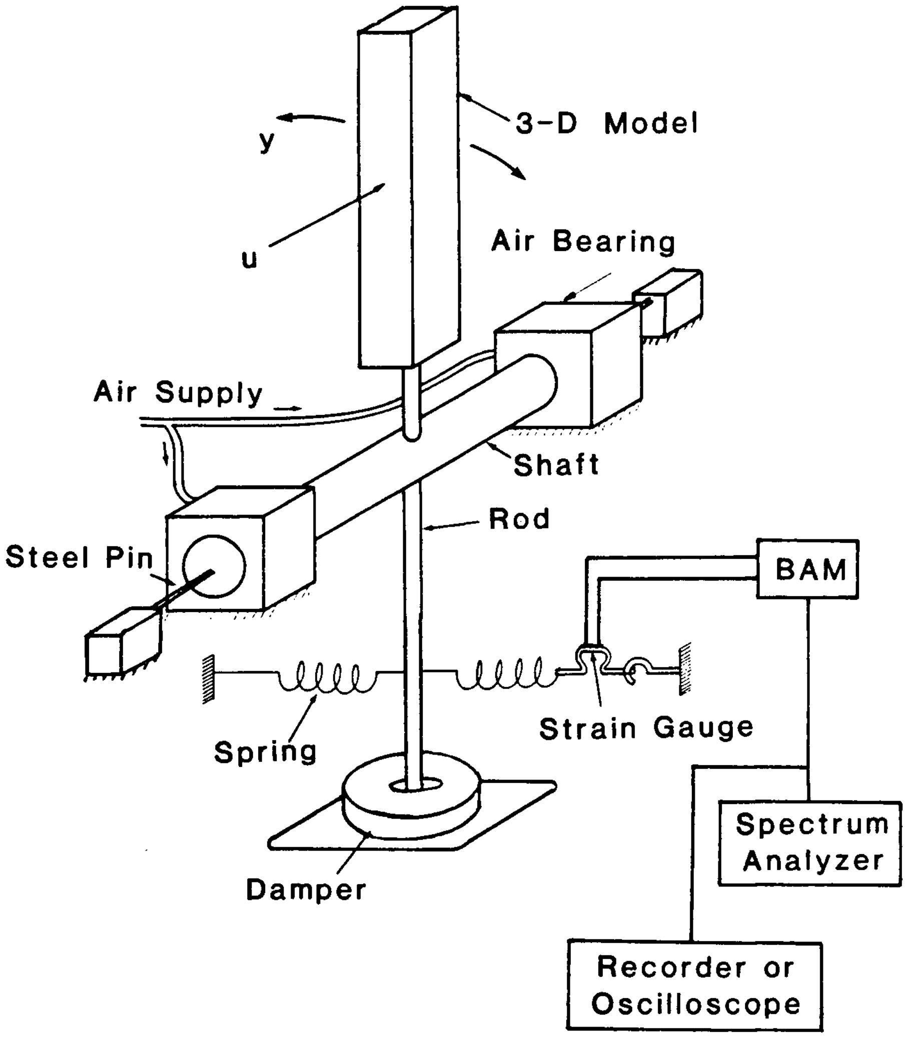

Fig. 55 Wind tunnel set-up for the three-dimensional tests

ment was modified to include two adjustable, hardened steel pins acting on the shaft center of rotation. They fully secured the model without adding any significant inherent damping. Light, 50.8 cm (20") long, square and circular cylinders, similar in design to their two-dimensional counterparts described in section 4.2.2, were used in the test program. Particular attention was directed towards the upper connecting end where an aluminum rod extended half way inside the model. Reinforcements were used to maximize structural rigidity. A physical description of the models is presented in Table III. Two springs provided the desired stiffness to the system, while a strain gauge mounted in series with a Bridge Amplifier Meter and a spectrum analyser (same as the instrumentation used in Chapter 3) recorded the displacement.

Table III   Physical description of the three-dimensional aerodynamic models

MODEL#	1	2	3	4
CROSS-SECTION	102mm	51 mm	102 mm	51 mm
LENGTH (mm)	508	508	508	483
MATERIAL	BALSA & ALUMINUM	BALSA & ALUMINUM	PCV	BALSA
MASS (g)	644	244	515	253

4.3.3 Model Characteristics

The static side forces were first measured on the square cylinders in laminar flow. The resulting aerodynamic coefficient was found to be much lower than that of the two-dimensional models. The slope at zero degree angle of attack is small ($dC_{fy}/d\alpha \approx 0.60$ for model#2), probably due to suction across the opening in the bottom wall (Fig. 56a). The end effect at the top is also likely to contribute to generally lower C_{fy}. The higher blockage continues to show a larger excitation with a slope of 1.4 at $\alpha = 0°$ and an improved curve for C_{fy} until $\alpha = 10°$ (model#1, Fig. 56b). Combined with a nonuniform horizontal displacement along the length of the model due to rotation, this should generate weaker galloping instabilities than those of the two-dimensional case (for the same tip displacement). The integration of the side force is presented in terms of a moment coefficient in Fig. 56(c). A small gap of 0.48 cm between the wind tunnel bottom wall and the models was used throughout the tests.

Measurements of the natural frequency in free oscillations and the spring stiffness were used to arrive at a system inertia of 0.2021 Kg-m^2 for a total mass of 1.044 Kg. More significant contributions came from the aerodynamic model and the damper rod support, due to their relative height extending away from the pivot point. With an inherent damping of 0.1%, or less, derived from the amplitude decay curve of the system without damper (Fig. 57), the aerodynamic reduced damping $\eta_{r,a}$ based on the cylinder tip deflection was found to be in the range 0.85-1.13. It was again noticed that η_s generally increased with amplitude in free vibration. Earlier work by Sullivan[94] used a constant viscous damping and the agreement with theory was found to be reasonable. The value at low amplitude was thus assumed to be valid throughout the range as explained earlier in section 4.2.4 (different loading). The Strouhal number for the 10.2 cm square model was found to be 0.12 (Fig. 58). Its lower value than that of the two-dimensional cylinder is compatible with the results of other investigations[105]. The vortex shedding excitation away from

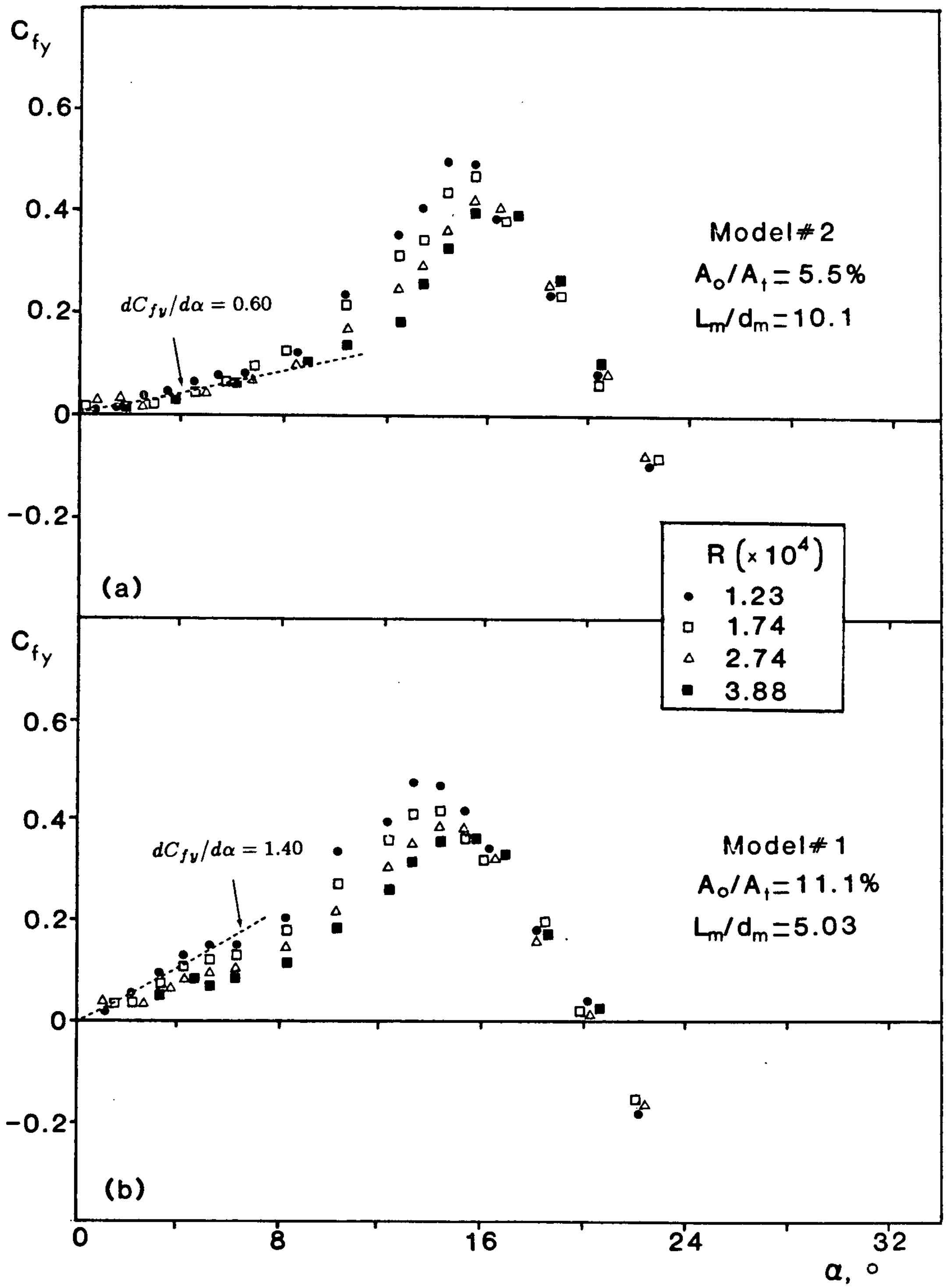

Fig. 56 Static side force for three-dimensional square prisms as: (a) measured on model#2; (b) on model#1;

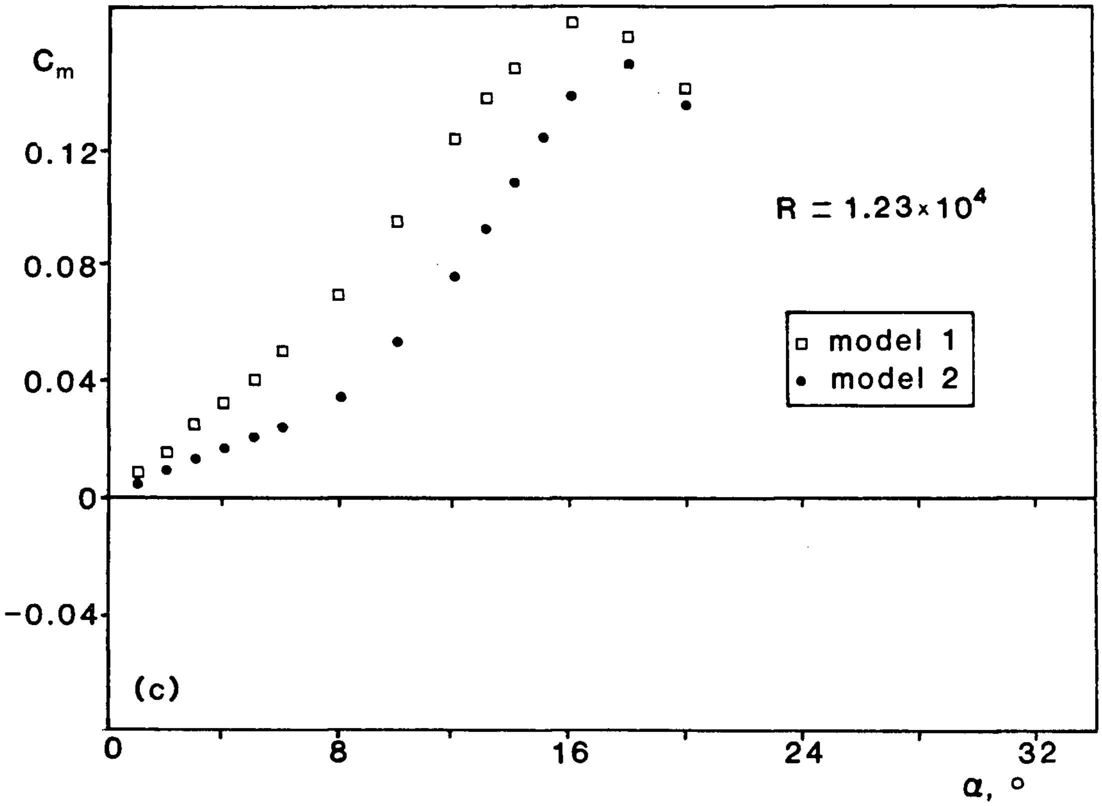

Fig. 56 Static side force for three-dimensional square prisms as: (c) expressed as a moment coefficient

resonance was too difficult to monitor for the other models. The calibration procedure was repeated for each set of springs affecting the force per unit displacement transmitted to the strain gauge. It was similar to that described in section 4.2.3.

A last point addresses the position of the damper with respect to the structure. Dampers were first installed at the top of the cylinder, as would be the case in a real life situation. However, a significant weakening of the galloping instabilities was usually observed, with, at times, complete suppression of oscillations even before the liquid was inserted. This can be expected as the axisymmetric shape of the damper contributes to the drag without generating any static side force. Its signif-

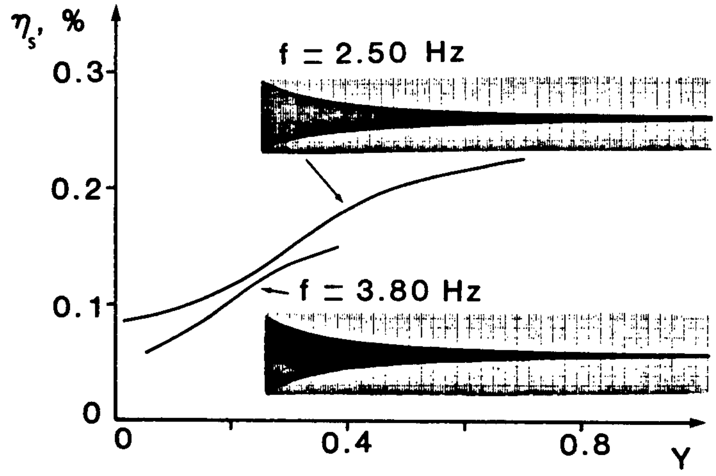

Fig. 57 Inherent damping ratio for the 3-D set-up and two frequencies of excitation

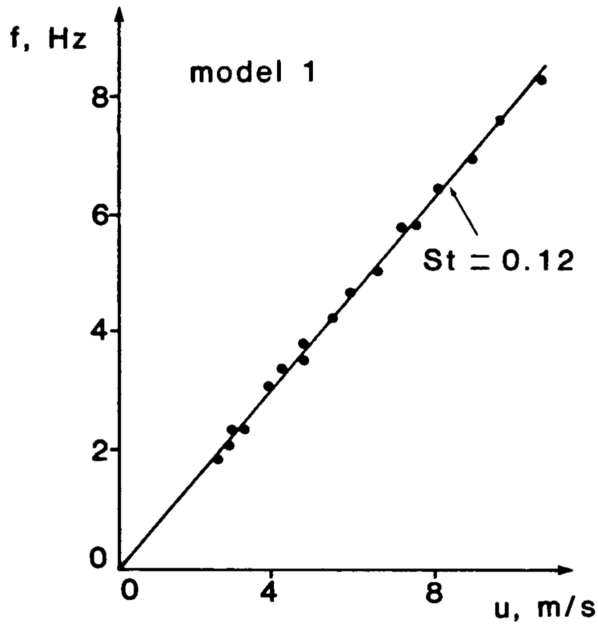

Fig. 58 Strouhal number for the large square cylinder

icant size thus resulted in a drop in C_{fy}. Fig. 59 illustrates the effect in laminar flow. Without damper, the aerodynamic model#4 exhibits a well defined vortex resonance peak followed by the onset of galloping at $U = 6.0$. With the empty damper, the interference is such that galloping never occurs. Hence the damper was supported outside the wind tunnel such that its displacement was equal to the cylinder tip deflection.

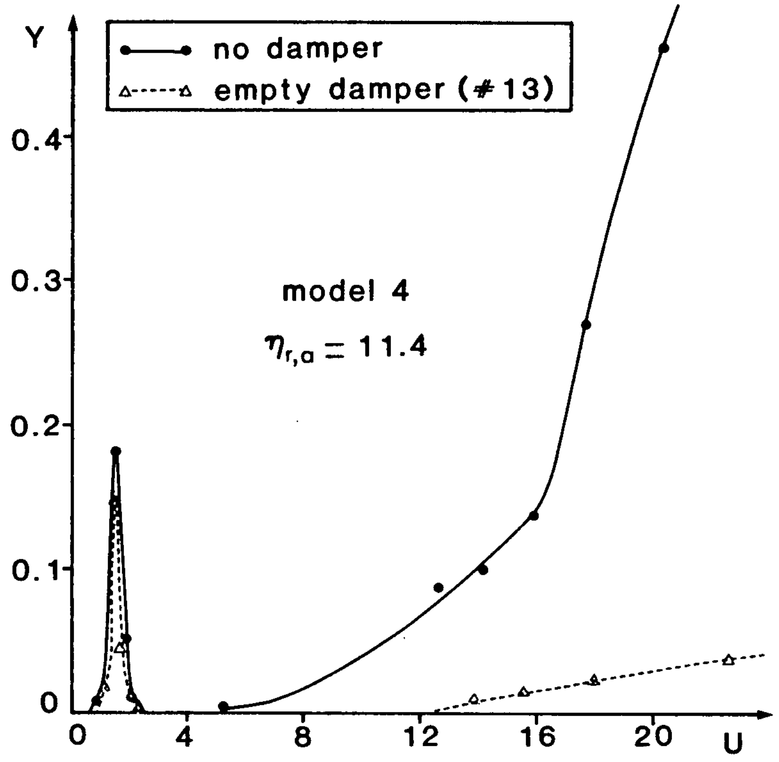

Fig. 59 Effect of damper position on the response of a square prism

4.3.4 Results and Discussion

4.3.4.1 Vortex Resonance Response of a Circular Cylinder

The tests conducted at a frequency of 2.50 Hz showed that relatively low liquid heights can suppress the oscillations. The damper with $h/d = 0.046$ limited the response to $Y \approx 0.15$ in both laminar and turbulent flows, while Y remained lower than 0.05 for $h/d = 1/8$ (Fig. 60). No response was noticeable with the half-full

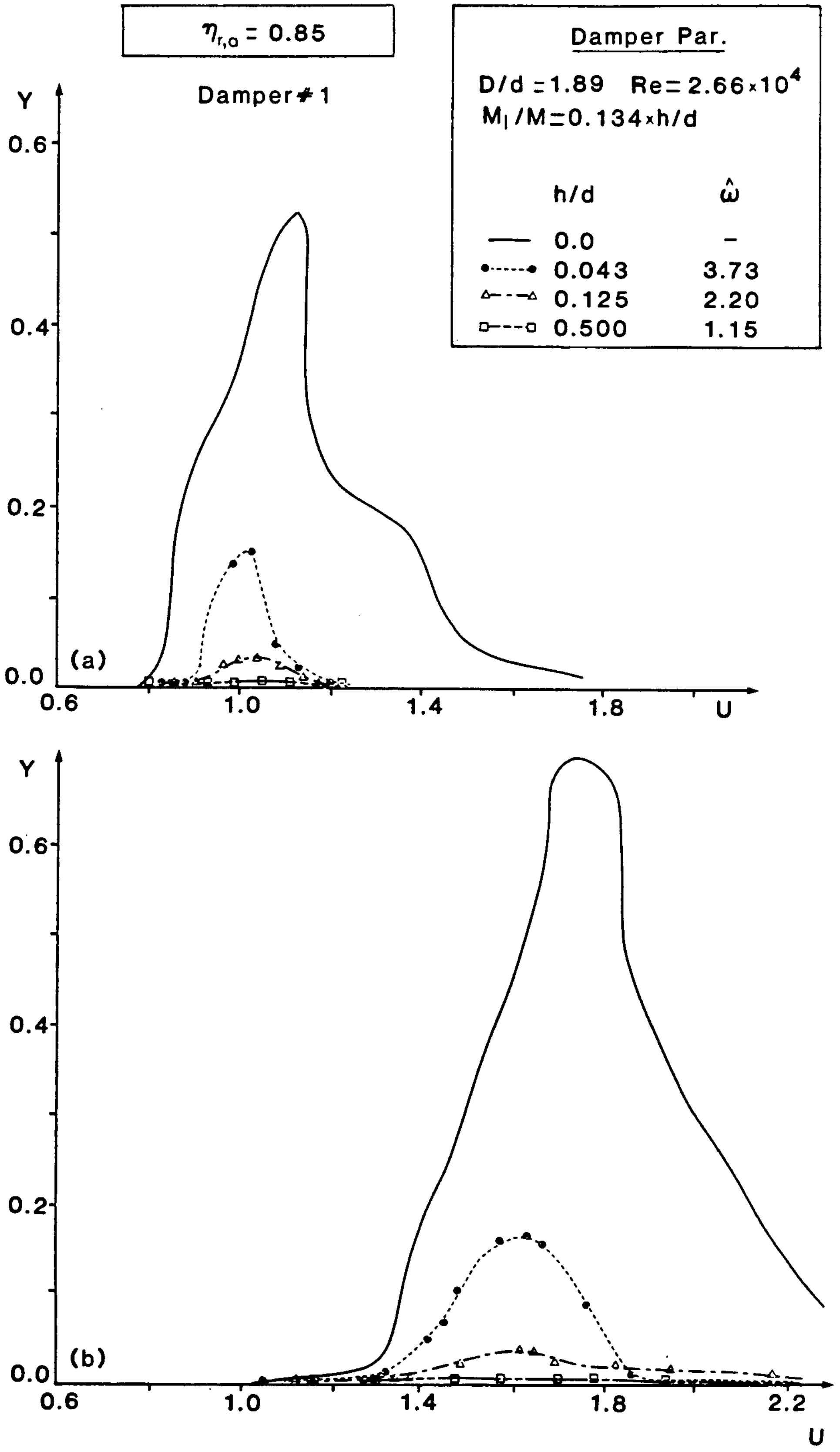

Fig. 60 Vortex resonance response of model#3 as affected by h/d and $\hat{\omega}$ in: (a) laminar flow; (b) turbulent flow

damper, even with the baffle or inner tube configurations, as illustrated in Fig. 61. This is consistent with the weaker excitation of the three-dimensional models reported in the literature[106]. It is interesting to note that the response is slightly higher in turbulent flow. This is somewhat unexpected as the vortex formation is thought to be less organized here as compared to the laminar condition. Perhaps the characteristic velocity profiles (Fig. 62), together with a different blockage ratio, are responsible for such behavior. The large scale turbulence induced resonant interactions reported in reference 106 is another possibility.

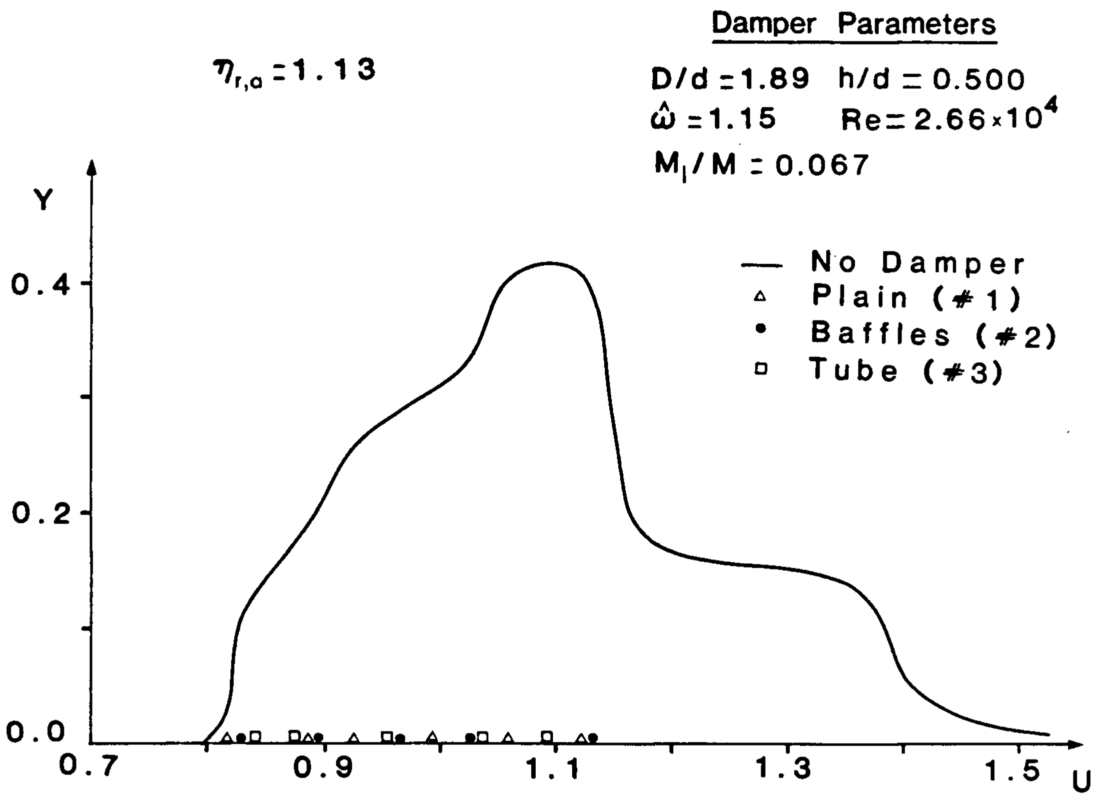

Fig. 61 Effect of internal configuration on the 3-D model response

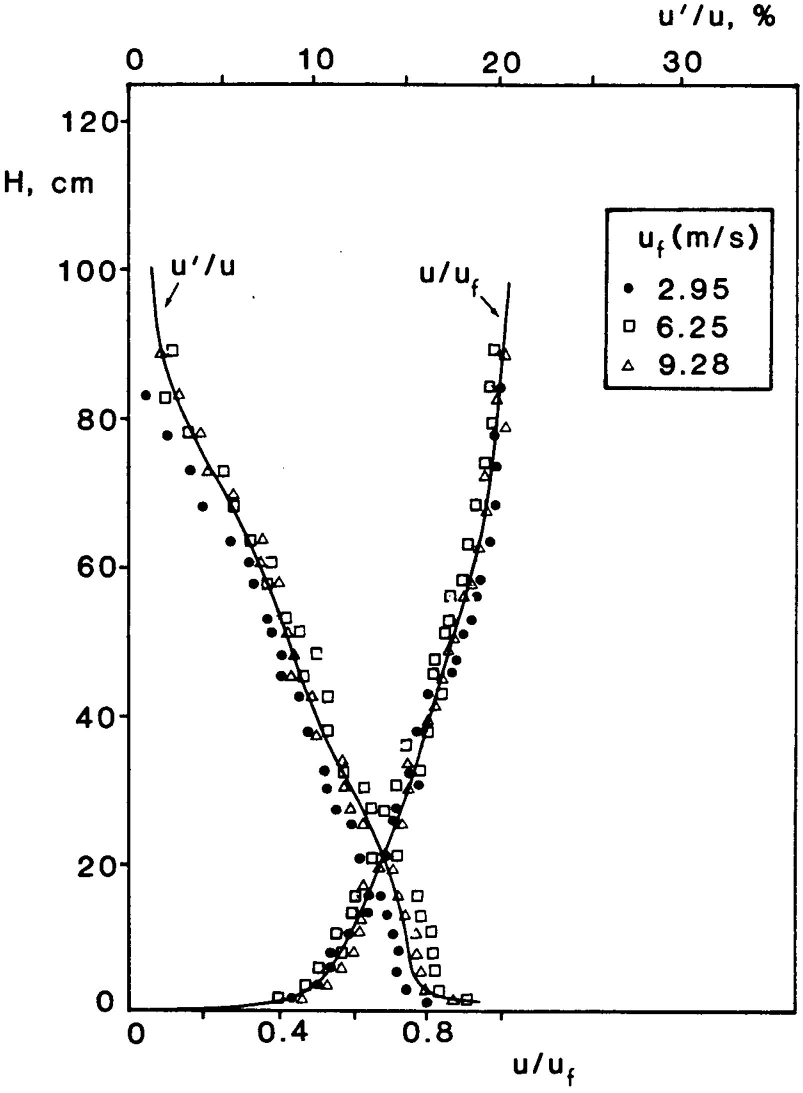

Fig. 62 Boundary layer velocity profile as recorded during the 3-D tests

In general, the damper performance was found to be quite comparable in both laminar and turbulent flows, with the vortex resonance shifting from $U \approx 1.0$ (laminar) to 1.6 (turbulent case). However, amplitude decay plots for $h/d = 1/8$ and 1/2 indicate the damping to be generally lower for the three-dimensional models compared to their two-dimensional counterpart (Fig. 63a and b), and gradually decreases with the amount of rotation as defined in Fig. 63(d). $\eta_{r,l}$ is fairly constant

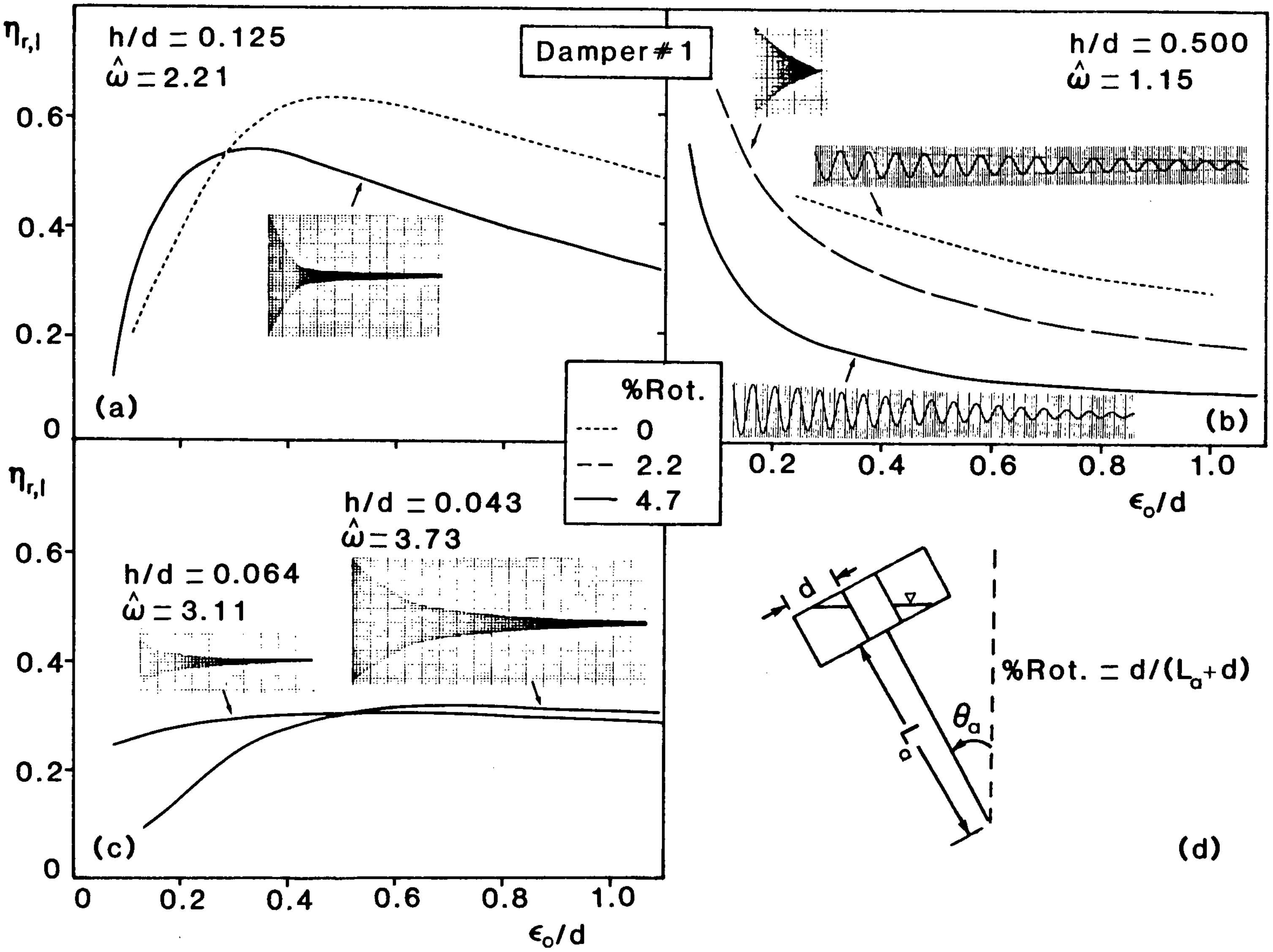

Fig. 63 Damping characteristics as affected by liquid height for nutation dampers undergoing rotation

at high ϵ_0/d (Fig. 63c). The dependence on $\hat{\omega}$ is quite pronounced: the same type of damper but of different diameter ratios shows reversed performance according to the exciting frequency. At f=1.00 Hz, damper#13 ($D/d = 15.2$) has a larger liquid motion which suppresses the oscillations, while for $D/d = 1.89$ (damper#1) the model response reaches an amplitude $Y = 0.37$ (Fig. 64a). However, at f=2.50 Hz, damper#13 allows Y to grow to 0.1 while no response is observed for the smaller diameter ratio (Fig 64b). It should be mentioned that the results for the system without dampers do not collapse onto the same curves for all frequencies (Fig. 65). This is likely due to the variation in inherent damping as affected by the use of different springs.

4.3.4.2 Vortex Resonance and Galloping Response of a Square Cylinder

With a low value of reduced aerodynamic damping ratio, the model in laminar flow exhibited vortex resonance merging with the onset of galloping instability (similar to the two-dimensional case). The forces are, of course, weaker on the 5.1 cm cross-section (system frequency of 2.5 Hz) and damper#1 with $h/d = 1/8$ essentially suppressed the vibrations over the entire range of U (Fig. 66a), while allowing for an amplitude build-up of $Y = 0.10$ during vortex resonance on the 10.2cm model (Fig. 67a). The same arrangement remained effective in turbulent flow with Y slowly increasing towards 0.1 until the galloping onset velocity was reached at $U = 5.0$ (model#1, Fig. 67b). No resonant peak was visible here, thus suggesting that the vortex shedding excitation is small in this type of flow. Similar

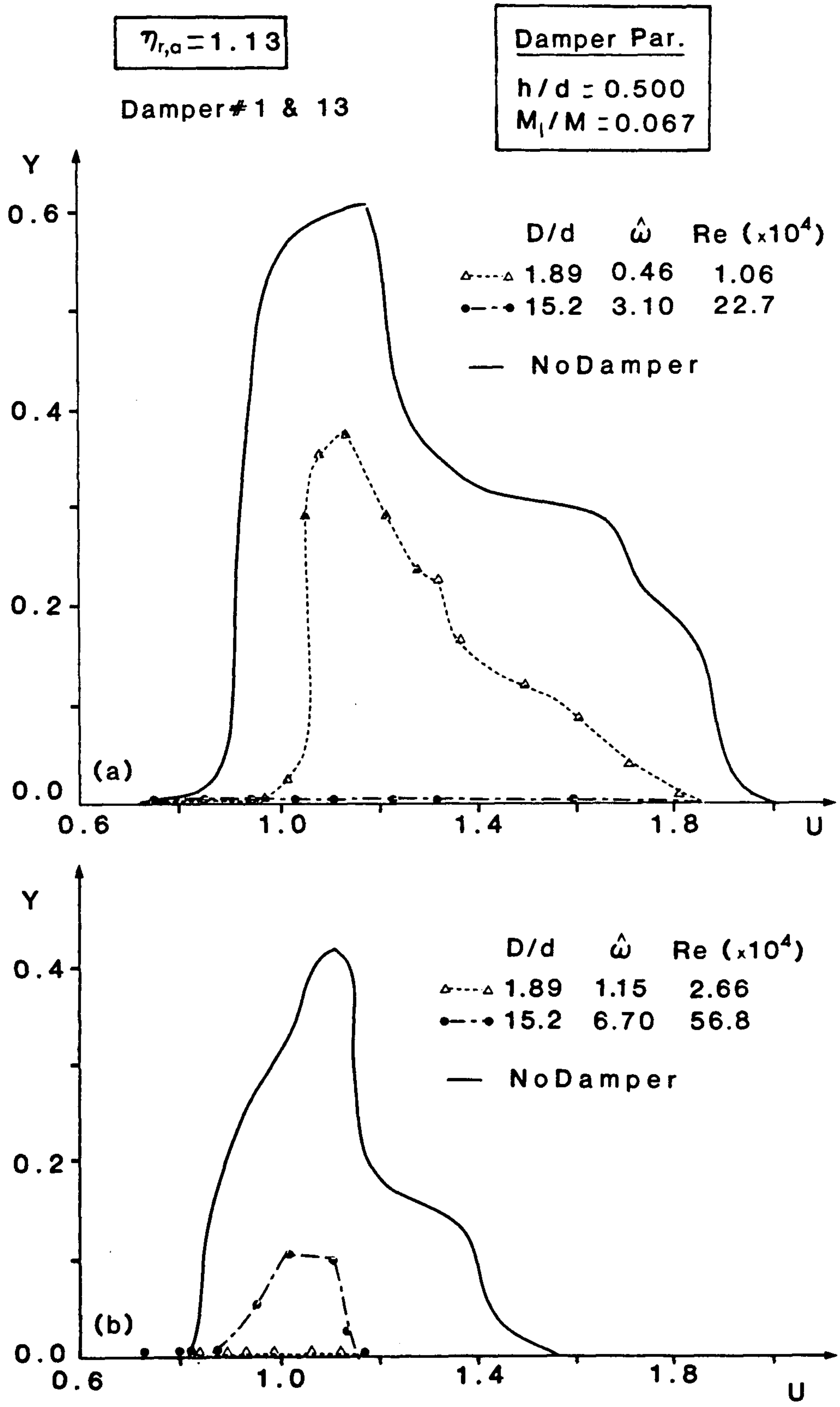

Fig. 64 Effect of D/d and $\hat{\omega}$ on the vortex resonance response of model#3

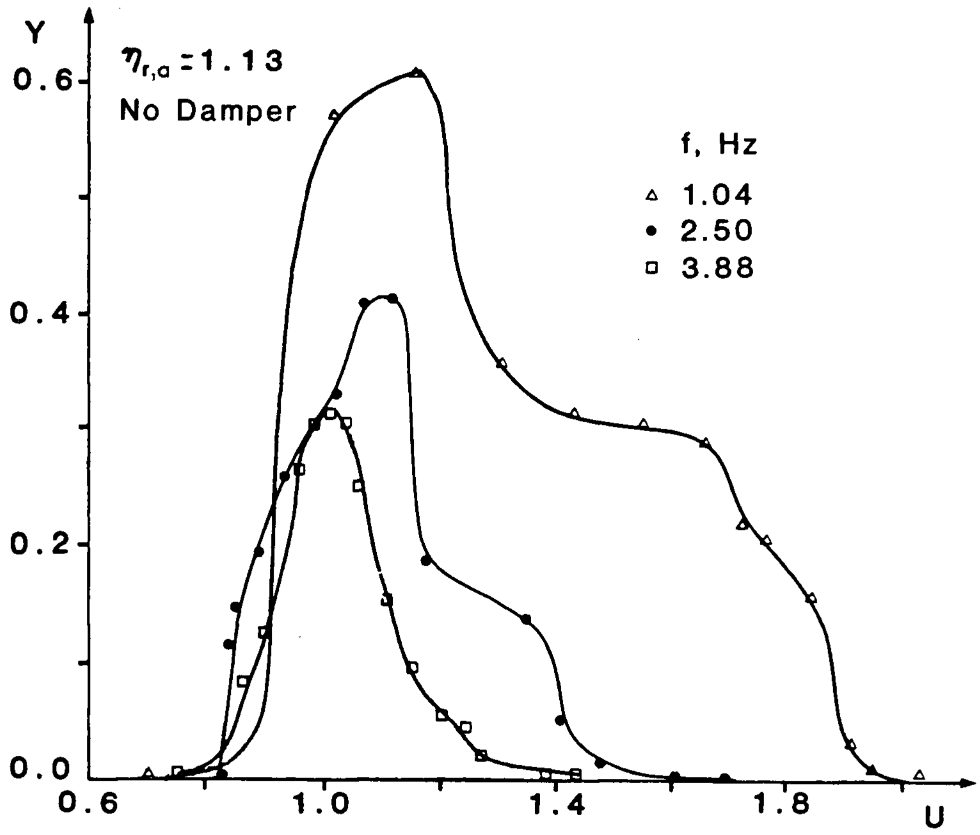

Fig. 65 Vortex resonance response for model#3 without dampers at various frequencies

trends can be observed at smaller liquid heights, with a large response at resonance for the laminar case for $h/d = 0.064$ (Fig. 67a), as opposed to the significant galloping oscillations with the boundary layer pofile (Fig.67b). This agrees with other studies[107] indicating turbulence increases the static side force coefficient. With the addition of liquid at $h/d = 1/4$, the amplitude is further reduced to $Y \approx 0.04$ in laminar flow (vortex resonance) and 0.05 with turbulence ($U = 5.0$), while being totally eliminated for $h/d \geq 3/8$. Similar trends were observed on the 5.1 cm model with smaller liquid heights, as shown in Fig. 68. $\hat{\omega}$ remains the controlling parameter, as demonstrated in Fig. 69(a) with the half-full damper#1 excited at the various frequencies, or in Fig. 69(b) with two different diameter ratios. Damper#8 with

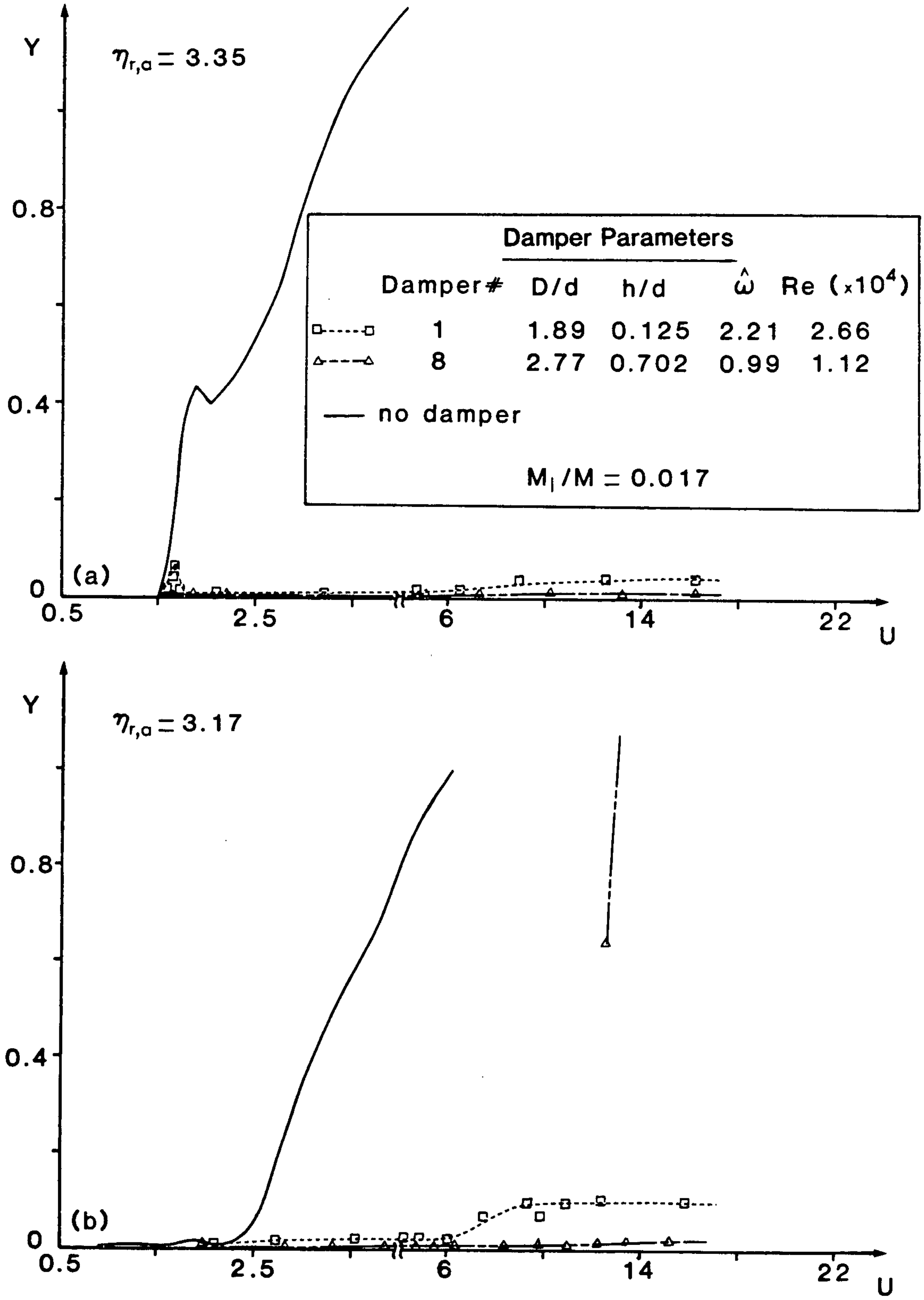

Fig. 66 Galloping response in 3-D for model#2 with nutation dampers in: (a) laminar flow; (b) turbulent flow

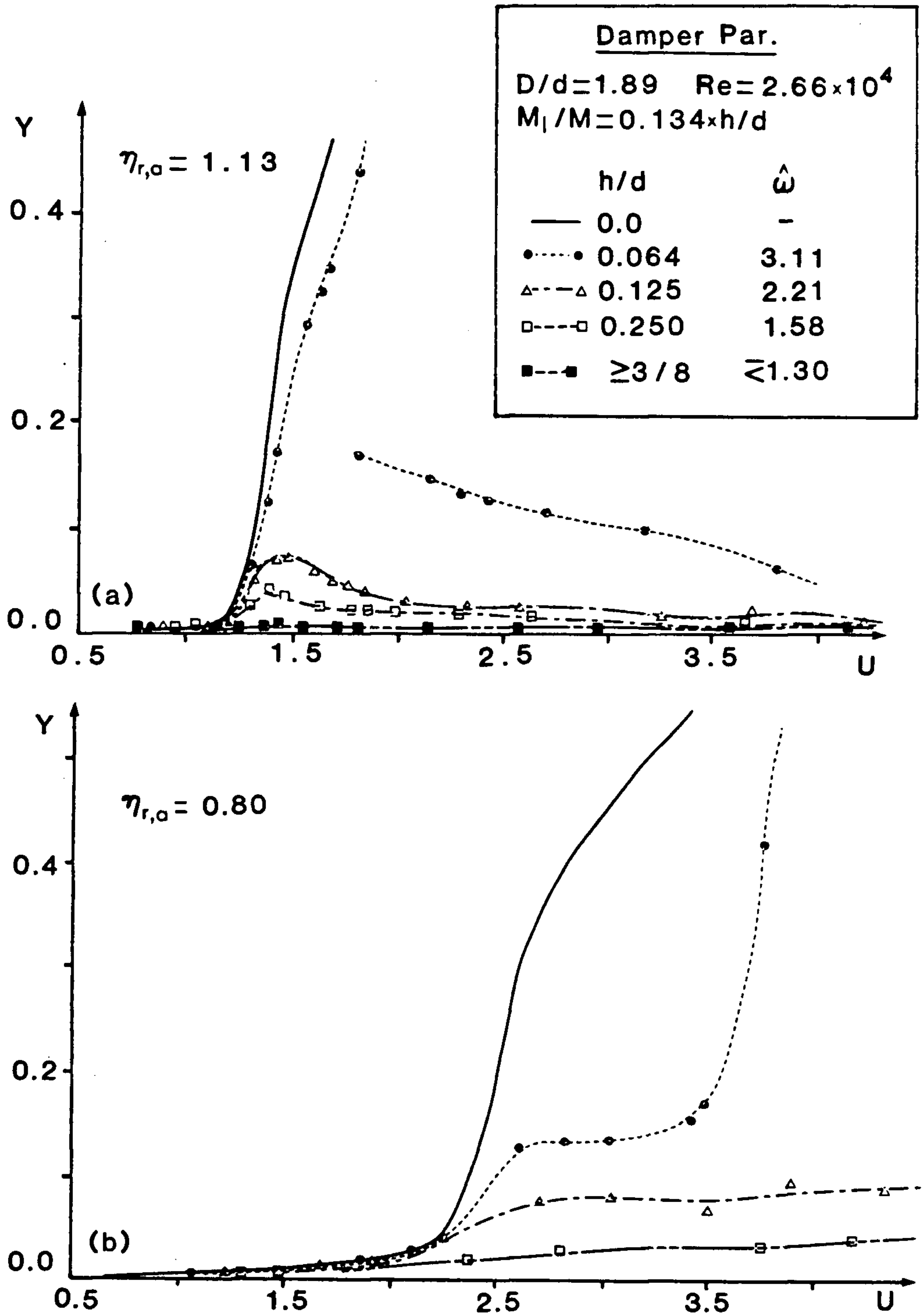

Fig. 67 Galloping response in 3-D for model#1 with nutation dampers in: (a) laminar flow; (b) turbulent flow

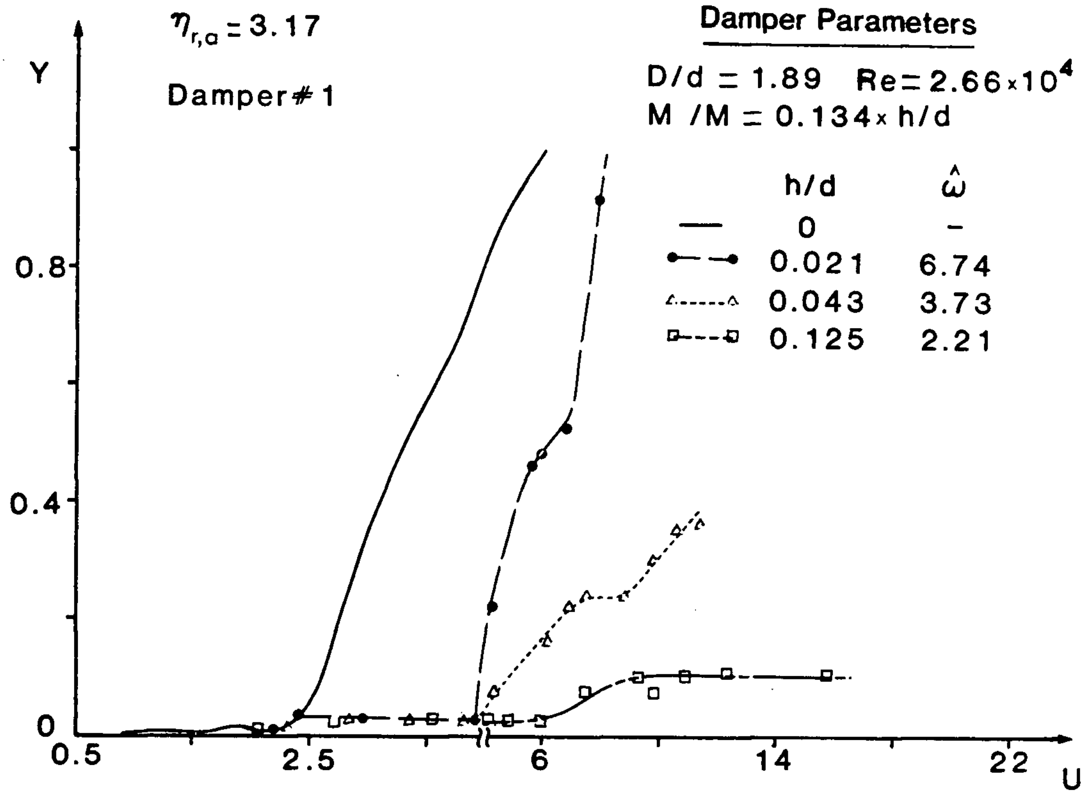

Fig. 68 Effect of low liquid heights on the 3-D galloping response of model#2

$h/d = 1/2$ and $\hat{\omega}$ very close to 1.0 is more effective than damper#1 at $h/d = 1/8$ and $\hat{\omega} = 2.21$ at low amplitudes in turbulent flow (Fig. 66b), as expected from the sloshing resonance characteristics. However, an upper branch was found with damper#8 in the presence of an initial disturbance suggesting a region of lower damping at higher amplitudes. This was not observed with damper#1 as expected from the hardening characteristics at low liquid height resulting in an increase in $\eta_{r,l}$ with displacement.

The galloping theory can be used here to predict some of the results obtained in laminar flow. Although a local force coefficient is preferable to the average values

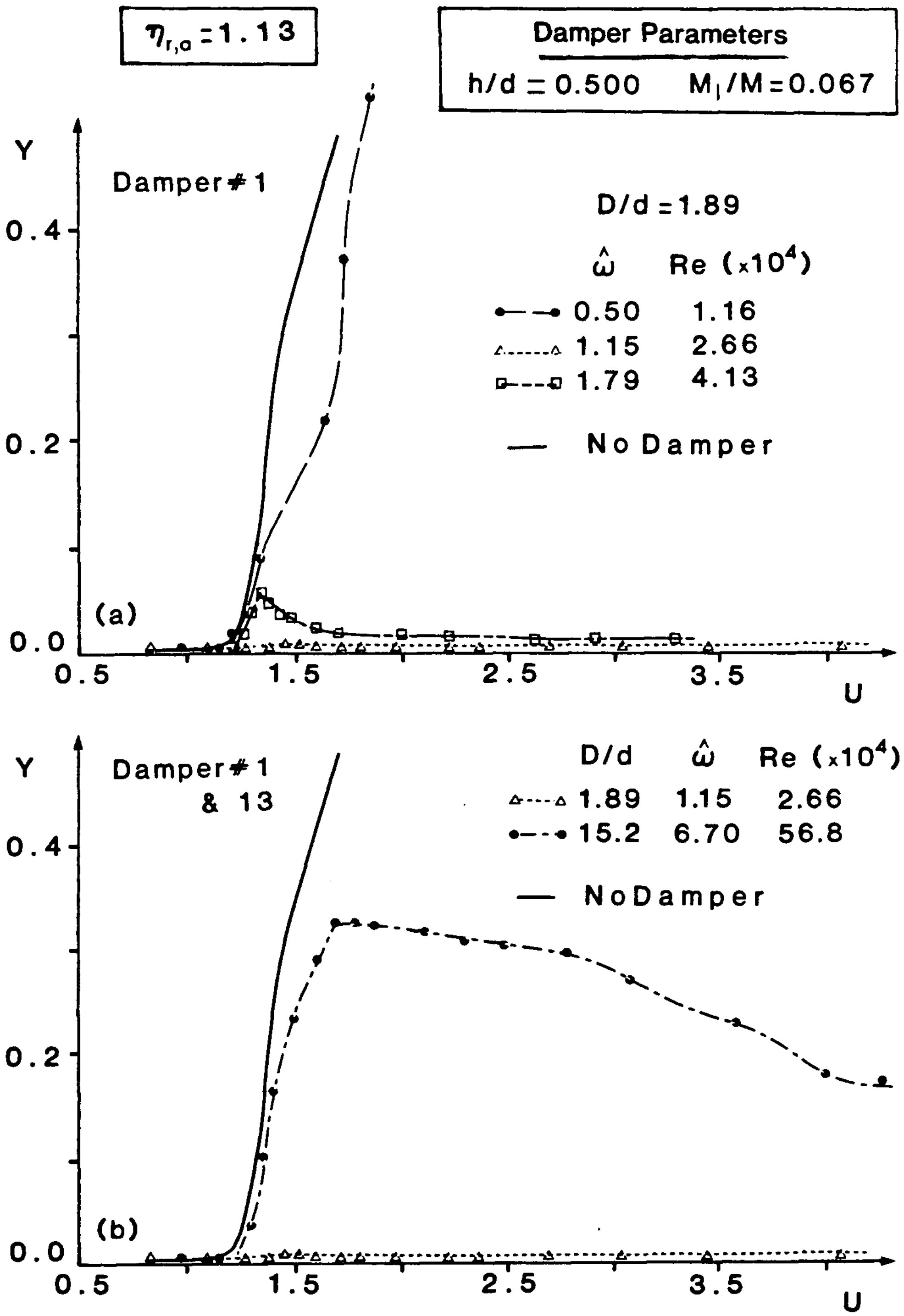

Fig. 69 Effect of D/d and $\hat{\omega}$ on the 3-D galloping response of model#2

of Fig. 56[94], the first term A_1 of the polynomial fit, found to be 0.316 and 0.251 for model#1 and 2 , respectively, suggests the onset velocity to exceed the investigated range of U (up to 4.5 and 18 for the two models, respectively) provided the damping ratio for the system is more than 0.45%. This condition is met for damper#1 with $h/d = 1/8$ and $\epsilon_0/d \geq 0.080$ (Fig. 63a) or a corresponding $Y \geq 0.02$ for the larger square prism. The configuration with $h/d = 0.064$, found to exhibit a more uniform damping versus amplitude characteristic and a maximum $\eta_{r,l} \approx 0.031$ in free oscilllations, is also expected to delay galloping beyond the imposed boundaries for U. This, of course, is also true for larger amounts of liquid ($h/d \geq 1/4$). The absence of oscillations observed at higher velocities for all cases in laminar flow thus conforms with the predictions. No static forces were measured for the turbulent case and therefore no such analysis can be carried out here. It is, however, interesting to notice that small liquid heights, i.e., $h/d = 0.064$ or 0.043, postponed the instabilities in a way similar to the two-dimensional flow case with $h/d = 1/8$ (Fig. 51), where a stalled progression for Y (Figs. 67b, 68) corresponds to the region where $\eta_{r,l}$ improves with amplitude (Fig. 63c).

4.3.5 Concluding Comments

With the weaker excitation on a three-dimensional bluff body and the higher inertia ratio achieved by positioning the damper at a distance from the center of rotation equivalent to the tip of the structure, relatively smaller amounts of liquid were needed to control the oscillations. The important findings are listed below:

- The governing damping parameters in rotation are the same as those determined for translation. The response is quite sensitive to $\hat{\omega}$ and low liquid heights show improved performance at higher amplitudes.

- A relatively low liquid to system mass ratio of 1.5% (damper#1 with $h/d = 1/8$) was sufficient to keep $Y \leq 0.1$ in all cases. $\eta_{r,l}$ was, however, estimated to be lower than its two-dimensional counterpart in otherwise similar conditions of amplitude and frequency.

- Vortex resonance dominated the response of the lightly damped 10.2 cm square section cylinder in laminar flow while galloping was the governing mechanism in turbulent conditions. The oscillations on the circular model were also found to be higher in the boundary layer tunnel. Overall, the results justify the need to conduct tests in the simulated natural wind, the smooth air stream results being not conservative.

- Both experiments and the galloping theory predict the speed for onset of instability to be beyond the investigated range (for the dampers considered here). The transient effects are expected to be small with the weaker aerodynamic forces generating slow accelerations on the models. A steady-state approximation of the damping characteristics should therefore apply reasonably well.

4.4 Application to Transmission Lines

4.4.1 Preliminary Remarks

This series of tests was designed to demonstrate the applicability of the concept to wind-induced oscillations of transmission line. A two-dimensional cylinder with an arbitrarily chosen square section, mounted horizontally in the laminar flow wind tunnel, was used to generate both vortex resonance and galloping instabilities. Although this particular shape is not likely to be representative of a cable under icing conditions, it has a well documented response and permits a comparison with the results of the two-dimensional tests (section 4.2.5.2). The main objective is to assess performance of the nutation damper when a bluff body executes oscillations in the vertical direction as is the case with the transmission lines. The torus container is now part of a more complicated device, similar to the commonly used Stockbridge damper, so that the vertical motion of the aerodynamic model can generate a significant liquid sloshing to dissipate energy.

4.4.2 Test Arrangement and Model Description

A simple support consisting of 8 springs, two of which held by sensitive beam-like strain gauges to record the displacement, was positioned inside the wind tunnel (Figs. 70, 71a). A 86.4 cm (34") long, 10.2 cm (4") side square cross-section cylinder, with a mass of 1.279 Kg and otherwise similar in design to the two-dimensional models of section 4.2, was used in the test program.The 2.5 cm ($\approx$ 1") gap between each end of the model and the wind tunnel walls allowed for possible rolling motion and prevented the tunnel corners from interfering with large translational displacements. End plates (same dimensions as in section 4.2) were installed to promote flow two-dimensionality. Relatively thick aluminum reinforcements were used inside the structure for increased rigidity as well as to provide a firm base for mounting the springs and damper support. The nutation damper was fixed to a horizontal platform, connected by a torsional spring to a light metallic arm, in turn attached to the aerodynamic model (Fig. 71b). The arrangement allowed for the rotational degree of freedom needed to impart significant sloshing motion. The device was designed to minimize drag . Its width was facing the flow and spring arrangement located in the wake of the container. The center of gravity of the rotating part (damper and supporting platform) was kept under the axis of the cylinder to avoid inducing pitch motion of the model due to response of the damper. The previously described instrumentation of the three-dimensional tests was again used here.

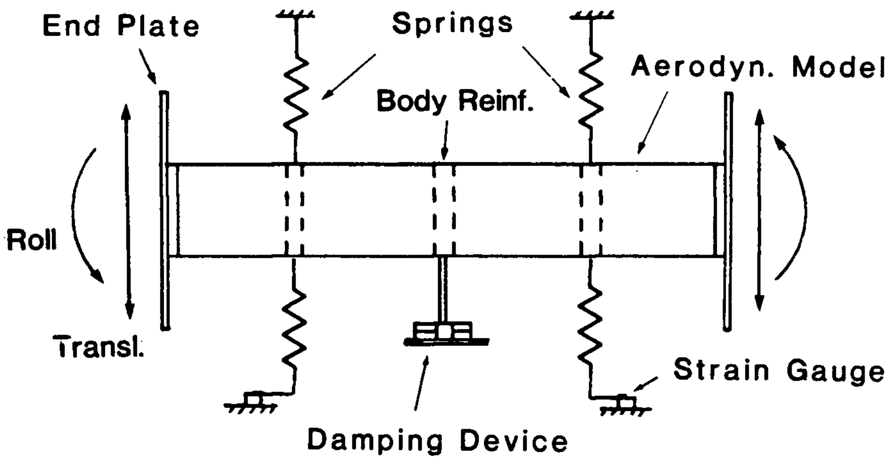

Fig. 70 Sketch of the horizontally mounted wind tunnel set-up

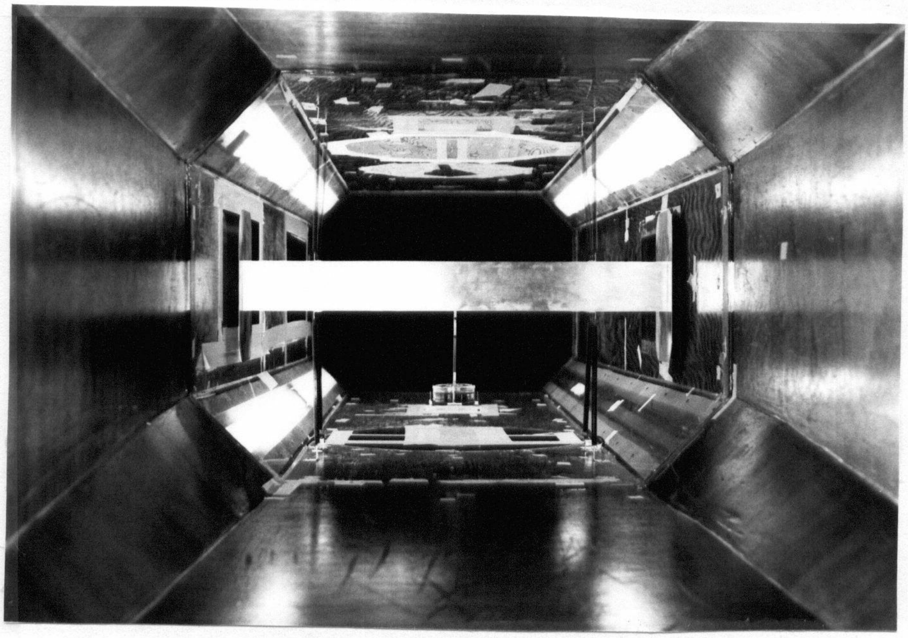

(a)

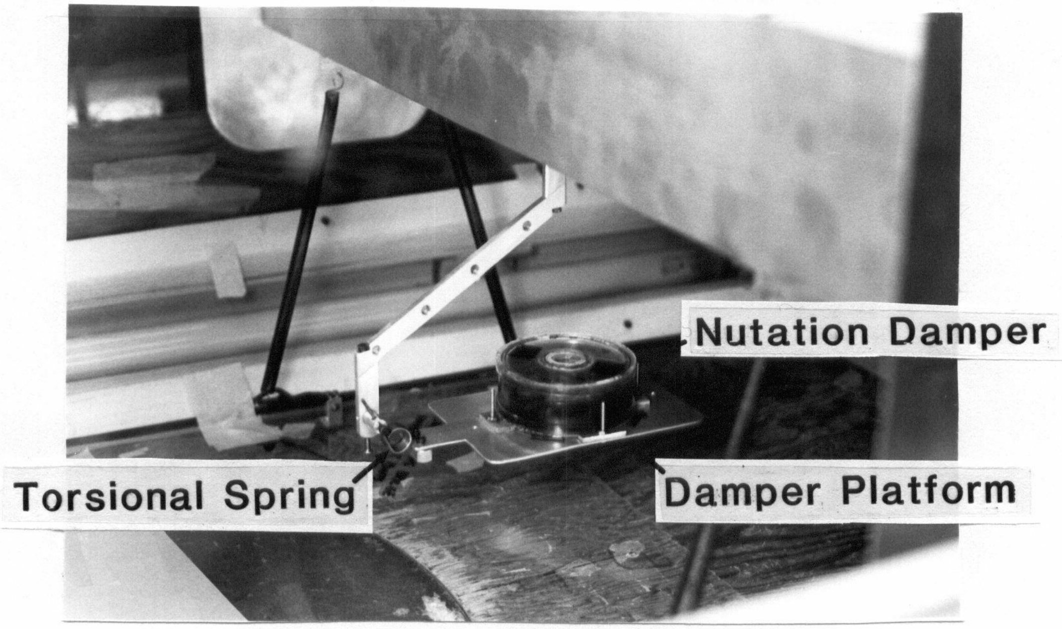

(b)

Fig. 71 Horizontally mounted wind tunnel set-up showing: (a) front view of the oscillating system; (b) close-up view of the damping device

4.4.3 Model Characteristics

The spring lengths were adjusted to ensure that the model at rest was centered at mid-height across the wind tunnel while providing a natural frequency $\omega_1 \approx 2$ Hz without damper (spring constant/unit length ≈ 3.60 N/m^2). With the installation of the rotating damping device, two distinct natural frequencies, characteristic of any two-degree-of-freedom system, were observed. They depend on the torsional spring stiffness and damper mass (Appendix VI.2). Although a number of parameters can be optimized to minimize the response of the model at resonance, the frequency ratio ω_2/ω_1 (ω_1=natural frequency of the model without damping device, ω_2=natural frequency of the damping device alone) was kept relatively close to 1.0 with aerodynamic model to damping device mass ratio $m_2/m_1 \approx 0.10$ (Appendix VI, eqs. VI.4, VI.7). A hard torsional spring with a stiffness constant of 0.557 N-m was used to test heavier nutation dampers while smaller amounts of liquid required the installation of a soft spring with $k_2 = 0.285$ N-m. The inherent damping ratio of the system (i.e., no damper) was estimated to be 0.04% corresponding to a very low $\eta_{r,a} = 0.75$, making the structure aerodynamically quite unstable. The energy dissipation in the rotating mechanism of the damper was investigated separately using the strain gauge arrangement of Chapter 3. A simple calibration procedure, with the beam positioned horizontally to support the damper (Fig. 72a), led to a free-oscillation damping ratio η_{s2} ($\eta_{s2} = \dfrac{C_{d2}}{2m_2\omega_2}$, where C_{d2} is the damping coefficient of the sytem) of approximately 3.0 to 4.0% (Fig. 72b). The experiment was repeated for the partially filled containers to express performance in terms of $\eta_{r,l}$.

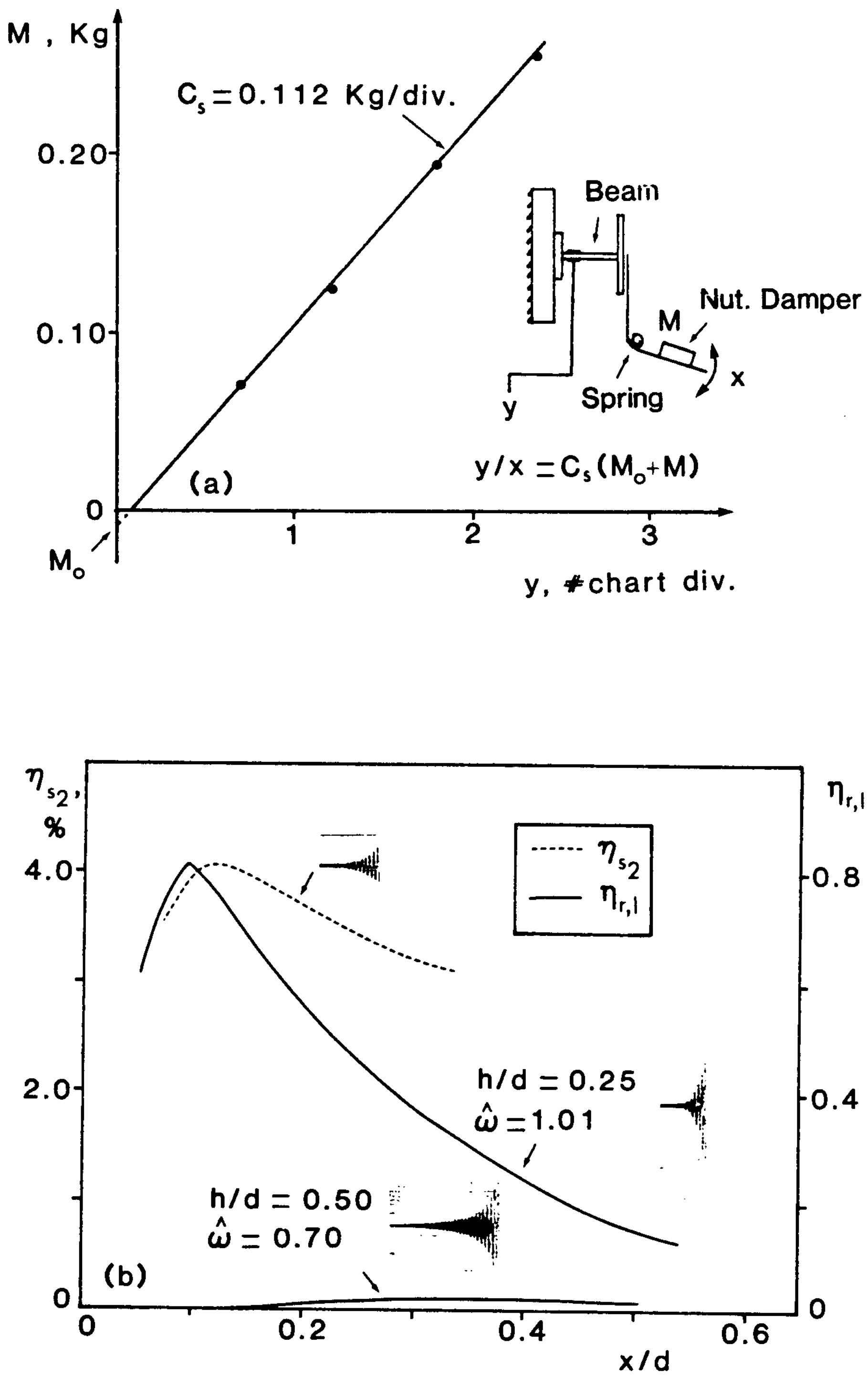

Fig. 72 Evaluation of the secondary system damping ratio showing: (a) calibration procedure; (b) η_{s2} and $\eta_{r,l}$ versus amplitude

4.4.4 Results and Discussion

In absence of the damping mechanism, a combined vortex shedding-galloping response, similar to that of the two-dimensional tests (section 4.2.4) was obtained for the square cylinder (Fig. 73a). The damping device was mounted but not activated, with the torsional spring replaced by a rigid bracket to account for the additional aerodynamic forces. Although the model was free to move in any direction, a well behaved one-degree-of-freedom vertical translation was observed throughout the test. This was however not the case with the action of the secondary system. Without liquid, the damper platform oscillated vigorously, and the inherent energy dissipation was sufficient to restrict the first vortex resonance amplitude Y to 0.265. The wind velocity is nondimensionalized with respect to ω_1 (natural frequency of the main system, $\approx$ 2.00 Hz) to show the shift in the response. Behind the resonance peak, the lock-in phenomenon was suddenly interrupted with a change in frequency, from 1.68 Hz (ω_{n1}) to 2.40 Hz (ω_{n2}). A beat motion during the transition (Fig. 73b) was often observed and a significant build-up in amplitude did not occur. With increase in wind speed, the response settled at 2.40 Hz and galloping finally occurred near $U = 7.0$ coupled with a rolling motion. The latter is probably due to a lack of uniformity along the cylinder length. With a natural frequency of 2.12 Hz, it was relatively easy to excite roll given the proper conditions, as discussed later.

The introduction of liquid reduced Y to 0.1 at resonance, for both $h/d = 1/4$ and 1/2 (Fig. 74). The arrangement proved to be effective at controlling both

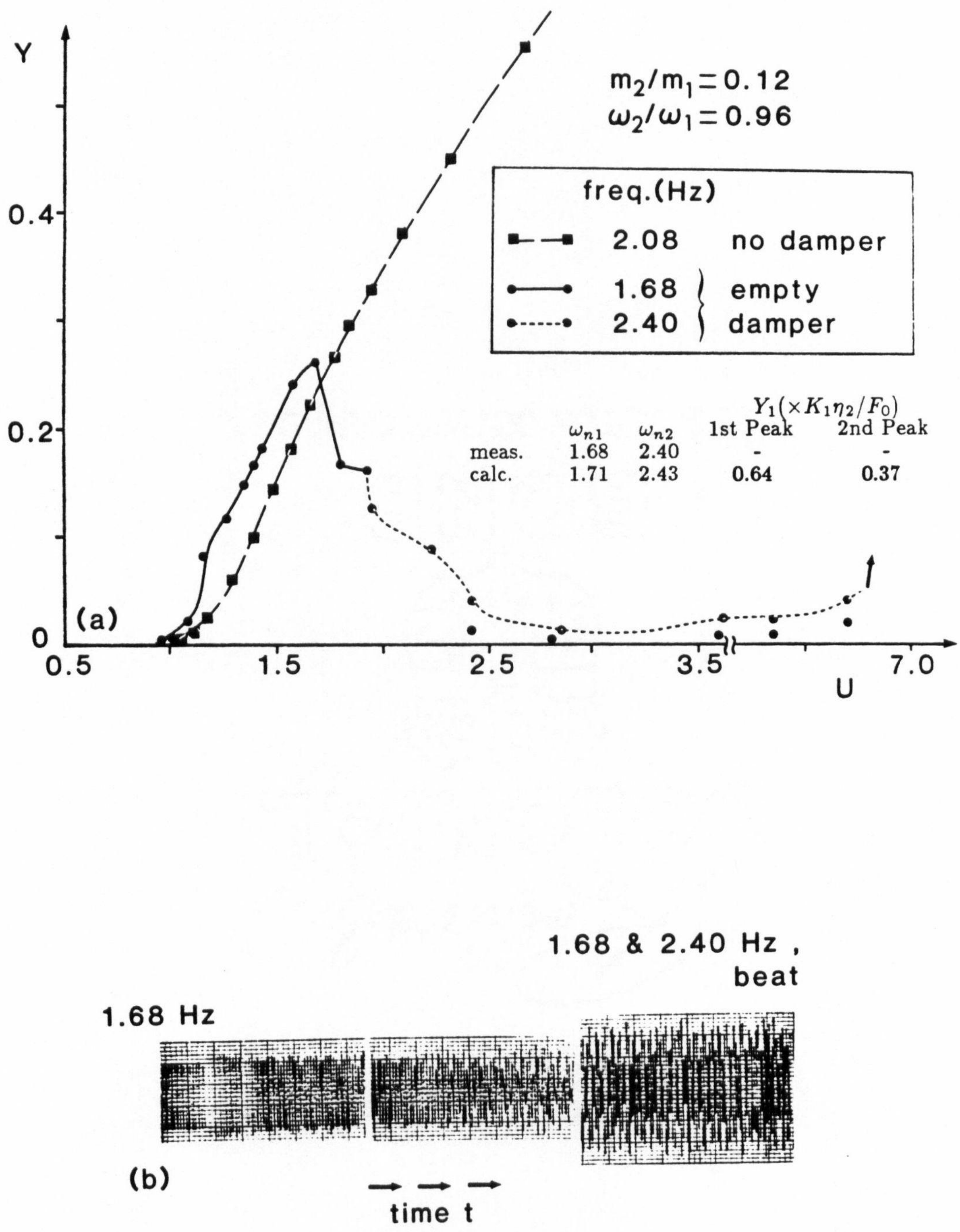

Fig. 73 Response of the system without damping liquid showing: (a) effect of auxiliary device; (b) beating motion

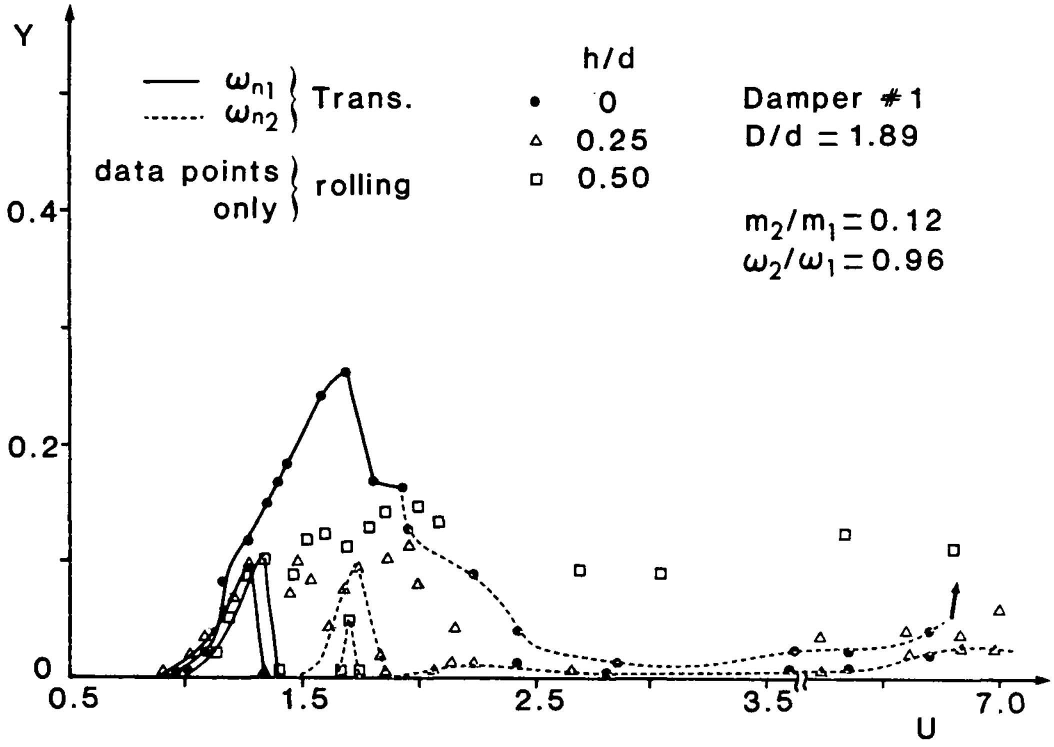

Fig. 74 Effect of liquid height on the system response

vortex resonance peaks, with the half-full damper performing better at ω_{n2}, where $\hat{\omega} = 1.11$. It should be mentioned here that the damping characteristics were found to be qualitatively quite similar to those of Chapter 3, with $\hat{\omega}$ close to 1.0 generating optimal $\eta_{r,l}$, as illustrated in Fig. 72(b). The reduced damping ratios were generally lower, a result consistent with the earlier discussion (section 4.3.4.2) which showed that rotation reduces efficiency. This, however, is not a problem here as the liquid to secondary system mass ratio was quite large, with peak $\eta_2 > 10\%$.

With the response of the damper, a strong rolling action often accompanied the plunging vortex resonance motion, as illustrated by the frequency spectrum of Fig. 75(a). It persisted at higher U (Fig. 75b). Under slightly different conditions, a galloping type of instability even occurred in roll (Fig. 76a). The damping mechanism was designed to respond to a translational motion only and therefore could not react to any rolling as it was positioned half-way along the model length. A different arrangement, with a damper fixed at each end of the cylinder and facing the axis perpendicular to the flow, would probably be more effective at controlling both modes and could be a subject of further studies (Fig. 77).

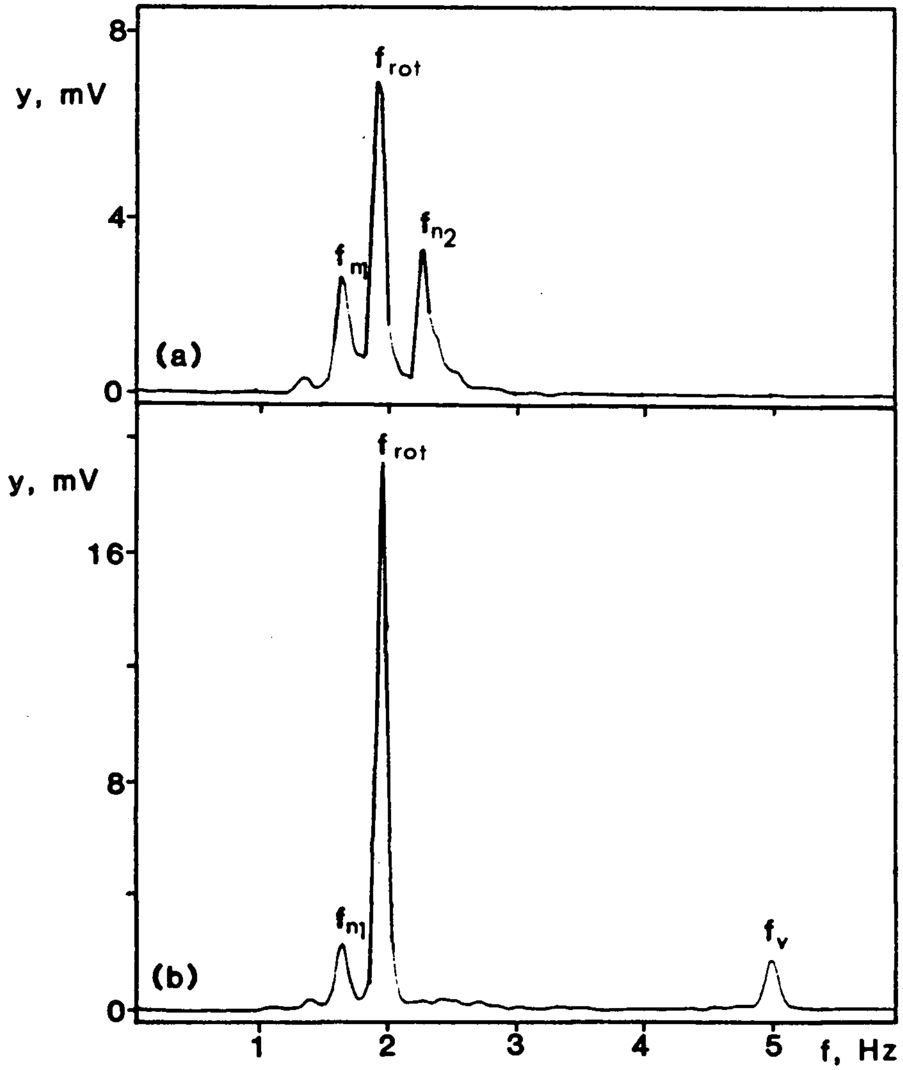

Fig. 75 Frequency spectrum of the response for: (a) $f_v \approx f_{rot}$; (b) $f_v \gg f_{rot}$

Fig. 76 also shows the effect of other parameters such as ω_2/ω_1 and m_2/m_1. The empty damper configuration now allows the response to exceed $Y = 0.35$ with $\omega_2/\omega_1 = 1.32$ (Fig. 76a), which represents a significant change compared with $Y = 0.265$ for $\omega_2/\omega_1 = 0.96$ shown earlier (Fig. 73a). The quarter-full damper is quite ineffective, but more liquid and $\hat{\omega}$ closer to 1.0 reduces Y to 0.2 at $h/d = 1/2$. Somewhat different results were obtained with a reduction in m_2/m_1. The first resonant region is now confined to 0.15 and 0.075, for the empty and half-full damper#8, respectively. A typical low damping vortex-galloping curve dictates the response at the other natural frequency (ω_{n2}, Fig. 76b). This overall behavior seems to agree qualitatively with the vibration absorber relation (VI.6) that predicts the resonant amplitude under a constant excitation F: the larger wind-induced oscillations correspond to higher calculated Y_1 (Figs. 73, 76). Although beyond the scope of this study, minimizing Y_1 is likely to result in a design quite effective in controlling the vibrations. Of course, a more rigorous analysis should include interactions between the system parameters and the aerodynamic forces.

4.4.5 Result Summary

The experiments showed that the partially filled torus containers are suitable for transmission line application as significant reduction in vibrations is possible. The following observations can be made:

- The presence of two resonant frequencies appears to be beneficial as their mutual

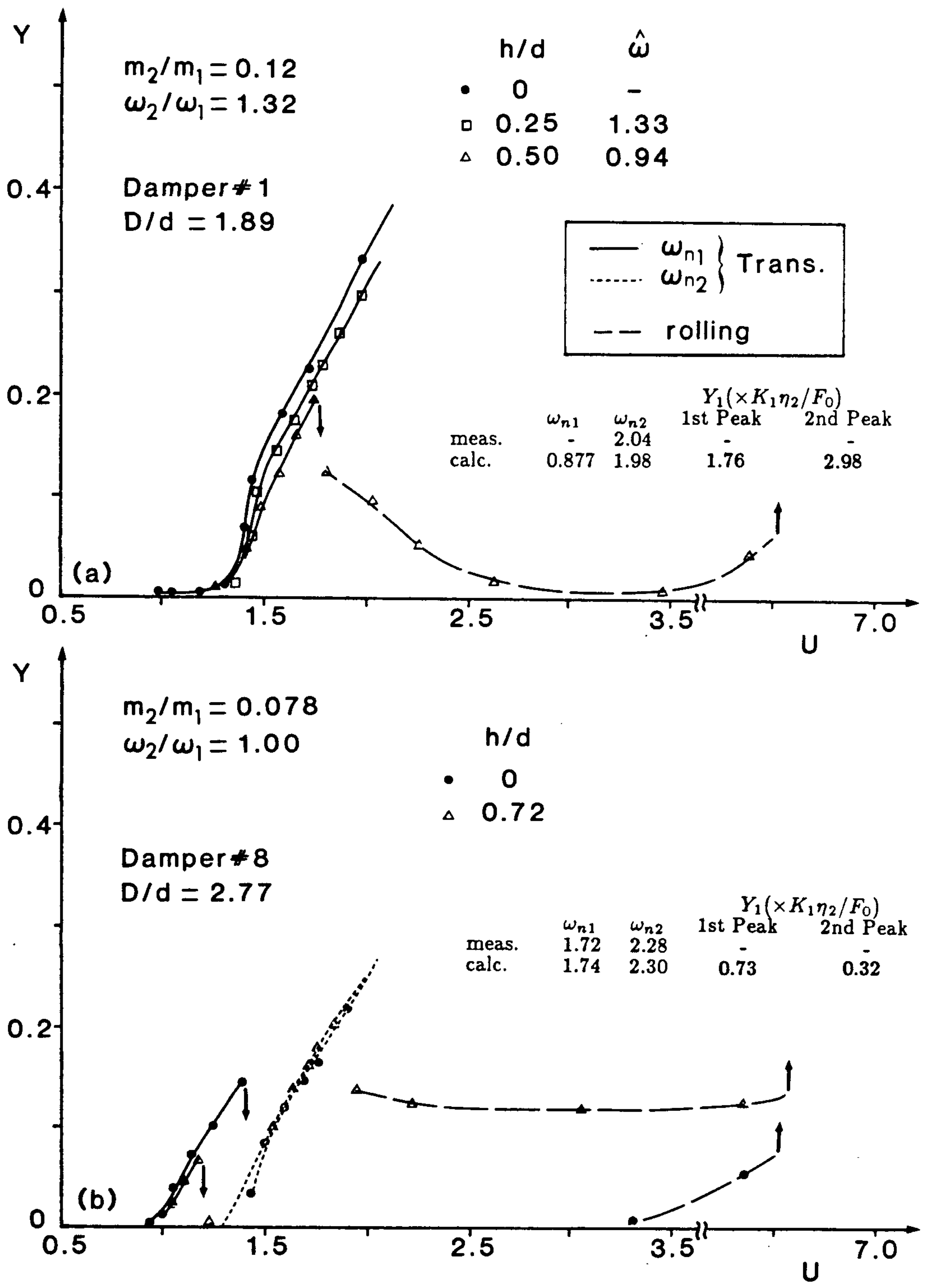

Fig. 76 Response of the model as affected by: (a) ω_2/ω_1; (b) m_2/m_1

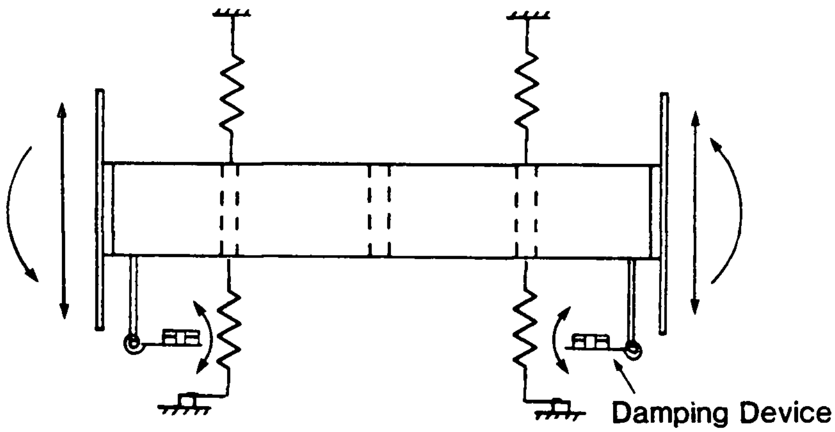

Fig. 77 Sketch of the two damper arrangement useful to control roll

interaction can disrupt the first vortex shedding lock-in region. On the other hand, the nutation dampers are then required to be effective for both excitations. This condition can be met by certain damper configurations. Alternatively, two separate containers designed for the individual frequency may be used.

- A combined vortex resonance-galloping curve can develop at either natural frequency for the lightly damped system, depending on the parameters ω_2/ω_1 and m_2/m_1. With an increase in damping, the onset of galloping is delayed and the model oscillates at ω_{n2}.

- The condition of liquid resonance still maximizes the energy dissipation. The reduced damping ratio continues to be lower in rotation compared to that in translation. A light support with the liquid positioned far away from the center of rotation can, however, give the desired energy dissipation.

- More systematic tests to optimize the system parameters (i.e., ω_2/ω_1, m_2/m_1, etc.), as well as a configuration that reduces rolling motion interfering with the main mode of vibration, would be necessary to properly assess and finalize the damper design.

5. CONCLUSIONS

This investigation has provided information useful in the design of nutation dampers for controlling wind-induced instabilities. With the objective of optimizing the energy dissipation parameters, it has also contributed to the understanding of nonlinear liquid sloshing problems using both theoretical and experimental procedures. Extensive tests with two and three dimensional models in laminar and turbulent flow wind tunnels suggest that the concept of nutation damping can effectively suppress both vortex resonance and galloping instabilities. Based on the study, the following general conclusions can be made:

(i) The damping characteristics have been established through a comprehensive test program evaluating influence of the damper's dimensionless parameters. The theoretical development proved useful in understanding the liquid motion and the corresponding role of nonlinearities leading to a consistent variation of the damping ratio with frequency, amplitude, liquid height, etc.

(ii) Reliance on the experimental results is still necessary as the potential flow approach in conjunction with the boundary layer correction, although predicting the correct trends, does not account for several mechanisms for energy dissipation. Discrepancies between calculations and measurements, in both viscous stresses and pressure fields, indicate that additional damping terms should be included in the equations governing the flow.

(iii) Whenever possible, dampers should be designed to operate at their liquid sloshing resonance, as shown by the theory, sloshing table experiments, and further verified by the wind tunnel tests. Conditions of low liquid heights and large diameter ratios are more efficient, resulting in higher peaks in damping ratios and a smaller variation with amplitude of excitation. Low Reynolds numbers and internal devices such as baffles or inner tubes should be avoided as they restrict the action of the free surface.

(iv) The damper behavior in rotation is similar to that in pure translation with optimal efficiency at the condition of sloshing resonance. However, free oscillation tests show the damping ratio to reduce with an increase in angular motion about the horizontal plane.

(v) The wind tunnel tests were useful in assessing the effect of external forces. In general, the better damping characteristics obtained during a steady-state excitation resulted in improved control of wind-induced oscillations. Time dependent parameters related to the acceleration of the structure proved to be significant for the case where the aerodynamic model is unstable and the damping ratio is strongly dependent on amplitude.

(vi) Relatively small nutation dampers were usually adequate to suppress the vibrations. The two-dimensional circular cylinder, with a low $\eta_{r,a}$ of 2.9, required a damping liquid to structure mass ratio lower than 1% under vortex resonance.

Somewhat larger ratios from 1% to 5% (depending on $\eta_{r,a}$) were necessary to significantly delay galloping of the square cross-section.

(vii) The weaker aerodynamic excitation associated with the three-dimensional models required even smaller dampers to be used, less than 1% in all cases. For square cylinders, vortex resonance is the main mechanism of instability in laminar flow whereas galloping governs the response in the turbulent wind, with maximum displacements approximately the same in either case for the range of wind speed investigated . The motion of the circular cylinder under vortex shedding was found to be of similar magnitude for both flow conditions, with a larger response for the model without dampers under turbulent excitation.

(viii) The nutation dampers can easily be applied to transmission lines with the design of a support allowing for rotational motion. They provided significant energy dissipation with an effective control of the instabilities. Results are promising and optimization of the system parameters can lead to further improvements.

(ix) Nutation dampers are particularly suited for structures with low natural frequencies. For example, at 0.3 Hz or less, it is estimated that a liquid to total mass ratio of 0.75% ($M_l/M = 3\%$) is capable of restricting the response of steel chimneys, with initial aerodynamic reduced damping of 1.9, to $Y \leq 0.1$ according to the available data (Appendix VII). Thus, in addition to being simpler in design, nutation dampers promise to be lighter compared to the conventional tuned mass devices.

Some Thoughts on Future Work

- The thesis has provided some insight into a class of nutation dampers' behavior. However, an accurate analytical prediction of the damping ratio still remains a challenging task. The proposed formulation, resulting in a 3rd order characteristic equation for the liquid's amplitude response, was found to be incomplete in spite of the special consideration given to the the important phenomenon of resonant interactions. A more sophisticated analytical or numerical scheme accounting for additional sources of dissipation would therefore be worth investigating. This can be combined with a more elaborate experimental procedure to detect and study the nonlinear component of the response through the use of large-scale models, surface sensors, etc.

- The time-dependent sloshing response was shown to be significant during the wind tunnel tests, as the liquid is initially at rest and damping is generated by the motion (as for any type of tuned mass damper). A systematic study providing the damping characteristics versus rate of amplitude change (i.e., $d\hat{\epsilon}/dt$, $d^2\hat{\epsilon}/dt^2$, etc.) would therefore be quite useful in practical applications. This could be included into a broader evaluation of the performance under different types of excitation encountered in other fields (e.g., earthquake and ocean engineering problems) where such dampers could be used.

BIBLIOGRAPHY

[1] Hirsch, G., and Ruschewey, H., "Full Scale Measurements on Chimney Stacks", *Journal of Industrial Aerodynamics*, Vol. 1, 1975/76, pp. 341-347.

[2] Chaulia, P.B., "Failure Investigation in the Vertical Lap Joint in the Shell of Dolomite Kiln Chimney No. 1", *Central Mechanical Research Institute*, Durgapur-9, West Bengal, Report No. SA/AM/6-78, 1978.

[3] Scanlan, R.H., and Velozzi, J.W., "Catastrophic and Annoying Responses of Long-Span Bridges to Wind Action", *Annals of the New York Academy of Sciences*, Vol. 352, 1980, pp. 247-264.

[4] Scruton, C., and Walshe, D.E.J., "A Means for Avoiding Wind-Excited Oscillations of Structures with Circular or Nearly Circular Cross-Section", *National Physical Laboratory*, Report 335, 1957; also *British Patent* No. 907, 851.

[5] Price, P., "Suppression of the Fluid-Induced Vibration of Circular Cylinders", *Proceedings of the American Society of Civil Engineering*, Vol. 82, No. EM3, 1956, pp. 1-21.

[6] Wong, H.Y., "An Aerodynamic Means for Suppressing Vortex Induced Oscillations", *Proceedings of the Institute of Civil Engineers*, Vol. 63, 1977, pp. 693-699.

[7] Zdravkovich, M.M., "Review and Assessment of Various Aero and Hyrodynamic Means for Suppressing Vortex Shedding", *Proceedings of the 4th Colloquium on Industrial Aerodynamics*, Aachen, June 18-20, 1980, Part 2, pp. 29-47.

[8] Every, M.J., King, R., and Weaver, D.S., "Vortex-Excited Vibrations of Cylinders and Cables and their Suppression", *Ocean Engineering*, Vol. 9, No. 2, 1982, pp. 135-157.

[9] Wong, H.Y., and Cox, R.N., "The Suppression of Vortex-Induced Oscillations on Circular Cylinders by Aerodynamic Devices", *Proceedings of the 3rd Colloquium on Industrial Aerodynamics*, Aachen, June 14-16,1978, Part 2, pp. 185-204.

[10] Naudascher, E., Weske, J.R., and Fey, B., "Exploratory Study on Damping Galloping Vibrations", *Proceedings of the 4th Colloquium on Industrial Aerodynamics*, Aachen, June 18-20, 1980, Part 2, pp. 283-293.

[11] Reed, W.H., "Hanging Chain Impact Dampers: A Simple Method for Damping Tall Flexible Structures", *Proceedings of the International Research Seminar*, Ottawa, Sept. 11-15, 1967, Wind Effects on Structures, Vol.2, 1968, pp. 287-320.

[12] Den Hartog, J.P., "Self-Induced Oscillations", *Mechanical Vibrations*, Chapter 7, McGraw Hill, New York, 1956, pp. 305-309.

[13] Gasparini, D.A., Curry, L.W., and Debchaudhury, A., "Passive Viscoelastic Sys-

tems for Increasing the Damping of Buildings", *Proceedings of the 4th Colloquium on Industrial Aerodynamics*, Aachen, June 18-20, 1980, Part 2, pp. 257-266.

[14] Ogendo, J.E.W., Milsted, M.G., and Johns, D.J., "Response of Steel Chimney with Added Damping", *Journal of Wind Engineering and Industrial Aerodynamics*, Vol. 17, 1984, pp. 251-264.

[15] Wardlaw, R.L., and Cooper, K.R., "Dynamic Vibration Absorbers for Suppressing Wind-Induced Oscillations", *Proceedings of the 3rd Colloquium on Industrial Aerodynamics*, Aachen, June 14-16, 1978, Part 2, pp. 205-220.

[16] Hunt, J.B., "Applications of Rectilinear Passive Dynamic Vibration Absorber", *Dynamic Vibration Absorbers*, Garden City Press, Great Britain, 1979, Chapter 4, pp. 72-83.

[17] Ruscheweyh, H., "Straked In-Line Steel Stacks with Low Mass Damping Parameter", *Proceedings of the 4th Colloquium on Industrial Aerodynamics*, Aachen, June 18-20, 1980, Part2, pp. 195-204.

[18] Tanaka, H., and Mak, C.Y., "Effect of Tuned Mass Dampers on Wind Induced Response of Tall Buildings", *Journal of Wind Engineering and Industrial Aerodynamics*, Vol. 14, 1983, pp. 319-330.

[19] Stockbridge, G.H., "Overcoming Vibration in Transmission Cables", *Electrical World*, Vol. 86, 1925, pp. 1304-1305.

[20] Diana, G., Gasparetto, M., Tavano, F., and Cosmai, U., "Field Measurement and Field Data Processing on Conductor Vibration", *International Conference on Large High Voltage Electric Systems*, CIGRE 1982 Session, Sept. 1-9, Paris.

[21] Rawlins, C.B., "Wind Tunnel Measurements of the Power Imparted to a Model of a Vibrating Conductor", *IEEE Transactions of Power Apparatus and Systems*, Vol. PAS-102, No. 4, 1983, pp. 963-971.

[22] Schäfer, B., "Zur Entstehung und Unterdrückung winderregter Schwingungen an Freileitungen", *Vom Fachbereich Mechanik der Technischen Hochshule Darmstadt*, Dissertation, 1980.

[23] Hagedorn, P., "On the Computation of Damped Wind-Induced Excitation of Transmission Lines", *Journal of Sound and Vibration*, 1982, pp. 253-271.

[24] Claren, R., and Diana, G., "Mathematical Analysis of Transmission Line Vibrations", *IEEE Transactions on Power Apparatus and Systems*, Vol. PAS-88, No. 12, 1969, pp. 1741-1771.

[25] Healey, M.D., "Semi-Active Control of Wind-Induced Oscillations in Structures", *University of Illinois*, M.A.Sc. Thesis, Urbana, 1983.

[26] Chowdhury, A.H., Iwuchukwu, M.D., and Garske, J.J., "The Past and Future of Seismic Effectiveness of Tuned Mass Dampers", *North Dakota State University*,

Department of Civil Engineering Report.

[27] Yang, J.N., "Control of tall Buildings under Earthquake Excitation", *Journal of Sound and Vibration*, Vol. 108, No. EM5, 1982, pp. 833-849.

[28] Hirsch, G., "Control of Wind-Induced Vibrations of Civil Engineering Structures", *Proceedings of the 4th Colloquium on Industrial Aerodynamics*, Aachen, June 18-20, 1980, Part 2, pp. 237-256.

[29] Hirsch, G., Rusheweyh, H., and Zutt, H., "Failure of a 140 m High Steel Chimney Caused by Wind Excited Oscillations Transverse to the Wind Direction", *International Conference on Steel Plate Structures*, Session 7, Paper No. 34.

[30] Rohman, M.A., "Structural Control Using Active Tuned Mass Dampers", *Proceedings of the American Society of Civil Engineers*, Vol. 107, No. EM5, 1981, p. 990.

[31] Brunner, A., "Amortisseurs d'oscillations hydrauliques pour cheminées", *La Houille Blanche*, Les instabilitées en hydraulique et en mécanique des fluides, compte rendu des huitièmes journées de l'hydraulique, Lille, Juin 1984, Tome 10, pp. 258-263.

[32] Berlamont, J., and Vanderstappen, N., "The Effect of Baffles in a Water Tower Tank", *Proceedings of the 5th International Conference on Wind Engineering*, Vol. 2, 1979, pp. 1195-1201.

[33] Modi, V.J., Sun, J.L.C., Shupe, L.S., and Solyomvari, A.S., "Suppression of Wind-Induced Instablities Using Nutation Dampers", *Proceedings of the Indian Academy of Sciences*, Vol. 4, Part 4, 1981, pp. 461-470.

[34] Bauer, H.F., "Oscillations of Immiscible Liquids in a Rectangular Container. A New Damper for Excited Structures", *Journal of Sound and Vibration*, Vol. 93, 1984, Part 1, pp. 117-133.

[35] Kwek, K.C.S., "Damping Increase with Tuned Mass Damper", *Journal of Sound and Vibration*, Vol. 110, No. 11, 1984, pp. 1645-1649.

[36] Sneider, C.C., and Likins, P.W., "Nutation Dampers versus Precession Dampers for Axisymmetric Spinning Spacecraft", *Journal of Spacecrafts and Rockets*, Vol. 10, No. 3, 1973, pp. 218-222.

[37] Alfriend, K.T., and Spencer, T.M., "Comparison of Filled and Partly Filled Nutation Dampers", *AAS/AIAA Astrodynamics Specialist Conference*, Lake Tahoe, Nevada, Aug. 3-5, 1981, Paper No. 81-141.

[38] Alfriend, K.T., and Hubert, C.H., "Stability of Dual-Spin Satellite with Two Dampers", *Journal of Spacecraft and Rockets*, Vol. 11, No. 7, 1974, pp. 469-474.

[39] Bryson, A.E., and Barnejee, A.K., "Stabilization of a Spinning Spacecraft with Liquid Slosh", *AIAA Guidance, Navigation and Control Conference*, Williamsburg, Virginia, Aug. 18-20, 1986.

[40] Cloutier, G.J., "Variable Spin Rate, Two-Degree-of-Freedom Nutation Damper Dynamics", *AAS/AIAA Astrodynamics Specialist Conference*, Nassau, Bahamas, July 28-30, 1975, Paper No. AAS75-045.

[41] Malik, N.K., and Geol, P.S., "Passive Nutation Dampers for Spinning Satellites", *Indian Space Research Organization*, Bangalore, Technical Note ISRO-ISAC-TN-06-77, 1977.

[42] Alfriend, K.T., "Gravity Effects in the Testing of Nutation Dampers", *Proceedings of the CNES-ESA Conference on Attitude Control of Space Vehicles - Technoligical and Dynamical Problems Associated with the Presence of Liquids*, Toulouse, Oct. 10-12, 1977, ESA SP-129, pp. 193-197.

[43] Agrawal, B.N., and James, P., "Energy Dissipation due to Liquid Slosh in Spinning Spacecraft", *Proceedings of the 3rd VPI and SU/AIAA Symposium of Dynamics and Control of Large Flexible Spacecraft*, July 1981.

[44] Alfriend, K.T., "Partially Filled Viscous Ring Nutation Damper", *Journal of Spacecrafts and Rockets*, Vol. 11, No. 3, 1974, pp. 456-462.

[45] Tossman, B.E., "Testing Attitude Dampers", *International Federation of Automatic Control Workshop*, Aug. 23, 1983, Stanford, California.

[46] Cooper, R.M., "Dynamics of Liquids in Moving Containers", *ARS Journal*, Vol. 30, No. 8, 1960, pp. 725-729.

[47] Abramson, H.N., "Dynamic Behavior of Liquid in Moving Container", *Applied Mechanic Review*, Vol. 16, No. 7, 1963, pp. 501-506.

[48] Jacobsen, L.S., "Impulsive Hydrodynamics of Fluid Inside a Cylindrical Tank and a Fluid Surrounding a Cylindrical Pier", *Bulletin of the Seismological Society of America*, Vol. 39, 1949, pp. 189-209.

[49] Housner, G.W., "Dynamic Pressures on Accelerated Fluid Containers", *Bulletin of the Seismological Society of America*, Vol. 47, 1957, pp. 15-35.

[50] Housner, G.W., "The Dynamic Behavior of Water Tanks", *Bulletin of the Seismological Society of America*, Vol. 53, No. 2, 1963, pp. 381-387.

[51] Graham, E.W., and Rodriguez, A.M., "The Characteristics of Fuel Motion which Affect Airplane Dynamics", *Transaction of the ASME*, Journal of Applied Mechanics, Vol. 19, 1952, pp. 381-388.

[52] Chu, W.H., "Sloshing of Liquids in Cylindrical Tanks of Elliptic Cross-Section", *ARS Journal*, Vol. 30, No. 4, 1960, pp. 360-363.

[53] Bauer, H.F., "Theory of the Fluid Oscillations in a Circular Ring Tank Partially Filled with Liquid", *NASA Technical Note D-557*, Washington, 1960.

[54] Abramson, N., Garza, L.R., and Kana, P.P., "Liquid Sloshing in Comparti-

mented Cylindrical Tanks", *ARS Journal*, Vol. 32, No. 6, 1962, pp. 978-988.

[55] Hwang, C., "Longitudinal Sloshing of Liquid in a Flexible Hemispherical Tank", *Transactions of the ASME*, Journal of Applied Mechanics, 1964, Paper No. 65-APM-14.

[56] Budiansky, B., "Sloshing of Liquids in Circular Canal and Spherical Tanks", *Journal of the Aerospace Sciences*, Vol. 27, No. 3, 1960, pp. 161-173.

[57] Su, T.C., Lou, Y.K., Flipse, J.E., and Bridges, T.J., "A Numerical Analysis of Large Amplitude Liquid Sloshing in Baffled Containers", *U.S. Department of Transportation*, Marine Administration, 1982, Report No. MA-RD-940-82046.

[58] Haroun, M.A., and Tayel, M.A., "Axisymmetric Vibrations of Tanks - Numerical", *Proceedings of the American Society of Civil Engineers*, Journal of Engineering Mechanics, Vol. 111, No. 3, 1985, pp. 329-345.

[59] Abramson, N., Chu, W.H., and Ransleben, G.E., "Representation of Fuel Sloshing in Cylindrical Tanks by an Equivalent Mechanical Model", *ARS Journal*, 1961, pp. 1697-1705.

[60] Berlot, R.R., "Production of Rotation in a Confined Liquid through Translational Motion of the Boundaries", *Transactions of the ASME*, Journal of Applied Mechanics, 1959, pp. 513-516.

[61] Bauer, H.F., "Nonlinear Mechanical Model for the Description of Propellant Sloshing", *AIAA Journal*, Vol. 4, No. 9, 1966, pp. 1662-1668.

[62] Sayar, B.A., "Fluid Slosh Damper", *Georgia Institute of Technology*, Ph.D Thesis, 1970.

[63] Hutton, R.E., "An Investigation of Resonant, Nonlinear, Non-Planar Free Surface Oscillations of a Fluid", *NASA Technical Note D-1870*, Washington, 1963.

[64] Woodward, J.H., and Bauer, H.F., "Fluid Behavior in a Longitudinally Excited Cylindrical Tank of Arbitrary Cross-Section", *AIAA Journal*, Vol. 8, No. 4, 1970, pp. 713-719.

[65] Abramson, H.N., Chu, W.H., and Kana, D.D., "Some Studies of Nonlateral Sloshing in Rigid Containers", *Transactions of the ASME*, Journal of Applied Mechanics, Vol. 33, 1966, pp. 777-784.

[66] Chen, P.Y., "On the Nonlinear Oscillations of Fluids in a Rigid Container with Application to Vibration Reduction", *Georgia Institute of Technology*, Ph.D Thesis, 1970.

[67] Miles, J.W., "Nonlinear Surface Waves in Closed Basins", *Journal of Fluid Mechanics*, Vol. 75, Part 13, 1976, pp. 419-448.

[68] Whitham, G.B., "A General Approach to Linear and Nonlinear Dispersive

Waves Using a Lagrangian", *Journal of Fluid Mechanics*, Vol. 22, Part 2, 1965, pp. 273-283.

[69] Luke, J.C., "A Variational Principle for a Fluid with a Free Surface", *Journal of Fluid Mechanics*, Vol. 27, Part 2, 1967, pp. 395-397.

[70] Seliger, R.L., and Whitham, G.B., "Variational Principles in Continuum Mechanics", *Proceedings of the Royal Society of London*, Series A, Vol. 305, 1968, pp. 1-25.

[71] Miles, J.W., "Resonantly Forced Surface Waves in a Circular Cylinder", *Journal of Fluid Mechanics*, Vol. 149, 1984, pp. 15-31.

[72] Miles, J.W., "Internally Resonant Surface Waves in a Circular Cylinder", *Journal of Fluid Mechanics*, Vol. 149, 1984, pp. 1-14.

[73] Benney, D.J., "Nonlinear Gravity Wave Interaction", *Journal of Fluid Mechanics*, Vol. 14, Part 4, 1962, pp. 577-584.

[74] Bretherton, F.P., "Resonant Interactions between Waves. The Case of Discrete Oscillations". *Journal of Fluid Mechanics*, Vol. 20, Part 3, 1964, pp. 457-479.

[75] McGolrick, L.F., "On Wilton's Ripples: A Special Case of Resonant Interactions", *Journal of Fluid Mechanics*, Vol. 42, Part 1, 1970, pp. 193-200.

[76] Philips, O.M., "Wave Interactions - The Evolution of an Idea", *Journal of Fluid Mechanics*, Vol. 106, 1981, pp. 215-227.

[77] Ibrahim, R.A., and Barr, A.D.S., "Autoparametric Resonance in a Structure Containing Liquid, Part 1: Two Mode Interaction", *Journal of Sound and Vibration*, Vol. 42, Part 2, 1975, pp. 159-179.

[78] Isaacson, L.K., and Marshall, A.S.G., "Nonlinear Resonant Interactions in Cavity Flows", *AIAA Journal*, Vol. 21, No. 5, 1983, pp. 785-786.

[79] Hunt, J.N., "Viscous Damping of Waves over an Inclined Bed in a Channel of Finite Width", *La Houille Blanche*, Vol. 7, 1952, pp. 836-842.

[80] Ursell, F., "Edge Waves on a Sloping Beach", *Proceedings of the Royal Society of London*, Series A, Vol. 214, 1952, pp. 79-97.

[81] Case, K.M., and Parkinson, W.C., "Damping of Surface Waves in an Incompressible Liquid", *Journal of Fluid Mechanics*, Vol. 2, Part 2, 1957, pp. 172-184.

[82] Miles, J.W., "Surface Waves in Closed Basins", *Proceedings of the Royal Society of London*, Series A, Vol. 297, 1967, pp. 459-475.

[83] Su, T.C., "The Effect of Viscosity on Free Oscillations of Fluid-Filled Spherical Shells", *Journal of Sound and Vibration*, Vol. 74, Part 2, 1981, pp. 205-220.

[84] Mahony, J.J., and Pritchard, W.G., "Wave Reflection from Beaches", *Journal of Fluid Mechanics*, Vol. 101, Part 4, 1980, pp. 809-832.

[85] Johnson, R.E., "On the Transverse Secondary Flow in Wave Channels", *Transactions of the ASME*, Journal of Applied Mechanics, Vol. 50, 1983, pp. 244-250.

[86] Das, K.P., "A Korteweg-de-Vries Equation Modified by Viscosity for Waves in a Channel of Uniform but Arbitrary Cross-Section", *Physics of Fluids*, Vol. 28, Part 3, 1985, pp. 770-775.

[87] Silviera, A.M., Stephens, D.G., and Leonard, H.W., "An Experimental Investigation of Liquid Oscillations in Tanks with Various Baffles", *NASA Technical Note D-715*, Washington, 1961.

[88] Stephens, D.G., Leonard, H.W., and Perry, T.W.P., "Investigation of the Damping of Liquids in Right-Circular Cylindrical Tanks, Including the Effect of a Time Variant Depth", *NASA Technical Note D-1367*, Washington, 1962.

[89] Summer, I.E., and Stophan, A.J., "An Experimental Investigation of the Viscous Liquid Sloshing in Spherical Tanks", *NASA Technical Note D-1991*, Washington, 1963.

[90] Welt, F., "A Parametric Study of Nutation Dampers", *University of British Columbia*, M.A.Sc. Thesis, 1983.

[91] Griffin, O.M., "Vibrations and Flow-Induced Forces Caused by Vortex Shedding", *Proceedings of the ASME Joint Multidivisional Symposium on Flow-Induced Vibrations*, 1984, ASME Winter Annual Meeting, New Orleans, Louisiana, Dec. 1984, Vol. 1, 1984, pp. 1-13.

[92] Adami, H., and Batch, B.A., "Aeolian Vibrations of Turbulent Busbars in Outdoor Substations",*Electra*, No. 75, 1981, pp. 99-120.

[93] Parkinson, G.V., and Smith, J.D., "The Square Prism as an Aeroelastic Non-Linear Oscillator", *Quarterly Journal of Applied Mathematics*, Vol. 17, No. 2, pp. 225-239.

[94] Sullivan, P., "Aeroelastic Galloping of Tall Structures in Simulated Wind", *University of British Columbia*, M.A.Sc. Thesis, 1977.

[95] Bajkowski, J., and Szemplinska-Stupnika, W., "Internal Resonance - Simulation versus Analytical Results", *Journal of Sound and Vibration*, Vol. 104, Part 2, 1986, pp. 259-275.

[96] Lamb, H., "Viscosity", *Hydrodynamics*, Chapter 9, Dover Publication Inc., 1945, pp. 581.

[97] Bearman, P.W., Gartshore, I.S., Maull, D.J., and Parkinson, G.V., "Experiments on Flow-Induced Vibration of a Square-Section Cylinder", *Proceedings of the ASME Joint Multidivisional Symposium on Flow-Induced Vibrations*, 1984,

ASME Winter Annual Meeting, New Orleans, Louisiana, Dec. 1984, Vol. 1, pp. 85-101.

[98] Stansby, P.K., "The Effect of End Plates on the Base Pressure Coefficient of a Circular Cylinder", *Aeronautical Journal*, 1974, pp. 36-37.

[99] Wawzonek, M., "Aeroelastic Behavior of Square Prisms in a Uniform Flow", *University of British Columbia*, M.A.Sc. Thesis, 1977.

[100] Brooks, P.N.H., "Experimental Investigation of the Aeroelastic Instability of Bluff Two-Dimensional Cylinders", *University of British Columbia*, M.A.Sc. Thesis, 1960.

[101] Diana, G, and Falco, M., "On the Forces Transmitted to a Vibrating Cylinder by a Blowing Fluid", *Meccanica*, Vol. 6, 1971, pp. 9-22.

[102] Hartlen, R.T., and Currie, I.G., "Lift Oscillator Model of Vortex-Induced Vibration", *Journal of Mechanics Division*, Proceedings of the American Society of Civil Engineering, Vol. 96, No. EM5, 1970, pp. 577-591.

[103] Feng, C.C., "The Measurement of Vortex-Induced Effect Past Stationary and Oscillating Circular and D-Section Cylinders", *University of British Columbia*, M.A.Sc. Thesis, 1968.

[104] Obasaju, E.D., "Forced Vibration Study of the Aeroelastic Instability of a Square Section near Resonance", *Journal of Wind Engineering and Industrial Aerodynamics*, Vol. 12, 1983, pp. 313-327.

[105] Sakamoto, M., and Arie, M., "Vortex Shedding from a Rectangular Prism and a Circular Cylinder Placed Vertically in a Turbulent Boundary Layer", *Journal of Fluid Mechanics*, Vol. 126, 1983, pp. 147-165.

[106] Nakamura, Y., and Ohya, Y., "Vortex Shedding from Square Prisms in Smooth and Turbulent Flows", *Journal of Fluid Mechanics*, Vol. 164, 1986, pp. 77-89.

[107] Bokaian, A., and Geoola, F., "Effect of Vortex Shedding on Nearly Galloping Instability", *Journal of Engineering Mechanics*, The American Society of Civil Engineering, Vol. 11, No. 3, 1985, pp. 329-345.

[108] Jordan, D.W., and Smith, P., "Forced Oscillations: Harmonic and Subharmonic Response, Stability, Entrainment", *Nonlinear Differential Equations*, Chapter 7, Clarendon Press, Oxford, 1977, pp. 180-187.

[109] Telionis, D.P., "Oscillations with Zero Means", *Unsteady Viscous Flows*, Chapter 4, Springer-Verlag New York Inc., 1981, pp. 162-179.

[110] Harris, C.M., and Crede, C.E., "Dynamic Vibration Absorbers and Auxiliary Mass Dampers", *Shock and Vibration Handbook, 2nd Edition*, Chapter 6, McGraw Hill, 1976, pp. 8-11.

[111] Parkinson, G.V., "Mathematical Models of Flow-Induced Vibrations", *Flow-Induced Structural Vibrations*, IUTAM-IAH Symposium, Karlsrule, 1972, pp. 81-127.

[112] Vickery, B.J., and Basu, R., "Simplified Approach to the Evaluation of an Across-Wind Response of Chimneys", *Journal of Wind Engineering and Industrial Aerodynamics*, Vol. 14, 1983, pp. 153-166.

[113] Basu, R.I., and Vickery, B.J., "Across-Wind Vibrations of Structures of Circular Cross-Section. Part II. Development of a Mathematical Model for Full-Scale Application", *Journal of Wind Engineering and Industrial Aerodynamics*, Vol. 12, 1983, pp. 75-97.

[114] Vickery, B.J., Isyumov, N., and Davenport, A.G., "The Role of Damping, Mass and Stiffness in the Reduction of Wind Effects on Structures", *Journal of Wind Engineering and Industrial Aerodynamics*, Vol. 11, 1983, pp. 285-294.

APPENDIX I: NONLINEAR FREE SURFACE CONDITION

1. Basic Equation

In polar coordinates, the kinematic boundary condition:

$$\frac{\partial \eta_f}{\partial t} + \frac{\partial \tilde{\Phi}}{\partial r}\frac{\partial \eta_f}{\partial r} + \frac{1}{r^2}\frac{\partial \tilde{\Phi}}{\partial \theta}\frac{\partial \eta_f}{\partial \theta} = \frac{\partial \tilde{\Phi}}{\partial z}; \tag{I.1}$$

and the Bernouilli's equation applied to the free surface (i.e., $z = \eta_f$)

$$gz + \frac{\partial \tilde{\Phi}}{\partial t} + \frac{1}{2}(\nabla\tilde{\Phi})^2 = -\frac{\partial^2 x}{\partial t^2} r\cos\theta; \tag{I.2}$$

can be combined by eliminating η_f explicitly. This yields the following expression at $z = \eta_f$[63]

$$\begin{aligned}
&\frac{\partial^2 \tilde{\Phi}}{\partial t^2} + g\frac{\partial \tilde{\Phi}}{\partial z} + 2\frac{\partial \tilde{\Phi}}{\partial r}\frac{\partial^2 \tilde{\Phi}}{\partial r \partial t} + \frac{2}{r^2}\frac{\partial \tilde{\Phi}}{\partial \theta}\frac{\partial^2 \tilde{\Phi}}{\partial \theta \partial t} + 2\frac{\partial \tilde{\Phi}}{\partial z}\frac{\partial^2 \tilde{\Phi}}{\partial t \partial z} + (\frac{\partial \tilde{\Phi}}{\partial r})^2\frac{\partial^2 \tilde{\Phi}}{\partial r^2} \\
&+(\frac{\partial \tilde{\Phi}}{\partial z})^2\frac{\partial^2 \tilde{\Phi}}{\partial z^2} + \frac{1}{r^4}(\frac{\partial \tilde{\Phi}}{\partial \theta})^2\frac{\partial^2 \tilde{\Phi}}{\partial \theta^2} - \frac{1}{r^3}\frac{\partial \tilde{\Phi}}{\partial r}(\frac{\partial \tilde{\Phi}}{\partial \theta})^2 + \frac{2}{r^2}\frac{\partial \tilde{\Phi}}{\partial r}\frac{\partial \tilde{\Phi}}{\partial \theta}\frac{\partial^2 \tilde{\Phi}}{\partial \theta \partial r} \\
&+2\frac{\partial \tilde{\Phi}}{\partial r}\frac{\partial \tilde{\Phi}}{\partial z}\frac{\partial^2 \tilde{\Phi}}{\partial z \partial r} + \frac{2}{r^2}\frac{\partial \tilde{\Phi}}{\partial \theta}\frac{\partial \tilde{\Phi}}{\partial z}\frac{\partial^2 \tilde{\Phi}}{\partial \theta \partial z} \\
&\qquad = -\frac{\partial^3 x}{\partial t^3} r\cos\theta + \frac{\partial^2 x}{\partial t^2}[\frac{1}{r}\frac{\partial \tilde{\Phi}}{\partial \theta}\sin\theta - \frac{\partial \tilde{\Phi}}{\partial r}\cos\theta].
\end{aligned} \tag{I.3}$$

2. Perturbation Series Expansion

Introducing:

$$\tilde{\Phi} = \epsilon^q\tilde{\Phi}^{(1)} + \epsilon^{2q}\tilde{\Phi}^{(2)} + \epsilon^{3q}\tilde{\Phi}^{(3)} + ...; \tag{I.4}$$

$$\eta_f = \epsilon^q\eta_f^{(1)} + \epsilon^{2q}\eta_f^{(2)} + \epsilon^{3q}\eta_f^{(3)} + ...; \tag{I.5}$$

and substituting into (I.2) gives $\eta_f^{(1)}$, $\eta_f^{(2)}$ and $\eta_f^{(3)}$ in terms of $\tilde{\Phi}^{(1)}$, $\tilde{\Phi}^{(2)}$, and $\tilde{\Phi}^{(3)}$. By using a Taylor series expansion around $z = \eta_f$ as

$$\tilde{\Phi}_{z=\eta_f} = \tilde{\Phi}_{z=0} + \eta_f\frac{\partial \tilde{\Phi}}{\partial z}|_{z=0} + \frac{1}{2}\eta_f^2\frac{\partial^2 \tilde{\Phi}}{\partial z^2}|_{z=0} + ..., \tag{I.6}$$

and replacing for η_f (section I.3) gives an expression for $\tilde{\Phi}_{z=\eta_f}$ in terms of $\tilde{\Phi}_{z=0}$, needed to get the full nonlinear free surface conditions. Relation (I.3) then reduces to

$$\epsilon^q A^{(1)} + \epsilon^{2q}A^{(2)} + \epsilon^{3q}A^{(3)} = 0 + ...$$

at $z=0$, or expressed in dimensionless form:

$$A^{(1)} = \frac{\partial^2\hat{\Phi}^{(1)}}{\partial\tau^2} + \frac{1}{\alpha_{11}\lambda_{11}}\frac{\partial\hat{\Phi}^{(1)}}{\partial\hat{z}}; \tag{I.7}$$

$$\begin{aligned}A^{(2)} =& \frac{\partial^2\hat{\Phi}^{(2)}}{\partial\tau^2} + \frac{1}{\alpha_{11}\lambda_{11}}\frac{\partial\hat{\Phi}^{(2)}}{\partial\hat{z}} + 2\frac{\partial\hat{\Phi}^{(1)}}{\partial\hat{r}}\frac{\partial^2\hat{\Phi}^{(1)}}{\partial\hat{r}\partial\tau} + \frac{2}{\hat{r}^2}\frac{\partial\hat{\Phi}^{(1)}}{\partial\theta}\frac{\partial^2\hat{\Phi}^{(1)}}{\partial\theta\partial\tau}\\ &+ 2\frac{\partial\hat{\Phi}^{(1)}}{\partial\hat{z}}\frac{\partial^2\hat{\Phi}^{(1)}}{\partial\hat{z}\partial\tau} - \alpha_{11}\lambda_{11}\frac{\partial\hat{\Phi}^{(1)}}{\partial\tau}\left(\frac{\partial^3\hat{\Phi}^{(1)}}{\partial\hat{z}\partial\tau^2} + \frac{1}{\alpha_{11}\lambda_{11}}\frac{\partial^2\hat{\Phi}^{(1)}}{\partial\hat{z}^2}\right);\end{aligned} \tag{I.8}$$

$$\begin{aligned}A^{(3)} =& \frac{\partial^2\hat{\Phi}^{(3)}}{\partial\tau^2} + \frac{1}{\alpha_{11}\lambda_{11}}\frac{\partial\hat{\Phi}^{(3)}}{\partial\hat{z}} + 2\left[\frac{\partial\hat{\Phi}^{(1)}}{\partial\hat{r}}\frac{\partial^2\hat{\Phi}^{(2)}}{\partial\hat{r}\partial\tau} + \frac{\partial\hat{\Phi}^{(2)}}{\partial\hat{r}}\frac{\partial^2\hat{\Phi}^{(1)}}{\partial\hat{r}\partial\tau}\right]+\\ &\frac{2}{\hat{r}^2}\left[\frac{\partial\hat{\Phi}^{(1)}}{\partial\theta}\frac{\partial^2\hat{\Phi}^{(2)}}{\partial\theta\partial\tau} + \frac{\partial\hat{\Phi}^{(2)}}{\partial\theta}\frac{\partial^2\hat{\Phi}^{(1)}}{\partial\theta\partial\tau}\right] + 2\left[\frac{\partial\hat{\Phi}^{(1)}}{\partial\hat{z}}\frac{\partial^2\hat{\Phi}^{(2)}}{\partial\hat{z}\partial\tau} + \frac{\partial\hat{\Phi}^{(2)}}{\partial\hat{z}}\frac{\partial^2\hat{\Phi}^{(1)}}{\partial\hat{z}\partial\tau}\right.\\ &- \alpha_{11}\lambda_{11}\left\{\frac{\partial\hat{\Phi}^{(1)}}{\partial\tau}\left[\frac{\partial^3\hat{\Phi}^{(2)}}{\partial\hat{z}\partial\tau^2} + \frac{1}{\alpha_{11}\lambda_{11}}\frac{\partial^2\hat{\Phi}^{(2)}}{\partial\hat{z}^2}\right] + \frac{\partial\hat{\Phi}^{(2)}}{\partial\tau}\left[\frac{\partial^3\hat{\Phi}^{(1)}}{\partial\hat{z}\partial\tau^2}\right.\right.\\ &\left.\left.+ \frac{1}{\alpha_{11}\lambda_{11}}\frac{\partial^2\hat{\Phi}^{(1)}}{\partial\hat{z}^2}\right]\right\} + \left(\frac{\partial\hat{\Phi}^{(1)}}{\partial\hat{r}}\right)^2\frac{\partial^2\hat{\Phi}^{(1)}}{\partial\hat{r}^2} + \frac{1}{\hat{r}^4}\left(\frac{\partial\hat{\Phi}^{(1)}}{\partial\theta}\right)^2\frac{\partial^2\hat{\Phi}^{(1)}}{\partial\theta^2}\\ &+ \left(\frac{\partial\hat{\Phi}^{(1)}}{\partial\hat{z}}\right)^2\frac{\partial^2\hat{\Phi}^{(1)}}{\partial\hat{z}^2} - \frac{1}{\hat{r}^3}\frac{\partial\hat{\Phi}^{(1)}}{\partial\hat{r}}\left(\frac{\partial\hat{\Phi}^{(1)}}{\partial\theta}\right)^2 + 2\frac{\partial\hat{\Phi}^{(1)}}{\partial\hat{r}}\frac{\partial\hat{\Phi}^{(1)}}{\partial\hat{z}}\frac{\partial^2\hat{\Phi}^{(1)}}{\partial\hat{r}\partial\hat{z}}\\ &+ \frac{2}{\hat{r}^2}\frac{\partial\hat{\Phi}^{(1)}}{\partial\hat{r}}\frac{\partial\hat{\Phi}^{(1)}}{\partial\theta}\frac{\partial^2\hat{\Phi}^{(1)}}{\partial\hat{r}\partial\theta} + \frac{2}{\hat{r}^2}\frac{\partial\hat{\Phi}^{(1)}}{\partial\hat{z}}\frac{\partial\hat{\Phi}^{(1)}}{\partial\theta}\frac{\partial^2\hat{\Phi}^{(1)}}{\partial\hat{z}\partial\theta} - \frac{\alpha_{11}\lambda_{11}}{2}\left[\frac{\partial^3\hat{\Phi}^{(1)}}{\partial\hat{z}\partial\tau^2}\right.\\ &\left.+ \frac{1}{\alpha_{11}\lambda_{11}}\frac{\partial^2\hat{\Phi}^{(1)}}{\partial\hat{z}^2}\right]\left[\left(\frac{\partial\hat{\Phi}^{(1)}}{\partial\hat{r}}\right)^2 + \frac{1}{\hat{r}^2}\left(\frac{\partial\hat{\Phi}^{(1)}}{\partial\theta}\right)^2 + \left(\frac{\partial\hat{\Phi}^{(1)}}{\partial\hat{z}}\right)^2\right]\\ &- \alpha_{11}\lambda_{11}\left\{2\frac{\partial\hat{\Phi}^{(1)}}{\partial\tau}\left[\frac{\partial^2\hat{\Phi}^{(1)}}{\partial\hat{r}\partial\hat{z}}\frac{\partial^2\hat{\Phi}^{(1)}}{\partial\hat{r}\partial\tau} + \frac{\partial\hat{\Phi}^{(1)}}{\partial\hat{r}}\frac{\partial^3\hat{\Phi}^{(1)}}{\partial\hat{z}\partial\hat{r}\partial\tau} + \frac{1}{\hat{r}^2}\frac{\partial^2\hat{\Phi}^{(1)}}{\partial\hat{z}\partial\theta}\frac{\partial^2\hat{\Phi}^{(1)}}{\partial\theta\partial\tau}\right.\right.\\ &\left.\left.+ \frac{1}{\hat{r}^2}\frac{\partial\hat{\Phi}^{(1)}}{\partial\theta}\frac{\partial^3\hat{\Phi}^{(1)}}{\partial\hat{z}\partial\theta\partial\tau} + \frac{\partial^2\hat{\Phi}^{(1)}}{\partial\hat{z}^2}\frac{\partial^2\hat{\Phi}^{(1)}}{\partial\hat{z}\partial\tau} + \frac{\partial\hat{\Phi}^{(1)}}{\partial\hat{z}}\frac{\partial^3\hat{\Phi}^{(1)}}{\partial\hat{z}^2\partial\tau}\right]\right\}\\ &+ (\alpha_{11}\lambda_{11})^2\left\{\left[\frac{\partial^3\hat{\Phi}^{(1)}}{\partial\hat{z}\partial\tau^2} + \frac{1}{\alpha_{11}\lambda_{11}}\frac{\partial^2\hat{\Phi}^{(1)}}{\partial\hat{z}^2}\right]\frac{\partial\hat{\Phi}^{(1)}}{\partial\tau}\frac{\partial^2\hat{\Phi}^{(1)}}{\partial\hat{z}\partial\tau} + \left[\frac{\partial^4\hat{\Phi}^{(1)}}{\partial\hat{z}^2\partial\tau^2}\right.\right.\\ &\left.\left.+ \frac{1}{\alpha_{11}\lambda_{11}}\frac{\partial^3\hat{\Phi}^{(1)}}{\partial\hat{z}^3}\right]\frac{\partial\hat{\Phi}^{(1)}}{\partial\tau}\right\} + \hat{r}\hat{\omega}^2\cos\theta\cos\hat{\omega}\tau.\end{aligned} \tag{I.9}$$

3 Free Surface Equation

Using expressions (I.2), (I.4), (I.5) and (I.6), and using nondimensional parameter $\hat{\eta}_f = \frac{\eta_f}{R_0}$, results in

$$\begin{aligned}\hat{\eta}_f =& \hat{\epsilon}^q\alpha_{11}\lambda_{11}\left[s_i\hat{\omega}\hat{r}\cos\theta\cos\hat{\omega}\tau - \frac{\partial\hat{\Phi}^{(1)}}{\partial\tau}\right] - \hat{\epsilon}^{2q}\alpha_{11}\lambda_{11}\left[\frac{\partial\hat{\Phi}^{(2)}}{\partial\tau}\right.\\ &\left.+ \alpha_{11}\lambda_{11}\left(s_i\hat{\omega}\hat{r}\cos\theta\cos\hat{\omega}\tau - \frac{\partial\hat{\Phi}^{(1)}}{\partial\tau}\right)\frac{\partial^2\hat{\Phi}^{(1)}}{\partial\hat{z}\partial\tau} + \frac{1}{2}(\nabla\hat{\Phi}^{(1)})^2\right] + \ldots,\end{aligned} \tag{I.10}$$

where $s_i = 1$ for $q = 1$, and zero otherwise, and $\hat{z} = 0$.

APPENDIX II: NONLINEAR, NONRESONANT POTENTIAL FLOW SOLUTION

1. Second Order Terms

Substituting for

$$\hat{\Phi}^{(1)} = \sum_i f_{1i} C_1(\lambda_{1i}\hat{r}) \frac{\cosh \lambda_{1i}(\hat{z}+\hat{h})}{\cosh \lambda_{1i}\hat{h}} \cos\theta \cos\hat{\omega}\tau$$

into the second order free surface boundary condition (relation I.8) and rearranging yields,

$$\begin{aligned}\frac{\partial^2 \hat{\Phi}^{(2)}}{\partial \tau^2} + \frac{1}{\alpha_{11}\lambda_{11}} \frac{\partial \hat{\Phi}^{(2)}}{\partial \hat{z}} = \sum_i \sum_j \frac{f_{1i} f_{1j}}{2} \Big\{ & [C_1'(\lambda_{1i}\hat{r}) C_1'(\lambda_{1j}\hat{r}) \\ & + \frac{1}{\hat{r}^2} C_1(\lambda_{1i}\hat{r}) C_1(\lambda_{1j}\hat{r}) + AK_{ij} C_1(\lambda_{1i}\hat{r}) C_1(\lambda_{1j}\hat{r})] \\ & + [C_1'(\lambda_{1i}\hat{r}) C_1'(\lambda_{1j}\hat{r}) - \frac{1}{\hat{r}^2} C_1(\lambda_{1i}\hat{r}) C_1(\lambda_{1j}\hat{r}) \\ & + AK_{ij} C_1(\lambda_{1i}\hat{r}) C_1(\lambda_{1j}\hat{r})] \cos 2\theta \Big\} \sin 2\hat{\omega}\tau. \qquad (II.1)\end{aligned}$$

Assuming $\hat{\Phi}^{(2)} = \sum_m \sum_n f_{nm} C_n(\lambda_{nm}\hat{r}) \frac{\cosh \lambda_{nm}(\hat{z}+\hat{h})}{\cosh \lambda_{nm}\hat{h}} \cos n\theta \sin p\hat{\omega}\tau$, and integrating $(II.1)$ as

$$\int_a^1 (II.1) C_n(\lambda_{nm}\hat{r}) \hat{r} d\hat{r}$$

to use Bessel function orthogonality condition (Appendix V.1), it is found that

$$\begin{aligned}\hat{\Phi}^{(2)} = \sum_n \Big\{ & f_{0n} C_0(\lambda_{0n}\hat{r}) \frac{\cosh \lambda_{0n}(\hat{z}+\hat{h})}{\cosh \lambda_{0n}\hat{h}} \\ & + f_{2n} C_2(\lambda_{2n}\hat{r}) \frac{\cosh \lambda_{2n}(\hat{z}+\hat{h})}{\cosh \lambda_{2n}\hat{h}} \cos 2\theta \Big\} \sin 2\hat{\omega}\tau, \qquad (II.2)\end{aligned}$$

where:

$$f_{2n} = \sum_i \sum_j f_{1i} f_{1j} \Omega_{0n},$$

$$\text{for} \quad \Omega_{0n} = \frac{[LL_{110}(i,j,n) + JJ_{110}(i,j,n) + AK_{ij} KK_{110}(i,j,n)]}{2\hat{\omega}[(\hat{\omega}_{0n}/\hat{\omega})^2 - 4]\Lambda_{0n}};$$

$$\text{and} \quad f_{2n} = \sum_i \sum_j f_{1i} f_{1j} \Omega_{2n},$$

$$\text{for} \quad \Omega_{2n} = \frac{[LL_{112}(i,j,n) - JJ_{112}(i,j,n) + AK_{ij} KK_{112}(i,j,n)]}{2\hat{\omega}[(\hat{\omega}_{2n}/\hat{\omega})^2 - 4]\Lambda_{2n}/\lambda_{2n}^2}.$$

Here LL's, JJ's and KK's are Bessel function triple product integrals, Λ's are coefficients related to $\int C_n^2(\lambda_{nm}\hat{r})\hat{r}d\hat{r}$ as defined in Appendix V.1.2, and

$$AK_{ij} = \alpha_{1i}\alpha_{1j}\lambda_{1i}\lambda_{1j} + \hat{\omega}^2\frac{\alpha_{11}\alpha_{1j}\lambda_{11}\lambda_{1j}}{2} - \frac{1}{2}\lambda_{1j}^2. \qquad (II.3)$$

It can be shown quite readily that the solution is singular for $(\hat{\omega}_{ln}/\hat{\omega})^2 - 4 = 0$ $(l = 0, 2)$, as f_{0n} and f_{2n} become unbounded. Furthermore, it is of order $\hat{\epsilon}^{-1}$ for $(\hat{\omega}_{ln}/\hat{\omega})^2 - 4 = \nu_0\hat{\epsilon}$, where ν_0 is of order 1, a condition that makes the original perturbation series expansion invalid as some of the terms are now of the 1st order. Expression (II.2) thus only applies for:

$$(\frac{\hat{\omega}_{ln}}{\hat{\omega}})^2 - 4 > \nu_0\hat{\epsilon}; \qquad (II.4)$$

$$\text{or,} \quad |\frac{\hat{\omega}_{ln}}{\hat{\omega}} - 2| > \frac{\nu_0\hat{\epsilon}}{4}. \qquad (II.5)$$

2. Stability and 3rd Order Equation

A standard stability analysis assumes a general 1st order solution of the form[108],

$$\hat{\Phi}^{(1)} = \sum_i [(e_{1i}\cos\theta + e_{3i}\sin\theta)\cos\hat{\omega}\tau + (e_{2i}\cos\theta + e_{4i}\sin\theta)\sin\hat{\omega}\tau]C_1(\lambda_{1i}\hat{r})\frac{\cosh\lambda_{1i}(\hat{z}+\hat{h})}{\cosh\lambda_{1i}\hat{h}},$$

where e_{1i}, e_{2i}, e_{3i} and e_{4i} are function of the slow time scale $\tau_2 = \hat{\epsilon}\tau$, thus following a procedure similar to Hutton's theory of resonant oscillations in circular cylinders[63]. Subsequent substitutions into (I.8) and (I.9) lead to the 3rd order system of equations:

$$\Big\{\frac{de_{1i}}{d\tau_2} + p_{2n} + D_1\sum_i e_{2i}[\sum_j\sum_k(e_{1j}e_{1k} + e_{2j}e_{2k} + e_{3j}e_{3k} + e_{4j}e_{4k})] + DD_1\sum_i e_{3i}[\sum_j\sum_k(e_{2j}e_{3k} - e_{1j}e_{4k}]\Big\}\cos\theta\sin\hat{\omega}\tau = 0;$$

$$\Big\{\frac{de_{2i}}{d\tau_2} + p_{1n} - D_1\sum_i e_{1i}[\sum_j\sum_k(e_{1j}e_{1k} + e_{2j}e_{2k} + e_{3j}e_{3k} + e_{4j}e_{4k}] + DD_1\sum_i e_{4i}[\sum_j\sum_k(e_{2j}e_{3k} - e_{1j}e_{4k})]\Big\}\cos\theta\cos\hat{\omega}\tau = 0;$$

$$\Big\{\frac{de_{3i}}{d\tau_2} + p_{4n} - D_1\sum_i e_{4i}[\sum_j\sum_k(e_{1j}e_{1k} + e_{2j}e_{2k} + e_{3j}e_{3k} + e_{4j}e_{4k}] + DD_1\sum_i e_{1i}[\sum_j\sum_k(e_{2j}e_{3k} - e_{1j}e_{4k})]\Big\}\sin\theta\cos\hat{\omega}\tau = 0;$$

$$\left\{\frac{de_{4i}}{d\tau_2} + p_{3n} + D_1 \sum_i e_{3i}[\sum_j \sum_k (e_{1j}e_{1k} + e_{2j}e_{2k} + e_{3j}e_{3k} + e_{4j}e_{4k})] + DD_1 \sum_i e_{2i}[\sum_j \sum_k (e_{2j}e_{3k} - e_{1j}e_{4k})]\right\} \sin\theta \sin\hat{\omega}\tau = 0.$$

Here D_1 and DD_1 are complicated, frequency dependent expressions otherwise similar to K_1 and KK_1 of Appendix III.1, while p_{1n},..., p_{4n} are the third order terms:

$$p_{1n} = D_1 \sum_i \sum_j \sum_k e_{1i}e_{1j}e_{1k}; \qquad p_{2n} = p_{3n} = p_{4n} = 0. \tag{II.4}$$

The stability of the solution previously derived is studied by considering a disturbance in the ith mode such as:

$$e_{1i} = f_{1i} + A_1 e^{\lambda\tau_2}; \quad e_{2i} = A_2 e^{\lambda\tau_2}; \quad e_{3i} = A_3 e^{\lambda\tau_2}; \quad \text{and} \quad e_{4i} + A_4 e^{\lambda\tau_2}.$$

Substituting into (II.4) leads to the following conditions:

$$\lambda^2 = -3(D_1 f_{1i}^2)^2; \tag{II.5}$$

$$\lambda^2 = -(f_{1i}^2)^2[D_1(D_1 - D_{11})]. \tag{II.6}$$

The solution is stable for nonpositive real part of λ and requires $D_1(D_1 - D_{11}) > 0$ in (II.6).

APPENDIX III: NONLINEAR, RESONANT POTENTIAL FLOW SOLUTION

1. No Interactions

Using Hutton's theory for a circular cylinder[63] and substituting for the Bessel function solution of the torus problem, it is found that:

- Detuning parameter:

$$\nu_1 = 0; \qquad \nu_2 = \nu = \frac{\hat{\omega}^2 - 1}{\hat{\omega}^2 \hat{\epsilon}^{2/3}}. \tag{III.1}$$

- Coefficients of the 3rd order equation for f_{11}:

$$F_1 = \frac{C_1(\lambda_{11}) - aC_1(\lambda_{11}a)}{\Lambda_{11}}; \qquad K_1 = \frac{\lambda_{11}^2}{\Lambda_{11}}[SUM1 + G1]; \qquad KK_1 = \frac{\lambda_{11}^2}{\Lambda_{11}}[SUM2 + G2], \tag{III.2}$$

where:

$$SUM1 = \frac{1}{32}\Big\{-18I_1(1,1,1,1) + \lambda_{11}^2(3 - 7\alpha_{11}^2)I_2(1,1,1,1) + 3\lambda_{11}^4\alpha_{11}^2(3 - \alpha_{11}^2)I_3(1,1,1,1) + 6I_4(1,1,1,1) + 3\lambda_{11}^2(3 - 7\alpha_{11}^2)I_5(1,1,1,1) - 12I_6(1,1,1,1) + 6I_7(1,1,1,1)\Big\};$$

$$SUM2 = \frac{1}{16}\Big\{-6I_1(1,1,1,1) + \lambda_{11}^2(1 + 19\lambda_{11}^2)I_2(1,1,1,1) + \lambda_{11}^4\alpha_{11}^2(3 - \alpha_{11}^2)I_3(1,1,1,1) + 2I_4(1,1,1,1) + \lambda_{11}^2(3 - 7\alpha_{11}^2)I_5(1,1,1,1) - 4I_6(1,1,1,1) + 2I_7(1,1,1,1)\Big\};$$

$$G1 = \sum_n\Big\{[CK_1KK_{101}(1,n,1) - II_{101}(1,n,1)]\Omega_{0n} + [\frac{CK_2}{2}KK_{121}(1,n,1) - \frac{1}{2}II_{121}(1,n,1) - JJ_{121}(1,n,1)]\Omega_{2n}\Big\};$$

$$G2 = \sum_n\Big\{[CK_1KK_{101}(1,n,1) - 2II_{101}(1,n,1)]2\Omega_{0n} + [-CK_2KK_{121}(1,n,1) + II_{1,2,1}(1,n,1) + 2JJ_{121}(1,n,1)]\Omega_{2n}\Big\};$$

Here I_1, I_2,...,I_7 are Bessel function multiple product integrals defined in Appendix V.1.2 with:

$$\Omega_{0n} = \frac{f_{0n}}{f_{11}^2}; \quad \Omega_{2n} = \frac{f_{2n}}{f_{11}^2};$$

and

$$CK_1 = \alpha_{0n}\alpha_{11}\lambda_{0n}\lambda_{11} - \frac{1}{2}\lambda_{0n}^2 + \lambda_{11}^2(1-\alpha_{11}^2);$$
$$CK_2 = \alpha_{2n}\alpha_{11}\lambda_{2n}\lambda_{11} - \frac{1}{2}\lambda_{2n}^2 + \lambda_{11}(1-\alpha_{11}^2). \qquad (III.3)$$

- Coefficients for stability relations:

$$B = 4KK_1^2 f_{11}[f_{11}^3 + \frac{3KK_1 - 2K_1}{4KK_1^2}F_1];$$
$$C = 4KK_1^2(KK_1 - 2K_1)\frac{F_1}{f_{11}}(f_{11}^3 + \frac{F_1}{KK_1})[f_{11}^3 + \frac{K_1F_1}{2KK_1(KK_1-2K_1)}]. \qquad (III.4)$$

2. Resonant Interactions

2.1 Second Order Terms and Detuning Parameters

Substituting equalities (6) and (15) into (I.7), and (14) into (I.8) yield, after neglecting the amplitude time derivatives and phase angles, the following second order relation :

$$\begin{aligned}
&-\nu_1 f_{11} C_1(\lambda_{11}\hat{r})\cos\theta\cos\hat{\omega}\tau - \beta_1\varsigma_{21}C_2(\lambda_{21}\hat{r})\cos 2\theta\sin 2\hat{\omega}\tau \\
&+\frac{\partial^2\hat{\Phi}^{(2)}}{\partial\tau^2} + \frac{1}{\alpha_{11}\lambda_{11}}\frac{\partial\hat{\Phi}^{(2)}}{\partial\hat{z}} + \frac{f_{11}^2}{2}\Big\{[C_1'^2(\lambda_{11}\hat{r}) + \frac{C_1^2(\lambda_{11}\hat{r})}{\hat{r}^2} \\
&+AK_0C_1^2(\lambda_{11}\hat{r})] + [C_1'^2(\lambda_{11}\hat{r}) - \frac{C_1^2(\lambda_{11}\hat{r})}{\hat{r}^2} + AK_0C_1^2(\lambda_{11}\hat{r})]\cos 2\theta\Big\}\sin 2\hat{\omega}\tau \\
&+f_{11}\varsigma_{21}\Big\{\Big[[\frac{C_1'(\lambda_{11}\hat{r})C_2'(\lambda_{21}\hat{r})}{2} + \frac{C_1(\lambda_{11}\hat{r})C_2(\lambda_{21}\hat{r})}{\hat{r}^2} \\
&+AK_1\frac{C_1(\lambda_{11}\hat{r})C_2(\lambda_{21}\hat{r})}{2}]\cos\theta + [\frac{C_1'(\lambda_{11}\hat{r})C_2'(\lambda_{21}\hat{r})}{2} - \frac{C_1(\lambda_{11}\hat{r})C_2(\lambda_{21}\hat{r})}{\hat{r}^2} \\
&+AK_1\frac{C_1(\lambda_{11}\hat{r})C_2(\lambda_{21}\hat{r})}{2}]\cos 3\theta\Big]\cos\hat{\omega}\tau + \Big[[\frac{3C_1'(\lambda_{11}\hat{r})C_2'(\lambda_{21}\hat{r})}{2} \\
&+\frac{3C_1(\lambda_{11}\hat{r})C_2(\lambda_{21}\hat{r})}{\hat{r}^2} + AK_2\frac{C_1(\lambda_{11}\hat{r})C_2(\lambda_{21}\hat{r})}{2}]\cos\theta + [\frac{3C_1'(\lambda_{11}\hat{r})C_2'(\lambda_{21}\hat{r})}{2} \\
&-\frac{3C_1(\lambda_{11}\hat{r})C_2(\lambda_{21}\hat{r})}{\hat{r}^2} + AK_2\frac{C_1(\lambda_{11}\hat{r})C_2(\lambda_{21}\hat{r})}{2}]\cos 3\theta\Big]\cos 3\hat{\omega}\tau\Big\} \\
&+\varsigma_{21}^2\Big\{[C_2'^2(\lambda_{21}\hat{r}) + 4\frac{C_2^2(\lambda_{21}\hat{r})}{\hat{r}^2} + AK_3C_2^2(\lambda_{21}\hat{r})] + [C_2'^2(\lambda_{21}\hat{r}) - \frac{4C_2^2(\lambda_{21}\hat{r})}{\hat{r}^2} \\
&+AK_3C_2^2(\lambda_{21}\hat{r})]\cos 4\theta\Big\}\sin 4\hat{\omega}\tau = 0. \qquad (III.5)
\end{aligned}$$

Here:

$$AK_0 = \frac{(3\alpha_{11}^2 - 1)\lambda_{11}^2}{2};$$
$$AK_1 = (\alpha_{11}^2 - 1)\lambda_{11}^2 - \alpha_{11}\alpha_{21}\lambda_{11}\lambda_{21} + \frac{1}{2}\lambda_{21}^2;$$

$$AK_2 = (\alpha_{11}^2 - 1)\lambda_{11}^2 + 5\alpha_{11}\alpha_{21}\lambda_{11}\lambda_{21} - \lambda_{21}^2;$$
$$AK_3 = \frac{(-2\alpha_{21}^2 + 1)}{2}\lambda_{21}^2 + 2\alpha_{21}\alpha_{11}\lambda_{21}\lambda_{11}.$$

Assuming $\hat{\Phi}^{(2)} = \sum_m \sum_n \begin{pmatrix} d_{mn} \\ \\ e_{mn} \end{pmatrix} C_n(\lambda_{nm}\hat{r}) \frac{\cosh \lambda_{nm}(\hat{z}+\hat{h})}{\cosh \lambda_{nm}\hat{h}} \cos n\theta \begin{pmatrix} \cos p\hat{\omega}\tau \\ \\ \sin p\hat{\omega}\tau \end{pmatrix}$,
and integrating (III.5) as

$$\int_a^1 (III.5) C_n(\lambda_{nm}\hat{r})\hat{r}d\hat{r}$$

to use the Bessel function orthonogality condition as before, it is found that,

$$\hat{\Phi}^{(2)} = \hat{\Phi}_1^{(2)} + \hat{\Phi}_2^{(2)}, \tag{III.6}$$

where:

$\hat{\Phi}_1^{(2)}$ = no interaction solution, i.e. relation 12, with $n \geq 2$ in ψ_{2n};

$$\begin{aligned}
\hat{\Phi}_2^{(2)} = \sum_n \Big\{ & [d_{1n}C_1(\lambda_{1n}\hat{r}) \frac{\cosh \lambda_{1n}(\hat{z}+\hat{h})}{\cosh \lambda_{1n}\hat{h}} \cos\theta \\
& \quad + e_{1n}C_3(\lambda_{3n}\hat{r}) \frac{\cosh \lambda_{3n}(\hat{z}+\hat{h})}{\cosh \lambda_{3n}\hat{h}} \cos 3\theta] \cos \hat{\omega}\tau \\
& + [d_{3n}C_3(\lambda_{3n}\hat{r}) \frac{\cosh \lambda_{3n}(\hat{z}+\hat{h})}{\cosh \lambda_{3n}\hat{h}} \cos 3\theta \\
& \quad + e_{3n}C_1(\lambda_{1n}\hat{r}) \frac{\cosh \lambda_{1n}(\hat{z}+\hat{h})}{\cosh \lambda_{1n}\hat{h}} \cos\theta] \cos 3\hat{\omega}\tau \\
& + [d_{4n}C_4(\lambda_{4n}\hat{r}) \frac{\cosh \lambda_{4n}(\hat{z}+\hat{h})}{\cosh \lambda_{4n}\hat{h}} \cos 4\theta \\
& \quad + e_{4n}C_0(\lambda_{0n}\hat{r}) \frac{\cosh \lambda_{0n}(\hat{z}+\hat{h})}{\cosh \lambda_{0n}\hat{h}}] \sin 4\hat{\omega}\tau,
\end{aligned} \tag{III.7}$$

with:

$$d_{1n} = \Omega_{1n} f_{11}\varsigma_{21};$$
$$\Omega_{1n} = -\frac{[II_{121}(1,1,n) + JJ_{121}(1,1,n) + \frac{AK_1}{2}KK_{121}(1,1,n)]}{(\hat{\omega}_{1n}^2 - 1)\Lambda_{1n}/\lambda_{1n}^2}; \quad n \geq 2;$$
$$e_{1n} = \gamma_{1n} f_{11}\varsigma_{21};$$
$$\gamma_{1n} = -\frac{[\frac{1}{2}II_{123}(1,1,n) - JJ_{123}(1,1,n) + \frac{AK_1}{2}KK_{123}(1,1,n)]}{(\hat{\omega}_{3n}^2 - 1)\Lambda_{3n}/\lambda_{3n}^2};$$
$$d_{3n} = \Omega_{3n} f_{11}\varsigma_{21};$$
$$\Omega_{3n} = -\frac{[\frac{3}{2}II_{123}(1,1,n) - 3JJ_{123}(1,1,n) + \frac{AK_2}{2}KK_{123}(1,1,n)]}{(\hat{\omega}_{3n}^2 - 9)\Lambda_{3n}/\lambda_{3n}^2};$$

$$e_{3n} = \gamma_{3n} f_{11} \varsigma_{21};$$

$$\gamma_{3n} = -\frac{[\frac{3}{2} II_{121}(1,1,n) + 3JJ_{121}(1,1,n) + \frac{AK_2}{2} KK_{121}(1,1,n)]}{(\hat{\omega}_{1n}^2 - 9)\Lambda_{1n}/\lambda_{1n}^2};$$

$$d_{4n} = \Omega_{4n} \varsigma_{21}^2;$$

$$\Omega_{4n} = -\frac{[II_{224}(1,1,n) - 4JJ_{224}(1,1,n) + AK_3 KK_{224}(1,1,n)]}{(\hat{\omega}_{4n}^2 - 16)\Lambda_{4n}/\lambda_{4n}^2};$$

$$e_{4n} = \gamma_{4n} \varsigma_{4n}^2;$$

$$\gamma_{4n} = -\frac{[II_{220}(1,1,n) + 4JJ_{220}(1,1,n) + AK_3 KK_{224}(1,1,n)]}{(\hat{\omega}_{0n}^2 - 16)\Lambda_{0n}/\lambda_{0n}^2}.$$

Here $d_{11} = d_{21} = 0$ for the resonant interaction with mode (2,1), and $d_{31} = d_{41} = \ldots = 0$ with the higher modes, to eliminate secular terms.

Regrouping $\cos\theta \cos\hat{\omega}\tau$ terms in (III.5), it follows that

$$\nu_1 f_{11} C_1(\lambda_{11}\hat{r}) - f_{11}\varsigma_{21}[\frac{C_1'(\lambda_{11}\hat{r})C_2'(\lambda_{21}\hat{r})}{2} + \frac{C_1(\lambda_{11}\hat{r})C_2(\lambda_{21}\hat{r})}{\hat{r}^2} + AK_1 \frac{C_1(\lambda_{11}\hat{r})C_2(\lambda_{21}\hat{r})}{2}] = 0. \qquad (III.8)$$

Integrating as

$$\int_a^1 (III.8) C_1(\lambda_{11}\hat{r})\hat{r}d\hat{r},$$

leads to

$$\nu_1 = a_1 \varsigma_{21},$$

$$\text{where,} \quad a_1 = \frac{[\frac{1}{2} II_{121}(1,1,1) + JJ_{121}(1,1,1) + \frac{AK_1}{2} KK_{121}(1,1,1)]}{\Lambda_{11}/\lambda_{11}^2}.$$

Using (6), this results in

$$\nu_2 = \frac{\hat{\omega}^2 - 1}{\hat{\omega}^2 \hat{\epsilon}^{2/3}} - \frac{a_1 \varsigma_{21}}{\hat{\epsilon}^{1/3}},$$

$$\text{or} \quad \nu_2 = \nu - a_1^* \varsigma_{21}, \quad \text{with} \quad a_1^* = \frac{a_1}{\hat{\epsilon}^{1/3}}.$$

Similarly,

$$\beta_1 \varsigma_{21} C_2(\lambda_{21}\hat{r}) - \frac{f_{11}^2}{2}[C_1'^2(\lambda_{11}\hat{r}) - \frac{C_1{}^2(\lambda_{11}\hat{r})}{\hat{r}^2} + AK_0 C_1{}^2(\lambda_{11}\hat{r})] = 0, \qquad (III.9)$$

which, after integrating as

$$\int_a^1 (III.9) C_2(\lambda_{21}\hat{r})\hat{r}d\hat{r}$$

$$\text{gives:} \quad \beta_1 = b_1 \frac{f_{11}^2}{\varsigma_{21}},$$

where, $b_1 = \dfrac{1}{2}\dfrac{[II_{112}(1,1,1) - JJ_{112}(1,1,1) + AK_0KK_{112}(1,1,1)]}{\Lambda_{21}/\lambda_{21}^2}$.

Furthermore, from (15):

$$\beta_2 = \beta - b_1^* \frac{f_{11}^2}{\varsigma_{21}}, \quad \text{with,} \quad \beta = \frac{4\hat{\omega}^2 - \hat{\omega}_{21}^2}{\hat{\omega}^2 \hat{\epsilon}^{2/3}}; \quad \text{and} \quad b_1^* = \frac{b_1}{\hat{\epsilon}^{1/3}}.$$

2.2 Third Order Equation

It should be recognized that equality (6) is equivalent to

$$\frac{1}{\hat{\omega}} = 1 - \frac{\nu_1}{2}\hat{\epsilon}^{1/3} - \frac{(\nu_2 + \nu_1^2/4)}{2}\hat{\epsilon}^{2/3} - \dots \quad . \qquad (III.10)$$

Applying (6) to relation (I.5), (III.10) to (I.8), and substituting for $\hat{\Phi}^{(1)}$ and $\hat{\Phi}^{(2)}$ into (I.9) yields

$$\begin{aligned}
&\Big\{-\nu_2 f_{11} C_1(\lambda_{11}\hat{r}) + \frac{\nu_1}{2} f_{11}\varsigma_{21}\Big[\frac{C_1'(\lambda_{11}\hat{r})C_2'(\lambda_{21}\hat{r})}{2} + \frac{C_1(\lambda_{11}\hat{r})C_2(\lambda_{21}\hat{r})}{\hat{r}^2} \\
&+(AK_1 + 2\alpha_{11}^2\lambda_{11}^2 - 4\alpha_{11}\alpha_{21}\lambda_{11}\lambda_{21})\frac{C_1(\lambda_{11}\hat{r})C_2(\lambda_{21}\hat{r})}{2}\Big]\Big\}\cos\theta\cos\hat{\omega}\tau \\
&+\Big\{-\beta_2\varsigma_{21}C_2(\lambda_{21}\hat{r}) + \frac{\nu_1}{4} f_{11}^2\Big[C_1'^2(\lambda_{11}\hat{r}) - \frac{C_1^2(\lambda_{11}\hat{r})}{\hat{r}^2} + (AK_0 \\
&+\alpha_{11}^2\lambda_{11}^2)C_1^2(\lambda_{11}\hat{r})\Big]\cos 2\theta\sin 2\hat{\omega}\tau + \frac{\partial^2\hat{\Phi}^{(3)}}{\partial\tau^2} + \frac{1}{\alpha_{11}\lambda_{11}}\frac{\partial\hat{\Phi}^{(3)}}{\partial\hat{z}} \\
&-P_{11}\cos\theta\cos\hat{\omega}\tau - Q_{22}\cos 2\theta\sin 2\hat{\omega}\tau - P_{31}\cos 3\theta\cos\hat{\omega}\tau \\
&-\dots - P_{nm}\cos n\theta\cos m\hat{\omega}\tau - Q_{nm}\cos n\theta\sin m\hat{\omega}\tau = 0. \qquad (III.11)
\end{aligned}$$

Here P_{nm}'s and Q_{nm}'s are complicated expressions representative of the various mode shapes of $\hat{\Phi}^{(1)}$ and $\hat{\Phi}^{(2)}$, and

$$P_{11} = P_{11}^1 + P_{11}^2.$$

Note:

$$\begin{aligned}
P_{11}^1 &= \text{term of the no interaction case,} \\
&= -\sum_n \Big\{ f_{11}f_{0n}[CK_0C_1(\lambda_{11}\hat{r})C_0(\lambda_{0n}\hat{r}) - C_1'(\lambda_{11}\hat{r})C_0'(\lambda_{0n}\hat{r})] \\
&+ \frac{f_{11}f_{0n}}{2}[CK_1C_1(\lambda_{11}\hat{r})C_2(\lambda_{2n}\hat{r}) - 2\frac{C_1(\lambda_{11}\hat{r})C_2(\lambda_{2n}\hat{r})}{\hat{r}^2} \\
&- C_1'(\lambda_{11}\hat{r})C_2'(\lambda_{2n}\hat{r})]\Big\} + \frac{1}{32}f_{11}^3\Big\{-18[C_1'^2(\lambda_{11}\hat{r})C_1''(\lambda_{11}\hat{r})] \\
&+ \lambda_{11}^2(3 - 7\alpha_{11}^2)\frac{C_1^3(\lambda_{11}\hat{r})}{\hat{r}^2} + 3\lambda_{11}^4\alpha_{11}^2(3 - \alpha_{11}^2)C_1^3(\lambda_{11}\hat{r}) \\
&+ 6\frac{C_1^3(\lambda_{11}\hat{r})}{\hat{r}^4} + 3\lambda_{11}^2(3 - 7\alpha_{11}^2)C_1(\lambda_{11}\hat{r})C_1'^2(\lambda_{11}\hat{r}) \\
&- 12\frac{C_1(\lambda_{11}\hat{r})C_1'^2(\lambda_{11}\hat{r})}{\hat{r}^2} + 6\frac{C_1'(\lambda_{11}\hat{r})C_1^2(\lambda_{11}\hat{r})}{\hat{r}^3}\Big\} + \hat{r}\hat{\omega}^2, \qquad (III.12)
\end{aligned}$$

CK_1 and CK_2 are defined by (III.3); and

$$\begin{aligned}
P_{11}^2 &= \text{expression due to the interaction with second mode,}\\
&= -\sum_n \Big\{ \varsigma_{21} e_{1n} [C_2(\lambda_{21}\hat{r}) C_3(\lambda_{3n}\hat{r}) CK_3 - 9\frac{C_2(\lambda_{21}\hat{r}) C_3(\lambda_{3n}\hat{r})}{\hat{r}^2}\\
&\quad - \frac{3}{2} C_2'(\lambda_{21}\hat{r}) C_3(\lambda_{3n}\hat{r})] + \varsigma_{21} e_{3n} [C_2(\lambda_{21}\hat{r}) C_1(\lambda_{1n}\hat{r}) CK_4\\
&\quad - 5\frac{C_2(\lambda_{21}\hat{r}) C_1(\lambda_{1n}\hat{r})}{\hat{r}^2} - \frac{5}{2} C_2'(\lambda_{21}\hat{r}) C_1(\lambda_{1n}\hat{r})]\\
&\quad + \varsigma_{21} d_{1n} [C_1(\lambda_{11}\hat{r}) C_1(\lambda_{1n}\hat{r}) CK_5 - \frac{C_1(\lambda_{11}\hat{r}) C_1(\lambda_{1n}\hat{r})}{\hat{r}^2}\\
&\quad - \frac{1}{2} C_1'(\lambda_{11}\hat{r}) C_1'(\lambda_{1n}\hat{r})] + \varsigma_{21} d_{3n} [C_2(\lambda_{21}\hat{r}) C_3(\lambda_{3n}\hat{r}) CK_6\\
&\quad - 3\frac{C_2(\lambda_{21}\hat{r}) C_3(\lambda_{3n}\hat{r})}{\hat{r}^2} - \frac{1}{2} C_2'(\lambda_{21}\hat{r}) C_3'(\lambda_{3n}\hat{r})] \Big\}\\
&\quad + f_{11} \varsigma_{21}^2 \Big\{ - \frac{C_1''(\lambda_{11}\hat{r}) C_2^2(\lambda_{21}\hat{r})}{4} - \frac{C_1'(\lambda_{11}\hat{r}) C_2'(\lambda_{21}\hat{r}) C_2''(\lambda_{21}\hat{r})}{2}\\
&\quad + \frac{C_1(\lambda_{11}\hat{r}) C_2^2(\lambda_{21}\hat{r})}{\hat{r}^4} + \frac{C_1'(\lambda_{11}\hat{r}) C_2^2(\lambda_{21}\hat{r})}{\hat{r}^3}\\
&\quad + DK_1 C_1(\lambda_{11}\hat{r}) C_2^2(\lambda_{21}\hat{r}) + DK_2 \frac{C_2^2(\lambda_{21}\hat{r}) C_1(\lambda_{11}\hat{r})}{\hat{r}^2}\\
&\quad + \frac{DK_2}{4} C_1(\lambda_{11}\hat{r}) C_2^2(\lambda_{21}\hat{r}) + DK_3 C_2(\lambda_{21}\hat{r}) C_2'(\lambda_{21}\hat{r}) C_1'(\lambda_{11}\hat{r})\\
&\quad - 2\frac{C_2(\lambda_{21}\hat{r}) C_2'(\lambda_{21}\hat{r}) C_1'(\lambda_{11}\hat{r})}{\hat{r}^2} \Big\};
\end{aligned}$$

where:

$$\begin{aligned}
CK_3 &= \frac{1}{4}\lambda_{21}^2 - \frac{1}{2}\lambda_{3n}^2 - \alpha_{11}\alpha_{21}\lambda_{11}\lambda_{21} + \frac{1}{2}\alpha_{11}\alpha_{3n}\lambda_{11}\lambda_{3n} - \frac{3}{2}\alpha_{21}\alpha_{3n}\lambda_{21}\lambda_{3n};\\
CK_4 &= \frac{3}{4}\lambda_{21}^2 - \frac{1}{2}\lambda_{1n}^2 - 3\alpha_{11}\alpha_{21}\lambda_{11}\lambda_{21} + \frac{9}{2}\alpha_{11}\alpha_{1n}\lambda_{11}\lambda_{1n} - \frac{5}{2}\alpha_{21}\alpha_{1n}\lambda_{21}\lambda_{1n};\\
CK_5 &= \frac{1}{4}\lambda_{21}^2 - \frac{1}{2}\lambda_{1n}^2 - \alpha_{11}\alpha_{21}\lambda_{11}\lambda_{21} + \frac{1}{2}\alpha_{11}\alpha_{1n}\lambda_{11}\lambda_{1n} - \frac{1}{2}\alpha_{21}\alpha_{1n}\lambda_{21}\lambda_{1n};\\
CK_6 &= \frac{3}{4}\lambda_{21}^2 - \frac{1}{2}\lambda_{3n}^2 - 3\alpha_{11}\alpha_{21}\lambda_{11}\lambda_{21} + \frac{9}{2}\alpha_{11}\alpha_{3n}\lambda_{11}\lambda_{3n} - \frac{1}{2}\alpha_{21}\alpha_{3n}\lambda_{21}\lambda_{3n};\\
DK_1 &= -\frac{1}{8}\alpha_{21}^2\lambda_{21}^2\lambda_{11}^2 - \frac{1}{4}\alpha_{11}\alpha_{21}\lambda_{11}\lambda_{21}^3 + (1+\alpha_{11}^2)\alpha_{21}\alpha_{11}\lambda_{11}^3\lambda_{21}\\
&\qquad + \alpha_{11}^2(2 - \frac{9}{8}\alpha_{21}^2)\lambda_{11}^2\lambda_{21}^2;\\
DK_2 &= \frac{1}{2}\lambda_{11}^2(1-\alpha_{11}^2) - 2\alpha_{11}\alpha_{21}\lambda_{11}\lambda_{21};\\
DK_3 &= \frac{1}{4}\lambda_{21}^2(1-2\alpha_{21}^2) + 2\alpha_{11}^2\lambda_{11}^2 + \frac{1}{2}\alpha_{11}\alpha_{21}\lambda_{11}\lambda_{21}.
\end{aligned}$$

Similarly, Q_{22} contains interacting terms only as,

$$
\begin{aligned}
Q_{22} = -\sum_n \Big\{ & f_{11} e_{1n} [C_1(\lambda_{11}\hat{r}) C_3(\lambda_{3n}\hat{r}) CK_7 - 3\frac{C_1(\lambda_{11}\hat{r}) C_3(\lambda_{3n}\hat{r})}{\hat{r}^2} \\
& - C_1'(\lambda_{11}\hat{r}) C_3'(\lambda_{3n}\hat{r})] + f_{11} e_{3n} [C_1(\lambda_{11}\hat{r}) C_1(\lambda_{1n}\hat{r}) CK_8 \\
& + \frac{C_1(\lambda_{11}\hat{r}) C_1(\lambda_{1n}\hat{r})}{\hat{r}^2} - C_1'(\lambda_{11}\hat{r}) C_1'(\lambda_{1n}\hat{r})] \\
& + f_{11} d_{1n} [C_1(\lambda_{11}\hat{r}) C_1(\lambda_{1n}\hat{r}) CK_9 + \frac{C_1(\lambda_{11}\hat{r}) C_1(\lambda_{1n}\hat{r})}{\hat{r}^2} \\
& - C_1'(\lambda_{11}\hat{r}) C_1'(\lambda_{1n}\hat{r})] + f_{11} d_{3n} [C_1(\lambda_{11}\hat{r}) C_3(\lambda_{3n}\hat{r}) CK_{10} \\
& - 3\frac{C_1(\lambda_{11}\hat{r}) C_3(\lambda_{3n}\hat{r})}{\hat{r}^2} - C_1'(\lambda_{11}\hat{r}) C_3'(\lambda_{3n}\hat{r})] \\
& + \varsigma_{21} e_{4n} [C_2(\lambda_{21}\hat{r}) C_0(\lambda_{0n}\hat{r}) CK_{11} - 2C_2'(\lambda_{21}\hat{r}) C_0'(\lambda_{0n}\hat{r})] \\
& + \varsigma_{21} d_{4n} [C_2(\lambda_{21}\hat{r}) C_4(\lambda_{4n}\hat{r}) CK_{12} - 8\frac{C_2(\lambda_{21}\hat{r}) C_4(\lambda_{4n}\hat{r})}{\hat{r}^2} \\
& - C_2'(\lambda_{21}\hat{r}) C_4'(\lambda_{4n}\hat{r})] \Big\} + f_{11}^2 \varsigma_{21} \Big\{ -\frac{C_2''(\lambda_{21}\hat{r}) {C_1'}^2(\lambda_{11}\hat{r})}{4} \\
& - \frac{C_1'(\lambda_{11}\hat{r}) C_1''(\lambda_{11}\hat{r}) C_2'(\lambda_{21}\hat{r})}{2} + \frac{{C_1}^2(\lambda_{11}\hat{r}) C_2(\lambda_{21}\hat{r})}{\hat{r}^4} \\
& + \frac{1}{4}\frac{{C_1}^2(\lambda_{11}\hat{r}) C_2'(\lambda_{21}\hat{r})}{\hat{r}^3} + DK_4 \frac{{C_1}^2(\lambda_{11}\hat{r}) C_2(\lambda_{21}\hat{r})}{\hat{r}^2} \\
& + DK_5 \frac{{C_1}^2(\lambda_{11}\hat{r}) C_2(\lambda_{21}\hat{r})}{\hat{r}^2} + +DK_5 {C_1'}^2(\lambda_{11}\hat{r}) C_2(\lambda_{21}\hat{r}) \\
& + DK_6 C_1(\lambda_{11}\hat{r}) C_1'(\lambda_{11}\hat{r}) C_2'(\lambda_{21}\hat{r}) - \frac{1}{2}\frac{C_1'(\lambda_{11}\hat{r}) C_1(\lambda_{11}\hat{r}) C_2'(\lambda_{21}\hat{r})}{\hat{r}^2} \Big\} \\
& + \varsigma_{21}^2 \Big\{ -\frac{9}{16} C_2''(\lambda_{21}\hat{r}) {C_2'}^2(\lambda_{21}\hat{r}) + 3\frac{C_2^3(\lambda_{21}\hat{r})}{\hat{r}^4} + \frac{3}{4}\frac{C_2^2(\lambda_{21}\hat{r}) C_2'(\lambda_{21}\hat{r})}{\hat{r}^3} \\
& + DK_7 C_2^3(\lambda_{21}\hat{r}) + DK_8 \frac{C_2^3(\lambda_{21}\hat{r})}{\hat{r}^2} + DK_9 {C_2'}^2(\lambda_{21}\hat{r}) C_2(\lambda_{21}\hat{r}) \\
& - \frac{3}{2}\frac{{C_2'}^2(\lambda_{21}\hat{r}) C_2(\lambda_{21}\hat{r})}{\hat{r}^2} \Big\};
\end{aligned}
$$

where:

$$CK_7 = \frac{1}{4}\lambda_{11}^2(1-\alpha_{11}^2) + \frac{1}{4}\lambda_{3n}^2 - \frac{5}{4}\alpha_{11}\alpha_{3n}\lambda_{11}\lambda_{3n};$$

$$CK_8 = -\frac{3}{4}\lambda_{11}^2(1-\alpha_{11}^2) - \frac{1}{4}\lambda_{1n}^2 + \frac{5}{4}\alpha_{11}\alpha_{1n}\lambda_{11}\lambda_{1n};$$

$$CK_9 = \frac{1}{4}\lambda_{11}^2(1-\alpha_{11}^2) + \frac{1}{4}\lambda_{1n}^2 - \frac{5}{4}\alpha_{11}\alpha_{1n}\lambda_{11}\lambda_{1n};$$

$$CK_{10} = -\frac{3}{4}\lambda_{11}^2(1-\alpha_{11}^2) - \frac{1}{4}\lambda_{3n}^2 + \frac{5}{4}\alpha_{11}\alpha_{3n}\lambda_{11}\lambda_{3n};$$

$$CK_{11} = 16\alpha_{11}\alpha_{0n}\lambda_{11}\lambda_{0n} - 2\lambda_{21}\lambda_{0n}\alpha_{21}\alpha_{0n} - 8\alpha_{21}\alpha_{11}\lambda_{21}\lambda_{11} - \lambda_{0n}^2 + 2\lambda_{21}^2;$$

$$CK_{12} = 8\alpha_{11}\alpha_{4n}\lambda_{11}\lambda_{4n} - \alpha_{21}\alpha_{4n}\lambda_{21}\lambda_{4n} - 4\alpha_{21}\alpha_{11}\lambda_{21}\lambda_{11} - \frac{1}{2}\lambda_{4n}^2 + \lambda_{21}^2;$$

$$
\begin{aligned}
DK_4 &= \frac{5}{8}\alpha_{11}^2\lambda_{11}^2\lambda_{21}^2 + \frac{1}{4}\alpha_{11}\alpha_{21}\lambda_{11}^3\lambda_{21} - \frac{1}{8}\alpha_{11}\alpha_{21}\lambda_{11}\lambda_{21}^3 + \frac{1}{4}\alpha_{11}^3\alpha_{21}\lambda_{11}^3\lambda_{21};\\
DK_5 &= \frac{1}{8}\lambda_{21}^2 - \alpha_{11}\alpha_{21}\lambda_{11}\lambda_{21};\\
DK_6 &= \frac{1}{4}\lambda_{11}^2(1+\alpha_{11}^2);\\
DK_7 &= \frac{3}{4}\alpha_{11}^2\lambda_{11}^2\lambda_{21}^2(1+4\alpha_{21}^2) + \frac{3}{8}\alpha_{11}\alpha_{21}\lambda_{11}\lambda_{21}^3(7-3\alpha_{21}^2) - \frac{9}{32}\alpha_{21}^2\lambda_{21}^4;\\
DK_8 &= \frac{3}{8}\lambda_{21}^2(1-4\alpha_{21}^2) + \frac{5}{2}\alpha_{11}\alpha_{21}\lambda_{11}\lambda_{21};\\
DK_9 &= \frac{9}{32}\lambda_{21}^2(1-4\alpha_{21}^2) + \frac{15}{8}\alpha_{11}\alpha_{21}\lambda_{11}\lambda_{21}.
\end{aligned}
$$

Setting the terms with $\cos\theta\cos\hat{\omega}\tau$ and $\cos 2\theta \sin 2\hat{\omega}\tau$ in (III.11) to zero, integrating as

$$\int_a^1 (III.11)C_1(\lambda_{11}\hat{r})\hat{r}d\hat{r} \quad \text{and} \quad \int_a^1 (III.11)C_2(\lambda_{21}\hat{r})\hat{r}d\hat{r};$$

and replacing ν_1 by $a_1\varsigma_{21}$ leads to:

$$
\begin{aligned}
f_{11}(K_1 f_{11}^2 + E_1\varsigma_{21}^2 + \nu_2) + F_1 &= 0;\\
\varsigma_{21}(K_2\varsigma_{21}^2 + E_2 f_{11}^2 + \beta_2) &= 0,
\end{aligned}
\tag{III.13}
$$

where K_1 and F_1 are defined by (III.2), and

$$
\begin{aligned}
E_1 &= \frac{\lambda_{11}^2}{\Lambda_{11}}[SUM3 - G3 - H3];\\
E_2 &= \frac{\lambda_{21}^2}{\Lambda_{21}}[SUM4 - G4 - H4];\\
K_2 &= \frac{\lambda_{21}^2}{\Lambda_{21}}[SUM5 - G5].
\end{aligned}
\tag{III.14}
$$

Note:

$$
\begin{aligned}
SUM3 &= \frac{1}{4}I_1(1,2,2,1) - \frac{1}{2}I_1(2,1,2,1) + DK_2 I_2(2,2,1,1) + DK_1 I_3(2,2,1,1,)\\
&\quad + I_4(2,2,1,1) + \frac{DK_2}{4}I_5(2,2,1,1) + DK_3 I_5(2,1,2,1) - 2I_6(2,1,2,1)\\
&\quad + I_7(1,2,2,1);\\
SUM4 &= -\frac{1}{4}I_1(2,1,1,2) - \frac{1}{2}I_1(1,1,2,2) + DK_5 I_2(1,1,2,2) + DK_4 I_3(1,1,2,2)\\
&\quad + I_4(1,1,2,2) + DK_5 I_5(1,1,2,2) + DK_6 I_5(1,2,1,2) - \frac{1}{2}I_6(1,2,1,2)\\
&\quad + \frac{1}{4}I_7(2,1,1,2);\\
SUM5 &= -\frac{9}{16}I_1(2,2,2,2) + DK_8 I_2(2,2,2,2) + DK_7 I_3(2,2,2,2)\\
&\quad + 3I_4(2,2,2,2) + DK_9 I_5(2,2,2,2) - \frac{3}{2}I_6(2,2,2,2)
\end{aligned}
$$

$$+\frac{3}{4}I_7(2,2,2,2);$$

$$G3=\sum_n\Big\{[CK_3KK_{231}(1,n,1)-9JJ_{231}(1,n,1)-\frac{3}{2}II_{231}(1,n,1)]\gamma_{1n}$$
$$+[CK_4KK_{211}(1,n,1)-5JJ_{211}(1,n,1)-\frac{5}{2}II_{211}(1,n,1)]\gamma_{3n}$$
$$+[CK_5KK_{211}(1,n,1)-JJ_{211}(1,n,1)-\frac{1}{2}II_{211}(1,n,1)]\Omega_{1n}$$
$$+[CK_6KK_{231}(1,n,1)-3JJ_{231}(1,n,1)-\frac{1}{2}II_{231}(1,n,1)]\Omega_{3n}\Big\};$$

$$G4=\sum_n\Big\{[CK_7KK_{132}(1,n,1)-3JJ_{132}(1,n,1)-II_{132}(1,n,1)]\gamma_{1n}$$
$$+[CK_8KK_{112}(1,n,1)+JJ_{112}(1,n,1)-II_{112}(1,n,1)]\gamma_{3n}$$
$$+[CK_9KK_{112}(1,n,1)+JJ_{112}-II_{112}(1,n,1)]\Omega_{1n}$$
$$+[CK_{10}KK_{132}(1,n,1)-3JJ_{132}(1,n,1)-II_{132}(1,n,1)]\Omega_{3n}\Big\};$$

$$G5=\sum_n\Big\{[CK_{11}KK_{202}(1,n,1)-2II_{202}(1,n,1)]\gamma_{4n}$$
$$+[CK_{12}KK_{242}(1,n,1)-8JJ_{242}(1,n,1)-II_{242}(1,n,1)]\Omega_{4n}\Big\};$$

with,

$$\gamma_{in}=\frac{e_{in}}{f_{11}\varsigma_{21}},\quad \Omega_{in}=\frac{d_{in}}{f_{11}\varsigma_{21}},\quad n=1,2,3;$$
$$\gamma_{4n}=\frac{e_{4n}}{\varsigma_{21}^2};\quad \Omega_{4n}=\frac{d_{4n}}{\varsigma_{21}^2};$$

and

$$H3=\frac{a_1}{2}[a_1\frac{\Lambda_{11}}{\lambda_{11}^2}+(\alpha_{11}^2\lambda_{11}^2-2\alpha_{11}\alpha_{21}\lambda_{11}\lambda_{21})KK_{212}(1,1,1)];$$
$$H4=\frac{a_1}{2}[b_1\frac{\Lambda_{21}}{\lambda_{21}^2}+\alpha_{11}^2\lambda_{11}^2KK_{112}(1,1,1)].$$

2.3 Solution Stability

A general solution with nonzero time derivatives and phase angles, combined with a slow time scale $\tau_1=\hat{\epsilon}^{1/3}$, leads to a set of equations similar to (III.8) and (III.9) previously developed. On integration using the orthonogality conditions, as before, and introducing definition of the variables:

$$f_{11}^*=f_{11}\cos\varphi_{11};\quad e_{11}^*=-f_{11}\sin\varphi_{11};\quad \varsigma_{21}^*=\varsigma_{21}\cos\xi_{21};\quad e_{21}^*=\varsigma_{21}\sin\xi_{21},$$

to simplify cross product expressions of the form,

$$\cos(\hat{\omega}\tau+\varphi_{11})\sin(\hat{\omega}\tau+\varphi_{11})=\frac{1}{2}\sin 2(\hat{\omega}\tau+\varphi_{11});$$
$$\cos(\hat{\omega}\tau+\varphi_{11})\cos(2\hat{\omega}\tau+\xi_{21})=\frac{1}{2}\cos(\hat{\omega}\tau+\xi_{21}-\varphi_{11})+\frac{1}{2}\cos(3\hat{\omega}\tau+\xi_{21}+\varphi_{11});$$

etc., gives:

$$\begin{aligned}
-\nu_1 f_{11}^* + a_1(f_{11}^*\varsigma_{21}^* - e_{11}^* e_{21}^*) &= -2\frac{de_{11}^*}{d\tau_1}; \\
-\nu_1 e_{11}^* - a_1(f_{11}^* e_{21}^* + e_{11}^*\varsigma_{21}^*) &= 2\frac{df_{11}^*}{d\tau_1}; \\
-\beta_1\varsigma_{21}^* + b_1(f_{11}^{*2} - e_{11}^{*2}) &= 4\frac{de_{21}^*}{d\tau_1}; \\
-\beta_1 e_{21}^* - b_1(2f_{11}^* e_{11}^*) &= -4\frac{d\varsigma_{21}^*}{d\tau_1}.
\end{aligned} \tag{III.15}$$

Stability is studied in the neighbourhood of the steady-state solution derived earlier by introducing a disturbance such as:

$$f_{11}^* = f_{11} + A_1 e^{\lambda\tau_1}; \quad e_{11}^* = A_2 e^{\lambda\tau_1}; \quad \varsigma_{21}^* = \varsigma_{21} + A_3 e^{\lambda\tau_1}; \quad \text{and} \quad e_{21}^* = A_4 e^{\lambda\tau_1};$$

and recognizing that $\nu_1 = a_1\varsigma_{21}$, $\beta_1 = b_1\frac{f_{11}^2}{\varsigma_{21}}$. Now (III.15) reduces to

$$\begin{pmatrix} 0 & 2\lambda & a_1 f_{11} & 0 \\ -2\lambda & -2a_1\varsigma_{21} & 0 & -a_1 f_{11} \\ 2b_1 f_{11} & 0 & -b_1\frac{f_{11}^2}{\varsigma_{21}} & -4\lambda \\ 0 & -2b_1 f_{11} & 4\lambda & -b_1\frac{f_{11}^2}{\varsigma_{21}} \end{pmatrix} \begin{pmatrix} A_1 \\ A_2 \\ A_3 \\ A_4 \end{pmatrix} = 0. \tag{III.16}$$

This then yields (determinant=0)

$$16\lambda^2 + b_1^2\frac{f_{11}^4}{\varsigma_{21}^2} + 8a_1 b_1 f_{11}^2 = 0,$$

$$\text{or} \quad (4\lambda)^2 = -(b_1^2\frac{f_{11}^4}{\varsigma_{21}^2} + 8a_1 b_1 f_{11}^2).$$

The solution is stable for negative $(4\lambda)^2$, i.e.,

$$b_1^2\frac{f_{11}^4}{\varsigma_{21}^2} + 8a_1 b_1 f_{11}^2 > 0, \tag{III.17}$$

$$\text{or} \quad (\frac{f_{11}}{\varsigma_{21}})^2 > -8\frac{a_1}{b_1}. \tag{III.18}$$

APPENDIX IV: ADDED MASS AND DAMPING RATIOS: DETAILS OF THE ANALYSIS

1. Added Mass

1.1 General Procedure

The domain of integration in relation (21) is subdivided into two regions as

$$F = \int_{-h}^{0}\int_{0}^{2\pi} p\cos\theta r\,d\theta dz + \int_{0}^{\eta_f}\int_{0}^{2\pi} p\cos\theta r\,d\theta dz. \qquad (IV.1)$$

The total force is the expression evaluated at $r = R_0$ minus F at $r = R_i$. The procedure is similar to the one described in reference 65. It is based on a Taylor series expansion of p around $z = 0$ to eliminate the dependence of the second term on η_f,

$$p(r,\theta,z) = p(r,\theta,0) + z\frac{\partial p(r,\theta,z)}{\partial z}|_{z=0} + \frac{1}{2}z^2\frac{\partial^2 p(r,\theta,z)}{\partial z^2}|_{z=0} + \dots \quad . \qquad (IV.2)$$

Setting $z = \eta_f$ in the above relation, integrating over z from 0 to η_f, and solving for η_f in terms of p, $\frac{\partial p}{\partial z}$, etc., gives, after simplifications,

$$F \approx \int_{-h}^{0}\int_{o}^{2\pi} p\cos\theta r\,d\theta dz + \int_{0}^{2\pi}\frac{p_0^2}{2\rho g}\cos\theta r\,d\theta, \qquad (IV.3)$$

where $p_0 = p(r,\theta,0)$. Pressures are found from Bernouilli's equation (22) using $\tilde{\Phi}$ derived earlier. (IV.3) can then be integrated analytically, with only the third or lower order being retained in the final expression for simplicity. It should be mentioned that the following equalities were used for integration over dz:

$$\begin{aligned}
\int_{-\hat{h}}^{0}\frac{\cosh\lambda_n(\hat{z}+\hat{h})}{\cosh\lambda_n\hat{h}}\frac{\cosh\lambda_m(\hat{z}+\hat{h})}{\cosh\lambda_m\hat{h}}d\hat{z} &= \frac{\lambda_n\alpha_n-\lambda_m\alpha_m}{\lambda_n^2-\lambda_m^2} \quad \text{for} \quad n\neq m;\\
&= \frac{1}{2}\left(\frac{\hat{h}}{\cosh^2\lambda_n\hat{h}}+\frac{\alpha_n}{\lambda_n}\right)\\
&\qquad \text{for} \quad n=m;\\
\int_{-\hat{h}}^{0}\frac{\sinh\lambda_n(\hat{z}+\hat{h})}{\cosh\lambda_n\hat{h}}\frac{\sinh\lambda_m(\hat{z}+\hat{h})}{\cosh\lambda_m\hat{h}}d\hat{z} &= \frac{\lambda_n\alpha_m-\lambda_m\alpha_n}{\lambda_n^2-\lambda_m^2} \quad \text{for} \quad n\neq m;\\
&= \frac{1}{2}\left(\frac{-\hat{h}}{\cosh^2\lambda_n\hat{h}}+\frac{\alpha_n}{\lambda_n}\right)\\
&\qquad \text{for} \quad n=m.
\end{aligned} \qquad (IV.4)$$

Well known trigonometric relations such as:

$$\begin{aligned}
\int_{0}^{2\pi}\cos n\theta\cos m\theta\,d\theta &= 0 \quad \text{for} \quad n\neq m;\\
&= \pi \quad \text{for} \quad n=m,
\end{aligned}$$

were employed when integrating over θ.

1.2 Added Mass Higher Order Terms

The A's, B's and C_4 expressions of relation (24) are presented below:

(i) $$A_1 = \sum_i \sum_p f_{1i}\Big\{f_{0p}\frac{k_{10}(i,p)}{2} + \frac{f_{2p}}{2}[\frac{k_{12}(i,p)}{2} + l_{12}(i,p)]\Big\} + \frac{\alpha_{11}\lambda_{11}\hat{\omega}}{32}\sum_i\sum_j\sum_k f_{1i}f_{1j}f_{1k}[3(\alpha_{11}\lambda_{11})^2 w_{11}(i,j,k) + u_{11}(i,j,k)];$$

$$B_1 = \alpha_{11}\lambda_{11}\hat{\omega}^2\sum_i\sum_j f_{1i}[f_{0p}t_{10}(i,p) + \frac{f_{2p}}{2}t_{12}(i,p)];$$

(ii) $$A_2 = f_{11}\sum_p\Big\{(f_{11}^2 - \varsigma_{11}^2)\Omega_{0p}[\frac{k_{10}(1,p)}{2} - \lambda_{11}\alpha_{11}\hat{\omega}^2 t_{10}(1,p)] + \frac{\Omega_{2p}}{2}[(f_{11}^2 + 3\varsigma_{11}^2)\frac{k_{12}(1,p)}{2} + (f_{11}^2 + 4\varsigma_{11}^2)l_{12}(1,p) - (f_{11}^2 + \varsigma_{11}^2)\alpha_{11}\lambda_{11}\hat{\omega}^2 t_{12}(1,p)] + \frac{\alpha_{11}\lambda_{11}\hat{\omega}}{32}[(f_{11}^2 + 11\varsigma_{11}^2)u_{11}(1,1,1) + (\alpha_{11}\lambda_{11})^2(3f_{11}^2 + \varsigma_{11}^2)w_{11}(1,1,1)]\Big\};$$

$$B_2 = f_{11}\sum_p\Big\{(f_{11}^2 - \varsigma_{11}^2)\Omega_{0p}[\frac{k_{10}(1,p)}{2} + \alpha_{11}\lambda_{11}\hat{\omega}^2 t_{10}(1,p)] + \frac{\Omega_{2p}}{2}[(f_{11}^2 - \varsigma_{11}^2)\frac{k_{12}(1,p)}{2} + (f_{11}^2 - 2\varsigma_{11}^2)l_{12}(1,p) + (f_{11}^2 + \varsigma_{11}^2)\alpha_{11}\lambda_{11}\hat{\omega}^2 t_{12}(1,p)] + \frac{\alpha_{11}\lambda_{11}\hat{\omega}}{32}[(f_{11}^2 - 7\varsigma_{11}^2)u_{11}(1,1,1) + (\alpha_{11}\lambda_{11})^2(3f_{11}^2 + 5\varsigma_{11}^2)w_{11}(1,1,1)]\Big\};$$

(iii) $$A_3 = f_{11}\varsigma_{21}\Big\{\sum_p \Omega_{1p}\frac{\alpha_{1p}}{\lambda_{1p}}[C_1(\lambda_{1p}) - aC_1(\lambda_{1p}a)] - \frac{1}{2}[\frac{k_{21}(1,1)}{2} + l_{21}(1,1) - \alpha_{11}\lambda_{11}\hat{\omega}t_{21}(1,1)]\Big\};$$

$$B_3 = f_{11}\varsigma_{21}\Big\{\sum_p 3\gamma_{1p}\frac{\alpha_{3p}}{\lambda_{3p}}[C_3(\lambda_{3p}) - aC_3(\lambda_{3p}a)] - \frac{1}{2}[\frac{k_{21}(1,1)}{2} + l_{21}(1,1) + \alpha_{11}\lambda_{11}\hat{\omega}t_{21}(1,1)]\Big\};$$

$$A_4 = A_2 + f_{11}\varsigma_{21}^2\sum_p\Big\{(\frac{\Omega_{1p} - \gamma_{3p}}{2})[\frac{k_{12}(1,p)}{2} + l_{12}(1,p)] + (\frac{\gamma_{1p} - \Omega_{3p}}{2}[\frac{k_{23}(1,p)}{2} + 3l_{23}(1,p)] + \alpha_{11}\lambda_{11}\hat{\omega}^2[(\frac{\Omega_{1p} - 3\gamma_{3p}}{2})t_{21}(1,p) + (\frac{\gamma_{1p} - 3\Omega_{3p}}{2})t_{23}(1,p)] + \frac{\alpha_{11}\lambda_{11}\hat{\omega}}{2}[u_{21}(1,1,1) + \frac{\alpha_{21}^2\lambda_{21}^2}{4}w_{21}(1,1,1)]\Big\};$$

$$B_4 = B_2 + f_{11}\varsigma_{21}^2\sum_p\Big\{\frac{\Omega_{1p}}{2}[\frac{k_{21}(1,p)}{2} + l_{21}(1,p)] + \frac{\gamma_{1p}}{2}[\frac{k_{23}(1,p)}{2}$$

$$+ 3l_{23}(1,p)] + \frac{\gamma_{4p}}{2}k_{10}(1,p) + \alpha_{11}\lambda_{11}\hat{\omega}^2[\frac{\Omega_{1p}}{2}t_{21}(1,p) + \frac{\gamma_{1p}}{2}t_{23}(1,p)$$
$$+ 2\gamma_{4p}t_{10}(1,p)] + \frac{\alpha_{11}\lambda_{11}\hat{\omega}}{4}[u_{21}(1,1,1) + (\frac{\alpha_{21}^2\lambda_{21}^2}{4}$$
$$+ \alpha_{21}\lambda_{21}\alpha_{11}\lambda_{11})w_{21}(1,1,1)]\Big\};$$

$$C_4 = f_{11}\varsigma_{21}^2\sum_p\Big\{\frac{\gamma_{3p}}{2}[\frac{k_{21}(1,p)}{2} + l_{21}(1,p)] + \frac{\Omega_{3p}}{2}[\frac{k_{23}(1,p)}{2} + 3l_{23}(1,p)]$$
$$+ \frac{\gamma_{4p}}{2}k_{10}(1,p) + \alpha_{11}\lambda_{11}\hat{\omega}^2[\frac{\gamma_{3p}}{2}t_{21}(1,p) + \frac{\Omega_{3p}}{2}t_{23}(1,p) + 2\gamma_{4p}t_{10}(1,p)]$$
$$- \frac{\alpha_{11}\lambda_{11}\hat{\omega}}{4}[u_{21}(1,1,1) + (\frac{\alpha_{21}^2\lambda_{21}^2}{4} - \alpha_{21}\lambda_{21}\alpha_{11}\lambda_{11})w_{21}(1,1,1)]\Big\},$$

where k's and l's are combinations of the Bessel and hyperbolic function, and t's, u's and w's are the Bessel function products, as defined in Appendices V.2.3 and V.1.3. ς_{11}^2 is taken to be zero when using A_2 and B_2 in the expressions for A_4 and B_4.

2. Damping Ratio

2.1 Correction Velocity $\vec{u}_2$

2.1.1 First Order $\vec{u}_2^{(1)}$

Taking $\vec{u}_2$ to be harmonic, i.e., $\vec{u}_2 = \vec{U}_2 e^{in\omega_e t}$, equation (30a) becomes

$$in\omega_e\vec{U}_2^{(1)} = \nu_f[\frac{1}{r}\frac{\partial}{\partial r}(r\frac{\partial\vec{U}_2^{(1)}}{\partial r}) + \frac{1}{r^2}\frac{\partial^2\vec{U}_2^{(1)}}{\partial\theta^2} + \frac{\partial^2\vec{U}_2^{(1)}}{\partial z^2}]. \qquad (IV.5)$$

Neglecting curvature effects, i.e., $\frac{1}{r}\frac{\partial}{\partial r}(r\frac{\partial\vec{U}_2^{(1)}}{\partial r}) \approx \frac{\partial^2\vec{U}_2^{(1)}}{\partial r^2}$, and assuming the gradients perpendicular to the boundaries to be large compared to the change in other directions, i.e.,

$$\frac{\partial^2\vec{U}_2^{(1)}}{\partial r^2} \gg \frac{\partial^2\vec{U}_2^{(1)}}{\partial z^2}, \quad\text{and}\quad \frac{\partial^2\vec{U}_2^{(1)}}{\partial r^2} \gg \frac{1}{r^2}\frac{\partial^2\vec{U}_2^{(1)}}{\partial\theta^2},$$

near the vertical and bottom walls, reduces (IV.5) to:

$$\vec{U}_2^{(1)} = \frac{\nu_f}{in\omega_e}\frac{\partial^2\vec{U}_2^{(1)}}{\partial z^2} \quad\text{near}\quad r = R_0 \quad\text{or}\quad r = R_i; \qquad (IV.6)$$

$$\vec{U}_2^{(1)} = \frac{\nu_f}{in\omega_e}\frac{\partial^2\vec{U}_2^{(1)}}{\partial z^2} \quad\text{near}\quad z = -h. \qquad (IV.7)$$

Setting $\vec{U}_2^{(1)} = Ae^{\lambda r}$ near $r = R_0$ and $r = R_i$, and substituting into (IV.6) gives

$$\lambda^2 = \frac{in\omega_e}{\nu_f}, \qquad (IV.8)$$

or $\vec{U}_2^{(1)} = \overline{a_1} e^{\lambda_1 r} + \overline{a_2} e^{\lambda_2 r}$, where $\lambda_1 = \sqrt{\dfrac{in\omega_e}{\nu_f}}$ and $\lambda_2 = -\lambda_1$.

Introducing the boundary conditions: $\vec{u}_2^{(1)} = -\nabla\tilde{\Phi}^{(1)}$ at $r = R_0$, R_i; $\vec{u}_2^{(1)} = 0$ far away from the solid walls, taking the real part and defining the dimensionless velocity,

$$\hat{u}_2 = \frac{\vec{u}_2}{R_0\omega_{11}}, \qquad (IV.9)$$

yields a nonzero solution near the rigid wall for the various cases considered here.

(i) <u>Nonresonant case</u>

$$\hat{u}_2^{(1)} = -e^{\Omega}\overline{a_1}\cos(\hat{\omega}\tau + \Omega), \qquad (IV.10)$$

where

$$\overline{a_1} = \begin{pmatrix} 0 \\ -\sum\limits_i f_{1i}\dfrac{C_1(\lambda_{1i}R)}{R} g_{1i}\sin\theta \\ \sum\limits_i f_{1i}C_1(\lambda_{1i}R)\acute{g}_{1i}\cos\theta \end{pmatrix}, \quad \text{near} \quad \hat{r} = R, \quad R = 1 \quad \text{or} \quad a,$$

as expressed in the (r, θ, z) cylindrical coordinates, and $\Omega = \dfrac{(\hat{r}-1)l}{\sqrt{2}}$, for $R = 1$, and $\Omega = -\dfrac{(\hat{r}-a)}{\sqrt{2}}l$, for $R = a$, with $l = \sqrt{Re}$. Also $g_{1i} = \dfrac{\cosh\lambda_{1i}(\hat{z}+\hat{h})}{\cosh\lambda_{1i}\hat{h}}$ (Appendix V), and $\acute{g}_{1i} = dg/d\hat{z}$. The velocity near $\hat{z} = -\hat{h}$ is similarly derived from (IV.7), and has the same form as (IV.10) where

$$\overline{a_1} = \begin{pmatrix} \sum\limits_i f_{1i}\dfrac{C_1'(\lambda_{1i}\hat{r})}{\cosh\lambda_{1i}}\cos\theta \\ -\sum\limits_i f_{1i}\dfrac{C_1(\lambda_{1i}\hat{r})}{\hat{r}\cosh\lambda_{1i}}\sin\theta \\ 0 \end{pmatrix}, \quad \text{and} \quad \Omega = -\frac{(\hat{z}+\hat{h})}{\sqrt{2}}l.$$

(ii) <u>Resonant, No Interaction Case</u> (Planar and Nonplanar)

$$\hat{u}_2^{(1)} = -e^{\Omega}[\overline{a_1}\cos(\hat{\omega}\tau + \Omega) + \overline{b_1}\sin(\hat{\omega}\tau + \Omega)], \qquad (IV.11)$$

where Ω and $\overline{a_1}$ are the same as for case (i), with $i = 1$ only, and $\overline{b_1}$ accounts for the nonplanar terms as

$$\overline{b_1} = \begin{pmatrix} 0 \\ \varsigma_{11}\dfrac{C_1(\lambda_{11}R)}{R} g_{11}\cos\theta \\ \varsigma_{11}C_1(\lambda_{11}R)\acute{g}_{11}\sin\theta \end{pmatrix}, \quad \begin{pmatrix} \varsigma_{11}\dfrac{C_1'(\lambda_{11}\hat{r})}{\cosh\lambda_{11}\hat{h}}\sin\theta \\ \varsigma_{11}\dfrac{C_1(\lambda_{11}\hat{r})}{\hat{r}\cosh\lambda_{11}\hat{h}}\cos\theta \\ 0 \end{pmatrix},$$

near $\hat{r} = R$, and $\hat{z} = -\hat{h}$, respectively.

(iii) Resonant, Interacting Case

$$\hat{u}_2^{(1)} = -[e^{\Omega}\overline{a_1}\cos(\hat{\omega}\tau + \Omega) + e^{\Omega\sqrt{2}}\overline{b_2}\sin(2\hat{\omega}\tau + \Omega\sqrt{2})], \qquad (IV.12)$$

where $\overline{a_1}$ and Ω are identical to those of case (ii), and $\overline{b_2}$ is given by,

$$\overline{b_2} = \begin{pmatrix} 0 \\ 2\varsigma_{21}\dfrac{C_2(\lambda_{21}R)}{R}g_{21}\cos 2\theta \\ \varsigma_{21}C_2(\lambda_{21}R)\acute{g}_{21}\sin 2\theta \end{pmatrix}, \quad \begin{pmatrix} \varsigma_{21}\dfrac{C_2'(\lambda_{21}\hat{r})}{\cosh\lambda_{21}\hat{h}}\sin 2\theta \\ 2\varsigma_{21}\dfrac{C_2(\lambda_{21}\hat{r})}{\hat{r}\cosh\lambda_{21}\hat{h}}\cos 2\theta \\ 0 \end{pmatrix},$$

near $\hat{r} = R$, and $\hat{z} = -\hat{h}$, respectively.

2.1.2 Second Order $\vec{u}_2^{(2)}$

Equation (30b) becomes

$$e^{in\omega_e t}[in\omega_e\vec{U}_2^{(2)} - \nu_f\frac{\partial^2\vec{U}_2^{(2)}}{\partial r^2}] = -[(\vec{u}_2^{(1)}\cdot\nabla)\vec{u}_2^{(1)} + (\nabla\tilde{\Phi}^{(1)}\cdot\nabla)\vec{u}_2^{(1)} + (\vec{u}_2^{(1)}\cdot\nabla)\nabla\tilde{\Phi}] \qquad (IV.13)$$

near $r = R_o$, R_i, or near $z = -h$ by replacing $\dfrac{\partial^2\vec{U}_2^{(2)}}{\partial r^2}$ with $\dfrac{\partial^2\vec{U}_2^{(2)}}{\partial z^2}$. Considering the simpler nonresonant case where $\hat{\Phi}^{(1)} = \sum_i f_{1i}C_1(\lambda_{1i}\hat{r})g_{1i}\cos\theta\cos\hat{\omega}\tau$ and $\vec{u}_2^{(1)} = -e^{\Omega}\overline{a_1}\cos(\hat{\omega}\tau + \Omega)$, and using $\nabla = (\dfrac{\partial}{\partial r}, \dfrac{1}{r}\dfrac{\partial}{\partial\theta}, \dfrac{\partial}{\partial z})$, it is found that near $\hat{r} = R$ ($R = 1$ or a)

$$-[(\vec{u}_2^{(1)}\cdot\nabla)\vec{u}_2^{(1)} + (\nabla\tilde{\Phi}^{(1)}\cdot\nabla)\vec{u}_2^{(1)} + (\vec{u}_2^{(1)}\cdot\nabla)\nabla\tilde{\Phi}] = R_0\omega_{11}^2\Big\{\overline{e_{11}}\frac{e^{2\Omega}}{2}[1+ \cos 2(\hat{\omega}\tau + \Omega)] + \overline{e_2}\frac{e^{\Omega}}{2}[\cos\Omega + \cos(2\hat{\omega}\tau + \Omega)]\Big\}, \qquad (IV.14)$$

where:

$$\overline{e_{11}} = -\sum_i\sum_j f_{1i}f_{1j}C_1(\lambda_{1i}R)C_1(\lambda_{1j}R)\begin{pmatrix} 0 \\ \dfrac{\sin 2\theta}{2R}(\dfrac{g_{1i}g_{1j}}{\hat{r}^2} - \acute{g}_{1i}\acute{g}_{1j}) \\ \dfrac{\sin^2\theta}{\hat{r}R}g_{1i}\acute{g}_{1j} + \cos^2\theta\,\acute{g}_{1i}\acute{g}_{1j} \end{pmatrix};$$

$$\overline{e_2} = \overline{e_{21}} + \overline{e_{22}};$$

$$\overline{e_{21}} = -\sum_i \sum_j f_{1i} f_{1j} C_1(\lambda_{1i}\hat{r}) C_1(\lambda_{1j} R) \begin{pmatrix} 0 \\ \frac{\sin 2\theta}{2R}[2\frac{g_{1i}g_{1j}}{\hat{r}^2} - \acute{g}_{1i}\acute{g}_{1j}(1+\frac{R}{r})] \\ \frac{\sin^2\theta}{\hat{r}^2}[g_{1i}\acute{g}_{1j} + \acute{g}_{1i}g_{1j}\frac{\hat{r}}{R}] \\ +2\cos^2\theta \dot{g}_{1i}\ddot{g}_{1j} \end{pmatrix};$$

$$\overline{e_{22}} = -\sum_i \sum_j f_{1i} f_{1j} C_1'(\lambda_{1i}\hat{r}) C_1(\lambda_{1j} R) \begin{pmatrix} \frac{\sin^2\theta}{\hat{r}R} g_{1i}g_{1j} + \cos^2\theta \dot{g}_{1i}\dot{g}_{1j} \\ -\frac{\sin 2\theta}{2R} g_{1i}g_{1j}\frac{l}{\sqrt{2}} \\ \cos^2\theta g_{1i}\acute{g}_{1j}\frac{l}{\sqrt{2}} \end{pmatrix}.$$

Upon substitution of (IV.14) into (IV.13), an analytical solution for $\vec{U}_2^{(2)}$ can be found by introducing the simplifications of the Taylor series expansion near the boundary, i.e.,

$$\begin{aligned} C_1(\lambda_{1i}\hat{r}) &= C_1(\lambda_{1i}R) + (\hat{r}-R)C_1'(\lambda_{1i}R) + \frac{1}{2}(\hat{r}-R)^2 C_1''(\lambda_{1i}R) + \dots; \\ C_1'(\lambda_{1i}\hat{r}) &= C_1'(\lambda_{1i}R) + (\hat{r}-R)C_1''(\lambda_{1i}R) + \frac{1}{2}(\hat{r}-R)^2 C_1'''(\lambda_{1i}R) + \dots \end{aligned} \qquad (IV.15)$$

for $R = 1$ or a. Furthermore, the correction velocity is significant only fo Ω of order 1, which implies that the boundary layer thickness is of order l^{-1}, since $\Omega = \pm\frac{(\hat{r}-R)}{\sqrt{2}}l$ from previous development. Recognizing that $C_1'(\lambda_{1i}R) = 0$ and l is a large number leads to:

$$\begin{aligned} C_1(\lambda_{1i}\hat{r}) &\approx C_1(\lambda_{1i}R); \\ C_1'(\lambda_{1i}\hat{r}) &\approx (\hat{r}-R)C_1''(\lambda_{1i}R). \end{aligned} \qquad (IV.16)$$

Taking $\hat{r} \approx R$ and substituting (IV.16) into expressions for $\overline{e_{11}}$ and $\overline{e_2}$ yields a closed form solution for $\vec{u}_2^{(2)}$. Neglecting terms of order l^{-1}, applying the boundary condition $\vec{u}_2^{(2)} = -\nabla\tilde{\Phi}^{(2)}$ at $\hat{r} = R$, and nondimensionalizing acccording to (IV.9) gives

$$\begin{aligned} \hat{u}_2^{(2)} = \frac{1}{\hat{\omega}}\Big\{ &\frac{\overline{e_{11}^*}}{4}(1-e^{2\Omega}) - \frac{\overline{e_{21}^*}}{2}\sin\Omega + \frac{\overline{e_{22}^*}}{2}\Big[1 + [(1-\Omega)\sin\Omega - \cos\Omega]\Big] \\ &- \sin 2(\hat{\omega}\tau + \Omega)\frac{\overline{e_{11}^*}}{4}e^{2\Omega} + \sin(2\hat{\omega}\tau + \Omega)[\frac{\overline{e_{21}^*}}{2} + \frac{\overline{e_{22}^*}}{2}(\Omega+1)]e^{\Omega} \\ &- \cos(2\hat{\omega}\tau + \Omega)\frac{\overline{e_{22}^*}}{4}e^{\Omega} + \sin(2\hat{\omega}\tau + \Omega\sqrt{2})[\frac{\overline{e_{11}^*}}{4} - \frac{\overline{e_{21}^*}}{2} - \frac{\overline{e_{22}^*}}{2} \\ &- \overline{E_3}]e^{\Omega\sqrt{2}} + \cos(2\hat{\omega}\tau + \Omega\sqrt{2})\frac{\overline{e_{22}^*}}{2}e^{\Omega\sqrt{2}}\Big\}, \end{aligned} \qquad (IV.17)$$

where $\overline{e_{11}^*}$, $\overline{e_{21}^*}$ and $\overline{e_{22}^*}$ are equivalent to $\overline{e_{11}}$, $\overline{e_{21}}$ and $\overline{e_{22}}$ when $C_1(\lambda_{1i}\hat{r})$ is replaced by $C_1(\lambda_{1i}R)$, $C_1'(\lambda_{1i}\hat{r})l/\sqrt{2}$ by $C_1''(\lambda_{1i}R)$, and $\hat{r}$ by R, with

$$\overline{E_3} = \sum_p \begin{pmatrix} 0 \\ -2f_{2p}\dfrac{C_2(\lambda_{2p}R)}{R}\sin 2\theta g_{2p} \\ f_{0p}C_0(\lambda_{0p}R)\acute{g}_{0p} + f_{2p}C_2(\lambda_{2p}R)\acute{g}_{2p}\cos 2\theta \end{pmatrix}.$$

$\hat{u}_2^{(2)}$ thus includes exponentially decaying, $2\hat{\omega}\tau$ terms, and asymptotically growing time independent terms across the boundary layer. The steady component must, however, decay in a region extending further into the flow, and is responsible for the presence of the so-called "streaming layer"[109]. Solving for the corresponding velocity profile however adds another degree of complexity and is not considered in this analysis.

A similar development can be carried out near $\hat{z} = -\hat{h}$. Although an exact solution for (IV.13) can be found, it is easier to make simplifications similar to (IV.15):

$$\begin{aligned} \cosh\lambda_{1i}(\hat{z}+\hat{h}) &\approx 1; \\ \sinh\lambda_{1i}(\hat{z}+\hat{h}) &\approx (\hat{z}+\hat{h}); \end{aligned} \qquad (IV.18)$$

near $\hat{z} = -\hat{h}$. This leads to an expression for $\hat{u}_2^{(2)}$ identical to (IV.17), with now different vectors $\overline{e_{11}^*}$, $\overline{e_{21}^*}$, $\overline{e_{22}^*}$, and $\overline{E_3}$. Applying the procedure to the resonant cases also gives results of the same form, where additional steady and harmonic, $2\hat{\omega}\tau$ terms now account for the nonplanar mode, and expressions in $\hat{\omega}\tau$, $3\hat{\omega}\tau$ and $4\hat{\omega}\tau$ originate from the resonant interactions.

2.2 Reduced Damping Ratio

2.2.1 Contribution from Rigid Boundary

By neglecting terms of order 1, small compared to l, the dissipated energy per cycle from the first term of relation (32) becomes:

$$E_d \approx \mu \int_0^{\frac{2\pi}{\omega_e}} \Big\{ \int_v [(\frac{\partial u_{2z}}{\partial r})^2 + (\frac{\partial u_{2\theta}}{\partial r})^2] dv \Big\} dt, \quad \text{near} \quad r = R_0, \quad R_i; \quad (IV.19)$$

$$E_d \approx \mu \int_0^{\frac{2\pi}{\omega_e}} \Big\{ \int_v [(\frac{\partial u_{2r}}{\partial z})^2 + (\frac{\partial u_{2\theta}}{\partial z}^2] dv \Big\} dt, \quad \text{near} \quad z = -h; \quad (IV.20)$$

where $\vec{u}_2^{(2)} = (u_{2r}, u_{2\theta}, u_{2z})$ in the (r, θ, z) coordinates. By nondimensionalizing the above relations, taking the derivatives with respect to $\hat{r}$ and $\hat{z}$, squaring and integrating over v, the reduced damping ratio $\eta_{r,l}$ is obtained as per relation (34), where the nonlinear terms are listed below for the various cases of resonant and nonresonant conditions:

(i) $AA_1 = \dfrac{1}{4\sqrt{2}}\Big\{\dfrac{(155-16\sqrt{2})}{30}L_{11}^2 + \dfrac{(288-193\sqrt{2}))}{72}L_{22}^2$

$$+\frac{(382\sqrt{2}-567)}{225}L_{11}L_{12}+\frac{(18\sqrt{2}-40)}{3}L_{11}E_3$$
$$+\frac{(72-56\sqrt{2})}{9}L_{22}E_3+8E_3^2\Big\};$$

$$\text{(ii)}\quad AA_2=\frac{1}{4\sqrt{2}}\Big\{\frac{9\sqrt{2}}{10}M_{11}^2+\frac{11\sqrt{2}}{8}M_{22}^2-\frac{13}{25}M_{11}M_{22}+\frac{3\sqrt{2}}{2}M_{31}^2$$
$$+\frac{17\sqrt{2}}{8}M_{32}^2+\frac{(155-43\sqrt{2})}{30}M_{12}^2+\frac{(175-112\sqrt{2})}{6}M_{13}^2$$
$$+\frac{(72-73\sqrt{2})}{18}M_{42}^2+\frac{(511\sqrt{2}-657)}{18}M_{52}^2$$
$$+\frac{(382\sqrt{2}-450)}{225}M_{12}M_{42}+(\frac{272}{3}-\frac{2782\sqrt{2}}{45})M_{13}M_{52}$$
$$+\frac{(18\sqrt{2}-40)}{3}M_{12}E_3+\frac{(76-32\sqrt{2})}{3}M_{13}E_4$$
$$+\frac{(72-56\sqrt{2})}{9}M_{42}E_3+\frac{(252-224\sqrt{2})}{9}M_{52}E_4+8(E_3^2+E_4^2)\Big\};$$

$$(iii)\quad AA_3=AA_1^*+\frac{1}{4\sqrt{2}}\Big\{\frac{(872-225\sqrt{2})}{248}N_{11}^2+\frac{(1647+66\sqrt{2})}{288}N_{22}^2$$
$$+\frac{(178\sqrt{2}-105)}{51}M_{11}N_{11}-\frac{9}{100}M_{22}N_{11}+\frac{(199-135\sqrt{2})}{18}M_{11}N_{22}$$
$$+\frac{(400-253\sqrt{2})}{54}M_{22}N_{22}+\frac{(5608+425\sqrt{2})}{1800}N_{11}N_{22}$$
$$+\frac{(3\sqrt{2}-20)}{6}N_{11}E_7+\frac{5\sqrt{2}}{9}N_{22}E_7+\frac{993}{125}N_{71}^2+\frac{(4\sqrt{2}+\sqrt{6})}{8}N_{72}^2$$
$$+\frac{103}{125}N_{82}^2-\frac{1071}{250}N_{71}N_{72}-\frac{1231}{125}N_{71}N_{82}+\frac{597}{50}N_{72}N_{82}$$
$$+2\sqrt{2}E_7^2+4\sqrt{2}E_5^2+4\sqrt{6}E_6^2\Big\};$$

$$BB_3=2a_1E_5,$$

where $AA_1^*=AA_1$ when considering the first mode only, and L_{11}^2, L_{22}^2, $L_{11}L_{22}$,..., a_1E_5 are complicated expressions involving Bessel and hyperbolic function cross-products as defined in Appendix V, such as,

$$L_{11}^2=D_1(i,j,k,l)\frac{1}{4}[G_1^{11}(i,j,k,l)+G_2^{11}(i,j,k,l)(1+3\lambda_{1j}^2\lambda_{1l}^2+2\lambda_{1l}^2)$$
$$+G_3^{11}(i,j,k,l)]+D_2(i,j,k,l)\frac{1}{4}[\frac{G_1^{11}(i,j,k,l)}{a^6}+G_2^{11}(i,j,k,l)(\frac{1}{a^4}$$
$$+3\lambda_{1j}^2\lambda_{1l}^2+\frac{2\lambda_{1l}^2}{a^2})+\frac{G_3^{11}(i,j,k,l)}{a^2}]+F_{ijkl}\frac{1}{4}[3ID_1^{11}(i,j,k,l)$$
$$+2ID_2^{11}(i,j,k,l)+ID_3^{11}(i,j,k,l)+2ID_4^{11}(i,j,k,l)$$
$$-2ID_5^{11}(i,j,k,l)+2ID_6^{11}(i,j,k,l)+ID_7^{11}(i,j,k,l)];$$

$$L_{22}^2=D_3(i,j,k,l)\frac{1}{4}[G_1^{11}(i,j,k,l)+3G_2^{11}(i,j,k,l)]+D_4(i,j,k,l)$$

$$\frac{1}{4}[\frac{G_1^{11}(i,j,k,l)}{a^2} + 3G_2^{11}(i,j,k,l)] + F_{ijkl}\frac{\lambda_{1j}^2\lambda_{1l}^2}{4}[3ID_9^{11}(i,j,k,l) + ID_{10}^{11}(i,j,k,l)];$$

$$L_{11}L_{22} = D_5(i,j,k,l)\frac{1}{4}[G_1^{11}(i,j,k,l) - (3\lambda_{1j}^2 + 2)G_2^{11}(i,j,k,l)] + D_6(i,j,k,l)\frac{1}{4}[\frac{G_1^{11}(i,j,k,l)}{a^4} - (3\lambda_{1j}^2 + \frac{2}{a^2})G_2^{11}(i,j,k,l)] + F_{ijkl}\frac{\lambda_{1l}^2}{4}[3ID_8^{11}(i,j,k,l) - ID_{11}^{11}(i,j,k,l) - ID_{12}^{11}(i,j,k,l) + 2ID_{13}^{11}(i,j,k,l)];$$

$$L_{11}E_3 = D_7(i,j,2)[GG_1^{12}(i,j,n) - GG_2^{12}(i,j,n) - \frac{(1+\lambda_{1j}^2)}{2}GG_4^{12}(i,j,n)] + D_8(i,j,2)[\frac{GG_1^{12}(i,j,n)}{a^3} - \frac{GG_2^{12}(i,j,n)}{a} - \frac{(1/a^2 + \lambda_{ij}^2)}{2}GG_4^{12}(i,j,n)] - D_7(i,j,0)[GG_4^{10}(i,j,n)(1+\lambda_{1j}^2)] - D_8(i,j,0)[GG_4^{10}(i,j,n)(\frac{1}{a^2} + \lambda_{1j}^2)] - F_{ij0}[IDD_1^{10}(i,j,n) + IDD_2^{10}(i,j,n)] - \frac{F_{ij2}}{2}[IDD_1^{12}(i,j,n) - IDD_2^{12}(i,j,n) - 2IDD_3^{12}(i,j,n) - 2IDD_4^{12}(i,j,n) + 2IDD_6^{12}(i,j,n)];$$

$$LL_{22}E_3 = D_9(i,j,2)[GG_1^{12}(i,j,n) + \frac{1}{2}GG_4^{12}(i,j,n)] + D_{10}(i,j,2)[\frac{GG_1^{12}(i,j,n)}{a^2} + \frac{1}{2}GG_4^{12}(i,j,n)] + [D_9(i,j,0) + D_{10}(i,j,0)]GG_4^{10}(i,j,n) - F_{ij0}LL_{101}(i,n,j) - F_{ij2}[\frac{1}{2}LL_{121}(i,n,j) + JJ_{121}(i,n,j)];$$

$$M_{11}^2 = \frac{C_1^4(\lambda_{11})}{4}\Big\{G_1^{11}s_1^2 + G_2^{11}[(2s_2^2 - s_1^2)(1+2\lambda_{11}^2) + \lambda_{11}^4(2s_2^2+s_1^2)] + G_3^{11}s_1^2\Big\} + \frac{aC_1^4(\lambda_{11}a)}{4}\Big\{\frac{G_1^{11}s_1^2}{a^6} + G_2^{11}[(2s_2^2 - s_1^2)(\frac{1}{a^4} + 2\frac{\lambda_{11}^2}{a^2}) + \lambda_{11}^2(2s_2^2+s_1^2)] + G_3^{11}\frac{s_1^2}{a^2}\Big\} + \frac{1}{4\cosh^4\lambda_{11}\hat{h}}\Big\{ID_1^{11}(2s_2^2+s_1^2) + 2ID_2^{11}(2s_2^2-s_1^2) + 2s_2^2ID_4^{11} + s_1^2(ID_3^{11} - 2ID_5^{11} + 2ID_6^{11} + ID_7^{11})\Big\}.$$

Here:

$$s_1 = f_{11}^2 - \zeta_{11}^2 \quad \text{and} \quad s_2 = f_{11}^2 + \zeta_{11}^2;$$

$$M_{22}^2 = \frac{C_1^2(\lambda_{11})C_1''^2(\lambda_{11})}{4}[G_1^{11}s_2^2 + G_2^{11}(2s_2^2+s_1^2)] + \frac{aC_1^2(\lambda_{11}a)C_1''^2(\lambda_{11}a)}{4}[G_1^{11}\frac{s_2^2}{a^2} + G_2^{11}(2s_2^2+s_1^2)] + \frac{\lambda_{11}^4}{4\cosh^4\lambda_{11}\hat{h}}[(2s_2^2+s_1^2)ID_9^{11} + s_1^2ID_{10}^{11}];$$

$$M_{11}M_{22} = \frac{1}{4}C_1''(\lambda_{11})C_1^3(\lambda_{11})\Big\{G_1^{11}s_1^2 - G_2^{11}[2s_2^2(1+\lambda_{11}^2) + s_1^2\lambda_{11}^2]\Big\}$$

$$+\frac{aC_1''(\lambda_{11}a)C_1^3(\lambda_{11})}{4}\left\{G_{11}\frac{s_1^2}{a^4}-G_2^{11}[2s_2^2(\frac{1}{a^2}+\lambda_{11}^2)+s_1^2\lambda_{11}^2]\right\}$$
$$+\frac{\lambda_{11}^2}{4\cosh^4\lambda_{11}\hat{h}}[ID_8^{11}(2s_2^2+s_1^2)+2ID_{13}^{11}s_2^2-(ID_{11}^{11}+ID_{12}^{11})s_1^2];$$

$$M_{31}^2=4f_{11}^2\varsigma_{11}^2\left\{C_1^4(\lambda_{11})(G_1^{11}+2G_2^{11}+G_3^{11})+\frac{C_1^4(\lambda_{11})}{a}(\frac{G_1^{11}}{a^4}+\frac{2G_2^{11}}{a^2}+G_3^{11})\right\};$$

$$M_{32}^2=2f_{11}^2\varsigma_{11}^2\left\{G_1^{11}[C_1^2(\lambda_{11})C_1''^2(\lambda_{11})+\frac{C_1^2(\lambda_{11}a)C_1''^2(\lambda_{11}a)}{a}]+\frac{\lambda_{11}^4}{\cosh^4\lambda_{11}\hat{h}}ID_{10}^{11}\right\};$$

$$M_{13}^2=f_{11}^2\varsigma_{11}^2\left\{C_1^4(\lambda_{11})[G_1^{11}+G_2^{11}(\lambda_{11}^4-2\lambda_{11}^2-1)+G_3^{11}]+aC_1^4(\lambda_{11}a)[\frac{G_1^{11}}{a^6}+G_2^{11}(\lambda_{11}^4-\frac{2\lambda_{11}^2}{a^2}-\frac{1}{a^2})+\frac{G_3^{11}}{a^2}]+\frac{1}{\cosh^4\lambda_{11}\hat{h}}[ID_1^{11}-2ID_2^{11}+ID_3^{11}-2ID_5^{11}+2ID_6^{11}+ID_7^{11}]\right\};$$

$$M_{52}^2=f_{11}^2\varsigma_{11}^2\left\{[C_1^2(\lambda_{11})C_1''^2(\lambda_{11})+C_1^2(\lambda_{11}a)C_1''^2(\lambda_{11}a)a]G_2^{11}+\frac{\lambda_{11}^4}{\cosh^4\lambda_{11}\hat{h}}[ID_{10}^{11}+ID_9^{11}]\right\};$$

$$M_{13}M_{52}=f_{11}^2\varsigma_{11}^2\left\{C_1^3(\lambda_{11})C_1''(\lambda_{11})G_2^{11}(1-\lambda_{11}^2)+aC_1^3(\lambda_{11}a)C_1''(\lambda_{11}a)\;G_2^{11}(\frac{1}{a^2}-\lambda_{11}^2)+\frac{\lambda_{11}^2}{\cosh^4\lambda_{11}\hat{h}}[ID_8^{11}-ID_{11}^{11}-ID_{12}^{11}]\right\};$$

M_{12}^2, M_{42}^2 and $M_{12}M_{42}$ are identical to M_{11}^2, M_{22}^2 and $M_{11}M_{22}$, respectively, after permuting s_2 and s_1;

$$M_{12}E_3=\sum_n\Big\{f_{2n}s_2[C_2(\lambda_{2n})C_1^2(\lambda_{11})[GG_1^{12}(1,1,n)-GG_2^{12}(1,1,n)+\frac{GG_4^{12}(1,1,n)}{2}(1-\lambda_{11}^2)]+aC_2(\lambda_{2n}a)C_1^2(\lambda_{11}a)[\frac{GG_1^{12}(1,1,n)}{a^4}-\frac{GG_2^{12}(1,1,n)}{a^2}+\frac{GG_4^{12}(1,1,n)}{2}(\frac{1}{a^2}-\lambda_{11}^2)]-f_{0n}s_1[C_0(\lambda_{0n})C_1^2(\lambda_{11})\;GG_4^{10}(1,1,n)(1+\lambda_{11}^2)+aC_0(\lambda_{0n}a)C_1^2(\lambda_{11}a)GG_4^{10}(1,1,n)(\frac{1}{a^2}+\lambda_{11}^2)]-\frac{1}{2\cosh^2\lambda_{11}\hat{h}}\Big[\frac{f_{2n}s_2}{2\cosh\lambda_{2n}\hat{h}}[IDD_1^{12}(1,1,n)-IDD_2^{12}(1,1,n)-2IDD_3^{12}(1,1,n)-2IDD_4^{12}(1,1,n)+2IDD_6^{12}(1,1,n)]+[\frac{2f_{0n}s_1}{\cosh\lambda_{0n}\hat{h}}[IDD_1^{10}(1,1,n)+IDD_2^{10}(1,1,n)]]\Big]\Big\};$$

$$M_{13}E_4 = f_{11}\varsigma_{11}\sum_n \varsigma_{21}\Big\{C_2(\lambda_{2n})C_1^2(\lambda_{11})[-2GG_1^{12}(1,1,n) + 2GG_2^{12}(1,1,n)$$
$$+ GG_4^{12}(1,1,n)(1-\lambda_{11}^2)] + aC_2(\lambda_{2n}a)C_1^2(\lambda_{11}a)[\frac{-2GG_1^{12}(1,1,n)}{a^4}$$
$$+ 2\frac{GG_1^{12}(1,1,n)}{a^2} + GG_4^{12}(1,1,n)(\frac{1}{a^2} - \lambda_{11}^2)]$$
$$- \frac{1}{\cosh^2\lambda_{11}\hat{h}\cosh\lambda_{2n}\hat{h}}[IDD_1^{12}(1,1,n) - IDD_2^{12}(1,1,n)$$
$$+ 2IDD_6^{12}(1,1,n) - 2IDD_3^{12}(1,1,n) - 2IDD_4^{12}(1,1,n)]\Big\};$$

$$M_{42}E_3 = \sum_n \Big\{f_{2n}s_2\Big[C_1''(\lambda_{11})C_1(\lambda_{11})C_2(\lambda_{2n})[GG_1^{12}(1,1,2) + \frac{GG_4^{12}(1,1,n)}{2}]$$
$$+ aC_1''(\lambda_{11}a)C_1(\lambda_{11}a)C_2(\lambda_{2n}a)[\frac{GG_1^{12}(1,1,n)}{a^2} + \frac{GG_4^{12}(1,1,n)}{2}]\Big]$$
$$+ [C_1''(\lambda_{11})C_1(\lambda_{11})C_0(\lambda_{0n}) + aC_1'(\lambda_{11}a)C_1(\lambda_{11}a)C_0(\lambda_{0n}a)]$$
$$GG_4^{10}(1,1,n)f_{0n}s_1 - \frac{\lambda_{11}^2}{\cosh^2\lambda_{11}\hat{h}}\Big[\frac{f_{2n}s_2}{\cosh\lambda_{21}\hat{h}}[\frac{1}{2}LL_{121}(1,n,1)$$
$$+ JJ_{121}(1,n,1)] + \frac{f_{0n}s_1}{\cosh\lambda_{0n}\hat{h}}LL_{101}(1,n,1)\Big];$$

$$M_{52}E_4 = f_{11}\varsigma_{11}\sum_n \varsigma_{21}\Big\{[C_1(\lambda_{11})C_1''(\lambda_{11})C_2(\lambda_{2n})$$
$$+ aC_1(\lambda_{11}a)C_1''(\lambda_{11}a)C_2(\lambda_{2n}a)]GG_4^{12}(1,1,n)$$
$$- \frac{\lambda_{11}^2}{\cosh^2\lambda_{11}\hat{h}\cosh\lambda_{2n}\hat{h}}[LL_{121}(1,n,1) + 2JJ_{121}(1,n,1)]\Big\};$$

$$N_{11}^2 = \varsigma_{21}^4\Big\{C_2^4(\lambda_{21})[76G_1^{22} + G_2^{22}(\frac{3}{4}\lambda_{21}^4 + 2\lambda_{21}^2 - 32) + 4G_3^{22}] + aC_2^4(\lambda_{21}a)$$
$$[76\frac{G_1^{22}}{a^6} + G_2^{22}(\frac{3}{4}\lambda_{21}^4 + 2\frac{\lambda_{21}^2}{a^2} - \frac{32}{a^4}) + 4\frac{G_3^{22}}{a^2}] + \frac{1}{\cosh^4\lambda_{21}\hat{h}}[\frac{3}{4}ID_1^{22}$$
$$+ 2ID_2^{22} + ID_3^{22} + 5ID_4^{22} - 2ID_5^{22} + 8ID_6^{22} + 16ID_7^{22}]\Big\};$$

$$N_{22}^2 = \varsigma_{21}^4\Big\{C_2^2(\lambda_{21})C_2''^2(\lambda_{21})[4G_1^{22} + G_2^{22}] + aC_2^2(\lambda_{21}a)C_2''^2(\lambda_{21}a)[4\frac{G_1^{22}}{a^2}$$
$$+ G_2^{22}] + \frac{\lambda_{21}^2}{\cosh^4\lambda_{21}\hat{h}}[\frac{3}{4}ID_{12}^{22} + 4ID_{10}^{22}]\Big\};$$

$$M_{11}N_{11} = 2f_{11}^2\varsigma_{21}^2\Big\{C_1^2(\lambda_{11})C_2^2(\lambda_{21})G_1^{12}(\frac{\lambda_{21}^2}{4} + 1)(\lambda_{11}^2 + 1)$$
$$+ aC_1^2(\lambda_{11}a)C_2^2(\lambda_{21}a)G_1^{12}(\frac{\lambda_{21}^2}{4} + \frac{1}{a^2})(\lambda_{11}^2 + \frac{1}{a^2})$$
$$+ [\frac{ID_1^{21} + ID_2^{21} + 4ID_2^{12} + ID_4^{12}}{4\cosh^2\lambda_{11}\hat{h}\cosh^2\lambda_{21}\hat{h}}]\Big\};$$

$$M_{22}N_{11} = -2f_{11}^2\varsigma_{21}^2\Big\{C_1(\lambda_{11})C_1''(\lambda_{11})C_2^2(\lambda_{21})G_2^{12}(\frac{\lambda_{21}^2}{4}+1)$$
$$+aC_1(\lambda_{11}a)C_1''(\lambda_{11}a)C_2^2(\lambda_{21}a)G_2^{12}(\frac{\lambda_{21}^2}{4}+\frac{1}{a^2})$$
$$+\lambda_{11}^2\frac{[I_8(2,1,2,1)]}{4\cosh^2\lambda_{11}\hat{h}\cosh^2\lambda_{21}\hat{h}}\Big\};$$

$$M_{11}N_{22} = -f_{11}^2\varsigma_{21}^2\Big\{C_1^2(\lambda_{11})C_2''(\lambda_{21})C_2(\lambda_{21})G_2^{12}\frac{(\lambda_{11}^2+1)}{2}$$
$$+aC_1^2(\lambda_{11}a)C_2''(\lambda_{21}a)C_2(\lambda_{21}a)G_2^{12}\frac{(\lambda_{11}^2+1/a^2)}{2}$$
$$+\lambda_{21}^2\frac{[I_8(1,2,1,2)+I_6(1,2,1,2)]}{\cosh^2\lambda_{11}\hat{h}\cosh^2\lambda_{21}\hat{h}}\Big\};$$

$$M_{22}N_{22} = \frac{f_{11}^2\varsigma_{21}^2}{2}\Big\{[C_1(\lambda_{11})C_1''(\lambda_{11})C_2(\lambda_{21})C_2''(\lambda_{21})$$
$$+aC_1(\lambda_{11}a)C_1''(\lambda_{11}a)C_2(\lambda_{21}a)C_2''(\lambda_{21}a)]G_1^{12}$$
$$-\frac{\lambda_{11}^2\lambda_{21}^2}{\cosh^2\lambda_{11}\hat{h}\cosh^2\lambda_{21}\hat{h}}ID_9^{12}\Big\};$$

$$N_{11}N_{22} = \varsigma_{21}^4\Big\{C_2^3(\lambda_{21})C_2''(\lambda_{21})[16G_1^{22}+G_2^{22}(\frac{5}{4}\lambda_{21}^2-1)]$$
$$+aC_2^3(\lambda_{21}a)C_2''(\lambda_{21}a)[\frac{16G_1^{22}}{a^4}+G_2^{22}(\frac{5}{4}\lambda_{21}^2-\frac{1}{a^2})]$$
$$-\lambda_{21}^2\frac{[ID_8^{22}/2+8I_6(2,2,2,2)-2ID_{11}^{22}-8ID_{12}^{22}]}{\cosh^4\lambda_{21}\hat{h}}\Big\};$$

$$N_{11}E_7 = -\varsigma_{21}^2\sum_n\Big\{C_2^2(\lambda_{21})\Big[d_{4n}[8GG_1^{24}(1,1,n)-8GG_2^{24}(1,1,n)$$
$$+GG_4^{24}(1,1,n)(2-\frac{\lambda_{21}^2}{2})]C_4(\lambda_{41})+e_{4n}GG_4^{20}(1,1,n)(2$$
$$+\frac{\lambda_{21}^2}{2})C_0(\lambda_{0n})\Big]+aC_1^2(\lambda_{21}a)\Big[d_{4n}[8GG_1^{24}(1,1,n)-\frac{8GG_2^{24}(1,1,n)}{a^2}$$
$$+GG_4^{24}(1,1,n)(\frac{2}{a^2}-\frac{\lambda_{21}^2}{2})]C_4(\lambda_{4n}a)+e_{4n}GG_4^{20}(1,1,n)(\frac{2}{a^2}$$
$$+\frac{\lambda_{21}^2}{2})C_0(\lambda_{0n}a)\Big]+\frac{1}{\cosh^2\lambda_{21}\hat{h}}\Big[\frac{d_{4n}}{\cosh\lambda_{4n}\hat{h}}[-\frac{IDD_1^{24}(1,1,n)}{2}$$
$$+4IDD_2^{24}(1,1,n)-4IDD_3^{24}(1,1,n)-16IDD_4^{24}(1,1,n)]$$
$$+\frac{e_4n}{\cosh\lambda_{0n}\hat{h}}[IDD_1^{20}(1,1,n)+4IDD_2^{20}(1,1,n)]\Big]\Big\};$$

$$N_{22}E_7 = \varsigma_{21}^2\sum_n\Big\{C_2(\lambda_{21})C_2''(\lambda_{21})\Big[-d_{4n}C_4(\lambda_{4n})[8GG_1^{24}(1,1,n)$$
$$+\frac{GG_4^{24}(1,1,n)}{2}]-d_{4n}C_4(\lambda_{4n}a)a[\frac{8GG_1^{24}(1,1,n)}{a^2}+\frac{GG_4^{24}(1,1,n)}{2}]$$

$$+ e_{4n}GG_4^{20}[C_0(\lambda_{0n}) + aC_0(\lambda_{0n}a)]\Big] + \frac{\lambda_{21}^2}{\cosh^2\lambda_{21}\hat{h}}\Big[\frac{d_{4n}}{\cosh\lambda_{4n}\hat{h}}$$

$$[\frac{LL_{242}(1,n,1)}{2} - 8JJ_{242}(1,n,1)] + \frac{e_{4n}}{\cosh\lambda_{0n}\hat{h}}LL_{202}(1,n,1)]\Big]\Big\}.$$

Now, recognizing $g_1^2\dot{g}_2^2 \approx 4\dot{g}_1^2 g_2^2$ due to the resonant interaction gives:

$$N_{71}^2 = f_{11}^2\varsigma_{21}^2\Big\{C_2^2(\lambda_{21})C_1^2(\lambda_{11})[2G_1^{12} + \frac{G_3^{12}}{2} + (50 + 32\lambda_{11}^4)G_2^{12}]$$

$$+ aC_2^2(\lambda_{21}a)C_1^2(\lambda_{11}a)[2\frac{G_1^{12}}{a^6} + \frac{G_3^{12}}{2a^2} + (\frac{50}{a^4} + 32\lambda_{11}^4)G_2^{12}]$$

$$+ \frac{1}{\cosh^2\lambda_{11}\hat{h}\cosh^2\lambda_{21}\hat{h}}[\frac{I_8(1,2,1,2)}{8} + \frac{I_8(2,1,2,1)}{2}$$

$$+ I_8(1,1,2,2) + \frac{3}{2}I_9(2,2,1,1) + 10I_9(1,1,2,2) - 4I_9(1,2,1,2)$$

$$+ \frac{11}{4}ID_3^{12} - 8ID_5^{12} - ID_5^{21} + 4ID_6^{21} + 8ID_6^{12} + 11ID_7^{12}]\Big\};$$

$$N_{72}^2 = f_{11}^2\varsigma_{21}^2\Big\{C_2''^2(\lambda_{21})C_1^2(\lambda_{11})[\frac{G_1^{12} + G_2^{12}}{2}] + aC_2''^2(\lambda_{21}a)C_1^2(\lambda_{11}a)[\frac{G_1^{12}}{2a^2}$$

$$+ \frac{G_2^{12}}{2}] + \lambda_{21}^4\frac{[I_5(1,1,2,2) + I_2(1,2,1,2)]}{2\cosh^2\lambda_{21}\hat{h}\cosh^2\lambda_{11}\hat{h}}\Big\};$$

$$N_{82}^2 = f_{11}^2\varsigma_{21}^2\Big\{C_2^2(\lambda_{21})C_1''^2(\lambda_{21})(8G_1^{12} + 2G_2^{12}) + aC_2^2(\lambda_{21}a)C_1''^2(\lambda_{11}a)(\frac{8G_1^{12}}{a^2}$$

$$+ 2G_2^{12}) + \lambda_{11}^4\frac{[I_5(2,2,1,1) + 2I_2(1,2,1,2)]}{2\cosh^2\lambda_{21}\hat{h}\cosh^2\lambda_{11}\hat{h}}\Big\};$$

$$N_{71}N_{72} = f_{11}^2\varsigma_{21}^2\Big\{C_2(\lambda_{21})C_2''(\lambda_{21})C_1^2(\lambda_{11})G_1^{12}(\frac{1}{2} + 4\lambda_{11}^2)$$

$$+ aC_2(\lambda_{21}a)C_2''(\lambda_{21}a)C_1^2(\lambda_{11}a)G_1^{12}(\frac{1}{2a^2} + 4\lambda_{11}^2)$$

$$+ \lambda_{21}^2\frac{[I_6(1,2,1,2) - 2I_7(2,1,2,1) - 4I_8(1,2,1,2)]}{2\cosh^2\lambda_{11}\hat{h}\cosh^2\lambda_{21}\hat{h}}\Big\};$$

$$N_{71}N_{82} = f_{11}^2\varsigma_{21}^2\Big\{C_2^2(\lambda_{21})C_1''(\lambda_{11})C_1(\lambda_{11})(4G_1^{12} + 40G_2^{12})$$

$$+ aC_2^2(\lambda_{21}a)C_1''(\lambda_{11}a)C_1(\lambda_{11}a)(\frac{4G_1^{12}}{a^4} + \frac{40G_2^{12}}{a^2})$$

$$+ \lambda_{11}^2\frac{[I_6(2,2,1,1) + 5I_6(1,2,1,2) - 8I_7(1,2,1,2) - 4I_4(1,2,1,2)]}{2\cosh^2\lambda_{21}\hat{h}\cosh^2\lambda_{11}\hat{h}}\Big\};$$

$$N_{72}N_{82} = f_{11}^2\varsigma_{21}^2\Big\{[C_2''(\lambda_{21})C_1''(\lambda_{11})C_2(\lambda_{21})C_1(\lambda_{11})$$

$$+ aC_2''(\lambda_{21}a)C_1''(\lambda_{11}a)C_2(\lambda_{21}a)C_1(\lambda_{11}a)]8G_1^{12}$$

$$+ \lambda_{21}^2\lambda_{11}^2\frac{I_5(1,2,1,2)}{2\cosh^2\lambda_{21}\hat{h}\cosh^2\lambda_{11}\hat{h}}\Big\};$$

$$E_3^2 = \sum_n\sum_p\Big\{f_{2n}f_{2p}F^*(2,n,p) + 2f_{0n}f_{0p}F^*(0,n,p)\Big\};$$

where F^* is a function defined as:

$$F^*(i,n,p) = C_i(\lambda_{in})C_i(\lambda_{ip})[i^2\beta_{ii}(n,p) + \beta^*_{ii}(n,p)] + aC_i(\lambda_{in}a)C_i(\lambda_{ip}a)$$
$$[\frac{i^2\beta_{ii}(n,p)}{a^2} + \beta^*_{ii}(n,p)] + I2_{ii}(n,p) + i^2 J2_{ii}(n,p);$$

$$E_4^2 = \sum_n\sum_p \varsigma_{2n}\varsigma_{2p}F^*(2,n,p);$$

$$E_5^2 = \sum_n\sum_p [d_{1n}d_{1p}F^*(1,n,p) + e_{1n}e_{1p}F^*(3,n,p)];$$

$$E_6^2 = \sum_n\sum_p [d_{3n}d_{3p}F^*(3,n,p) + e_{3n}e_{3p}F^*(1,n,p)];$$

$$E_7^2 = \sum_n\sum_p [d_{4n}d_{4p}F^*(4,n,p) + e_{4n}e_{4p}F^*(0,n,p)];$$

$$a_1E_5 = f_{11}\sum_n d_{1n}F^*(1,1,n).$$

β and β^* functions are defined in Appendix V.

2.2.2 Free Surface Contibution

The vector $\overline{n} = (-\frac{\partial\eta_f}{\partial r}, -\frac{1}{r}\frac{\partial\eta_f}{\partial\theta}, 1)$ is normal to the free surface. Expressing η_f in terms of $\tilde{\Phi}$ and d^2x/dt^2 using relation (I.2), and substituting into the second term of equation (32) yields

$$E_d = \mu\int_0^{\frac{2\pi}{\omega_e}}\left\{\int_{z=0}\frac{\partial(\nabla\tilde{\Phi})^2}{\partial z}r\,d\theta dr\right\}dt + \text{higher order terms.} \qquad (IV.21)$$

Integration of the above equation gives the leading order terms presented in (35).

2.3 Energy Ratio

The procedure outlined in section 4.3 of Chapter 2 leads to the following equalities:

$$\begin{aligned}\hat{\epsilon}^{3q}BBB_n = \frac{\hat{\omega}}{2\pi}\int_0^{\frac{2\pi}{\hat{\omega}}}\Big\{\int_S 2[\alpha_{11}\lambda_{11}\frac{\partial\hat{\Phi}^{(1)}}{\partial\tau}\frac{\partial\hat{\Phi}^{(2)}}{\partial\tau} \\ + (\alpha_{11}\lambda_{11})^2(\frac{\partial\hat{\Phi}^{(1)}}{\partial\tau})^2\frac{\partial^2\hat{\Phi}^{(1)}}{\partial\hat{z}\partial\tau}]\hat{r}d\theta d\hat{r} \\ + \int_v \nabla\hat{\Phi}^{(1)}\cdot\nabla\hat{\Phi}^{(2)}\hat{r}d\theta d\hat{r}d\hat{z}\Big\}d\tau; \qquad (IV.22)\end{aligned}$$

$$\begin{aligned}\hat{\epsilon}^{4q}AAA_n = \frac{\hat{\omega}}{2\pi}\int_0^{\frac{2\pi}{\hat{\omega}}}\Big\{\int_S \alpha_{11}\lambda_{11}[(\frac{\partial\hat{\Phi}^{(2)}}{\partial\tau})^2 + (\alpha_{11}\lambda_{11})^2(\frac{\partial\hat{\Phi}^{(1)}}{\partial\tau})^2\frac{\partial^2\hat{\Phi}^{(1)}}{\partial\hat{z}\partial\tau} \\ - \frac{1}{4}(\nabla\hat{\Phi}^{(1)})^4 - 2\frac{\partial\hat{\Phi}^{(2)}}{\partial\tau}\frac{\partial\hat{\Phi}^{(1)}}{\partial\tau}\frac{\partial^2\hat{\Phi}^{(1)}}{\partial\hat{z}\partial\tau} + \alpha_{11}\lambda_{11}(\frac{\partial\hat{\Phi}^{(1)}}{\partial\tau})^2\nabla\hat{\Phi}^{(1)} \\ \cdot\frac{\partial(\nabla\hat{\Phi}^{(1)})}{\partial\hat{z}}]\hat{r}d\theta d\hat{r} + \int_v(\nabla\hat{\Phi}^{(2)})^2\hat{r}d\theta d\hat{r}d\hat{z}\Big\}d\tau, \qquad (IV.23)\end{aligned}$$

For the particular cases ($n = 1, 2, 3$):

(i) $BBB_1 = 0;$

$$
\begin{aligned}
AAA_1 = {} & 2VS(f_{0n}, f_{0m}) + VS(f_{2n}, f_{2m}) - (\alpha_{11}\lambda_{11})^2\hat{\omega}^3 \\
& \sum_i \sum_j \sum_n \alpha_{1i}\lambda_{1i} f_{1i} f_{1j} [2f_{0n} KK_{110}(1,1,n) + f_{2n} KK_{112}(1,1,n)] \\
& - \frac{\alpha_{11}\lambda_{11}}{64} \sum_i \sum_j \sum_k \sum_l f_{1i} f_{1j} f_{1k} f_{1l} \Big\{ 9[ID_{14}^{11}(i,j,k,l) \\
& + ID_{12}^{11}(i,j,k,l)] + 6ID_{13}^{11}(i,j,k,l) + ID_{15}^{11}(i,j,k,l)[9(\alpha_{1i}\alpha_{1j} \\
& \alpha_{1k}\alpha_{1l}\lambda_{1i}\lambda_{1j}\lambda_{1k}\lambda_{1l}) - 6\hat{\omega}^2(\alpha_{1i}\lambda_{1i}\lambda_{1j}^2 + \alpha_{1i}\lambda_{1j}\lambda_{1i}^2)\alpha_{11}\lambda_{11} \\
& - 36\hat{\omega}^4(\alpha_{11}\lambda_{11})^2(\alpha_{1i}\alpha_{1j}\lambda_{1i}\lambda_{1j})] + 6ID_{16}^{11}(i,j,k,l)[3\alpha_{1k}\lambda_{1k}\alpha_{1l}\lambda_{1l} \\
& - \hat{\omega}^2\alpha_{11}\lambda_{11}(\alpha_{1i}\lambda_{1i} + \alpha_{1j}\lambda_{1j}] + 2ID_{10}(i,j,k,l)[3\alpha_{1k}\lambda_{1k}\alpha_{1l}\lambda_{1l} \\
& - \hat{\omega}^2\alpha_{11}\lambda_{11}(\alpha_{1i}\lambda_{1i} + \alpha_{1j}\lambda_{1j})] \Big\},
\end{aligned}
$$

(ii) $BBB_2 = 0;$

$$
\begin{aligned}
AAA_2 = {} & 2VS(f_{0n}, f_{0m}) + VS(f_{2n}, f_{2m}) + VS(\varsigma_{2n}, \varsigma_{2m}) - (\alpha_{11}\lambda_{11}\hat{\omega})^3 \\
& [2f_{0n}(f_{11}^2 - \varsigma_{11}^2) KK_{110}(1,1,n) + f_{2n}(f_{11}^2 + \varsigma_{11}^2) KK_{112}(1,1,n)] \\
& - \frac{\alpha_{11}\lambda_{11}}{64} \Big\{ [9(f_{11}^4 + \varsigma_{11}^4) + 6f_{11}^2\varsigma_{11}^2](ID_{14}^{11} + ID_{12}^{11}) + 2[3(f_{11}^4 + \varsigma_{11}^4) + \\
& 2f_{11}^2\varsigma_{11}^2] ID_{13}^{11} + (\alpha_{11}\lambda_{11})^4 ID_{15}^{11}[3(f_{11}^4 + \varsigma_{11}^4)(3 - \frac{4\hat{\omega}^2}{\alpha_{11}^2} - 12\hat{\omega}^4) + 2f_{11}^2\varsigma_{11}^2 \\
& (3 - \frac{8\hat{\omega}^2}{\alpha_{11}^2} - 12\hat{\omega}^4)] + (\alpha_{11}\lambda_{11})^2 ID_{16}^{11}[6(f_{11}^4 + \varsigma_{11}^4)(3 - 2\hat{\omega}^2) \\
& + 4f_{11}^2\varsigma_{11}^2(3 - 4\hat{\omega}^2)] + (\alpha_{11}\lambda_{11})^2 ID_{10}^{11}[2(f_{11}^4 + \varsigma_{11}^4)(3 - 2\hat{\omega}^2) \\
& + 8f_{11}^2\varsigma_{11}62(1 + 2\hat{\omega}^2)],
\end{aligned}
$$

(iii)

$$
\begin{aligned}
BBB_3 = {} & 2[f_{11}WS(d_{1n}, d_{1m}) + \varsigma_{21}(f_{2n}, f_{2m})](1 + \alpha_{11}\lambda_{11}\hat{\omega}^2) \\
& - 6(\alpha_{11}\lambda_{11}\hat{\omega})^3 f_{11}^2\varsigma_{21} KK_{121}(1,1,1);
\end{aligned}
$$

$$
\begin{aligned}
AAA_3 = {} & AAA_1^* + VS(d_{1n}, d_{1m}) + VS(e_{1n}, e_{1m}) + VS(e_{3n}, e_{3m}) \\
& + VS(d_{3n}, d_{3m}) + 2VS(e_{4n}, e_{4m}) + VS(d_{4n}, d_{4m}) \\
& - (\alpha_{11}\lambda_{11}\hat{\omega})^3 \sum_n \Big\{ 32\varsigma_{21}^2[2e_{4n}KK_{220}(1,1,n) + d_{4n}KK_{224}(1,1,n)] + \\
& \frac{5}{2} f_{11}\varsigma_{21}[(d_{1n} - 3e_{3n})KK_{121}(1,1,n) + (e_{1n} - 3d_{3n}) \\
& KK_{123}(1,1,n)] \Big\} - \frac{\alpha_{11}\lambda_{11}}{64} \Big\{ \varsigma_{21}^4[9(ID_{14}^{22} + 16ID_{12}^{22}) + 24ID_{13}^{22} + \\
& (\alpha_{21}\lambda_{21})^4 ID_{15}^{22}(18 - 12\hat{\omega}^2) + (\alpha_{21}\lambda_{21})^2 ID_{10}^{22}(24 - 16\hat{\omega}^2)] \\
& + f_{11}^2\varsigma_{21}^2[2(ID_{14}^{12} + 4ID_{12}^{12}) + 8ID_{17}^{12} + 2ID_{17}^{21} + 16(\alpha_{11}\lambda_{11})^4 ID_{15}^{11}(2 \\
& - 34\hat{\omega}^2 - \frac{21}{4}\hat{\omega}^4) + 4(\alpha_{11}\lambda_{11})^2 ID_{16}^{12}(8 - 2\hat{\omega}^2) + 4(\alpha_{11}\lambda_{11})^2 ID_{16}^{21}(\frac{1}{2} \\
& - 32\hat{\omega}^2) + 40(\alpha_{11}\lambda_{11})^2 ID_{10}^{12}(1 - \hat{\omega}^2) + 16(\alpha_{11}\lambda_{11})^2 ID_{13}^{12} \Big\},
\end{aligned}
$$

where:

$$AAA_1^* = AAA_1 \quad \text{for the case where } i = j = k = l = 1;$$

$$VS(r_{in}, r_{im}) = (\alpha_{11}\lambda_{11}\hat{\omega}^2)\sum_n [i^2 r_{in}^2 \frac{\Lambda_{jn}}{\lambda_{jn}^2}] + WS(r_{in}, r_{im});$$

$$WS(r_{in}, r_{im}) = \sum_n \sum_m r_{in} r_{im} \beta_{ij}(n,m)[IA_{jj}(n,m) + j^2 JA_{jj}(n,m) + \alpha_{jn}^2 \Lambda_{jn}];$$

with $j = i$ when $r_{in} = f_{on}, f_{2n}, d_{1n}, d_{3n}, d_{4n}$,
and $j = 0, 1, 3$ for $r_{in} = e_{4n}, e_{3n}$, and e_{1n}, respectively.

APPENDIX V: USEFUL BESSEL AND HYPERBOLIC FUNCTION RELATIONS AND DEFINITIONS

1. Bessel Functions

1.1 Orthonogality Condition

$$\int_a^1 C_n(\lambda_{np}\hat{r})C_m(\lambda_{mq}\hat{r})\hat{r}d\hat{r} = 0, \quad \text{if} \quad \lambda_{np} \neq \lambda_{mq};$$

$$= \frac{\Lambda_{np}}{\lambda_{np}^2}, \quad \text{if} \quad \lambda_{np} = \lambda_{mq},$$

$$\text{where} \quad \Lambda_{np} = \frac{1}{2}\left\{(\lambda_{np}^2 - n^2)C_n^2(\lambda_{np}) - (\lambda_{np}^2 a^2 - n^2)C_n^2(\lambda_{np}a)\right\}.$$

1.2 Cross-Product Integrals

$$I_1(i,j,k,l) = \int_a^1 C_i''(\lambda_{i1}\hat{r})C_j'(\lambda_{j1}\hat{r})C_k'(\lambda_{k1}\hat{r})C_l(\lambda_{l1}\hat{r})\hat{r}d\hat{r};$$

$$I_2(i,j,k,l) = \int_a^1 C_i(\lambda_{i1}\hat{r})C_j(\lambda_{j1}\hat{r})C_k(\lambda_{k1}\hat{r})C_l(\lambda_{l1}\hat{r})\frac{d\hat{r}}{\hat{r}};$$

$$I_3(i,j,k,l) = \int_a^1 C_i(\lambda_{i1}\hat{r})C_j(\lambda_{j1}\hat{r})C_k(\lambda_{k1}\hat{r})C_l(\lambda_{l1}\hat{r})\hat{r}d\hat{r};$$

$$I_4(i,j,k,l) = \int_a^1 C_i(\lambda_{i1}\hat{r})C_j(\lambda_{j1}\hat{r})C_k(\lambda_{k1}\hat{r})C_l(\lambda_{l1}\hat{r})\frac{d\hat{r}}{\hat{r}^3};$$

$$I_5(i,j,k,l) = \int_a^1 C_i'(\lambda_{i1}\hat{r})C_j'(\lambda_{j1}\hat{r})C_k(\lambda_{k1}\hat{r})C_l(\lambda_{l1}\hat{r})\hat{r}d\hat{r};$$

$$I_6(i,j,k,l) = \int_a^1 C_i'(\lambda_{i1}\hat{r})C_j'(\lambda_{j1}\hat{r})C_k(\lambda_{k1}\hat{r})C_l(\lambda_{l1}\hat{r})\frac{d\hat{r}}{\hat{r}};$$

$$I_7(i,j,k,l) = \int_a^1 C_i'(\lambda_{i1}\hat{r})C_j(\lambda_{j1}\hat{r})C_k(\lambda_{k1}\hat{r})C_l(\lambda_{l1}\hat{r})\frac{d\hat{r}}{\hat{r}^2};$$

$$I_8(i,j,k,l) = \int_a^1 C_i''(\lambda_{i1}\hat{r})C_j'(\lambda_{j1}\hat{r})C_k''(\lambda_{k1}\hat{r})C_l'(\lambda_{l1}\hat{r})\hat{r}d\hat{r};$$

$$I_9(i,j,k,l) = \int_a^1 C_i'(\lambda_{i1}\hat{r})C_j'(\lambda_{j1}\hat{r})C_k(\lambda_{k1}\hat{r})C_l(\lambda_{l1}\hat{r})\frac{d\hat{r}}{\hat{r}^3}.$$

In the following, (i,j,k,l) is omitted when $i = j = k = l = 1$.

$$ID_1^{nm}(i,j,k,l) = \int_a^1 C_n''(\lambda_{ni}\hat{r})C_n'(\lambda_{nj}\hat{r})C_m''(\lambda_{mk}\hat{r})C_m'(\lambda_{ml}\hat{r})\hat{r}d\hat{r};$$

$$ID_2^{nm}(i,j,k,l) = \int_a^1 C_n''(\lambda_{ni}\hat{r})C_n'(\lambda_{nj}\hat{r})C_m'(\lambda_{mk}\hat{r})C_m(\lambda_{ml}\hat{r})\frac{d\hat{r}}{\hat{r}};$$

$$ID_3^{nm}(i,j,k,l) = \int_a^1 C_n'(\lambda_{ni}\hat{r})C_n'(\lambda_{nj}\hat{r})C_m'(\lambda_{mk}\hat{r})C_m'(\lambda_{ml}\hat{r})\frac{d\hat{r}}{\hat{r}};$$

$$ID_4^{nm}(i,j,k,l) = \int_a^1 C_n'(\lambda_{ni}\hat{r})C_n(\lambda_{nj}\hat{r})C_m'(\lambda_{mk}\hat{r})C_m(\lambda_{ml}\hat{r})\frac{d\hat{r}}{\hat{r}^3};$$

$$ID_5^{nm}(i,j,k,l) = \int_a^1 C_n'(\lambda_{ni}\hat{r})C_n'(\lambda_{nj}\hat{r})C_m'(\lambda_{mk}\hat{r})C_m(\lambda_{ml}\hat{r})\frac{d\hat{r}}{\hat{r}^2};$$

$$ID_6^{nm}(i,j,k,l) = \int_a^1 C_n'(\lambda_{ni}\hat{r})C_n(\lambda_{nj}\hat{r})C_m(\lambda_{mk}\hat{r})C_m(\lambda_{ml}\hat{r})\frac{d\hat{r}}{\hat{r}^4};$$

$$ID_7^{nm}(i,j,k,l) = \int_a^1 C_n(\lambda_{ni}\hat{r})C_n(\lambda_{nj}\hat{r})C_m(\lambda_{mk}\hat{r})C_m(\lambda_{ml}\hat{r})\frac{d\hat{r}}{\hat{r}^5};$$

$$ID_8^{nm}(i,j,k,l) = \int_a^1 C_n''(\lambda_{ni}\hat{r})C_n'(\lambda_{nj}\hat{r})C_m'(\lambda_{mk}\hat{r})C_m(\lambda_{ml}\hat{r})\hat{r}d\hat{r};$$

$$ID_9^{nm}(i,j,k,l) = \int_a^1 C_n'(\lambda_{ni}\hat{r})C_n(\lambda_{nj}\hat{r})C_m'(\lambda_{mk}\hat{r})C_m(\lambda_{ml}\hat{r})\hat{r}d\hat{r};$$

$$ID_{10}^{nm}(i,j,k,l) = \int_a^1 C_n(\lambda_{ni}\hat{r})C_n(\lambda_{nj}\hat{r})C_m(\lambda_{mk}\hat{r})C_m(\lambda_{ml}\hat{r})\frac{d\hat{r}}{\hat{r}};$$

$$ID_{11}^{nm}(i,j,k,l) = \int_a^1 C_n'(\lambda_{ni}\hat{r})C_n(\lambda_{nj}\hat{r})C_m(\lambda_{mk}\hat{r})C_m(\lambda_{ml}\hat{r})\frac{d\hat{r}}{\hat{r}^2};$$

$$ID_{12}^{nm}(i,j,k,l) = \int_a^1 C_n(\lambda_{ni}\hat{r})C_n(\lambda_{nj}\hat{r})C_m(\lambda_{mk}\hat{r})C_m(\lambda_{ml}\hat{r})\frac{d\hat{r}}{\hat{r}^3};$$

$$ID_{13}^{nm}(i,j,k,l) = \int_a^1 C_n'(\lambda_{ni}\hat{r})C_n(\lambda_{nj}\hat{r})C_m'(\lambda_{mk}\hat{r})C_m(\lambda_{ml}\hat{r})\frac{d\hat{r}}{\hat{r}};$$

$$ID_{14}^{nm}(i,j,k,l) = \int_a^1 C_n'(\lambda_{ni}\hat{r})C_n'(\lambda_{nj}\hat{r})C_m'(\lambda_{mk}\hat{r})C_m'(\lambda_{ml}\hat{r})\hat{r}d\hat{r};$$

$$ID_{15}^{nm}(i,j,k,l) = \int_a^1 C_n(\lambda_{ni}\hat{r})C_n(\lambda_{nj}\hat{r})C_m(\lambda_{mk}\hat{r})C_m(\lambda_{ml}\hat{r})\hat{r}d\hat{r};$$

$$ID_{16}^{nm}(i,j,k,l) = \int_a^1 C_n'(\lambda_{ni}\hat{r})C_n'(\lambda_{nj}\hat{r})C_m(\lambda_{mk}\hat{r})C_m(\lambda_{ml}\hat{r})\hat{r}d\hat{r};$$

$$ID_{17}^{nm}(i,j,k,l) = \int_a^1 C_n'(\lambda_{ni}\hat{r})C_n'(\lambda_{nj}\hat{r})C_m(\lambda_{mk}\hat{r})C_m(\lambda_{ml}\hat{r})\frac{d\hat{r}}{\hat{r}};$$

$$LL_{nmp}(i,j,k) = \int_a^1 C_n'(\lambda_{ni}\hat{r})C_m'(\lambda_{mj}\hat{r})C_p(\lambda_{pk}\hat{r})\hat{r}d\hat{r};$$

$$JJ_{nmp}(i,j,k) = \int_a^1 C_n(\lambda_{ni}\hat{r})C_m(\lambda_{mj}\hat{r})C_p(\lambda_{pk}\hat{r})\frac{d\hat{r}}{\hat{r}};$$

$$KK_{nmp}(i,j,k) = \int_a^1 C_n(\lambda_{ni}\hat{r})C_m(\lambda_{mj}\hat{r})C_p(\lambda_{pk}\hat{r})\hat{r}d\hat{r};$$

$$IDD_1^{qp}(i,j,n) = \int_a^1 C_q''(\lambda_{qi}\hat{r})C_q'(\lambda_{qj}\hat{r})C_p(\lambda_{pn}\hat{r})\hat{r}d\hat{r};$$

$$IDD_2^{qp}(i,j,n) = \int_a^1 C_q'(\lambda_{qi}\hat{r})C_q(\lambda_{qj}\hat{r})C_p'(\lambda_{pn}\hat{r})\frac{d\hat{r}}{\hat{r}};$$

$$IDD_3^{qp}(i,j,n) = \int_a^1 C_q'(\lambda_{qi}\hat{r})C_q(\lambda_{qj}\hat{r})C_p(\lambda_{pn}\hat{r})\frac{d\hat{r}}{\hat{r}^2};$$

$$IDD_4^{qp}(i,j,n) = \int_a^1 C_q(\lambda_{qi}\hat{r})C_q(\lambda_{qj}\hat{r})C_p(\lambda_{pn}\hat{r})\frac{d\hat{r}}{\hat{r}^3};$$

$$IDD_5^{qp}(i,j,n) = \int_a^1 C_q'(\lambda_{qi}\hat{r})C_q'(\lambda_{qj}\hat{r})C_p'(\lambda_{pn}\hat{r})d\hat{r};$$

$$IDD_6^{qp}(i,j,n) = \int_a^1 C_q'(\lambda_{qi}\hat{r})C_q'(\lambda_{qj}\hat{r})C_p(\lambda_{pn}\hat{r})\frac{d\hat{r}}{\hat{r}};$$

$$IA_{nm}(i,j) = \int_a^1 C_n'(\lambda_{ni}\hat{r})C_m'(\lambda_{mj}\hat{r})\hat{r}d\hat{r};$$

$$JA_{nm}(i,j) = \int_a^1 C_n(\lambda_{ni}\hat{r})C_m(\lambda_{mj}\hat{r})\frac{d\hat{r}}{\hat{r}}.$$

1.3 Simple Cross-Products

$$D_1(i,j,k,l) = \sum_i\sum_j\sum_k\sum_l f_{1i}f_{1j}f_{1k}f_{1l}C_1(\lambda_{1i})C_1(\lambda_{ij})C_1(\lambda_{ik})C_1(\lambda_{il});$$

$$D_2(i,j,k,l) = \sum_i\sum_j\sum_k\sum_l f_{1i}f_{1j}f_{1k}f_{1l}C_1(\lambda_{1i}a)C_1(\lambda_{ij}a)C_1(\lambda_{ik}a)C_1(\lambda_{il}a)a;$$

$$D_3(i,j,k,l) = \sum_i\sum_j\sum_k\sum_l f_{1i}f_{1j}f_{1k}f_{1l}C_1''(\lambda_{1i})C_1(\lambda_{ij})C_1''(\lambda_{ik})C_1(\lambda_{il});$$

$$D_4(i,j,k,l) = \sum_i\sum_j\sum_k\sum_l f_{1i}f_{1j}f_{1k}f_{1l}C_1''(\lambda_{1i}a)C_1(\lambda_{ij}a)C_1''(\lambda_{ik}a)C_1(\lambda_{1l}a)a;$$

$$D_5(i,j,k,l) = \sum_i\sum_j\sum_k\sum_l f_{1i}f_{1j}f_{1k}f_{1l}C_1(\lambda_{1i})C_1(\lambda_{1j})C_1''(\lambda_{1k})C_1(\lambda_{1l});$$

$$D_6(i,j,k,l) = \sum_i\sum_j\sum_k\sum_l f_{1i}f_{1j}f_{1k}f_{1l}C_1(\lambda_{1i}a)C_1(\lambda_{1j}a)C_1''(\lambda_{1k}a)C_1(\lambda_{1l}a)a;$$

$$D_7^p(i,j,n) = \sum_i\sum_j\sum_n f_{1i}f_{1j}f_{pn}C_1(\lambda_{1i})C_1(\lambda_{1j})C_p(\lambda_{pn});$$

$$D_8^p(i,j,n) = \sum_i\sum_j\sum_n f_{1i}f_{1j}f_{pn}C_1(\lambda_{1i}a)C_1(\lambda_{1j}a)C_p(\lambda_{pn}a)a;$$

$$D_9^p(i,j,n) = \sum_i\sum_j\sum_n f_{1i}f_{1j}f_{pn}C_1(\lambda_{1i})C_1''(\lambda_{1j})C_p(\lambda_{pn});$$

$$D_{10}^p(i,j,n) = \sum_i\sum_j\sum_n f_{1i}f_{1j}f_{pn}C_1(\lambda_{1i}a)C_1''(\lambda_{1j}a)C_p(\lambda_{pn}a)a;$$

$$t_{nm}(i,p) = C_n(\lambda_{ni})C_m(\lambda_{mp}) - aC_n(\lambda_{ni}a)C_m(\lambda_{mp}a);$$
$$v_{nm}(i,p) = C_n(\lambda_{ni})C_m(\lambda_{mp}) - \frac{C_n(\lambda_{ni}a)C_m(\lambda_{mp}a)}{a};$$
$$tt_{nm}(i,p) = C_n(\lambda_{ni})C_m(\lambda_{mp}) + aC_n(\lambda_{ni}a)C_m(\lambda_{mp}a);$$
$$vv_{nm}(i,p) = C_n(\lambda_{ni})C_m(\lambda_{mp}) + \frac{C_n(\lambda_{ni}a)C_m(\lambda_{mp}a)}{a};$$
$$u_{nm}(i,j,p) = C_n(\lambda_{ni})C_n(\lambda_{nj})C_m(\lambda_{mp}) - \frac{C_n(\lambda_{ni}a)C_n(\lambda_{nj}a)C_m(\lambda_{mp}a)}{a};$$
$$w_{nm}(i,j,p) = C_n(\lambda_{ni})C_n(\lambda_{nj})C_m(\lambda_{mp}) - aC_n(\lambda_{ni}a)C_n(\lambda_{nj}a)C_m(\lambda_{mp}a).$$

2. Hyperbolic Functions

2.1 Definitions and Cross-Product Integrals

$$g_{nm} = \frac{\cosh \lambda_{nm}(\hat{z}+\hat{h})}{\cosh \lambda_{nm}\hat{h}};$$
$$F_{ijkl} = \sum_i \sum_j \sum_k \sum_l \frac{f_{1i}f_{1j}f_{1k}f_{1l}}{\cosh \lambda_{1i}\hat{h} \cosh \lambda_{ij}\hat{h} \cosh \lambda_{ik}\hat{h} \cosh \lambda_{il}\hat{h}};$$
$$F_{ijp} = \sum_i \sum_j \sum_p \frac{f_{1i}f_{1j}f_{1p}}{\cosh \lambda_{1i}\hat{h} \cosh \lambda_{1j}\hat{h} \cosh \lambda_{1p}\hat{h}};$$
$$G_1^{nm}(i,j,k,l) = \int_{-\hat{h}}^{0} g_{ni}g_{nj}g_{mk}g_{ml}\,d\hat{z};$$
$$G_2^{nm}(i,j,k,l) = \int_{-\hat{h}}^{0} \acute{g}_{ni}g_{nj}\acute{g}_{mk}g_{ml}\,d\hat{z};$$
$$G_3^{nm}(i,j,k,l) = \int_{-\hat{h}}^{0} \acute{g}_{ni}\acute{g}_{nj}\acute{g}_{mk}\acute{g}_{ml}\,d\hat{z};$$
$$GG_1^{qp}(i,j,n) = \int_{-\hat{h}}^{0} g_{qi}g_{qj}g_{pn}\,d\hat{z};$$
$$GG_2^{qp}(i,j,n) = \int_{-\hat{h}}^{0} \acute{g}_{qi}\acute{g}_{qj}g_{pn}\,d\hat{z};$$
$$GG_3^{qp}(i,j,n) = \int_{-\hat{h}}^{0} g_{qi}g_{qj}\acute{g}_{pn}\,d\hat{z};$$
$$GG_4^{qp}(i,j,n) = \int_{-\hat{h}}^{0} \acute{g}_{qi}g_{qj}\acute{g}_{pn}\,d\hat{z}.$$

2.2 Simple Cross-Products

$$\beta_{nm}(i,p) = \frac{\lambda_{ni}\alpha_{ni} - \lambda_{mp}\alpha_{mp}}{\lambda_{ni}^2 - \lambda_{mp}^2}, \quad \text{for} \quad \lambda_{ni} \neq \lambda_{mp};$$
$$= \frac{1}{2}\left[\frac{\hat{h}}{\cosh^2 \lambda_{ni}\hat{h}} + \frac{\alpha_{ni}}{\lambda_{ni}}\right], \quad \text{for} \quad \lambda_{ni} = \lambda_{mp},$$
$$\beta^*_{nm}(i,p) = \frac{\lambda_{ni}\lambda_{mp}(\lambda_{ni}\alpha_{mp} - \lambda_{mp}\alpha_{ni})}{\lambda_{ni}^2 - \lambda_{mp}^2}, \quad \text{for} \quad \lambda_{ni} \neq \lambda_{mp};$$
$$= \frac{\lambda_{ni}^2}{2}\left[\frac{-\hat{h}}{\cosh^2 \lambda_{ni}\hat{h}} + \frac{\alpha_{ni}}{\lambda_{ni}}\right], \quad \text{for} \quad \lambda_{ni} = \lambda_{mp}.$$

2.3 Combinations of Hyperbolic and Bessel Function Cross-Products

$$k_{nm}(i,p) = \beta^*_{nm}(i,p)t_{nm}(i,p);$$
$$l_{nm}(i,p) = \beta_{nm}(i,p)v_{nm}(i,p);$$
$$kk_{nm}(i,p) = \beta^*_{nm}(i,p)tt_{nm}(i,p);$$
$$ll_{nm}(i,p) = \beta_{nm}(i,p)vv_{nm}(i,p);$$
$$I2_{nm}(i,j) = \frac{IA_{nm}(i,j)}{\cosh \lambda_{ni}\hat{h} \cosh \lambda_{mj}\hat{h}};$$
$$J2_{nm}(i,j) = \frac{JA_{nm}(i,j)}{\cosh \lambda_{ni}\hat{h} \cosh \lambda_{mj}\hat{h}}.$$

APPENDIX VI: MECHANICAL ANALOGY OF A LINEAR SYSTEM

1. One-Degree-of-Freedom

It is assumed that the action of the sloshing liquid within the nutation damper is modelled by a mass-spring-dashpot system as shown in Fig. VI-1.

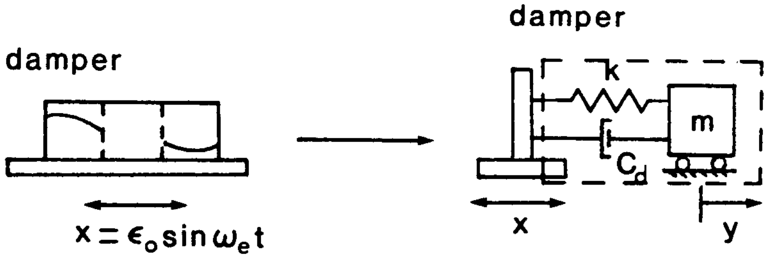

Fig. VI-1 Mechanical representation of a nutation damper

This common approach, incomplete as nonlinear effects are not included, can be a useful tool for understanding the more complex fluid mechanics problem. The motion of the liquid, represented by y here, imposes inertia and damping forces on the moving base (Fig. VI-2). They can be nondimensionalized in terms of an added mass and reduced damping ratio $|M_a/M_l|$ and $\eta_{r,l}$, respectively.

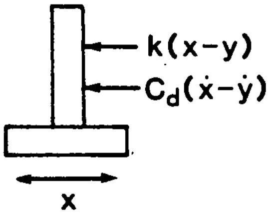

Fig. VI-2 Forces acting on the moving base

Standard vibration theory gives $(x-y)$, and in turn yields:

$$|\frac{M_a}{M_l}| = \frac{\hat{\omega}^2 - 1}{(\hat{\omega}^2-1)^2 + (2\eta\hat{\omega}^2)^2}; \quad \eta_{r,l} = \frac{\eta\hat{\omega}}{(\hat{\omega}^2-1)^2 + (2\eta\hat{\omega})^2}, \qquad (VI.1)$$

where:

$$\hat{\omega} = \frac{\omega_e}{\omega_n}; \quad \omega_n = \sqrt{k/m}, \quad \text{and} \quad \eta = \frac{C_d}{2m\omega_e}.$$

(VI-1) is plotted below against $\hat{\omega}$ for various η. The added mass is always zero at resonance ($\hat{\omega} = 1.0$), with diminishing maxima at larger damping (Fig. VI-3a), while $\eta_{r,l}$ shows higher and narrower peaks for decreasing η (Fig. VI-3b). The energy ratio is also derived as

$$E_{r,l} = \eta \frac{8\pi}{(1 + 1/\hat{\omega}^2)\hat{\omega}}, \tag{VI.2}$$

showing an increase with $\hat{\omega}$ for a given η (Fig. VI-3c).

2. Two-Degree-of-Freedom System

The aerodynamic model of section 4.4 fitted with the rotating damping device can be represented by the vibration absorber configuration shown below:

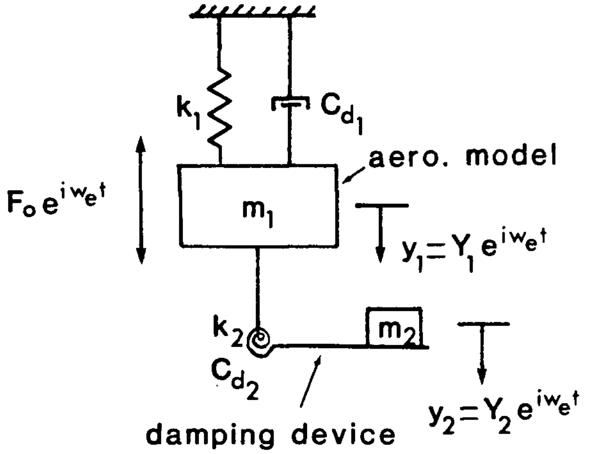

Fig. VI-4 Mechanical representation of the transmission line test arrangement

The standard formulation for such problems leads to the following eigenvalue equation[110],

$$\overline{\omega_n}^4 - \overline{\omega_n}^2(\omega_0^2 + 1 + s) + \omega_0^2 = 0, \tag{VI.3}$$

where $s = \frac{m_2}{m_1}$; $\omega_0 = \frac{\omega_1}{\omega_2}$; with $\omega_1^2 = \frac{k_1}{m_1}$, $\omega_2^2 = \frac{k_2}{m_2}$; and $\overline{\omega_n} = \frac{\omega_n}{\omega_2}$.
With the experimental determination of ω_1, ω_2, and ω_n, the inertia ratio s can subsequently be determined from (VI.3) as,

$$s = -\left(\frac{\omega_0^2}{\omega_n^2} - 1\right)\left(\overline{\omega_n^2}^2 - 1\right). \tag{VI.4}$$

Assuming C_1 to be small, the response of the model is,

$$Y_1 = \frac{F_0}{k_1}\omega_0^2 \left\{ \frac{(1 - \overline{\omega}^2) + \overline{\eta}_2^2}{\Delta^2 + \overline{\eta}_2^2 s_0^2} \right\}^{1/2}, \tag{VI.5}$$

where $\overline{\omega} = \frac{\omega_e}{\omega_2}$; Δ is the left hand side of relation (VI.3) when substituting $\overline{\omega_n}$ by $\overline{\omega}$; $\overline{\eta}_2 = \frac{C_{d2}}{m_2\omega_2}\overline{\omega}$; and $s_0 = \omega_0^2 - \overline{\omega}_n^2(1 + s)$. At resonance, (VI.5) reduces to

$$Y_1 = \frac{F_0}{k_1} \frac{[\overline{\eta}_2^2 + (1 - \overline{\omega}_n^2)^2]^{1/2}}{|\overline{\eta} s_0|}\omega_0^2, \tag{VI.6}$$

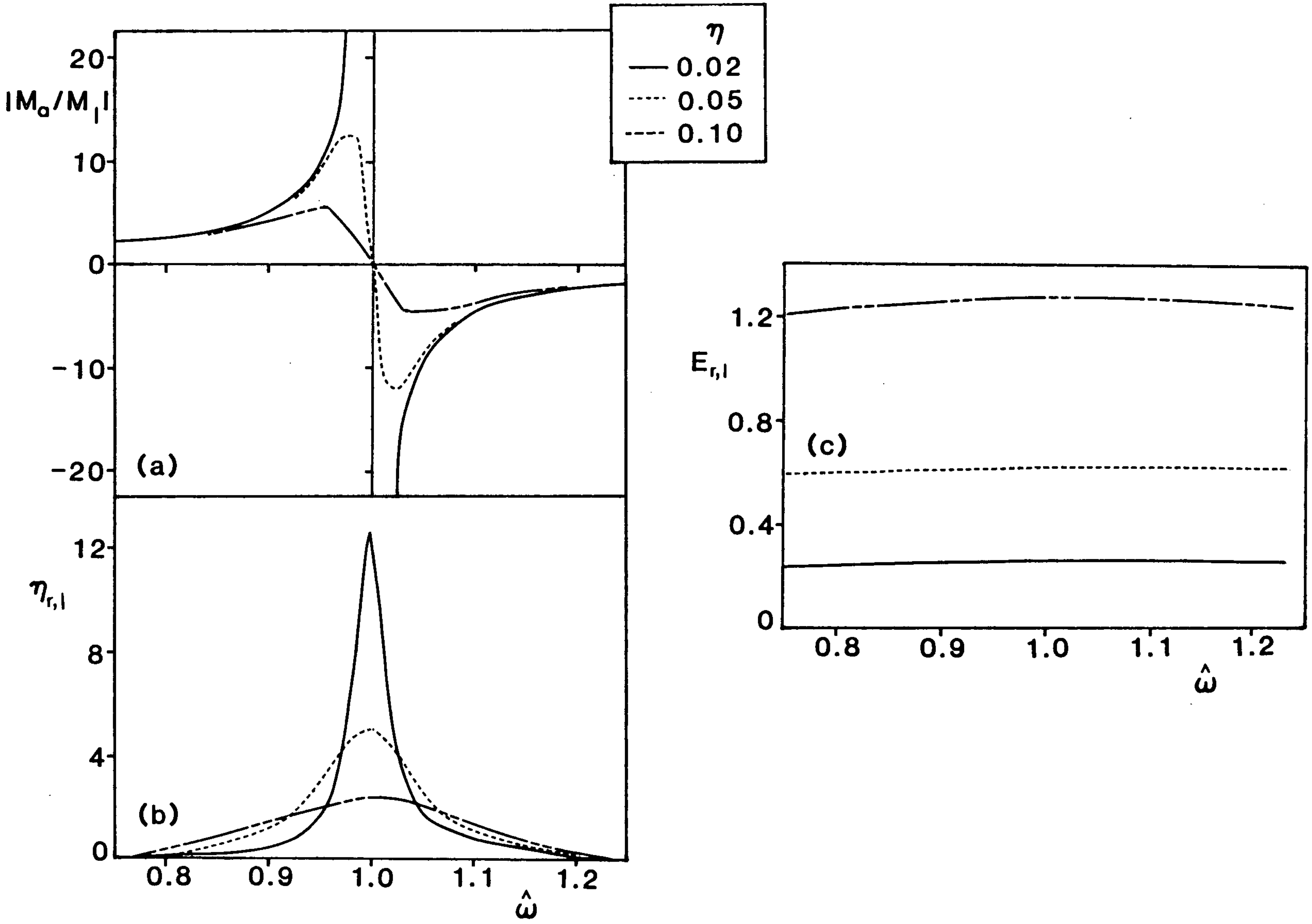

Fig. VI-3 One-degree-of-freedom system characteristics at resonance showing: (a) $|M_a/M_l|$; (b) $\eta_{r,l}$; (c) $E_{r,l}$

as $\Delta = 0$ and $\overline{\omega} = \overline{\omega}_n$. With the parameters of (VI.3), Y_1 is found to be a function of $\overline{\eta}_2$, ω_0 and s, for a model with given m_1, k_1, and exciting force F_0. Thus the damper design can be optimized.

Note: For the experiment,

$$m_1 = 1.600Kg.$$
$$m_2 = M_d + m_p \frac{l_p}{2L},$$

where:

M_d = damper mass;
m_p, l_p = damper plate mass and length, respectively;
L = distance from damper center of gravity to system center of rotation.

According to the inertia forces in the vertical direction (Fig. VI-6),

$$F = m_2 \ddot{y}_2 = M_d L \ddot{\Theta} + m_p \frac{l_p}{2} \ddot{\Theta}. \tag{VI.7}$$

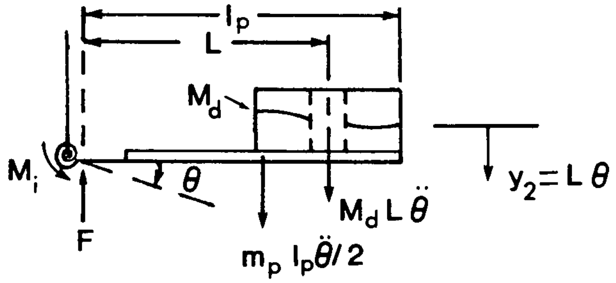

Fig. VI-5 Force diagram for the damping device

APPENDIX VII: WIND-INDUCED OSCILLATION AMPLITUDE CALCULATION

1. Galloping Theory with Equivalent Damping

According to Parkinson's theory[111], the amplitude Y is given by

$$\frac{dY^2}{d\tau} = nA_1U[(1-\frac{U_0}{U})Y^2 + \frac{B_3}{U}Y^4 + ... + \frac{B_NY^{N+1}}{U^{N-1}}], \qquad (VII.1)$$

where:

$$N = 1,3,5,..; \quad n = \frac{\rho_a L_m d_m^2}{2M}; \quad U_0 = \frac{2\eta}{nA_1};$$

A_1 = 1st coefficient of the polynomial fit for C_{fy};

$B_3, ..., B_N$ = integration constants times higher coefficients of C_{fy}.

A limit cycle is reached for

$$\frac{dY^2}{d\tau} = 0, \quad \text{stable for} \quad \frac{d[dY^2/d\tau]}{dY^2} < 0, \quad \text{i.e.,}$$

$$(1-\frac{U}{U_0}) + 2B_3(\frac{Y}{U})^2 + ... + \frac{N+1}{2}(\frac{Y}{U})^{N-1} < 0. \qquad (VII.2)$$

Based on the dissipated energy per cycle, the equivalent damping ratio is a function of Y (average amplitude for the cycle). A polynomial fit to follow its variation is used ,

$$\eta = D_0 + D_1Y + D_2Y^2 + ... + D_MY^M. \qquad (VII.3)$$

Relation (VII.1) is still valid as it also represents an average quantity for the cycle. U_0 is however no longer independent of Y and the stability equation becomes,

$$[\text{Left hand side of (VII.2)}]$$
$$-\frac{1}{nA_1U}[D_1Y^1 + 2D_2Y^2 + ... + MD_MY^M] < 0. \qquad (VII.4)$$

2. Vortex Resonance of a Full Scale Chimney Fitted with Nutation Dampers

Recently, mathematical models for circular cross-section structures have been developed to predict full- scale response[112–113]. The case of a uniform 5m diameter steel chimney with a height of 80 m, mass density of 1500 Kg/m, and structural damping of 0.3%, was considered by Vickery et al.[114] They determined that a damping ratio $\eta_s = 2.2\%$ is required to keep $Y \le 0.1$, with the response approximately proportional to $\eta_s^{-1/2}$ in the range of interest here. With a natural frequency of 0.3 Hz, such structure can be fitted with a nutation damper at the tip so that,

$$\eta_{r,l}\frac{M_l}{M_e} = \eta_s, \qquad (VII.5)$$

where the modal mass

$$M_e = \int_0^H m(z)|\frac{Y_p(z)}{Y}|^2 dz \qquad (VII.6)$$

is found to be 30 000 Kg. Here:

$$\begin{aligned} m(z) &= \text{chimney mass per unit length;} \\ z &= \text{vertical axis with origin at the ground level;} \\ H &= \text{height of the chimney;} \\ Y_p(z) &= \text{horizontal deflection at height } z; \\ Y &= \text{tip deflection.} \end{aligned}$$

Considering a nutation damper similar to model#7 used in this study with $h/d = 1/2$ and $D/d = 4.10$, the conditions of sloshing resonance requires:

$$\omega_e \approx \omega_{11}. \tag{VII.7}$$

Now, $$\omega_e = [\frac{\lambda_{11} g}{R_0} \tanh \lambda_{11} \hat{h}]^{1/2}, \tag{VII.8}$$

thus, $$R_0 = \frac{\lambda_{11} g}{(2\pi f_{11})^2} \tanh \frac{\lambda_{11}}{5.1}. \tag{VII.9}$$

$R_0 = 0.836$ m as $\lambda_{11} = 1.255$ for this damper, which yields
$d = 0.327$ m with a container liquid mass m_l given by,

$$m_l = \rho_l \pi (\frac{D}{d})(\frac{h}{d}) d^3. \tag{VII.10}$$

for oil, $m_l = 180.2$Kg.

From Chapter 3, $\eta_{r,l} \geq 1.0$ for $\epsilon_0/d \leq 1.0$ and $\hat{\omega} \approx 1.0$. At $Y = 0.1$ corresponding to $\eta_s = 0.022$, $\epsilon_0/d = 1.53$ and therefore it is assumed that $\eta_{r,l} < 1.0$ (the variation with amplitude is not too pronounced here and the steady-state results should apply reasonably well). Taking $\eta_{r,l} \approx 0.7$ leads to

$$M_l = 943 \quad \text{Kg},$$

thus requiring the use of 5 to 6 damper units (Fig. VII-1). If a lower response is needed, e.g. peak $Y = 0.06$, a damping of $\eta_s = 0.04$ is expected (from Y proportional to $\eta_s^{-1/2}$ relationship). ϵ_0/d is then 0.92 and $\eta_{r,l}$ is of order 1, which yields $M_l = 1200$ Kg, or about 7 units. This compares advantageously with the 1500 Kg pendulum tuned mass damper proposed in reference 114.

For higher frequencies such as f=0.8 Hz considered in the same article, more damper units are needed as a lower D/d ratio is required to meet the condition $\hat{\omega} = 1.0$. This further reduces efficiency and it is found that for $D/d = 1.89$ and $h/d = 0.5$,

$$R_0 = 0.302 \quad \text{m}, \quad d = 0.209 \quad \text{m},$$
$$m_l = 21.7 \quad \text{Kg (oil), and} \quad M_l = 2200 \quad \text{Kg}.$$

Thus installation of 102 damper units is required. A ring could easily be designed to fit all the containers, as illustrated in Fig. VII-2.

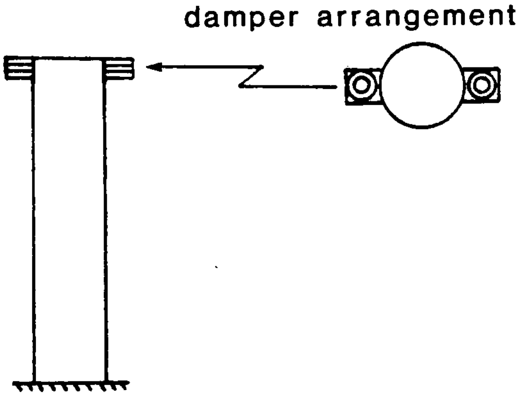

Fig. VII-1 Steel chimney with 6 nutation dampers

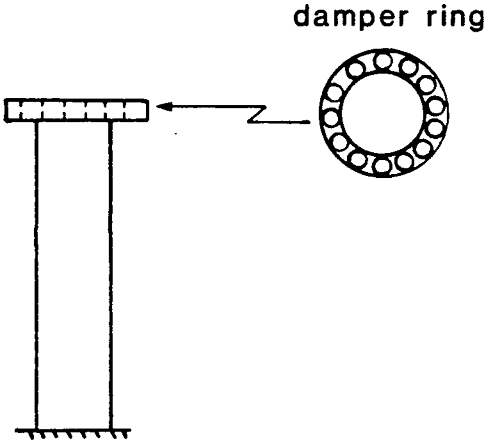

Fig. VII-2 Steel chimney with nutation damper ring

LIST OF PUBLISHED ARTICLES

- Modi, V.J., and Welt, F., "Nutation Dampers and Suppression of Wind Induced Instabilities", *Proceedings of the ASME Joint Multidivisional Symposium on Flow-Induced Vibration, 1984 ASME Winter Annual Meeting*, New Orleans, Louisiana, Dec. 1984, editors: M.P. Paidoussis, O.M. Griffin, and M. Sevik, Vol. 1, pp. 173-187.

- Modi, V.J., and Welt, F., "On the Control of Instabilities in Fluid-Structure Interaction Problems", *Proceedings of the 2nd International Symposium on Structural Control*, Waterloo, Canada, July 1985, Editor: H.H.E. Leipholz, pp. 473-495.

- Modi, V.J., Welt, F., and Irani, M.B., "On the Nutation Damping of Fluid-Structure Interaction Instabilities and its Application to Marine Risers", *Fifth International Symposium and Exhibition on Offshore Mechanics and Artic Engineering*, Tokyo, Japan, April 13-18, 1986, Paper No. OMAE-1197; also *Proceedings of the Conference*, Editors: J.S. Chung, et al., Vol. 3, ASME Publisher, New York, pp. 408-416.

- Modi, V.J., and Welt, F., "On the Control of Instabilities in Fluid-Structure Interaction Problems", Proceedings of the 4th IFAC Symposium on Control of Distributed Parameter Systems, Pasadena, California, U.S.A., June 30-July 3, 1986, editor: G. Rodriguez, Pergamon Press, London, in press.

- Modi, V.J., and Welt, F., "Visualization of Sloshing Motion in Nutation Dampers", *Proceedings of the 4th International Symposium on Flow Visualization*, Paris, France, Aug. 1986, Editor: C. Véret, Hemisphere Publishing Corporation, pp. 353-358.

- Welt, F., and Modi, V.J., "On the Control of Instabilities in Fluid-Structure Interaction Problems Using Nutation Dampers", *Proceedings of the 3rd Asian Congress of Fluid Mechanics*, Tokyo, Japan, Sept. 1-5, 1986, Editor in Chief: T. Matsui, pp. 616-619.

- Irani, M.B., Modi, V.J., and Welt, F., "Riser Dynamics with Internal Flow and Nutation Damping", *Proceedings of the 6th International Symposium on Offshore Mechanics and Artic Engineering*, Houston, Texas, U.S.A., March 1987, Editors: J.S. Chung, et al., Vol. 1, pp. 119-125.

- Modi, V.J., and Welt, F., "On the Vibration Control Using Nutation Dampers", *Proceedings of the International Conference on Flow Induced Vibrations*, Bow-

ness on Windermere, England, May 1987, the British Hydromechanics Research Association, pp. 369-376; also entitled "An Investigation of Nutation damping and its Application to Wind Engineering", *Proceedings of the 11th Congress of Apllied Mechanics*, June 1987, Vol. 2, pp. E-81-E-82.

- Modi, V.J., and Welt, F., "Damping of Wind Induced Oscillations Through Liquid Sloshing", *Proceedings of the 7th International Conference on Wind Engineering*, Aachen, Federal Republic of Germany, July 1987, Editors: C. Kramer and H. Gerhardt, pp. 143-152; also *Journal of Wind Engineering and Industrial Aerodynamics*, in press.

- Irani, M.B., Modi, V.J., and Welt, F., "Dynamics of Offshore Risers with Internal Flow in the Presence of Ocean Waves and Currents", *Proceedings of the IMACS/IFAC International Symposium on Modelling and Simulation of Distributed Parameter Systems*, Hiroshima, Japan, Oct. 1987, pp. 329-336.